CRANFIELD UNIVERSITY

MICHAŁ ORŁOWSKI

Experimental and Numerical Investigation on the Bird Impact Resistance of Novel Composite Sandwich Panels

School of Aerospace, Transport and Manufacturing (SATM)
Centre of Applied Mechanics

PhD Thesis
Academic year: 2014–2015

Supervisor: Prof. Rade Vignjevic
April 2015

CRANFIELD UNIVERSITY

School of Aerospace, Transport and Manufacturing (SATM)
Centre of Applied Mechanics

PhD Thesis
Academic year: 2014–2015

Michał Orłowski

Experimental and Numerical Investigation on the Bird Impact Resistance of Novel Composite Sandwich Panels

Supervisor: Prof. Rade Vignjevic
April 2015

This thesis is submitted in partial fulfilment of the requirements for the degree of *Philosophiæ Doctor* (PhD)

Abstract

Bird strikes represent a major hazard to the aerospace composite structures, due to their low impact resistance. Accurate selection and lay up of the materials in the composite structure can significantly improve the out of plane properties of the composites. However, application of the complex hybrid sandwich composites into bird strike proof structures was not investigated yet. Therefore, this work was focused on the soft body impact resistance of a novel composite design for aerospace applications. The investigation was divided into experimental and modelling parts.

In the beginning of this thesis, the numerical techniques for modelling of bird impact and composite materials were studied. The theoretical background for the corresponding issue was provided, followed by the thorough validation of the existing numerical approaches.

A Smooth Particle Hydrodynamic (SPH) method was chosen for the modelling of the soft body. This modelling technique was validated against experimental data for the rotating fan blade. Three parametric studies of bird impacting fan blades revealed strong influence of the bird impact location and timing on the final deformed shape of the blade. Moreover, it was proved that the SPH is capable of reproducing the exact load on the structure and is appropriate technique for modelling bird strikes.

After the validation of the SPH bird against the metallic structures, it was essential to investigate impact resistance of composite materials and available modelling techniques in LS-DYNA. Validation of existing failure composite material models was presented together with the validation of the delamination modelling techniques. Single element tests performed with the composite material models proven that MAT_59 is the most suitable, commercially available material model for modelling composite structures. Nevertheless, as every other material model in LS-DYNA,

MAT_59 does not engage equation of state. Lack of equation of state, does not allow for modelling of shock waves propagation in the material. Evaluation of delamination modelling techniques proven that delamination modelled with the cohesive elements is highly dependent on the mesh density. Moreover, it revealed that stability of the cohesive elements used for modelling the interface is questionable, due to the strain energy stored in the material. Based on the evaluation of the failure and delamination modelling techniques, the most suitable approaches were brought forward to the analysis stage of the new composite layup.

Furthermore, benefits of foam materials utilisation in a composite sandwich structures were presented together with an investigation for the most suitable foam modelling approach. The results of this investigation showed that only one of the examined material models was capable of modelling failure of the material due to the excessive shear deformation.

After the modelling approaches were validated and fully understood, two novel composite designs were introduced. The first of the new composite designs was made of a carbon fibre corrugated panel adhesively joined to the woven carbon fibre face sheets. Gaps between the composite panels were filled with polyurethane foam. The second of the new composite designs consisted of carbon fibre wrapped tubes, filled with polyurethane foam, embedded within the woven composite face sheets. The manufacturing process together with an adequate non-destructive inspection technique was provided in order to fully describe the novel design.

The final stage of examining the impact resistance of the new composite designs was performed with a high velocity soft body impact on the composite coupons. The experimental part of the process consisted of a design of the bird release system, calibration of the gas gun and the velocity measurement system, manufacturing and validation of birdlike gelatine projectiles used for the impact.

The experimental results obtained for the corrugated panel shown good impact resistance of the novel design. No internal or back surface damage was detected within the thermography inspection. Nevertheless, some extent of damage was observed on the impacted surface of the samples. Results obtained with the tubular structure shown excellent impact resistance of the novel layup. No damage was visible on external surfaces. Additionally, thermography inspection of the samples did not

reveal any internal damage of the composite panels. No indication of internal and back surface damage highlights very good impact resistance of the novel composite layups. Good impact resistance combined with a low structural weight makes both of the designs suitable for aerospace applications.

Numerical results obtained with LS-DYNA were compared to the experimental results, indicating good agreement between the analyses and experiment. However, some differences between the failure modes were observed. The differences between the numerical and experimental results highlighted the need for development of more reliable composite material models, especially for dynamic analyses.

Acknowledgements

First of all I would like to thank my supervisor Professor Rade Vignjevic for the opportunity of being involved in this project and for his support and advice. I am extremely grateful for his scientific contribution to my work. I very appreciate the patience and understanding at the times when I struggled to find motivation.

Great thanks to Dr Tom De Vuyst, Dr Kevin Hughes and Dr James Campbell for their patience and for sharing their knowledge with me. Without their invaluable help with technical issues and the experiment arrangements I would not be able to finish the project. Thanks also to Jarryd Braithwaite for helping with the experiments. Great thanks to Dr Alex Skordos and Jim Hurley for enabling me to work in their laboratory and for help I received with the manufacturing of composite samples. Special thanks to Dr Pavan Addepalli for his help with the thermographic inspection of the samples.

I would like to thank to my parents for al their support, patience and understanding during my PhD. Without them and their motivation it would be difficult for me to get to the point I am now.

Great thanks to Katarzyna Ledwoch for being with me during the hardest time of my PhD studies. Without her support and patience it would be difficult to complete the write up on time.

Special thanks to my best friend Stefan Velikov for his help, motivation and his contribution to improve my English. He was always there for me, sharing good and bad moments of my PhD adventure.

I would also like to thank Michał Czapiński, Tongyu Wu, Giacomo Struzziero, Artur Kopczyński, Tomek Stańkowski and Michele Vianello for being my friends and going

together with me through all the stages of my studies. Great thanks also to Mikołaj Łukaszewicz and Tomek Dudziak as they helped me many times during my stay in Cranfield.

Thanks to all my office mates for sharing with me the working space and all the good time we had together in our PhD room. Thanks to your help and good words every scientific problem I encountered never broke my faith in my skills and knowledge.

I would also like to thank all my friends from the Cranfield Volleyball Club for representing and defending colours of University at courts around UK. It was a pleasure and honour to play with you guys.

Last but not least, I would like to thank my friends from Poland for their interest and motivation along my studies. I could always count on their good words and support during the hard times.

Contents

List of Tables

List of Figures

Nomenclature

α	nonlinear shear stress parameter
β	the ratio of mode mixity
δ	displacement
$\dot{\delta}$	displacement rate
$\dot{\varepsilon}$	strain rate
η	parameter
γ	material parameter/ volumetric strain
γ_0	Gruneisen coefficient
μ	coefficient
ν	Poisson's ratio
ω	angular velocity/ damage parameter
ρ	density
σ	stress
σ_c	strength
σ_t	strength
σ_y	yield strength

$\tau_j k$	shear stress in 'jk' plane/ interface traction
θ	angle
ε	strain/elongation at break
ε_j	strain in 'j' direction
ε_{fi}	failure strain
A	area
B	material parameter
b	first order volume correction coefficient
C	strain rate dependence coefficient/ velocity curve intercept
c	speed of sound
C_v	heat capacity
D	diameter
d	damage parameter/ damage coefficient
E	Young's modulus (elastic modulus)/ energy
e	penetration depth/ failure parameter
E_h	plastic modulus
E_i	internal energy/ impact energy
EN	stiffness in normal direction
ET	stiffness in transverse direction
F	force/ load
F_c	contact force
F_j	parameter, for j=1,. . . ,6

F_{jk}	parameter, for j,k=1,. . . ,6
G	shear modulus
G_{iC}	critical energy release rate
h	length / height
K	stiffness
L	length
l	length
m	mass/ temperature dependence exponent/ parameter
n	strain hardening exponent
P	pressure
P^{max}	maximum load
Q	momentum
R	radius
r	radius
S	slope coefficient
S_{XY}	shear strength in XY plane
T	temperature/ peak traction in normal direction
t	time/ thickness
U	velocity
V	velocity
v	velocity
w	width

X	longitudinal strength
Y	transverse strength
Z	normal strength

Abbreviations

ALE	Arbitrary Lagrangian Eulerian
BVID	Barely Visible Impact Damage
CISMG	Crashworthiness, Impact and Structural Mechanics Group
CSP	Corrugated sandwich panel
CZM	Cohesive Zone Model
DCB	double cantilever beam
EOS	Equation of state
FAA	Federal Aviation Administration
FE	Finite Element
FEM	Finite Elements Method
fps	frames per seconds
IBRG	International Bird Strike Research Group
IEPH	Isotropic- Elastic- Plastic- Hydrodynamic
MMB	mixed mode bending
NDI	Non Destructive Inspection
NDT	Non Destructive Technique
PPT	pulsed-phase thermography
PT	pulsed thermography
PUR	polyurethane
PVC	polyvinyl chloride
RSAI	residual strength after impact
SOP	Statement of Procedure

SPH	Smooth Particle Hydrodynamics
SSNGG	single stage nitrogen gas gun
SSP	standard sandwich panel
TSP	Tubular sandwich panel
UD	unidirectional
VMS	Velocity Measurement System

Chapter 1

Introduction

1.1 Composites and bird strike

Demand for weight reduction and increase of aircraft performance brought aircraft manufacturers toward the use of composite materials. First the secondary, and lately the primary, aircraft metallic structures started to be replaced with composite counterparts. The application of composite material enables for a significant weight reduction of the structures, which often comes with superior strength properties of the material. However, the excellent in-plane properties of the composites come together with very low impact resistance and through-thickness performance. The low impact performance of aircraft composite structures represents a major hazard in conjunction with the considerable risk related to bird strikes.

The first bird encounter was reported in the Wright brothers' diaries in 1905. Since then, the International Bird Strike Committee has reported 108 destroyed aircraft and 276 fatalities caused by bird strikes (Thorpe, 2012). According to the Federal Aviation Administration (FAA) (Dolber et al., 2014), 71% and 74% of the bird strikes on commercial and general aviation aircraft respectively occurred at or below 500 feet above ground level. In addition to the safety hazard, bird strikes cause significant economic losses to the airlines. Minimum cost of 117,740 of aircraft downtime hours and over a $187 million in direct or other monetary losses was projected to be the annual cost of wildlife strikes in the USA civil aviation industry (Dolber et al., 2014). In order to reduce the risk and losses related to bird strikes, the aerospace

authorities have developed a number of tests which need to be fulfilled by aircraft components before aircraft certification. Therefore, the composite counterparts also need to prove their survivability within the certification bird impact tests.

To improve bird impact resistance of the composite materials and to preserve the mass reduction trend in aerospace, novel composite sandwich panels were introduced within this work. Sandwich structures offer significant weight reduction by implementation of low density cores within the fibre reinforced face sheets. However, similarly to solid composites, sandwich composites suffer from very low impact resistance. Therefore, to improve the impact resistance of the sandwich composite structures, two novel designs with through thickness core reinforcement were proposed and investigated for their soft body impact resistance. In addition to an experimental bird impact test, a modelling approach was proposed for the completeness of the investigation.

1.2 Aims and objectives

The aim of the research work presented in this thesis was to investigate the bird impact resistance of two novel reinforced sandwich panels. The reinforcement of the sandwich panel was obtained by implementation of a corrugated panel and composite tubes within the sandwich panel foam core. The core reinforcement targeted to improve the impact resistance of the sandwich panels.

In order to achieve this aim, the following objectives were identified:

- Understand the bird impact theory and investigate the bird modelling techniques,
- Validation of the SPH method for the bird modelling through parametric studies of bird impact on engine fan blades,
- Understand and validate the numerical approaches for modelling of failure and damage in composite materials in transient finite element software LS-DYNA,
- Understand and validate the numerical methods for modelling the response of sandwich panel low density foam cores,

- Material selection and manufacturing of the corrugated and tubular sandwich samples,
- Manufacturing and validation of the gelatine birds,
- Non destructive inspection of the novel sandwich panels before and after bird impact test,
- Bird impact tests on the corrugated and tubular sandwich panels,
- Modelling of bird impact on the corrugated and tubular composite sandwich panels,
- Comparison of numerical and experimental results for the bird impact test on corrugated and tubular sandwich panels,
- Comparison of numerical results between the novel sandwich panels and standard sandwich panel of equivalent thickness.

1.3 Outline

Chapter 2 provides the background on the theory of bird strike. Furthermore, the numerical modelling techniques used for modelling of bird impact are provided, followed by a description of the model development. Finally, the results of the three parametric studies performed on the rotating metallic fan blade are described. The parametric studies investigated the bird shape, impact timing and bird impact location influence on the final deformed shape of the impacted blade.

Chapter 3 provides the theoretical background for modelling of failure and delamination of composite materials. In the beginning the impact resistance and damage modes of composites are introduced. Furthermore, the numerical techniques for modelling failure and delamination in LS-DYNA are described and validated with simple numerical analyses. Finally, the concluding remarks are presented based on the validations tests.

Chapter 4 provides an introduction to composite sandwich structures and their impact resistance. Furthermore, it introduces and explains the modelling techniques

for low density foam cores. Subsequently, the introduced modelling techniques for low density foams were validated through a range of different tests. The validation tests consisted of compression of single elements and indentation of foam blocks. In the end of the chapter the conclusions drawn from the validation tests are presented.

Chapter 5 explains all the steps necessary to perform the bird impact experiment. In the first part of the chapter, the design of the novel composite panels is introduced. This is followed by a description of the manufacturing process of the novel composite sandwich panels. Moreover, the manufacturing process of the gelatine birds and foam samples for the compression tests is described. The following subsection presents the gas gun and its calibration, and the design process for the bird release system essential for the experiment. Finally, the inspection of the samples before the impact tests was performed using infrared thermography.

Chapter 6 provides a description of the bird impact experiment. Subsequently, the non-destructive inspection of the impacted samples is described. Finally, the discussion of the experimental results is presented followed by the conclusions drawn from the impact tests.

Chapter 7 presents the model development for the numerical analyses of the bird impact tests. Further, the results of the numerical analyses are presented in terms of the failure of the composite samples and the energy absorption. The numerical results were compared to the results obtained from the impact tests. Moreover, the numerical results for the novel composite sandwich structures were compared to the numerical results obtained for the equivalent solid panels. Finally the conclusions from the numerical investigation are presented.

Chapter 8 contains the overall thesis conclusions and recommendations for future work.

Chapter 2

Modelling of bird strike on metallic fan blade

2.1 Introduction

This chapter provides the background on the theory of bird strike and the numerical results for the analysis of bird impact on a rotating metallic fan blade. The research was published in the International Journal of Impact Engineering (Vignjevic et al., 2013).

For better understanding, the structure of this chapter is illustrated in Figure 2.1.

Section 2.2 provides the theoretical background for the bird strike analysis. Impact phases, shock wave and release wave formation during the impact event are described. Furthermore, the momentum transfer and impact force during the bird impact are presented. Moreover, the importance of the Equation of State and slicing of the bird on the impact analysis is highlighted.

The subsequent section provides a brief overview on the bird modelling techniques in the finite element (FE) code.

Subsequently, the bird modelling is presented. In this section, geometries applicable to represent birds are introduced. Moreover, the selection of the bird material model is presented.

The subsequent section provides a description of the blade and rotor modelling. All the information regarding the geometry of the fan stage, the blade mesh and the selection of the blade material model are presented.

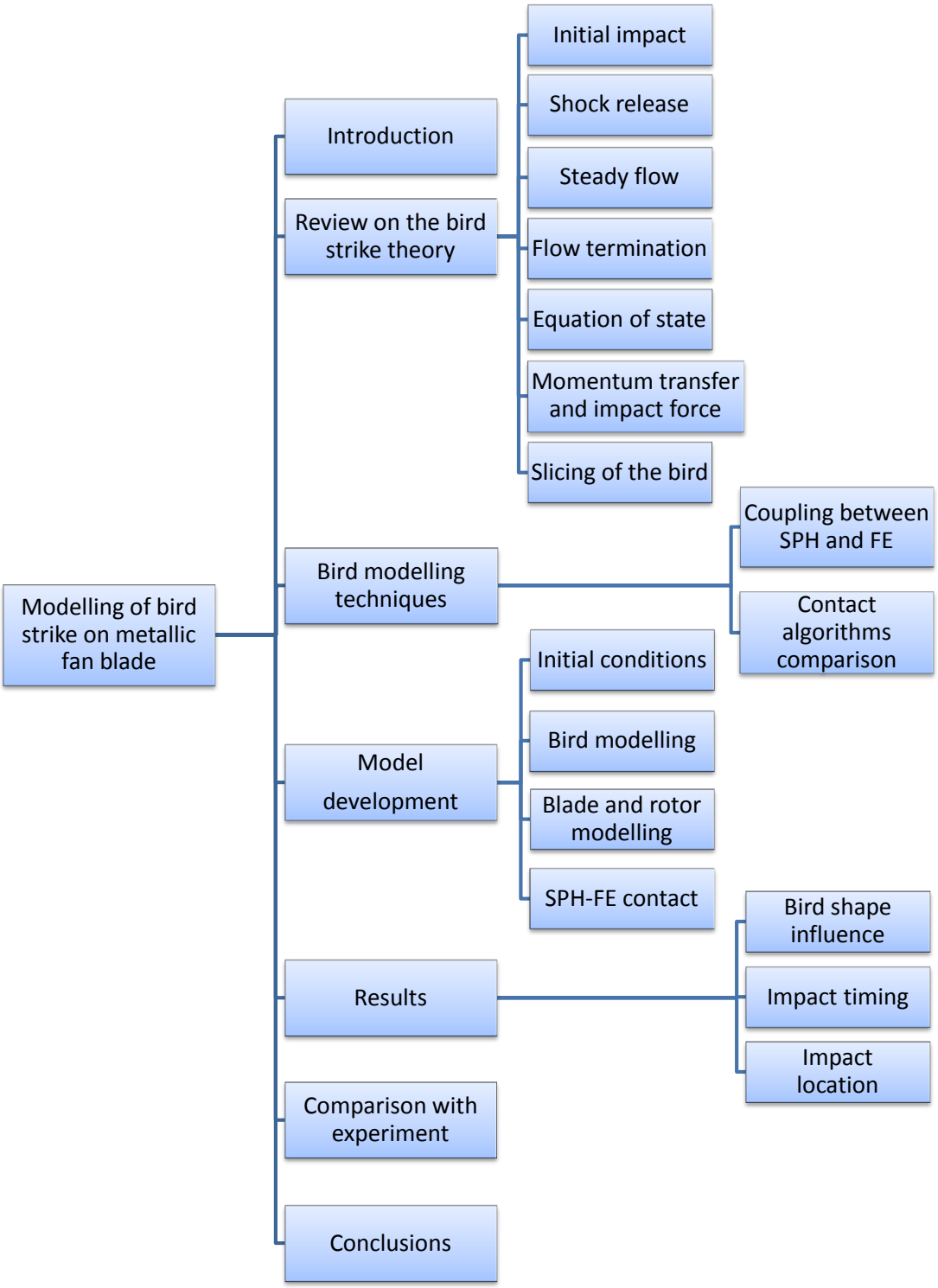

FIGURE 2.1: Chapter 2 structure.

The following section describes the initial conditions of the analysis. Treatment of contact between the bird (SPH particles) and the blade (FE mesh), was one of the key aspects in the bird strike analysis. The particle to node and the particle to surface contact algorithms, available in the code, were assessed and their performance compared. Moreover, this section describes the pre-stress of the blade due to the centrifugal force.

The next section describes the results of three parametric analyses, namely: influence of the bird shape; the bird impact location and impact timing. Stress distribution, contact forces graphs and the displacement for the crucial cross-sections of the blade are presented in this section.

Subsequently, the simulation results from the parametric studies were compared and validated against the final deformed shape of the blade recovered from the bird strike test.

Finally, the conclusions drawn from the bird strike analyses and comparison to the experimental results are presented.

2.2 Review on bird strike modelling

In bird ingestion tests, aircraft engines have to demonstrate their ability to withstand bird ingestion and, following the ingestion, to produce enough thrust as required by safety regulations. Aircraft engine full scale testing is very expensive and, in order to decrease the cost of engine development, a range of analytical methods applicable to bird strike simulation have been developed (Mao et al., 2008).

One of the first authors who provided significant insights into problems associated with bird strike were Wilbeck and Barber (1978). They demonstrated that during high velocity impacts the material constituting the bird could be modelled as a fluid with negligible viscosity. This assumption was possible because the bird tissue strength is significantly lower than the stresses generated inside the bird during the impact event (Wilbeck, 1978).

Projectile response during an impact event was divided by Martin (1990) into five categories based on the impact velocity: elastic, plastic, hydrodynamic, sonic or

explosive. The elastic impact is characterised by the projectile bounce from the target due to the higher material strength than the stresses induced inside the body. With the velocity increase, the internal stresses generated in the body exceed the material initial yield strength and the body deforms plastically. Further increase of the impact velocity causes fluid-like behaviour of the projectile material. In this type of impact, the projectile strength is highly exceeded by the internal stresses generated within the body, and the material response is controlled by the material density rather than the material strength. Since the bird tissue strength is low in comparison to the internal stresses after impact, its behaviour can be described as fluid-like behaviour and the bird impact is treated as a soft body impact (Martin, 1990).

Barber et al. (1978) showed that the bird could be treated as a hemispherical-ended cylinder with the similar mass, density and compressibility to the water. They stated that the bird impact has a non-steady fluid dynamic character and can be divided into four phases:

1. Initial impact - at this stage very high shock or Hugoniot pressures are generated
2. Shock release - high shock pressure is decreased to steady flow pressure
3. Steady flow of the bird material onto the target
4. Impact termination and extinction of the impact pressures and forces.

The shock propagation for a bird impact on a flat target is shown in Figure 2.2.

2.2.1 Initial impact

In the initial impact phase the shock pressure generated inside the bird is very high, however it lasts only for a few microseconds (Wilbeck and Barber, 1978). Immediately after the contact between the target and the bird, the front part of the bird relaxes on the target's face and the shock propagates into the bird. As the shock is propagating along the bird, the bird material is brought to rest behind the shock. Due to the high stress gradient in the neighbourhood of the projectile edges,

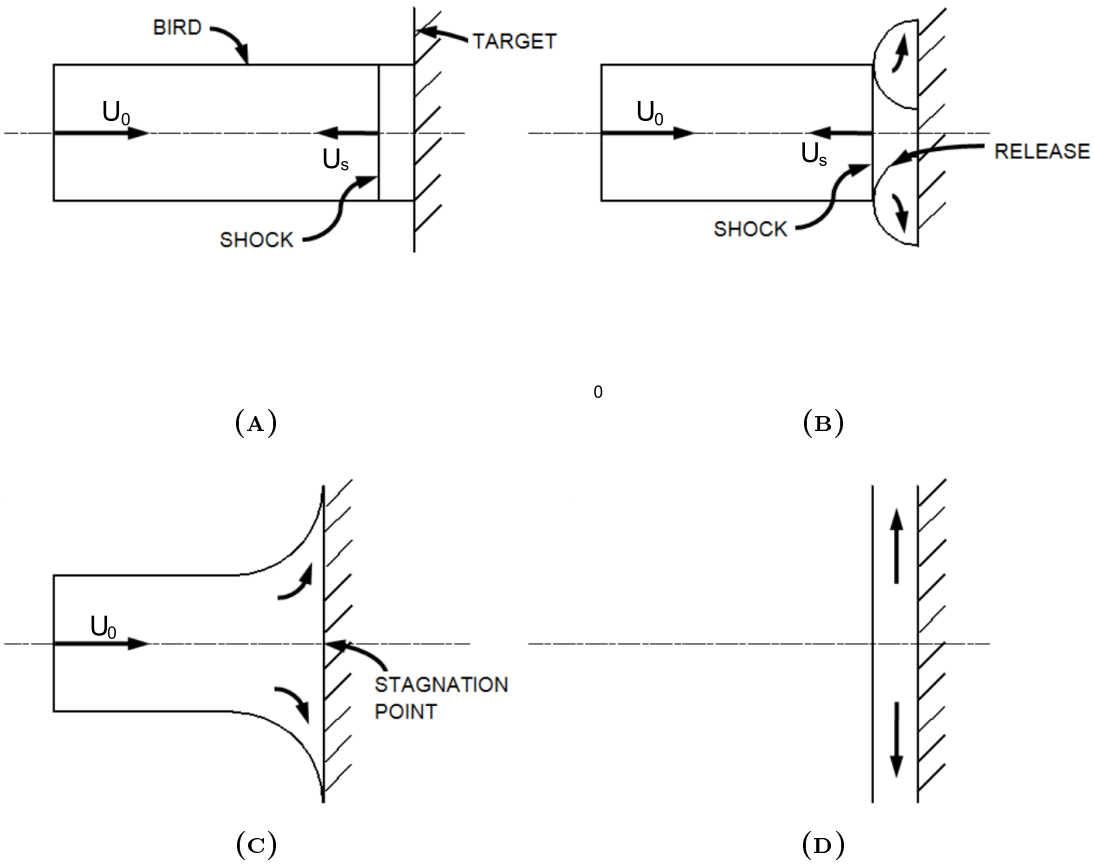

Figure 2.2: Impact phases: (A) Initial impact, (B) Impact decay, (C) Steady flow, (D) Impact termination (Barber et al., 1978).

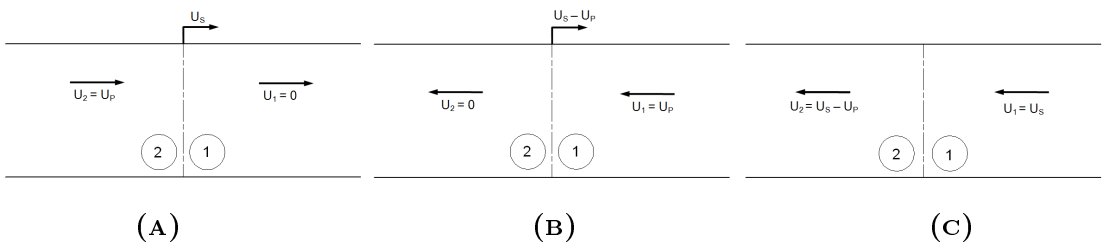

Figure 2.3: One dimensional shock flow: (A) Shock propagation into a fluid at rest, (B) Rest of the flow across the shock, (C) Standing shock (Wilbeck, 1978).

the material is accelerated radially outward and the release wave is formed. With the release wave propagating inward, the pressure in the projectile decreases. As soon as the release wave reaches the centre of the bird, the shock wave is completely released.

Wilbeck (1978) described the shock generated during a normal impact on a flat target as a one-dimensional, adiabatic and irreversible. Since the bird material behaves like a fluid, the propagation of the shock wave inside the bird can be described as the shock propagation into a fluid at rest. The mass and momentum conservation for the one dimensional shock flow at rest are described by Equations 2.1 and 2.2 respectively:

$$\rho_1 U_S = \rho_2 \left(U_S - U_P\right) \tag{2.1}$$

$$P_1 + \rho_1 U_S^2 = P_2 + \rho_2 (U_S - U_P)^2 \tag{2.2}$$

Where U_S is the velocity of the shock wave propagating into the fluid at rest and U_P is the velocity of the fluid particles behind the shock (see Figure 2.3). Combining equations 2.1 and 2.2 together results in the expression for the pressure behind the shock wave:

$$P_1 - P_2 = \rho_1 U_S U_P \tag{2.3}$$

The above equation describes the pressure in the shocked region, also known as the Hugoniot pressure, hence:

$$P_H = \rho_1 U_S U_P \tag{2.4}$$

In case of a cylinder impact on a rigid target, the velocity of the particles behind the shock is equal to the projectile's initial velocity, $U_P = U_0$ and the Hugoniot pressure expression takes the form of:

$$P_H = \rho_1 U_S U_0 \tag{2.5}$$

Equation 2.5 shows that the shock pressure is not only dependent on the impact velocity but also on the bird density and the shock velocity.

The preceding formulations are true for a soft body impact on a rigid target. Nevertheless, real structures like fan blades or leading edges are non rigid and their response cannot be neglected. Assuming that the target response is elastic, Wilbeck (1978) stated that only the local area of the target is affected during an impact. Figure 2.4 shows that initially the shock waves can be considered as planar, hence

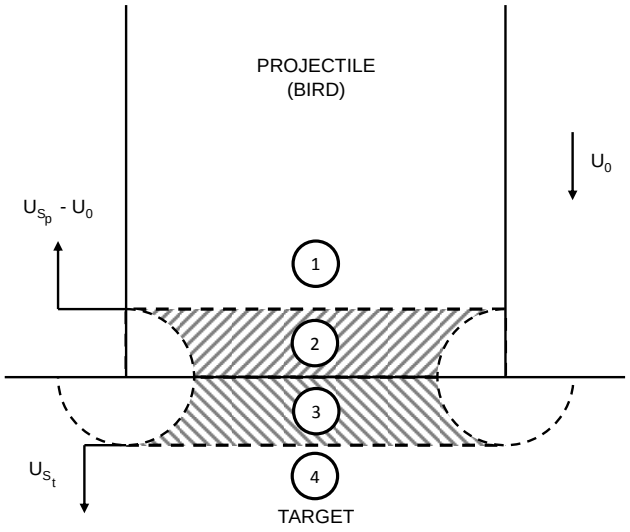

FIGURE 2.4: Early shock stage for the impact on an elastic target.

the equations for the one-dimensional shock describe the shock in the target and the projectile sufficiently well. However, in case of an impact on a non rigid target, the velocity of the fluid particles behind the shock is no longer equal to the initial velocity of the impactor. Therefore, the shock region can be described as:

$$P_2 = \rho_p \, U_{S_p} \, U_{P_p} \tag{2.6}$$

$$P_3 = \rho_t \, U_{S_t} \, U_{P_t} \tag{2.7}$$

Condition of equilibrium for the projectile - target interface requires:

$$\begin{aligned} P_2 &= P_3 \\ U_2 &= U_3 \end{aligned} \tag{2.8}$$

From the definition of the particle velocity:

$$U_{P_p} = U_0 - U_2 \tag{2.9}$$

$$U_{P_t} = U_3 - U_4 = U_2 \tag{2.10}$$

Combining Equations 2.9 and 2.10, the particle velocity is:

$$U_{P_t} = U_0 - U_{P_p} \tag{2.11}$$

Substituting the equilibrium conditions and combining them with the definition of the particle velocity, the equation for the projectile-target interface is:

$$P = \rho_p \, U_{S_p} \, U_0 \left(\frac{\rho_t \, U_{S_t}}{\rho_p \, U_{S_p} + \rho_t \, U_{S_t}} \right) \tag{2.12}$$

To confirm his theory, Wilbeck (1978) calculated the differences in pressures between the impact on rigid and deformable targets, using Equations 2.4 and 2.12. The differences between the Hugoniot pressures were approximately 8% lower for a titanium target and 4% lower for a steel target in comparison to the pressures calculated with the rigid target assumption.

In the case of thin targets, the initial shock is reflected off the rear surface of the target as a release wave which propagates toward the impact surface. The propagation of the reflected release wave causes shock wave unloading. Due to the small thickness of the target, the stress wave reflects continuously which leads to a decrease in pressure and increase in the local velocity of the target's particles. This leads to the deformation of the target structure and development of the velocity in the direction of impact, which eventually results in a decrease of relative velocity between the projectile and the target and a decrease in the flow pressures (Wilbeck, 1978).

2.2.2 Shock release

During the shock release phase, the release wave moves radially and propagates from the free edges of the bird towards the centre of the projectile. At this stage, the considered problem is not one-dimensional anymore and needs to be treated as a two-dimensional axisymmetric phenomenon (Barber et al., 1978). The shocked region in the bird just after impact is shown in Figure 2.5 B and the pressure in the shocked area is described by the Equation 2.5. It needs to be highlighted that the shock wave and release wave velocities highly exceed the initial impact velocity. Figure 2.5 C shows the convergence of the released waves at the centre of the impact, denoted as point B. The further propagation of the release waves causes their full convergence at the centre of the projectile, see Figure 2.5 D. At this stage, the fully shocked material does not longer exist. The curvature of the stress wave after full

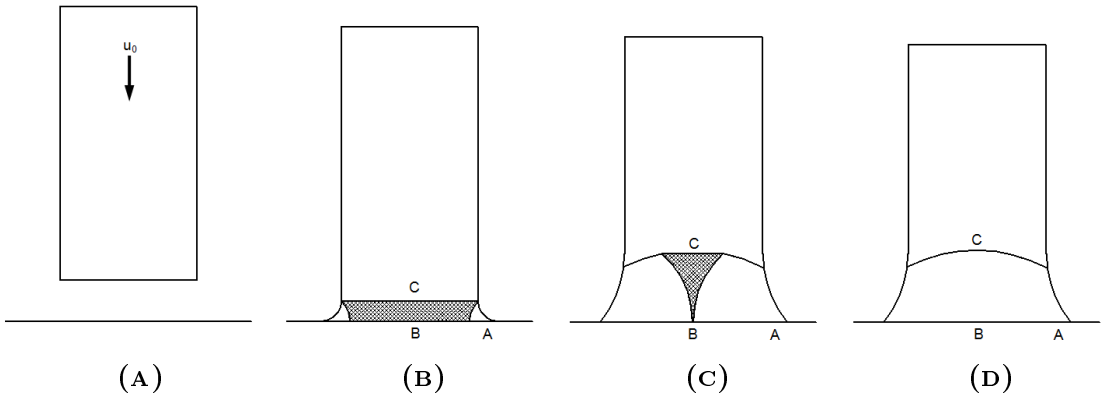

FIGURE 2.5: Shock and release waves in soft body impact: (A) Projectile before impact, (B) Shocked region immediately after impact, (C) Propagation of release waves, (D) Convergence of release waves in the centre axis of the projectile (Wilbeck, 1978).

convergence is caused by the radial propagation of the released waves (Barber et al., 1978, Wilbeck, 1978).

The duration of the shock pressure at the centre of impact is equal to the time required for the initial release wave to reach the centre of impact. Considering the release process as isentropic, the velocity of the initial release wave equals the speed of sound in the shocked material and the duration of Hugoniot pressure, t_B is given as:

$$t_B = \frac{R}{c_r} \tag{2.13}$$

Where R is the radius of the cylindrical projectile and c_r is the speed of sound in shocked continuum. The propagation of release waves determines the state at which the pressure in the centre of impact starts to decrease.

The end of the shock release stage is determined by the time of the release waves full convergence:

$$t_C = \frac{R}{\sqrt{c_r^2 - (U_S - U_0)^2}} \tag{2.14}$$

At this state the shock is weakened due to the rapid drop of shock pressure behind the shock wave.

2.2.3 Steady flow

Due to the permanent weakening of the shock during the impact release phase, the shock velocity and radial pressures decrease, which causes development of the shear stresses in the bird material. If the generated shear stresses are lower than the shear strength of the bird material, the radial motion of bird material is restricted. Surpassing the material shear strength by the shear stresses results in the flow of the material. Considering the bird impact in aerospace, the stresses generated inside the bird are higher than the bird's tissue strength and the bird can be considered to behave like a fluid (Barber et al., 1977, 1978, Wilbeck, 1978, Wilbeck and Barber, 1978).

Steady pressure and velocity fields are established for the steady flow condition after several reflections of the release waves. For the steady flow phase the pressure at the centre of impact for normal impact of the bird is described as:

$$P_S = \frac{1}{2}\rho_0 U^2 \tag{2.15}$$

Where P_S is the pressure at the centre of impact, also called stagnation pressure, and ρ_0 is the density of the bird material with zero porosity.

The conservation of momentum requires that during steady flow, the force applied to the target by a unit of fluid is equal to the axial momentum lost during impact, which can be expressed as:

$$\int_0^{t_D} \mathrm{F}\,\mathrm{d}t = \int_{U_0}^{U} \mathrm{M}\,\mathrm{d}U \tag{2.16}$$

Where, the force F is assumed to be constant during the steady flow phase and t_D represents the duration of the impact. Considering a unit of fluid with initial values of mass M, density ρ, length L and cross section area A, the Equation 2.16 becomes:

$$Ft_D = M(U - U_0) \tag{2.17}$$

The rebound velocity, U, is very small for most soft body impacts and can be neglected. In addition, the duration of impact for a unit of fluid length, L, can be expressed as the time required for the projectile to flow through its length:

$$t_D = \frac{L}{U_0} \tag{2.18}$$

Therefore, the force applied by the soft body on the surface of the target during the steady flow phase can be described as:

$$F = \rho A U_0^2 \tag{2.19}$$

2.2.4 Flow termination

During the steady flow phase the pressure in the fluid remains constant. When the rear part of the projectile enters the pressure wave front, the steady pressure field no longer exists due to the intrusion of the free surface. At that time, the pressure on the impacted surface is decreased and the steady flow phase is ended. Pressure reduces until the last particle of the projectile reaches the target surface. At this point, particle velocity component in the impact direction is equal to zero which corresponds to the end of the impact event. The total duration of the impact can be expressed with Equation 2.18.

2.2.5 Equation of State

Material properties of the target and projectile are necessary to determine pressures generated during the impact. These properties can be introduced to the problem with an equation of state (EOS), which allows for a description of shock wave propagation in the material and to accurately characterise the impact phenomenon. For the modelling purposes there are different equations of state incorporated into LS-DYNA. In this work the Murnaghan and the Gruneisen EOS were considered and they are described further in Sections 2.4.2.2 and 2.4.3.2.

2.2.6 Momentum transfer and impact force

Taking into consideration an impact on a rigid target and the assumption that bird behaves like a fluid, its motion before and after the impact event can be illustrated as shown in Figure 2.6 A. The momentum of the bird before an impact event can be simply described as a multiplication of the bird mass and its initial velocity. After the normal impact on the flat target, the bird momentum along its initial trajectory is equal to zero and the bird particles travel radially on the target. Therefore,

momentum transferred or impulse imparted by the bird to the target is equal to the bird's momentum before the impact (Barber et al., 1978). Since only the component of momentum normal to the target surface is transferred to the impacted body, the momentum transfer for the oblique impact can be described with Equation 2.20:

$$Q = MU_0 \sin\theta \tag{2.20}$$

Where θ is the angle between the surface of the impacted body and bird's initial trajectory.

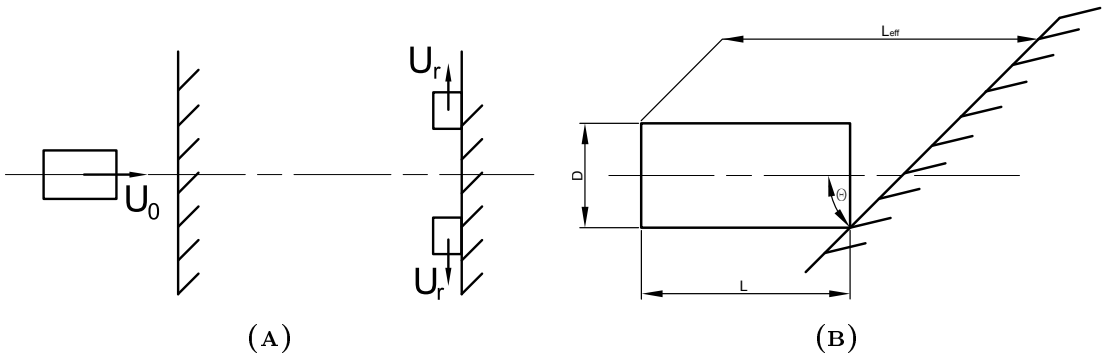

Figure 2.6: (A) Bird motion after impact, (B) Effective length of the bird.

Assuming that the bird's momentum, i.e. velocity, is constant before the impact event, the total duration of the impact can be expressed by Equation 2.18. The impact begins when the leading face of the bird reaches the target's surface and it lasts until the last particles of the bird relax on the impact surface. Equation 2.18 is true for a normal impact. For an oblique impact it is necessary to introduce an effective length of the bird, which can be defined as the sum of the bird's length and its diameter multiplied by the tangent of the impact angle (Barber et al., 1978). The effective length of the bird is illustrated in Figure 2.6 B and is given by Equation 2.21:

$$L_{eff} = L + D\tan\theta \tag{2.21}$$

Combining the momentum and effective length of the bird, it is possible to calculate the average impact force, defined as the momentum transfer divided by the duration of the impact. It is expressed by Equation 2.22:

$$F_{avg} = MU^2 \sin\theta L_{eff} \tag{2.22}$$

The definition of the above quantities - momentum transfer, impact duration and average impact force - provides parameters, which can be compared to the values measured during the experiments. Moreover, these parameters can be used to scale or non-dimensionalise measured values (Barber et al., 1978).

2.2.7 Slicing of the bird

In real life birds do not hit rigid or flat targets, but they are often injected into the aircraft engines. This provides a completely different behaviour of the bird and loading on the structure during the impact. In the case of an engine ingestion, the bird is sliced by the rotating blades and the behaviour of the bird is not comparable to the one observed in a normal or oblique impact.

Martindale (1994) described bird slicing as the process, in which the bird is sliced by the rotating fan blades. Due to the higher velocity the rotating blades accelerate bird slices in the direction of impact. As a consequence, a high pressure loading is generated on the blade rear surface. These findings were further discussed by Wilbeck (1978) who stated that bird momentum is transferred to the blade only by the cut part of the bird accelerated into the engine. The bird slicing mechanism is shown in Figure 2.7.

2.3 Bird modelling techniques

With the advancement in computational power and development of the explicit finite element method (FEM), the analysis of the structure behaviour under impact loading became possible. Events like bird strikes were possible to be numerically assessed with good agreement with results of experimental tests (Audic et al., 2000, Dobyns et al., 1998, Hanssen et al., 2006, Heimbs, 2011, Johnson and Holzapfel, 2003). Even though the advancement in the FEM allowed bird impact to be numerically modelled, the following difficulties identified by Mao et al. (2007) are still up to date: different methods for modelling the bird, projectile and target constitutive behaviour at high velocities, and the geometric complexity of the target and the bird.

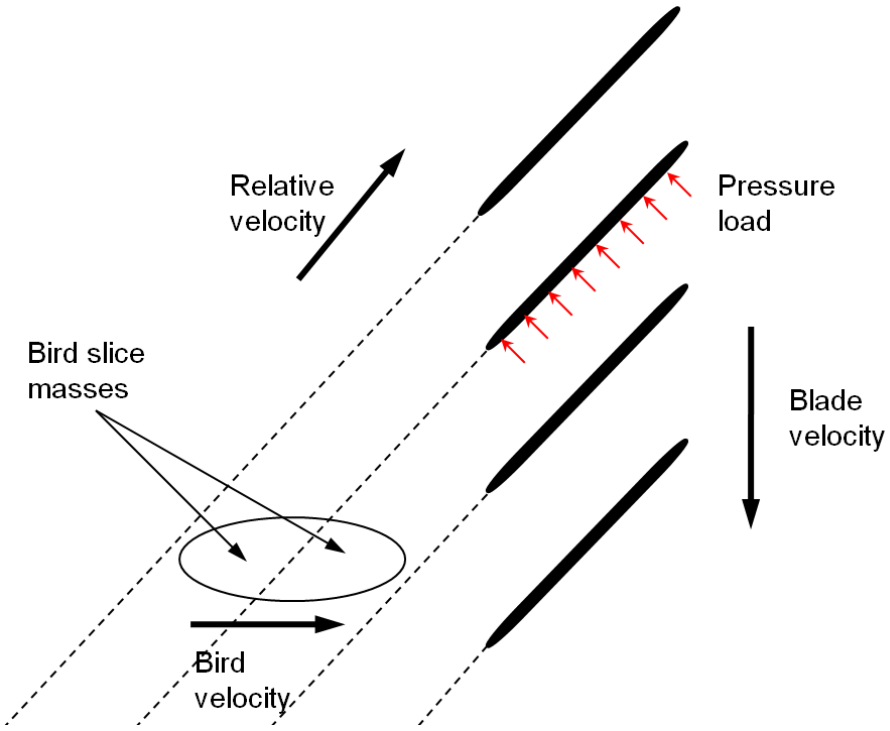

Figure 2.7: Bird slicing mechanism.

Three main FE methods have been used by researchers in modelling bird strike events, namely:

- The Lagrangian method (Airoldi and Cacchione, 2006, Dobyns et al., 1998, Goyal et al., 2013, Iannucci and Donadon, 2006, Langrand et al., 2002, Lavoie et al., 2009, M. V. Donadon, 2010, Mao et al., 2008, 2009, Stoll and Brockman, 1997)
- The Arbitrary Lagrangian - Eulerian (ALE) method (Goyal et al., 2006b, Langrand et al., 2002, Lavoie et al., 2009, McCallum and Constantinou, 2005)
- Smooth Particle Hydrodynamics method (Goyal et al., 2006a, Guida et al., 2011, Iannucci and Donadon, 2006, Johnson and Holzapfel, 2003, Lavoie et al., 2009, McCallum and Constantinou, 2005, McCarthy et al., 2005).

The Lagrangian method is a finite element method where the material nodes are coincident to the material points, which allows to track the data history of the

material as the nodes of the mesh deform together with the material. In the Lagrangian method, the continuum is discretised with elements and in each node of the element the constitutive equations are solved, which allows for calculation of the nodal displacements, stresses and strains in the element (Belytschko et al., 2000, Rao, 1999).

The Lagrangian method is the most popular and reliable method used to model deformable or non deformable structures. Nevertheless, difficulties arise when it comes to the bird modelling. During the impact, high stresses generated in the bird cause large deformation of the bird material, which results in adversely distorted elements and a significant reduction of the time step. Since the time step is proportional to the minimum element length (see Equation 2.23 below), the compression of the elements causes reduction of the time step. This significantly increases the computational cost of the analysis and can be an unacceptable factor in case of efficiency.

$$\Delta t = \frac{l_{min}}{c} \tag{2.23}$$

Where c is the speed of sound in the material.

Moreover, the excessive element deformation can lead to the problem of negative volume elements and failure of the simulation due to the production of a negative stiffness matrix. The problem of the reduction of the minimum time step and negative volume was overcame by the element erosion procedure for excessively distorted elements (Airoldi and Cacchione, 2005, Stoll and Brockman, 1997). However, elements erosion caused problems with artificial oscillations in the contact forces, which can be overcome by using very dense meshes (Langrand et al., 2002).

Another solution to avoid the problem of highly distorted meshes in the bird modelling with the Lagrangian method is the Eulerian approach, mostly used in fluid dynamics. In this method, the continuum moves within the fixed mesh, which allows for big deformations of the material with respect to the computational mesh. Despite its good handling with high material distortions, the Eulerian approach suffers from difficulties with tracking material history, as the grid is not connected to the material. Moreover, it experiences problems with definition of free surfaces (Stoker, 1999).

To overcome problems associated with the Lagrangian and Eulerian methods, a combination of both methods has been developed, called Arbitrary Lagrangian Eulerian (ALE)(Donea et al., 1982). In this method, the nodes of the mesh are not coincident to the material points, nor the mesh is fixed in the coordinate system. In ALE, the arbitrary motion of the computational mesh within the domain is allowed, which allows for the optimisation of the elements shapes, while the material history can be tracked by the motion of the mesh on the boundaries and interfaces of a multi-material system. However, Mao et al. (2007) stated that ALE suffers from heavy numerical dissipation and the solid-fluid interface is rather difficult to define for rotating blades. Moreover, Anghileri et al. (2005) found ALE not relevant for bird strike application due to the highly distorted mesh, which resulted in low accuracy of the results, even for very fine meshes at the contact interface.

Another approach to avoid the numerical instabilities and problems related to the highly distorted elements in utilisation of the Lagrangian method for high velocity impact, was development of meshless methods such as Smoothed Particle Hydrodynamics (SPH). It is a Lagrangian meshless method used to model motion of a continuum (fluids and solids). As in any Lagrangian method, the material history is easily tracked because particles are identified with a material point and as the material deforms the particles move with it. When initially developed, SPH was first applied to solve astrophysics problems of stellar dynamics (Gingold and Monaghan, 1977, Lucy, 1977). Since then, it has undergone significant development and it has been successfully applied to a wide range of engineering problems including bird strike. The SPH method is very good for modelling problems associated with impact characterised with large displacements, strong discontinuities and complex interface geometries (Chevrolet et al., 2002).

In the SPH method the continuum is discretised with a set of particles, which interact with each other within a sphere of radius equal to the smoothing length, h. The level of these interactions is described by Kernel functions and must decay outside the sphere (see Figure 2.8). The field variables are approximated by the Kernel interpolation at every point of the domain (Vignjevic and Campbell, 2009).

The SPH method used in this work is based on normalised corrected Kernel interpolation (Vignjevic et al., 2006a) which is first order consistent and conservative. It was observed that in the results presented below tensile instability caused by

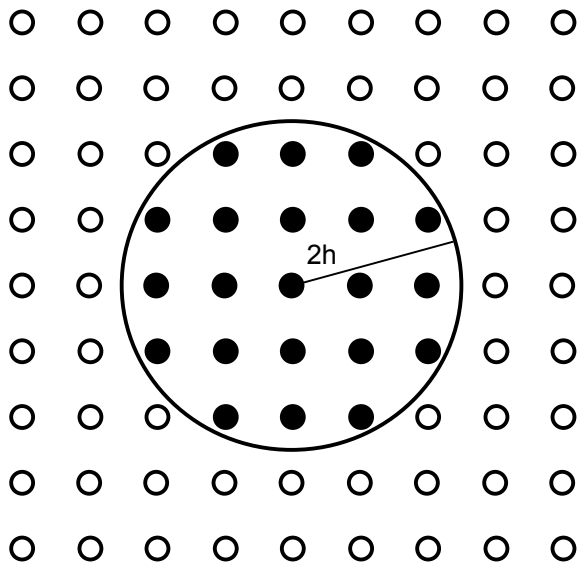

FIGURE 2.8: SPH particles interaction sphere.

the interaction of the constitutive relation and the Kernel function (Swegle et al., 1995) does not develop within the response time considered. This is compatible with the observations made by other investigators working on SPH modelling of transient fluid dynamics (McCarthy et al., 2005, Swegle et al., 1995, Vignjevic et al., 2006a,b).

2.3.1 Coupling between SPH and FE

The accuracy of the contact algorithms for contact between SPH particles and FE elements is especially important in fluid structure interaction problems such as aircraft ditching and bird strike. At present, there are two main approaches for the treatment of contact between the SPH particles and FE mesh: particle to node and particle to surface.

In the particle to node contact algorithm, FE nodes on the contact interface are treated as boundary SPH particles. Consequently, the SPH - FE contact is reduced to a particle to particle contact illustrated in Figure 2.9 A, i.e. interaction between two spheres of radius h (for details see (De Vuyst et al., 2005, Vignjevic et al., 2006b)). Contact between two particles is determined by checking the inter-particle distance. In this penalty based approach, contact forces are determined between pairs of particles and applied in the direction connecting the particle centres.

In the particle to surface algorithm, contact is imposed by checking the normal distance between a sphere of radius 0.5 h and the surface of the FE mesh, as illustrated in Figure 2.9 B. Interpenetration between the sphere and the surface indicates contact occurrence. In this contact algorithm, a restoring penalty force is applied to the particles and the finite element nodes (De Vuyst et al., 2005). The direction of restoring force is normal to the contact surface (FE mesh).

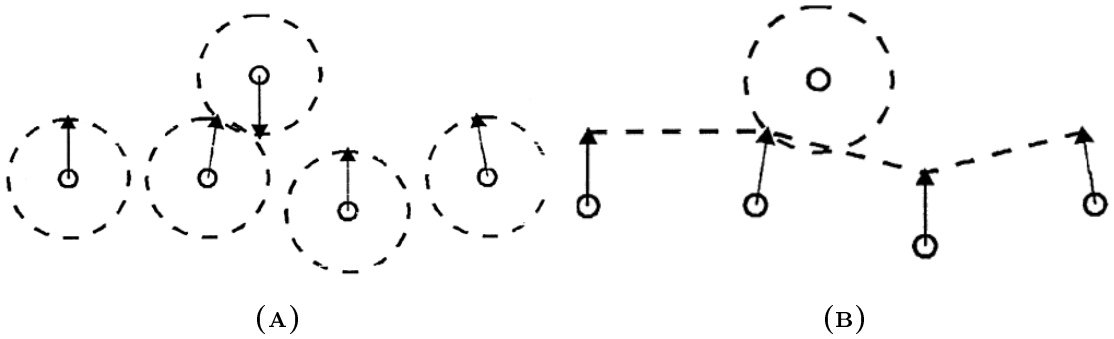

(A) (B)

Figure 2.9: FE-SPH contact types: (A) Particle-to-particle, (B) Particle-to-surface.

2.3.2 Contact algorithms comparison - elastic bar collision

Two analyses of a symmetric elastic bar impact were performed in order to investigate energy conservation and compare the particle to particle and the particle to surface SPH - FE contact algorithms. The initial configuration of the model is shown in Figure 2.10, with the SPH bar on the left with each particle shown as a sphere. The SPH block was given an initial velocity $V_0 = 200\ \frac{m}{s}$ and the FE block was given an equal velocity in the opposite direction. Both bars were made of an elastic material with steel properties. External surfaces were constrained in transverse directions, using symmetry planes, to prevent lateral movement after impact. The SPH block was discretised with 5120 particles and the FE block with 5120 elements.

Energy history graphs shown in Figure 2.11 and Figure 2.12 indicate that for particle to surface contact energy is not conserved in the elastic impact simulated. The kinetic energy drops from 390 kJ to 375 kJ after the elastic recovery. The internal energy in both cases rises at the moment of collision and drops off after the impact. Total energy graphs show lack of energy conservation in the case of analysis

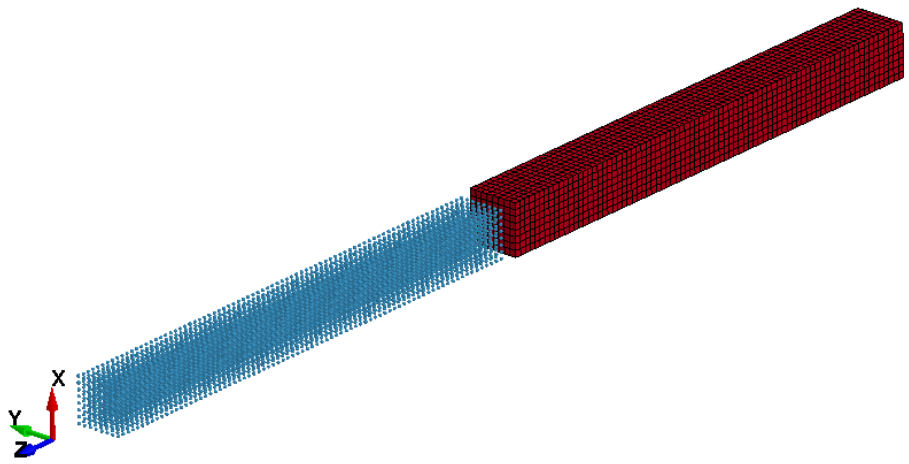

Figure 2.10: Bar impact configuration.

with particle to surface contact algorithm, while for the particle to node contact algorithm energy is conserved. For the particle to surface contact, energy is dissipated continuously during the contact between the bars. Elastically stored energy is recovered at the end of contact; however it does not reach initial magnitude. For particle to particle contact, total energy drops to certain level and then is recovered to the initial level after impact. Mesh sensitivity studies did not remove problem of energy dissipation from the analyses performed with particle to surface contact algorithm.

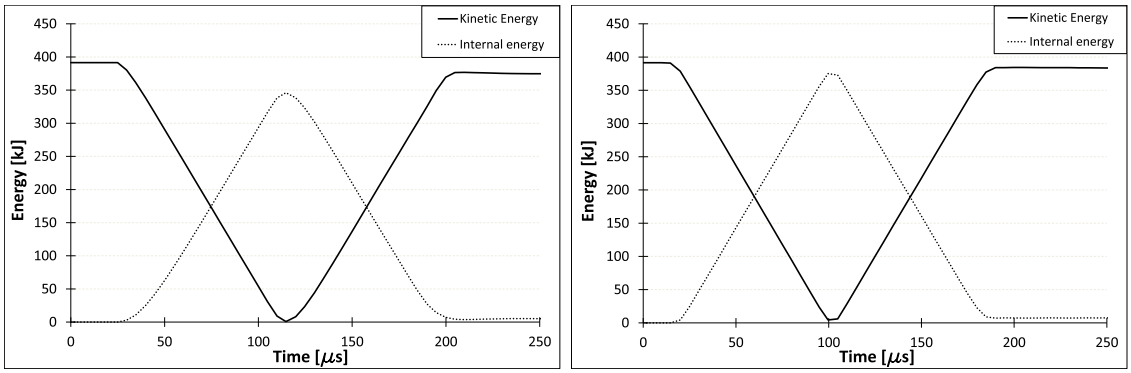

(A) (B)

Figure 2.11: Kinetic and internal energy: (A) Particle-to-surface, (B) Particle-to-particle.

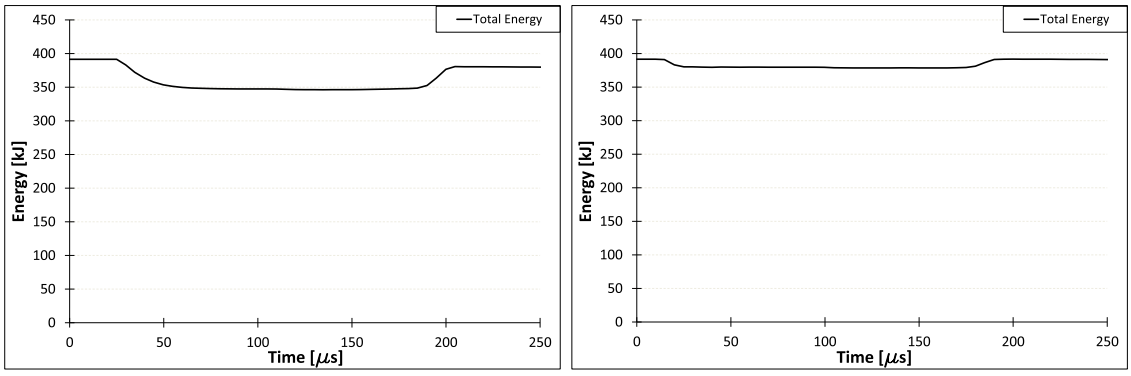

(A) (B)

FIGURE 2.12: Kinetic and internal energy: (A) Particle-to-surface, (B) Particle-to-particle.

Taking into consideration the above results the particle to particle contact algorithm was chosen for the bird strike analyses.

2.4 Model development

The bird strike simulation was performed with the Lawrence Livermore National Laboratory - DYNA3D code coupled with the in-house SPH solver developed at Cranfield University.

2.4.1 Initial conditions

The bird was given initial velocity of $V_0 = 77.2\ \frac{m}{s}$ while blades initial angular velocity was set to $\omega = 806\ \frac{rad}{s}$. Material initialisation card was used to assign rotational velocity to the system.

The simulation termination time was set to $t_t = 4\ ms$ in order to allow the deformed blade to settle into the new post impact equilibrium state.

2.4.2 Bird modelling

2.4.2.1 Bird geometry and meshing

In order to increase accuracy of artificial birds, the International Birdstrike Research Group (IBRG) studied biometric data of different bird species. Based on this data Budgey (2000) proposed relationship between bird mass and density as well as bird mass and bird body diameter, and the corresponding figures and equations are shown below:

$$\rho = -0.063 \times log_{10}\ m + 1.148 \tag{2.24}$$

$$log_{10}D = 0.335 \times log_{10}\ m + 0.900 \tag{2.25}$$

Where, m is mass of the bird, ρ bird density and D is bird body diameter.

Further more, Budgey (2000) found that a very important parameter in a bird strike test on fan blades is bird body diameter because of the slicing effect.

Currently three main shapes of artificial bird are used in bird strike tests and simulations. McCarthy et al. (2005)Langrand et al. (2002)and Airoldi and Cacchione (2005) used hemispherical-ended cylinder for their studies. An ellipsoidal bird shape was adopted and recommended by IBRG(Budgey, 2000). Airoldi and Cacchione (2006) and Stoll and Brockman (1997) considered birds in the shape of a flat-ended cylinder.

Due to the differences in the bird shape, the findings of the work referenced above are often contradictory, consequently it was decided to consider two different bird shapes, namely hemispherical-ended cylinder and ellipsoidal, see Figure 2.13. The hemispherical-ended cylinder was chosen because it is the most commonly used bird shape, while the ellipsoidal shape was chosen because it is the shape recommended by IBRG and more importantly it is the shape used in the test from which experimental data was used in this work.

The bird mass used in all simulations presented in this thesis is 0.680 kg and the length to diameter ratio was equal to two. According to equation (2.24) the density of the bird is $\rho = 970\ \frac{kg}{m^3}$ and consequently bird volume is:

$$V = \frac{m}{\rho} = 7.01 \cdot 10^{-3}\ m^3 \tag{2.26}$$

From the known bird volume bird diameter is easily determined as:

- For hemispherical-ended cylinder

$$V = \frac{5\pi D^3}{12} \Rightarrow D = 0.081\ m \tag{2.27}$$

- For ellipsoidal shape

$$V = \frac{5\pi D^3}{3} \Rightarrow D = 0.097\ m \tag{2.28}$$

According to equations (2.27) and (2.28), the diameter of the bird is equal to 0.081 m and 0.097 m for hemispherical and ellipsoidal bird respectively. Hence the length of the hemispherical bird is equal 0.162 m and the ellipsoidal 0.194 m.

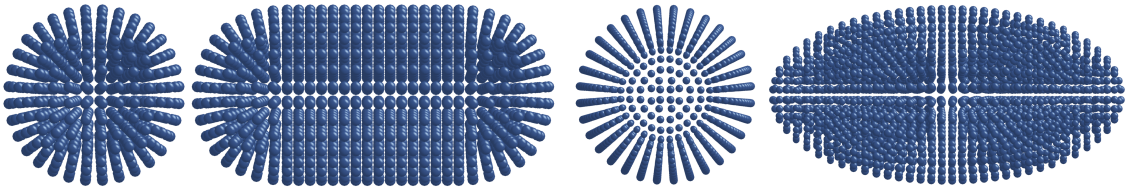

(A) Hemispherical bird (B) Ellipsoidal bird

Figure 2.13: Bird shapes: (A) Hemispherical bird, (B) Ellipsoidal bird.

In order to remove the influence of the discretisation density from the simulations, convergence analyses were preformed for the two bird shapes. The following two discretisation densities were determined as sufficient: the hemispherical ended bird was discretised with 5,120 particles and the ellipsoidal bird was discretised with 6,256 particles. The higher number of particles in the case of ellipsoidal bird was required to capture the ellipsoidal shape of the bird sufficiently accurately.

2.4.2.2 Bird material model

Another important aspect for bird modelling is selection of appropriate material model. As mentioned above, Wilbeck (1978) found that the bird could be considered as a volume of fluid in case of the high velocity impact. To improve simulation of

the bird slicing in impacts on fan blades, Anghileri and Sala (1996) proposed use of Isotropic-Elastic-Plastic-Hydrodynamic (IEPH) material model. The modelling based on IEPH material model was used in research performed by McCarthy et al. (2005) and Jenq et al. (2007), and it has been adopted in the work presented in this thesis. The material parameters used for this model are given in Table 2.1 (Anghileri and Sala, 1996).

Table 2.1: Bird material properties for isotropic-elastic-plastic-hydrodynamic material model (Anghileri and Sala, 1996).

Parameter		Value	Unit
Density	ρ	9.7×10^2	$\frac{kg}{m^3}$
Shear modulus	G	2.07	GPa
Yield stress	σ_0	0.02	MPa
Plastic modulus	E_h	0.001	MPa

The forces acting on the blade are mainly due to the change in the momentum of the bird as it hits the blade. In comparison, the force required for the blade to slice through the gelatine bird is small and hence the material model did not take into account shear failure and cut off value for tensile stress states.

In order to accurately model the hydrodynamic response it is necessary to use an Equation of State (EOS) with the IEPH material model. For this purpose Murnaghan EOS in the form (2.29) was chosen.

$$P = P_0 + B\left(\left(\frac{\rho}{\rho_0}\right)^{\gamma} - 1\right) \tag{2.29}$$

Where $P_0 = 0$ is the reference pressure, B and γ are material parameters, which have to be determined experimentally. The values for $B = 128MPa$ and $\gamma = 7.98$ were taken from McCarthy et al. (2005).

2.4.3 Blade and rotor modelling

The blade disk assembly considered in this work comes from an aircraft jet engine. It consists of 22 equally spaced (16.36°) blades attached to the disk. The geometry of

the blade, disk and blade - disk attachment was supplied by the engine manufacturer. In order to reduce run time only two blades were modelled, see Figure 2.14 A. In this two blade model the bird initially interacts with the leading blade, which due to high deformation contacts the trailing blade. These two interactions are the main source of the blade loading in the bird stroke event. Models containing three blade were investigated to confirm that there is no interaction between the impacted blade and the blade in front of it.

Rigid wall constraints were applied to the sides of the model to replace effects of the disk part, which was not included into the model. In order to remove mesh sensitivity and demonstrate convergence a number of simulations were performed with different

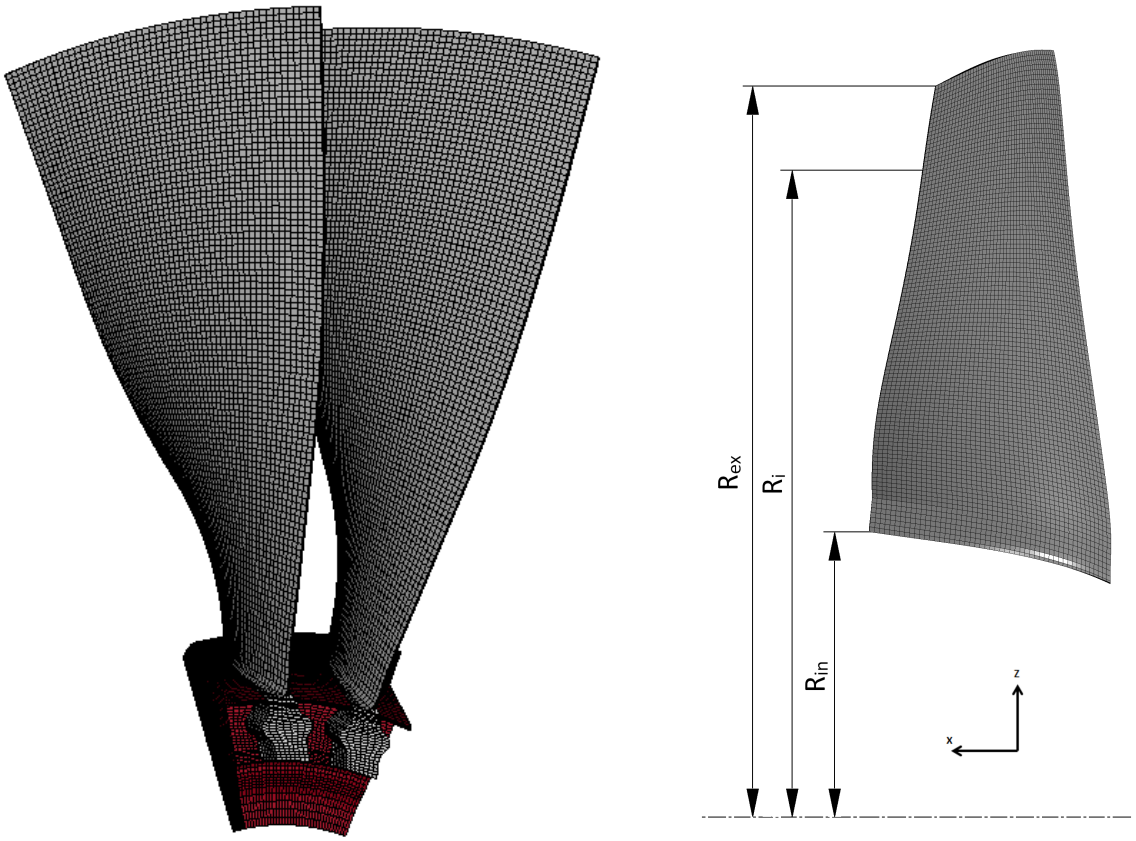

(A) (B)

Figure 2.14: (A) Finite element part of the model - blades and a part of the disk, (B) Blade dimensions measured from the leading edge.

blade mesh densities. The mesh chosen for the parametric studies presented in this thesis comprises 105,048 solid elements. The blade mesh and dimensions are shown in Figure 2.14 B. Corresponding radii are measured from the axis of rotation of the rotor. The external radius is measured to the tip of the blade, internal is measured to the root of the blade and initial impact radius defines the initial position of the bird centre of mass. These are equal to $R_{ex} = 570\ mm$, $R_{in} = 175\ mm$, $R_i = 514\ mm$ respectively.

2.4.3.1 Blade geometry and meshing

The blade and its support was meshed using TrueGrid software. Constant stress brick elements were used to mesh the blade and its attachment. Although plastic deformation due to in-plane and bending loads could be modelled using shell elements, the choice for brick elements allows through thickness stresses and wave propagation to be taken into account. This would not be possible using shell elements.

A number of analyses were performed with different mesh densities, including increased number of elements through the thickness; however, there was no considerable improvement of the results with the significant growth of the computational time. Hence, the blade was meshed with 21,400 elements: 107 elements along lengthwise, 50 elements width wise and 4 elements through the thickness.

Disk attachment to the shaft was modelled as rigid body joint. This allowed for the disk blade assembly to rotate. The rigid joint assumption implies that the engine shaft deformations are neglected during bird strike event.

In order to prevent unphysical deformations related to zero energy modes, stiffness hourglass control with exact volume integration (Lin, 2004) was applied to the model.

2.4.3.2 Blade material model

Mao et al. (2008) described bird strike as an event characterised by:

- High elastic and inelastic strains

- High strain rates
- Short duration with very high intensity
- Interaction between impact loads and response of the structure

In order to accurately model bird strike and reproduce relevant physics, the Johnson Cook viscoplasticity material model was selected to simulate behaviour of the blade and disk materials. This material model takes into account plastic strain, strain rate and temperature effects and therefore is appropriate for bird strike modelling.

The blade was assumed to be made of titanium alloy Ti-6Al-4V, with material parameters used (Lesuer, 2000) given in Table 2.2.

Table 2.2: Johnson Cook material properties for Ti-6Al-4V (Lesuer, 2000)

Parameter	Notation	Value	Unit
Density	ρ	4.42×10^3	$\frac{kg}{m^3}$
Yield stress	σ_y	1.098×10^3	MPa
Shear modulus	G	42×10^3	MPa
Strain hardening modulus	B	1.092×10^3	MPa
Strain rate dependence coefficient	C	0.014	MPa
Temperature dependence exponent	m	1.1	-
Strain hardening exponent	n	0.93	-
Melting temperature	T_m	1.878×10^3	K
Heat capacity	C_V	580	$\frac{J}{kgK}$

Table 2.3: Gruneisen EOS parameters for Ti-6Al-4V (Steinberg, 1996).

Parameter		Value	Unit
Velocity curve intercept	C	5.13×10^3	$\frac{m}{s}$
First slope coefficient	S_1	1.028	
Grüneisen coefficient	γ_0	1.23	
First order volume correction coefficient	b	0.17	

Although shock waves are not expected in the blade, the implementation of the Johnson Cook material model in the Dyna3D code is such that it requires an equation of state (EOS) to be defined. A Gruneisen EOS (2.30) was adopted in this work.

$$P = \frac{\rho_0 c^2 \mu \left[1 + \left(1 - \frac{\gamma_0}{2}\right)\mu - \frac{B}{2}\mu^2\right]}{\left[1 - (S_1 - 1) - S_2\frac{\mu^2}{\mu+1} - S_3\frac{\mu^3}{\mu+1}\right]^2} + (\gamma_0 + B\mu)\, E_i \tag{2.30}$$

Where P is pressure, ρ_0 initial density, c is the intercept of $V_s - V_p$ curve (in velocity units), S_1, S_2 and S_3 are the unitless coefficients of the slope of $V_s - V_p$ curve, γ_0 is the unitless Gruneisen coefficient, a is the unitless, first order volume correction to γ_0 and $\mu = \frac{\rho}{\rho_0} - 1$.

The parameters of this EOS for Ti-6Al-4V are given in Table 2.3 and were derived by Steinberg (1996).

2.4.3.3 Pre-stressed state of the blade

The pre-stressed state of the blade and its influence on the blade response was investigated by Miyachi et al. (1991). They found that the final deformed shape of a blade is sensitive to magnitude of the centrifugal force and that global bending effects decrease due to the rotation. However, local deformation of the blade was not affected by pre-stressing due to the rotation.

Dynamic relaxation was used to pre-stress the model. This was done by specifying a load curve for the body force load. The force was applied gradually to avoid dynamic overshoot. Dynamic relaxation factor and convergence tolerance were set to 0.9999 and 0.01 respectively. The resulting initial distribution of von Misses stress in the blade disk assembly is shown in Figure 2.15.

2.4.4 SPH - FE contact

A bird strike involves interaction between one or more birds and a part of the aircraft or engine structure, hence using an appropriate contact algorithm is important in modelling the impact event. More specifically, the loading the structure is exposed to in the simulated event depends on the contact algorithm, and consequently so

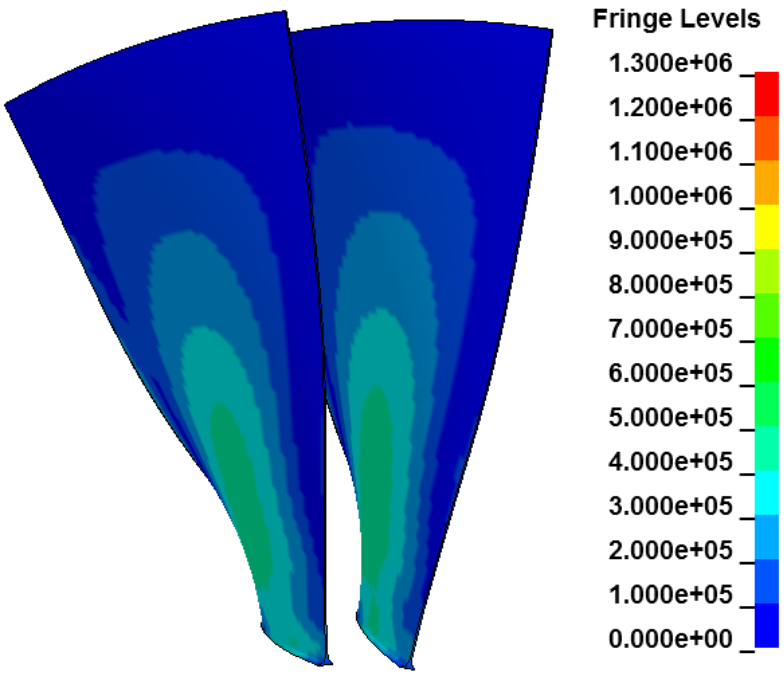

Figure 2.15: Initial stresses(v-M, kPa) in the system due to centrifugal force.

does the accuracy of the solution of the problem being investigated. To ensure correct treatment of contact a comparison of the particle to node and the particle to surface contact algorithms was made and discussed in this chapter.

In addition to the blade - bird contact, blade - blade contact was defined in anticipation of large deformations of the impacted blade and its interaction with the trailing blade. For this purpose DYNA3D automatic contact was used. The blade - disk interface was modelled with surface to surface contact.

2.5 Results

Following a convergence assessment and definition of an appropriate spatial discretisation density, a number of parametric studies were performed in order to assess the influence of differenct impact conditions on the blade response.

- The first study considered the influence of the bird shape on the plastic deformation of the blade.

- The second study examined the influence of impact timing in other words bird slice size (for multiple blade impacts).
- The third study considered the influence of impact location along the length of the blade.

2.5.1 Bird shape influence

For this analysis two different shapes of the bird were considered. The schematic representation of the initial configuration for the impacts is shown in the Figure 2.16. A section from the front of each bird has been removed to represent the mass removed from the bird by the blade in-front of the model leading blade. The red dashed line indicates the cut part of the bird. Results obtained with two blade model were validated by comparison to the results obtained with three blade model. No significant changes or improvement on the response of the impacted blade were noticed in case of three blade model, therefore it was decided to remove the blade in-front of the impacted blade from the analyses.

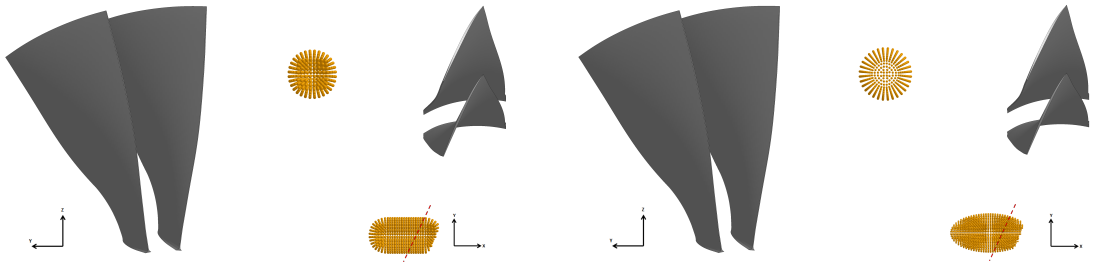

(A) Hemispherical bird (B) Ellipsoidal bird

FIGURE 2.16: Initial configuration of bird impact: (A) Hemispherical bird, (B) Ellipsoidal bird.

All other impact conditions were identical to enable direct comparison of the results. The impact location was at the radius of $514mm$ (86% of the blade span) from the rotation axis. This location corresponds to the predicted impact location in a test. Due to a degree of uncertainty in the exact impact location in the test one of the parametric studies considered this issue.

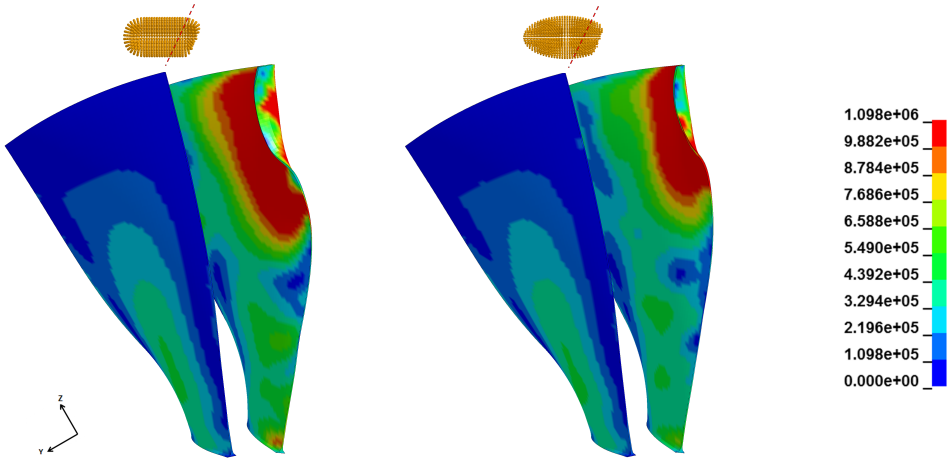

(A) Hemispherical bird (B) Ellipsoidal bird

Figure 2.17: V-M stresses (kPa), $t = 0.7ms$: (A) Hemispherical bird, (B) Ellipsoidal bird.

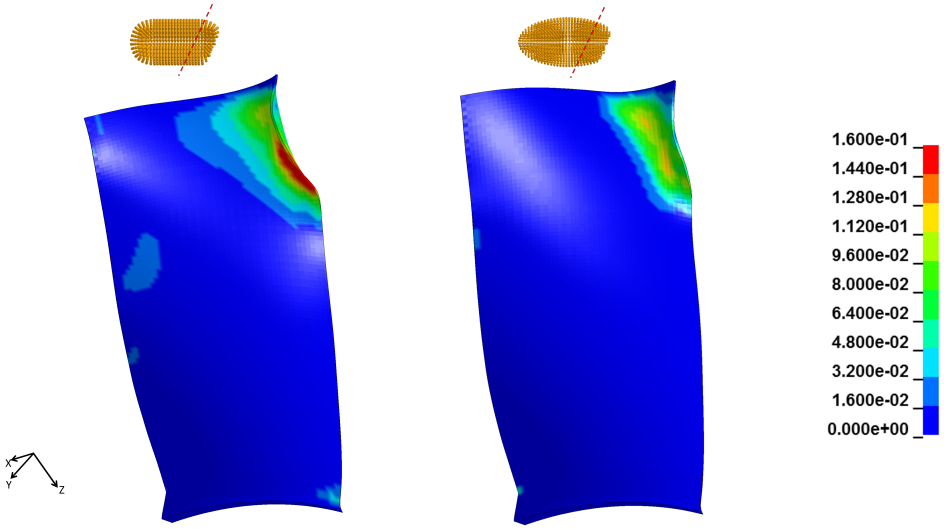

(A) Hemispherical bird (B) Ellipsoidal bird

Figure 2.18: Effective plastic strain, $t = 4ms$: (A) Hemispherical bird, (B) Ellipsoidal bird.

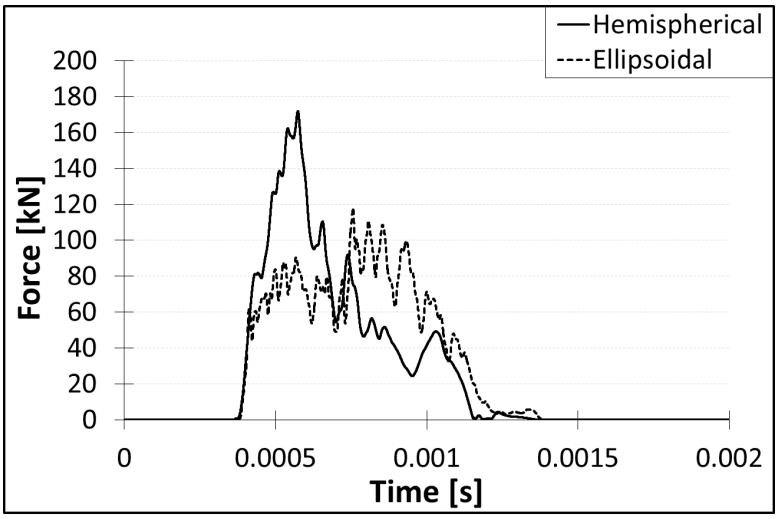

Figure 2.19: Contact forces induced by the hemispherical and ellipsoidal bird.

As shown in Figure 2.17, von Mises stresses induced during impact of the bird are in similar range for both shapes of the bird. However, stresses generated by the hemispherical bird are distributed over a larger area than in case of the ellipsoidal bird. Distributions of the effective plastic strain for the end of analysis are shown in Figure 2.18. For ellipsoidal bird the highest plastic strain was observed close to the impact location where the leading edge was bent. In the case of the hemispherical bird, plastic strain reached higher values and a larger area was plastically deformed compared to the ellipsoidal bird. The highest values were noticed on the leading edge of the leading blade. It is worth noting that plastic deformation also occurred close to the root of the leading blade.

In the case of the ellipsoidal bird impact, the leading blade suffered only local deformation (deformation of the close neighbourhood of the impacted area) while for the hemispherical bird, deformation of the blade was more widely spread (this is referred to as a global deformation, where the plastic deformation of the blade occurs away from the impacted area).

In the case of hemispherical bird impact, plastic deformation was also observed at the trailing edge of the impacted blade. This was caused by the contact with the front (cut off) part of the bird. For the hemispherical bird impact plastic deformation occurred close to the root of the leading edge of the leading blade due to the global bending of the blade.

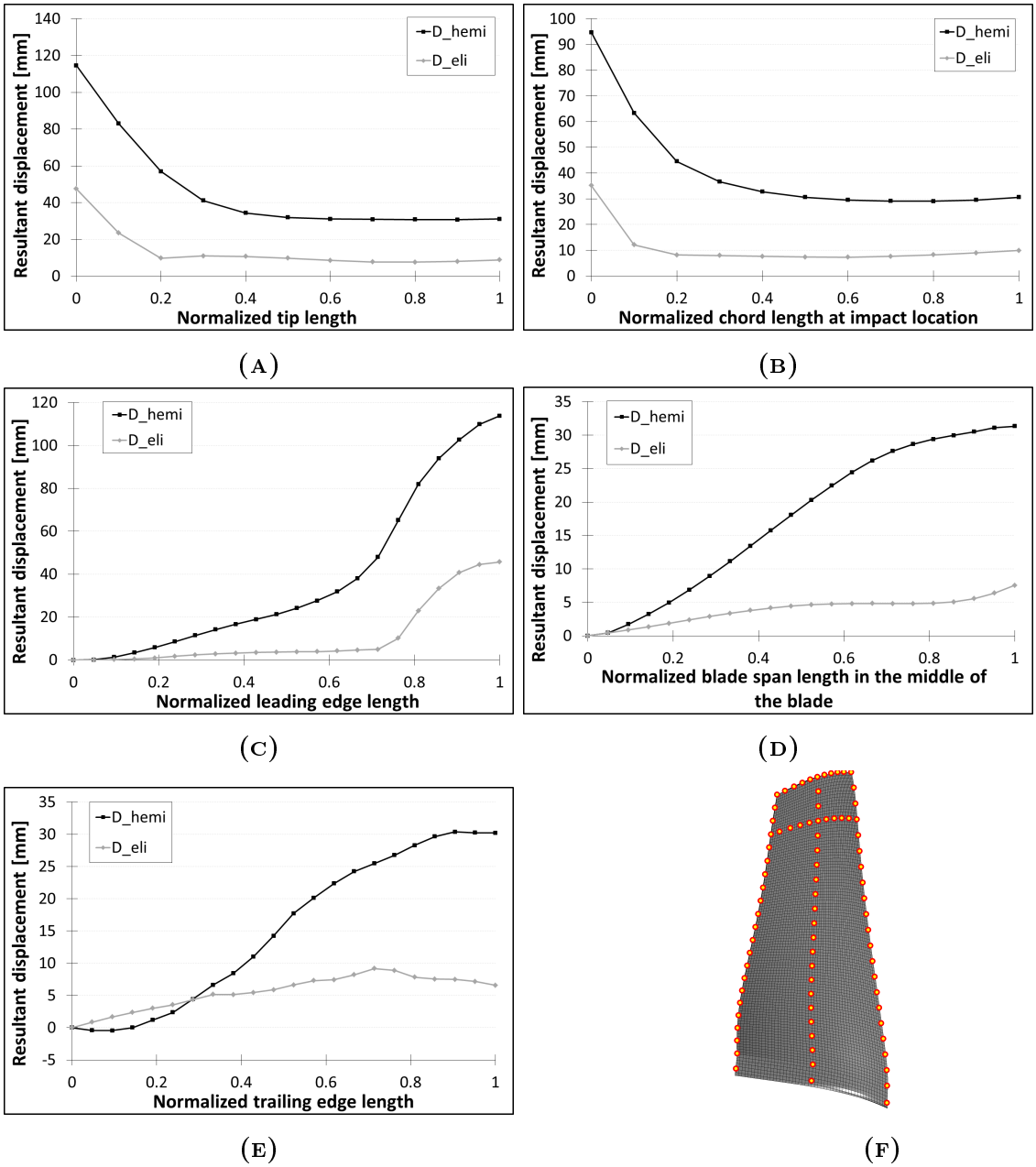

FIGURE 2.20: Displacement comparison for hemispherical and ellipsoidal bird impact: (A) Tip, (B) Impacted radius, (C) Leading edge, (D) Middle line across the blade span, (E) Trailing edge, (F) Displacement measurement points.

The time history of the impact induced contact force between the bird and the blades is shown in Figure 2.19. It can be seen that not only the main peak load generated by the impact on the leading blade was higher in case of the hemispherical bird but also the average contact force, acting on the considered blade, was higher (average contact force for the hemispherical bird $F_h = 91\ kN$, average contact force for the elliptical bird $F_e = 64\ kN$). Consequently, the blade impacted by the hemispherical bird was more distorted.

A comparison between the final deformed shapes (after elastic unloading) for the two bird model was done by comparing displacements along five blade cross sections. These include two cord wise sections at the blade tip and at the impact radius Figures 2.20 A and 2.20 B respectively, and three lengthwise sections at the leading edge, the mid line and the trailing edge, Figures 2.20 C, 2.20 D and 2.20 E respectively. The displacement measurement points are shown in Figure 2.20 F. These graphs show that for the whole blade the hemispherical bird impact resulted in the blade more severe deformation. Although the two chord wise profiles show a similar relative displacements, the span wise profiles show that the blade impacted by the hemispherical bird shows greater permanent global bending deformation.

As demonstrated above, the hemispherical bird induces higher loads and causes more severe damage to the blade. Therefore this shape of the bird is used in the parametric studies presented below.

2.5.2 Impact timing

In this assessment impacts with different levels of interaction between the bird and the leading blade were considered. Another way of describing the difference between these impacts would be by the amount of bird sliced off by the blade in front of the leading blade. The impact timings considered were defined by varying initial location of the bird along the X axis (axis collinear with the bird initial velocity vector) and the amount of the bird which is removed from the analysis. For the base analysis X_0 the bird axis of symmetry was located at radius $r_0 = 514\ mm$ from the axis of rotation of the blade assembly, i.e. in the Z direction. The tangential initial position of the bird relative to the blade was defined by an angle of 20.76° between the leading edge blade tip and the bird centre of gravity. The initial axial position

Table 2.4: Bird location for impact timing analyses.

Analysis	X location from the blade leading edge
X_0	14 mm
X_1	12 mm
X_2	10 mm
X_3	8 mm
X_4	6 mm
X_5	4 mm
X_6	2 mm
X_7	16 mm
X_8	18 mm
X_9	20 mm
X_10	22 mm

of the front end of the bird was located at $X = 14\ mm$ ahead of the leading edge blade tip. The exact location of the bird relative to the blade for all cases considered is given in Table 2.4.

Contact forces obtained in the impact timing analyses are shown in the Figure 2.21. The contact force graphs indicate that in all cases investigated above, the impact events were similarly characterised by a bird impact on the leading blade starting at response time $t = 0.4\ ms$. At the response time $t = 0.8\ ms$ the bird hits trailing blade and a second peak is seen in the force-time response. The contact force histories shown in Figure 2.21 A lead to the conclusion that distance from the blades, controlling the slice size, has a significant influence on the contact force pulse shape and length. The further the bird, the smaller the bird slice (size and consequently mass) is. Furthermore, the impact force peak value was influenced by the bird diameter at the impact location.

From Figure 2.21 B it could be seen that when the bird is sufficiently close to the blades, the contact force history has only one prominent peak. The second peak present in Figure 2.21 A is not prominent in Figure 2.21 B due to the fact that the slice size for the second blade was significantly reduced.

Overall, plastic deformation of the blade exposed to the primary bird impact was most pronounced in the case X_0. This is illustrated in the Figure 2.22 with plots of the blade deformed shapes and corresponding effective plastic strain distributions

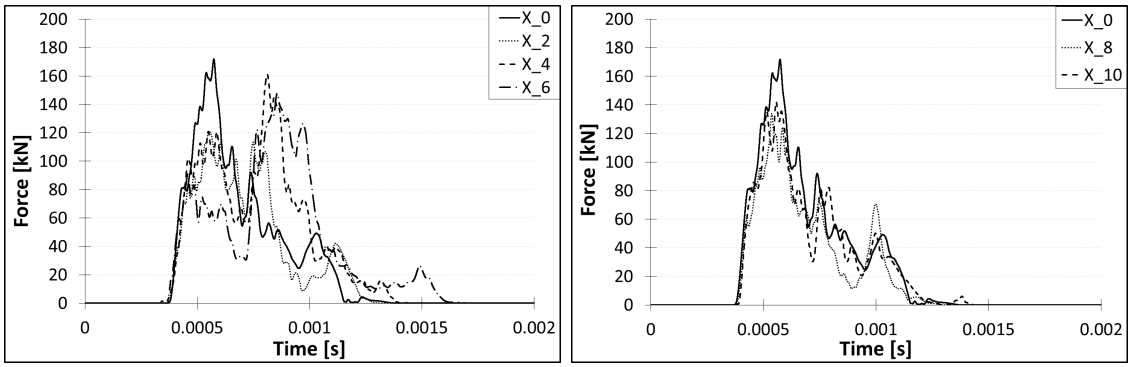

(A) (B)

FIGURE 2.21: Contact force histories for impact timing analyses: (A) $X\_0 - X\_6$, (B) X_0 and $X\_6 - X\_10$.

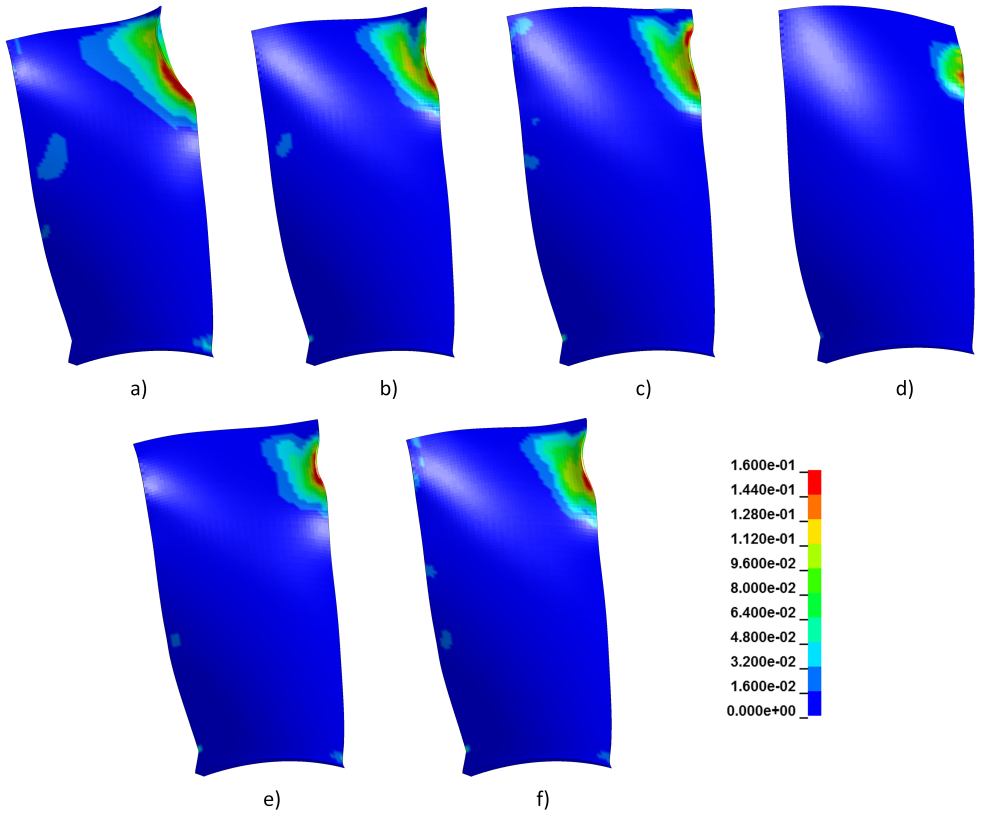

FIGURE 2.22: Plastic strain at $t = 4$ *ms* for impact timing analyses: (a) X_0, (b) X_2, (c) X_4, (d) X_6, (e) X_8, (f) X_10.

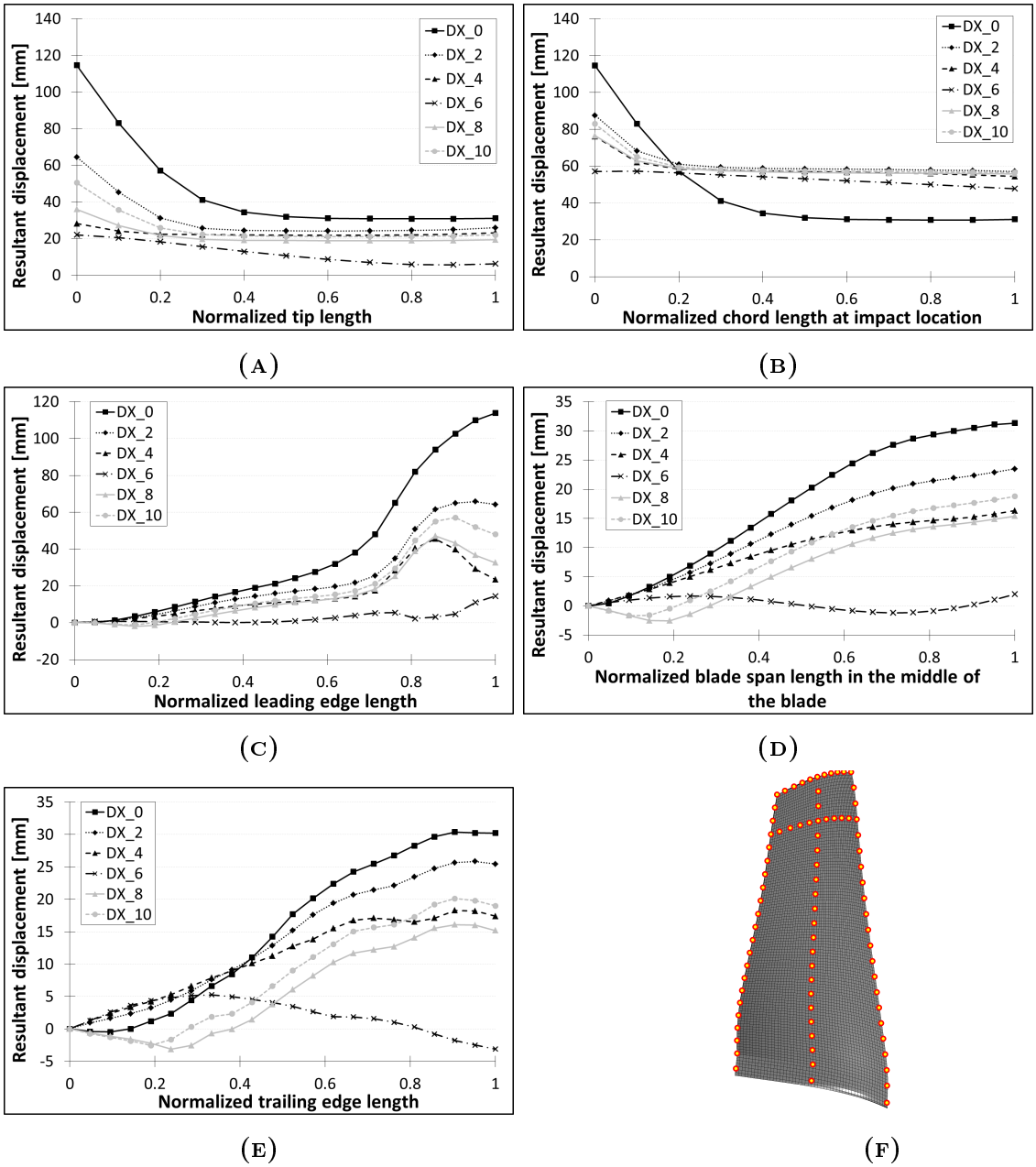

FIGURE 2.23: Displacement comparison for impact timing study: (A) Tip, (B) Impacted radius, (C) Leading edge, (D) Middle line across the blade span, (E) Trailing edge, (F) Displacement measurement points.

for the cases $X\_0 - X\_10$. The highest plastic strain is visible close the impact location and it spreads toward the trailing edge of the blade. The extent of the plastic deformation of the blade is related to the magnitude of the average impact force. In the X_0 case the average contact force (approximately 135 kN) was the highest. The higher plastic strain levels observed were also related to the additional loading caused by the contact between the leading and the trailing blade following the impact. For the cases X_2, X_4, X_6 and X_10 the average contact force was approximately 100 kN. The plastic strain distributions for those cases were similar.

Similar conclusions can be drawn from the comparison of permanent deformation of specific locations on the blade shown in Figure 2.23. The highest level of deformation was observed for the X_0 case.

Furthermore, the above results confirm that the deformation of the blade after impact is strongly related to the amount of the bird sliced by the former blade.

2.5.3 Bird impact location

This parametric analysis comprised nine impact cases (Z_0 to Z_8) performed in order to investigate the dependence of blade deformation on bird impact location along the blade length. In the first analysis (Z_0) impact location was at radius $r_0 = 514\ mm$ from the axis of rotation, i.e. in the Z direction.

Table 2.5: Bird location for impact location analyses.

Analysis	Z location from the rotational axis
Z_0	514 mm
Z_1	509 mm
Z_2	504 mm
Z_3	499 mm
Z_4	494 mm
Z_5	489 mm
Z_6	484 mm
Z_7	479 mm
Z_8	474 mm

For the remaining analyses impact distance was decreased by 5 *mm* in the Z direction, the different cases of parametric studies are shown in the Table 2.5.

The response of the blades was strongly dependent on the bird impact locations. Contact force graphs shown in Figure 2.24 show that as the impact location moves towards the rotational axis the contact forces were reduced. The contact force magnitude was related to the blade pitch angle which increases with the distance from rotation axis. Consequently, this influenced the bird slice size and its change of momentum during the impact.

Plastic deformation shown in Figure 2.25 is distributed over larger area for the cases where the average contact forces were higher. Pronounced plastic deformation is always observed near the impact location.

A comparison between the final deformed shapes (after elastic unloading) for the different impact locations was done by comparing displacements along five blade cross sections. These include two cord wise sections at the blade tip and at the impact radius Figures 2.26 A and 2.26 B respectively, and three lengthwise sections at the leading edge, the mid line and the trailing edge, Figures 2.26 C, 2.26 D and 2.26 E respectively. The displacement measurement points are shown in Figure 2.26 F. As expected the location of maximum leading edge deformation moves with the impact location, Figure 2.26 C, which also shows a different profile for the largest impact

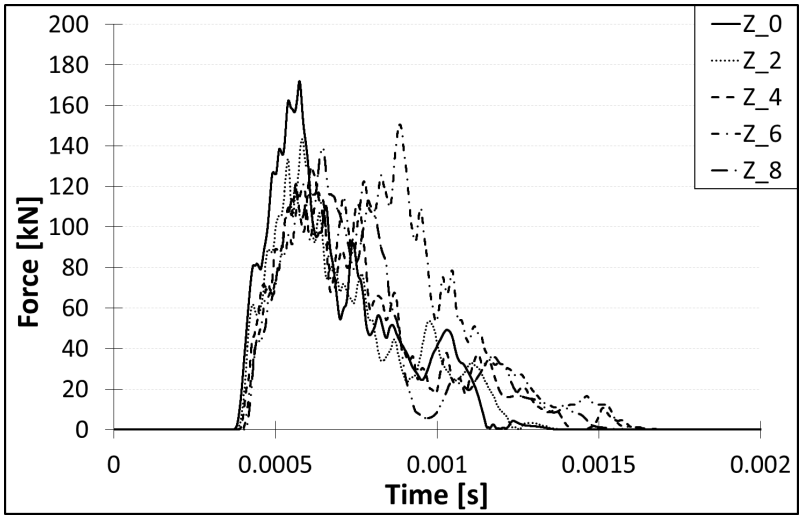

Figure 2.24: Contact force histories for impact location analyses $Z\_0 - Z\_8$.

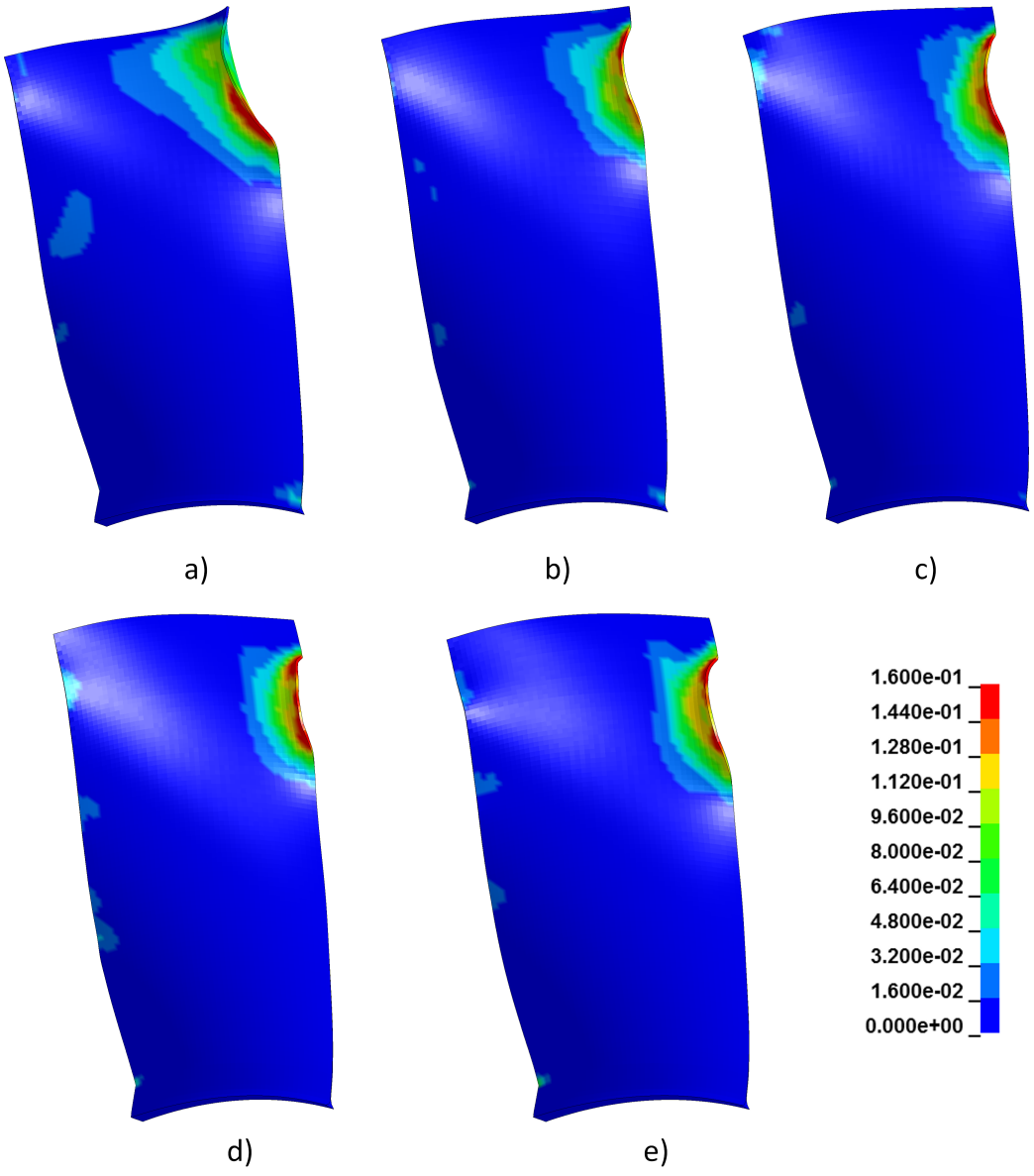

Figure 2.25: Plastic strain at $t = 4$ *ms* for impact location analyses: (a) Z_0, (b) Z_2, (c) Z_4, (d) Z_6, (e) Z_8.

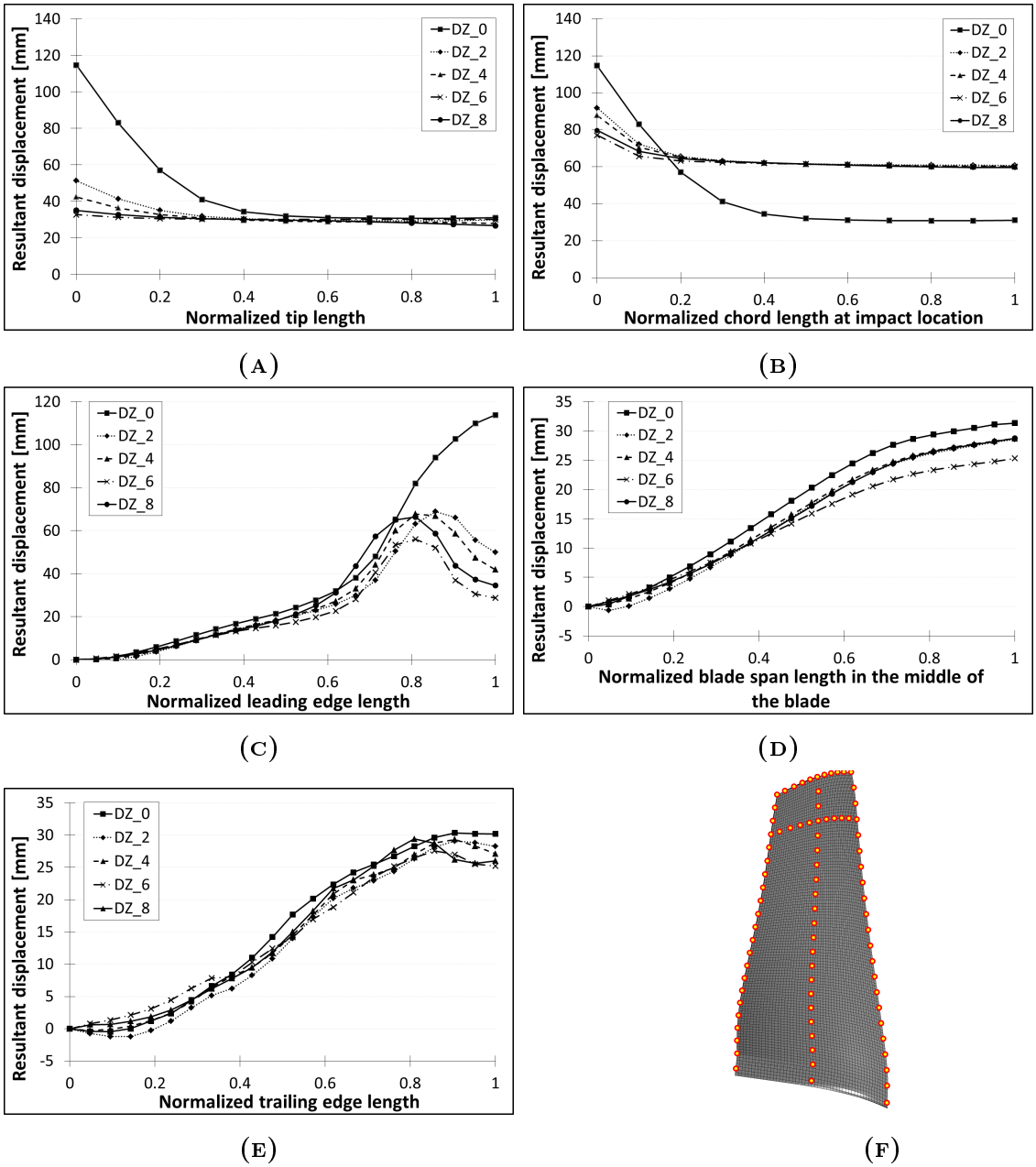

FIGURE 2.26: Displacement comparison for the bird impact location study: (A) Tip, (B) Impacted radius, (C) Leading edge, (D) Middle line across the blade span, (E) Trailing edge, (F) Displacement measurement points.

radius where the tip bending has occurred. The chord wise deflection plots show that the deformation on the trailing region of the blade is not significantly affected by the impact location.

2.6 Comparison with experiment

In order to assess the reliability of the model results presented in the previous sections, the results are compared to the result of a bird strike experiment. The blade was recovered from the bird strike test which was performed on a fully bladed fan. Based on safety regulations the bird was fired with an air canon into the engine at the critical location of the blade span (EASA, 2007).

The comparison with the test was performed by comparing the final deformed shape of the blade. The deformed shape of the blade after the bird strike tests was obtained by scanning the blades, and is displayed in yellow in Figure 2.27. It was not possible to control or measure the exact location and impact timing of the bird impact in the test. Therefore results form three analyses with different impact timing and locations are compared to the experimental results. A comparison of the final simulated and measured deformed shapes was done by assembling the blades together and is shown in Figure 2.27.

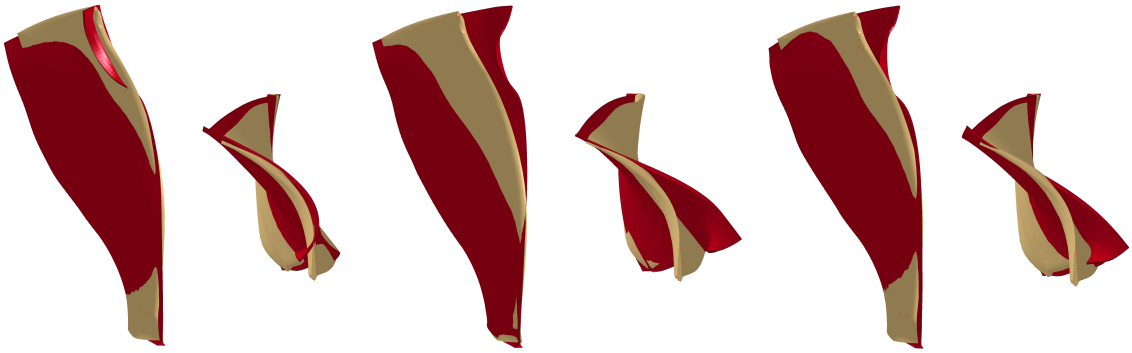

(A) X_0 (B) X_4 (C) Z_4

Figure 2.27: Comparison of the simulation (red) and the experimental (yellow) final deformed shapes - front and top views: (A) X_0, (B) X_4, (C) Z_4.

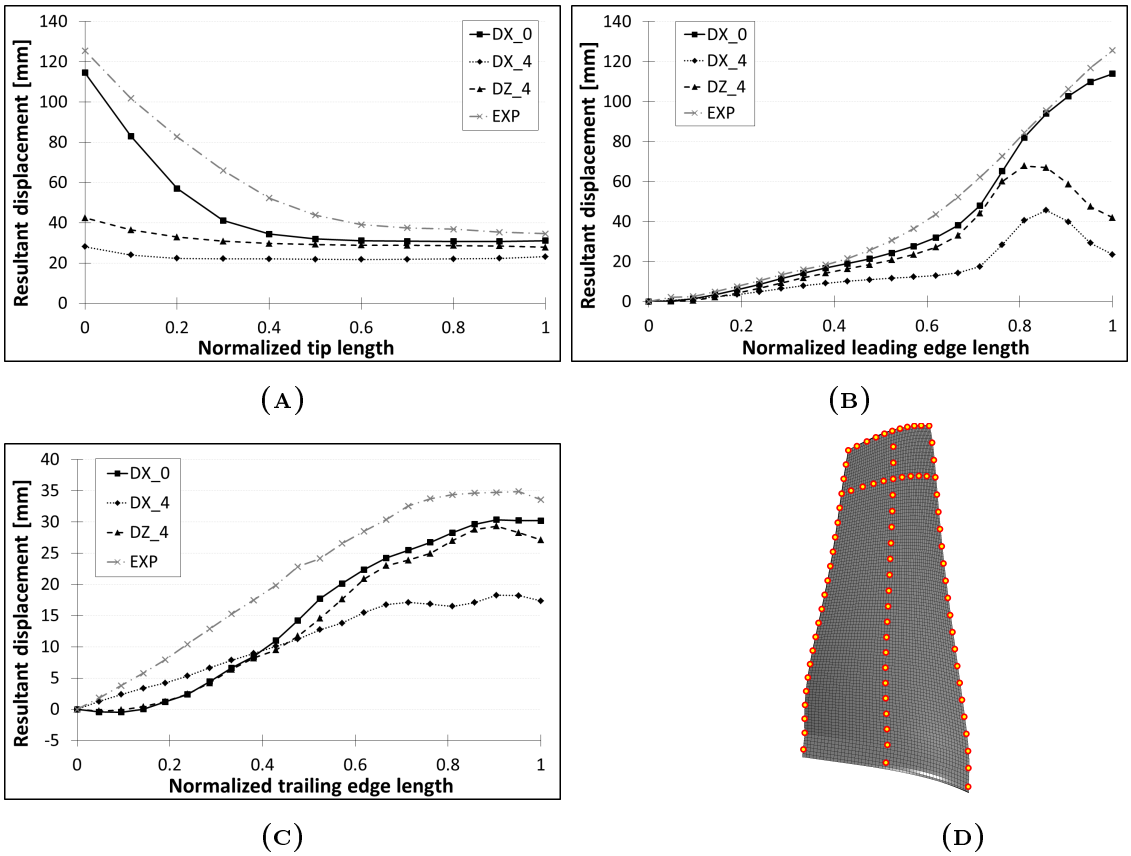

Figure 2.28: Displacement comparison of the simulation and experimental results: (A) Tip, (B) Leading edge, (C) Trailing edge, (D) Displacement measurement points.

A quantitative comparison is shown in Figure 2.28. From these figures it can be observed that in the cases X_4 and Z_4, the blade did not undergo significant twisting as in the X_0 case. In these cases only local deformation of the blade leading edge is observed. There was no twisting or bending of the blade. It can be seen that the final shape in the X_0 case is the closest to the experimental results. Bending and twisting of the blade match test results. Displacement of the leading and trailing edge of the blade obtained from the analysis X_0 correspond to the displacements of the blade obtained from the experiment. The main difference is in the local deflection of the leading edge of the blade.

2.7 Conclusions

- Three parametric studies were performed in order to improve the understanding of bird strike on jet engine blades and to validate the models against available experimental data. The first study considered the influence of the bird shape on the plastic deformation of the blade. The second study examined the influence of impact timing in other words bird slice size (for multiple blade impacts). The third study considered the influence of impact location along the length of the blade. Within these studies, it was paramount, from an engineering standpoint, to accurately reproduce the permanent deformation of the blade, as it is strongly related to engine damage.

- All analyses were performed with the finite element – SPH models for which, mesh sensitivity was removed through a convergence analyses. Contact algorithm comparison was done in order to model blade – bird interaction correctly. The particle to particle contact algorithm was used in all simulations, since there was energy dissipation in analyses performed with particle to surface contact algorithm.

- In the bird shape investigation hemispherical ended cylinder and ellipsoidal birds were considered. Bird shape had a significant influence on plastic deformation of the impacted blade. The bird body diameter and mass of the bird part cut off by the blade are two main parameters which affect the magnitude of the blade plastic deformation. A larger diameter, in the case of hemispherical bird, resulted in a higher magnitude of the blade loading and consequently a higher deformation of the blade.

- The simulation results indicate that there is a strong influence of bird impact timing and location on the extent of blade deformation. The differences in magnitude of the contact force vary between simulations and are related to the size of the bird slice. The contact force peak was the highest in the case where the bird is initially located at radius $r_0 = 514\ mm$ from the axis of rotation of the blade assembly. The tangential initial position of the bird relative to the blade was defined by an angle of 20.76° between the leading edge blade tip and the bird centre of gravity and the initial axial position of

the front end of the bird was located at $X = 14\ mm$ ahead of the leading edge blade tip (this is the case labelled as X_0 in the previous sections). Only in this case a contact between the leading and trailing blade was observed. In all other cases the contact force peaks were lower and caused only local deformation of the leading edge of the impacted blade. Furthermore, it was observed that with increase of the bird slice size cut by the first blade the magnitude of the contact forces acting on the second blade reduced.

- The study of the influence of impact location on the leading blade deformation revealed that the location of the bird impact have considerable influence on the blade response. This was mainly due to changes in the bird slice size caused by the change in the blade pitch at the impact location. In all the cases local deformation of the leading edge of the blade was significant. The numerical results were assessed by comparison with the blade recovered from the physical experiment and indicated a good level of reliability of the numerical results.

Chapter 3

Modelling of transient response of composites

3.1 Introduction

3.1.1 Composites in aerospace

Together with the advancement in technology, aircraft manufacturers started to look into reduction in total life cost of operating aeroplanes. This resulted in a demand for weight reduction and increased aircraft performance, which brought aircraft manufacturers to look into composite materials. In the beginning, secondary metallic structures, i.e. control surfaces or cowlings, started to be exchanged with composite counterparts. Lately, even the primary structures are made of composite materials. The best example of composites usage in aerospace is the Boeing 787, in which 50% of the used materials are composites (Boeing, 2014)(see Figure 3.1). The application of composites enables for significant reduction in weight of the structures, which often comes with superior strength properties of the material.

Also aircraft engine manufacturers draw their attention towards new materials. The application of composite materials to fan blades allows to decrease fuel consumption and increase the engine performance (Bunsell, 1988). The effect of this interest was the first composite fan blade manufactured by GE Aviation for GEnx engine in 1995 (GEAviation, 2014).

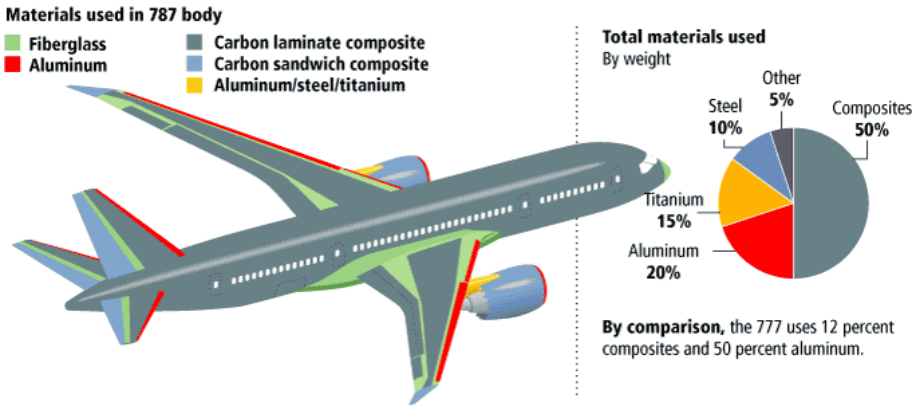

Figure 3.1: Materials used in Boeing 787 Dreamliner (Metallurgie, 2010).

Despite their excellent in-plane properties and low weight, composites suffer from one significant drawback, namely, low impact resistance and through-thickness performance. This weakness to out of plane impact loading conditions is the main drawback of composite materials, making composite structures extremely vulnerable to any kind of impact (Cui et al., 2009, Heimbs and Bergman, 2012). The low impact resistance restricts a wider application of the composite materials in aerospace due to the high probability of impact occurrence. Common examples of impact loadings on aircraft structures are tool or toolbox drops, bird strikes, hail stone and ice impacts, or hard body impacts involving runway debris or stones. Moreover, one of the most severe cases of the impact is the engine blade off, which is required as a part of the certification of the engine. Nowadays, the application of composites is extended and accelerated. It is related to the advancement in the modelling techniques and increased usage of FE analyses. Thanks to numerical simulations, the expenses and number of real tests can be reduced in the development process of aircraft structural components. However, competent application of numerical analyses requires the understanding of the theory hidden behind.

3.1.2 Structure of the chapter

This chapter provides the theoretical background and literature review on the composite modelling techniques available in the Transient Nonlinear Finite Element software (LS-DYNA).

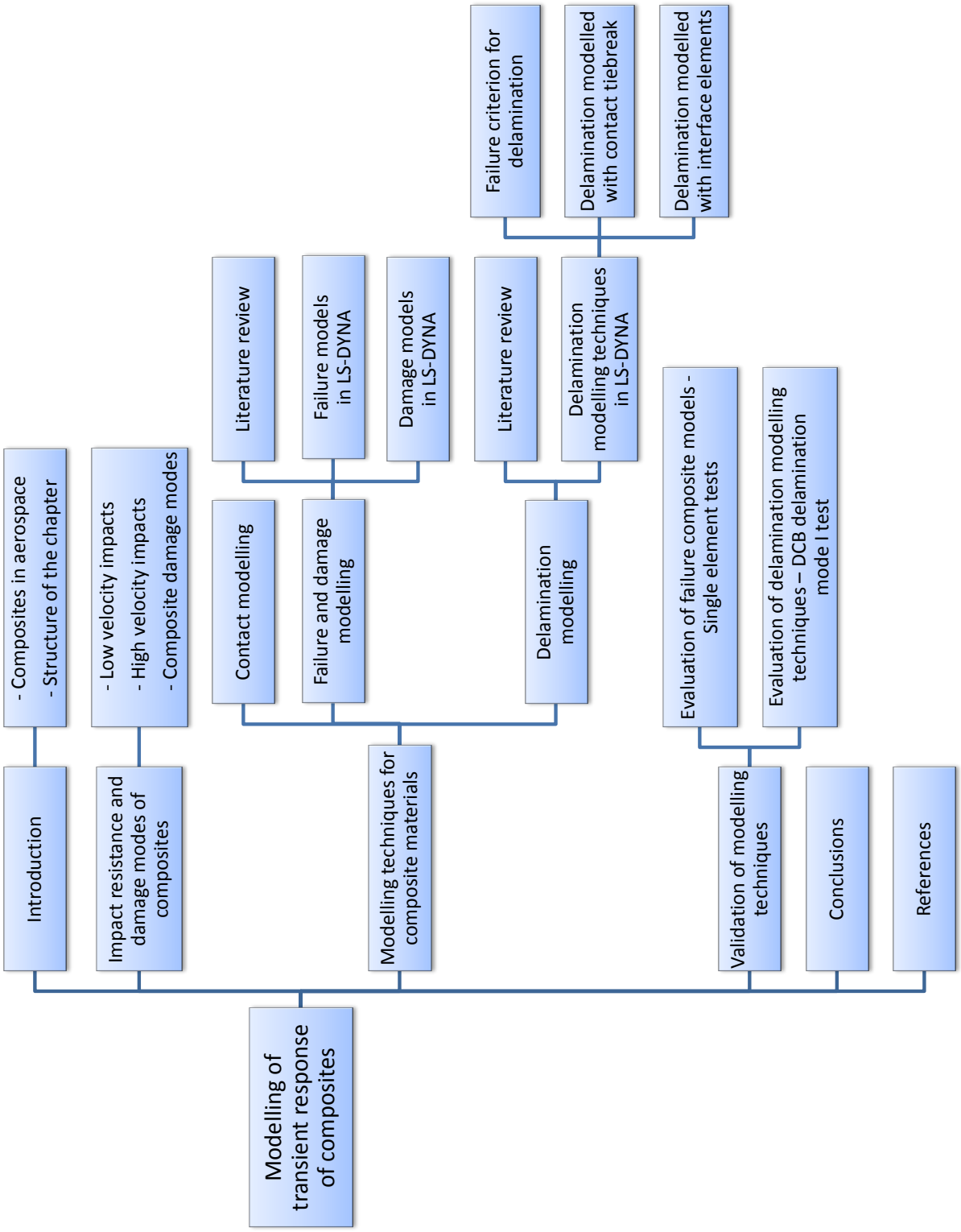

FIGURE 3.2: Chapter 3 structure.

The first section of this chapter introduces the interest in composite materials in the aerospace industry and provides description of the hierarchic structure of the chapter. For better understanding, the structure of this chapter is illustrated in Figure 3.2.

In the first part of the chapter, the impact resistance of the composite structures is described. It contains a brief introduction of the low and high velocity impacts. Furthermore, this section describes the physical behaviour of the composites under impact conditions and their corresponding impact damage modes.

The subsequent section introduces the numerical modelling techniques for composite materials. Since the scope of this project is related to the impact response of composites, only the modelling methods available in LS-DYNA are presented.

The first part of the numerical modelling techniques section explains how the interaction between two bodies, necessary for the modelling of impact events, is defined in the numerical analyses.

Furthermore, the theoretical background and the literature review on the composite failure and damage material models are provided. At this point, the numerical techniques for modelling failure and damage in composite materials are described. Subsequently, the formulation of the composite material models, available in LS-DYNA, is provided. The description of the composite material models was divided into failure and damage base material models.

The last part of section 3.3 introduces the delamination modelling techniques. The introduction to the delamination failure in composites is provided with the literature review. Furthermore, three delamination modelling techniques available in LS-DYNA are introduced. The first of these methods is strictly related to the failure of the material due to the tensile and shear stresses. This approach enables only to model delamination onset. The remaining two approaches require implementation of a tiebreak contact algorithm or decohesion elements between the neighbouring layers of elements. These methods allow to model opening of free surface. Thanks to that, the delamination propagation governed by the fracture mechanics can be modelled. In these two techniques, the delamination initiation is controlled by the failure criterion.

Due to the complexity of the problem related to the implementation of the cohesive elements for modelling delamination, deeper insight into this modelling technique was provided. First, the history of the interface elements was introduced with the literature review. It is followed by a characterisation of the cohesive element formulation, which describes the behaviour of the elements in order to understand the constitutive relations. Finally, the cohesive material models available for modelling interface in LS-DYNA were described.

Section 3.4 contains the validation of the composite modelling techniques, introduced in section 3.3.

The first part of validation section presents the validation of the composite material models available in LS-DYNA. Validation of the material models was performed with single solid element tests under tensile, compressive and shear loading conditions.

In addition to the validation of composite material models available in LS-DYNA, the evaluation of existing delamination modelling techniques was performed and presented in the second part of this section. The evaluation of modelling techniques for initiation and propagation of delamination was done with double cantilever beam delamination mode I analyses.

Finally, the last section of this chapter contains the conclusions drawn from the validation analyses.

3.2 Impact resistance and damage modes of composites

In general, aircraft structures are susceptible to two main groups of impacts, namely, low and high velocity impacts. Events such as tool or toolbox drop are low velocity impacts, while bird strikes, hail impact and runway debris are examples of high velocity impacts. Both of the impact groups are very dangerous for the composite material due to their low impact resistance. Even the low velocity impacts can cause damage, which afterwards can lead to failure of the component.

3.2.1 Low velocity impact

In the case of the low velocity impacts, the dynamic response of the structure is similar to the structure subjected to a quasi-static loading. The duration of the contact between the target and the impactor is long enough for the entire structure to respond. As a consequence, the global bending of the structure allows for energy absorption. The inertial effects can be neglected due to the low velocity of the projectile and relatively high duration of the event.

3.2.2 High velocity impact

In the case of the high velocity impacts, the response of the structure is controlled by the formation of shock and stress wave propagation through the material. The duration of the phenomenon is very short and the structure does not have enough time to respond globally, hence, the damage is more localised (Richardson and Wisheart, 1996). Due to the high velocity of the impactor, the inertial effects play a significant role in the response of the target structure, leading to the penetration of the target. The short duration of the phenomenon allows for neglection of the boundary effects due to termination of the event before the stress waves reach the edge of the target. According to (Cantwell and Morton, 1991), for the high velocity impact tests, a small coupon can be used to characterise the response of the whole structure. It is related to the highly localised response of the structure under high velocity impacts.

3.2.3 Composite damage modes

From a service point of view, low velocity impacts are extremely dangerous for the composite structures as they can cause interlaminar delaminations or back face tensile fractures (Zhang, 1998). This kind of damage is called the Barely Visible Impact Damage (BVID) and it is very difficult to detect during the visual inspections. Many researchers draw their attention to the problem related to low velocity impacts and the damage caused by this group of impacts on the composite structures.

Zhang (1998) distinguished four principal damage stages (see Figure 3.3), which can arise after low velocity impacts:

- Contact damage
- Delamination - separation of sublaminates from the laminate
- Fibre and matrix failure
- Fibre rupture or matrix crushing due to the tensile bending strain on the outer surface of the plate with delamination in the layer adjacent to the outer ply (Finn and Springer, 1993)

In the case of the low velocity impacts, the matrix damage and delamination is strongly related to the amount of the impact energy. However, impact energy is not the only factor which controls the damaged area. Another important parameter for the delamination extent and matrix fracture is the matrix toughness. The higher the toughness of the resin, the less damaged the area of the composite. Zhang (1998) found that delamination usually occurs in the interface between two plies of different orientation. Usually, delamination grows with distance from the impacted surface and is the largest in the interface near the bottom surface (Hitchen and Kemp, 1995).

Damage caused by the low velocity impacts significantly reduces the local stiffness and load bearing capability of the composite structures. Reduction of the stiffness results in additional deformation of the damaged area and further influences the delamination propagation. Siow and Shim (1998) showed that the compressive and tensile stiffness of the composite materials is reduced due to fibre failure in the impacted zone. However, reduction in the tensile stiffness and strength after impact is not as significant as it is for the compressive buckling strength of the post impacted structures (Abrate, 1998, Cantwell et al., 1986, Richardson and Wisheart, 1996). The reduction in the compressive strength after impact is up to 60% (DeMoura et al., 1997, Prichard and Hogg, 1990) from the initial compressive strength.

Since the impact resistance of the composite materials is dependent on many different factors (layer stacking (Fuoss et al., 1998, Hitchen and Kemp, 1995), laminate thickness (Liu et al., 1998) or shape and velocity of the impactor), every single composite layup has a different response and damage extent after impact. Therefore, extensive research on the composites residual strength after impact (RSAI) has been done. Cantwell and Morton (1990), Caprino (1984), Cui et al. (2009) studied the

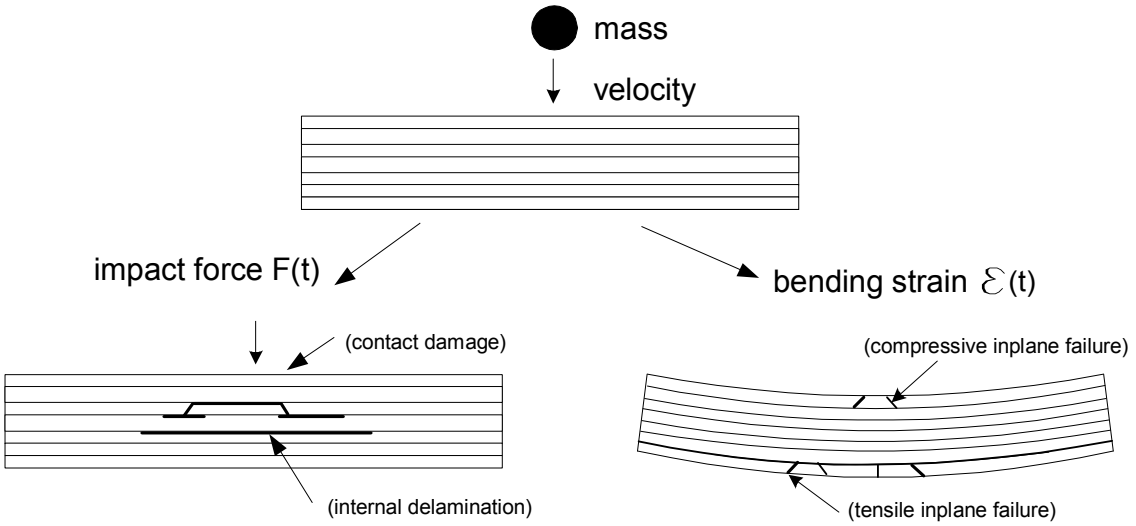

FIGURE 3.3: Impact phenomenon (Rajbhandari et al., 2002).

residual tensile strength of the impacted composite panels, DeMoura et al. (1997), Nguyen et al. (2006), Sanchez-Saez et al. (2005) performed experimental studies and developed numerical models for the prediction of the residual compressive strength after impact.

The threat from high velocity impacts in composite aircraft components is not smaller than in the case of the low velocity impacts. The structural response of composites under high velocity impacts is different and more complex than in the case of low velocity impacts, although some of the damage mechanisms are common to both cases (Cantwell, 1988).

In case of low velocity impacts, energy is absorbed by the layers far from the impact location due to the global bending of the structure, while during high velocity impacts, the response of the structure is more localised. The global response is reduced due to the short duration (high inertial effects) and restricted contact time between target and projectile. Moreover, in case of high velocity impacts, the damaged area is not related to the structure size, while for low velocity impacts such correlation was observed (Cantwell, 1988, Cantwell and Morton, 1989, 1990, Liu et al., 1998). Damage modes typical for the high velocity impacts are:

- Matrix cracking

- Perforation
- Delamination
- Spall
- Dishing
- Shear plugging

The damage formation, which may combine the modes, depends on the selected material, layer stacking, shape, size and velocity of the projectile, as well as, the target thickness. Since there are many parameters influencing the behaviour of the composite structures, it is very difficult to predict the damage modes in a potential high velocity impact.

3.3 Modelling techniques for composite materials

The development of computational techniques provided a tool to support the first stage of structural design and studies of composite structures behaviour under impact loads. For metallic structures, explicit FE analyses give good agreement with the real behaviour of those structures, and they are successfully used in the industry to predict impact damage. Damage mechanisms for composite materials are much more complex due to the wide range of fibre reinforcement and matrix types, different level of orthotropy and different damage modes - matrix or fibre dominated failure. Especially difficult in the case of modelling damage of the composite structures under impact loading is modelling of delamination and progressive failure of the structure.

This section provides a review on the simulation tools for modelling impact on composite structures in LS-DYNA.

3.3.1 Contact modelling

Impact is a phenomenon, which involves the interaction between two bodies - structure and impactor interface. In explicit FE codes, such interaction between the interfaces of two different components is treated as a contact problem. In order to enable a distinction between two bodies, the interfaces are divided into segments. Definition of master and slave segments allows for identification of the potential penetrations between these segments. For penalty based contacts, when a penetration is detected, a restoring force proportional to the penetration depth is applied to the interfaces to resist and eventually remove the penetration (LSTC, 2001). The restoring force is considered a tensile force and is estimated using springs, positioned between the contact surface and the impinging nodes. The contact force is given by Equation 3.1:

$$F_c = -eK_k \tag{3.1}$$

where, e is the penetration depth and K_k is the contact stiffness. The value of the contact stiffness needs to be of the same order of magnitude as the stiffness of the element in contact normal to the interface (Rajbhandari et al., 2002).

3.3.2 Failure and damage modelling

3.3.2.1 Literature review

A progressive failure of the component can be modelled in LS-DYNA using two different approaches. The first of these approaches enables to model failure of the component as a progressive failure of subsequent rows of elements. The second approach is to model the progressive damage of the material.

The first approach is governed by failure criteria, which allow for determination of laminate strength, based on the strength limit measurements for the corresponding type of load. As soon as the failure criterion is fulfilled, the corresponding material strength is reduced to zero.

The second approach enables for a progressive degradation of the material properties. This approach also employs failure criteria. As soon as the corresponding failure criterion is fulfilled, a gradual reduction of material properties is triggered. The

damage of the material progress until the material is not able to carry any load and material ultimate failure is reached.

Both of the methods available for the modelling of progressive failure of the structure utilise the failure criteria. In order to assess the failure of the composite or to trigger the damage in the material, under the corresponding type of load, a number of failure criteria were developed.

Existing failure criteria can be divided into two categories, which treat the failure modes of the composite laminates all together or independently (Bayandor et al., 2003).

The first category of the failure criteria takes into account the interaction between different stress components and incorporates all failure modes in a single expression. Examples of interactive criteria are Tsai-Hill and Tsai-Wu (Tsai and Wu, 1971) failure criteria. The Tsai-Hill failure criterion takes into account the interaction between the different stress components by analogy to the energy based von Mises yield criterion for metals. The Tsai-Wu failure criterion is a quadratic, stress based interactive failure criterion, which takes into account the interactions of multi-axial stress components based on material strength parameters (German, 1996) and is mostly used for the highly anisotropic composite materials (Abrate, 2008). Both of the failure criteria mentioned above do not distinguish between different modes of failure. Failure of the material occurs when the following inequality is fulfilled for the corresponding failure criteria (see Equations 3.2 and 3.3).

Tsai-Hill criterion:

$$\frac{\sigma_{11}^2}{X^2} - \frac{\sigma_{11}\sigma_{22}}{X^2} + \frac{\sigma_{22}^2}{Y^2} + \frac{\sigma_{12}^2}{S^2} \geq 1 \tag{3.2}$$

where, X is the material strength in fibre direction for tension or compression, Y is the material strength in transverse direction tension or compression, and S is the material in-plane shear strength.

Tsai-Wu criterion:

$$F_1\sigma_{11} + F_2\sigma_{22} + F_{11}\sigma_{11}^2 + F_{22}\sigma_{22}^2 + 2F_{12}\sigma_{11}\sigma_{22} + F_{66}\sigma_{12}^2 \geq 1 \tag{3.3}$$

where,

$$F_1 = \frac{1}{X_T} - \frac{1}{X_C};\ F_2 = \frac{1}{Y_T} - \frac{1}{Y_C};$$

$$F_{11} = \frac{1}{X_T X_C};\ F_{22} = \frac{1}{Y_T Y_C};\ F_{66} = \frac{1}{S^2}$$

and X_T and Y_T are respectively longitudinal and transverse tensile strengths, X_C and Y_C are compressive longitudinal and transverse material strengths, S is material in-plane shear strength. The parameter F_{12} is determined with a biaxial test.

The failure criteria in the second category can differentiate failure modes. There is no interaction between the modes of failure and the following failure modes are distinct: fibre failure in tension and compression, matrix failure in tension, compression and shear (Bayandor et al., 2003). The most common criteria of this category are the Maximum Stress or Maximum Strain criteria, the Hashin criterion (Hashin, 1980) and the Chang-Chang failure criterion (Chang and Chang, 1987). For these criteria, failure of the material occurs when the allowable stress (strain) limit is exceeded by the stresses (strains) in the material.

The implementation of damage schemes into composite material models allows for the gradual reduction of the material properties after a failure criterion is fulfilled. As soon as the failure criterion is satisfied, for the corresponding load case, degradation of the material properties begins. Degradation is performed according to the damage mode in the material and the reduction parameters need to be specified by the user. Softening of the material after damage is recommended to prevent numerical instabilities (Rajbhandari et al., 2002). Therefore, the degradation of the material properties is spread over a number of time steps. Gradual reduction of the material properties is highly desirable in the finite element codes, as due to discretisation of the continuum with finite elements, failure in the material is related to the failure of the entire element. Since the numerical failure of the material is controlled by the element size, the procedure of gradual stiffness reduction in the elements before the final failure provides more realistic behaviour of the material rather than instantaneous, complete drop of load bearing capability at a certain location in the structure. Nevertheless, not all composite material models account for the gradual degradation of material properties.

Crash simulations are widely employed in the design process in the automotive and aerospace industries. However, to accurately model composite behaviour under impact conditions, it is necessary to use an accurate and reliable material model. In order to cope with industries requirements, software developers collaborate with

research centres and national laboratories to develop new material models and increase the reliability of the existing ones. The currently available material models are divided into two categories: micro-mechanic based models and phenomenological (macroscopic, macro-mechanics) models (Altenbach, 2004, Xiao et al., 2009).

In micro-mechanic models, the deformation, damage and fracture of composites are treated separately for individual fibres, resin, their interface, as well as the interactions between the matrix and fibres. The prediction of a structural behaviour is based on the properties and behaviour of the individual constituents, modelled in a unit cell. The unit cells enable to establish the relationship between the properties of a separate composite component and the properties of the whole lamina. The damage progress is predicted based on the stress-strain response for a number of the unit cells, and is then mapped onto an element in a global scale. Nevertheless, there is a significant difficulty in modelling all damage modes and damage related softening effects in the complex micro-structure (Xiao et al., 2009). One of the approaches to overcome this problem is to introduce detailed large scale modelling (Quek et al., 2004a,b, Song et al., 2007). Another solution is to introduce necessary assumptions and simplifications at the unit cell level (Beard and Chang, 2002a,b, Flesher et al., 2011).

In contrast to the micro-mechanic based material models, the phenomenological models treat material behaviour at the continuum scale. Macro-mechanics models become the most commonly used in existing FE codes, because they do not consider the micro-structure of the component. Good example of the macro-mechanic model is the piecewise linear plasticity model, which employs a stress-strain relation to describe nonlinear deformations. Damage variables and damage evolution laws are used to describe continuum damage mechanics based phenomenological material models. However, determination of the damage parameters causes serious problems due to the difficulties with the measurement of these parameters. This problem is especially pronounced in case of composite materials, where damage parameters are obtained by curve fitting (Xiao et al., 2009) and are different for every composite layup. Therefore, it is of high importance to develop appropriate and reliable test methods for determination of the damage parameters and then, for development of reliable material models. However, special care needs to be taken when linking the test results to the damage parameters as the results of the experiments performed

in certain conditions cannot be easily transferred to different conditions.

To sum up, LS-DYNA provides tools, which distinguish failure modes and, in certain cases, allows for reduction of the material properties relevant to the failure mode. It also gives a possibility to model the initiation and propagation of damage and failure between the elements. Description and validation of the chosen composite material models with the corresponding failure criteria are provided further in this chapter.

3.3.2.2 Failure models in LS-DYNA

3.3.2.2.1 MAT_22 - Material Composite Damage

The phrase "damage" in the name of the material model is misleading because MAT_22 (Hallquist, 2006) is a composite failure material model. In-plane failure in the material is governed by the stress based Chang and Chang (1987) failure criterion. In addition to the in-plane failure criteria, a delamination failure criterion was implemented into MAT_22 by Hou et al. (2001).

This composite material model allows for modelling of failure in composite laminates with arbitrary ply orientation and for prediction of laminate ultimate strength, for both shell and solid elements. The model is divided into stress and failure analyses. As the load increases, first the stresses are calculated in the material, then the laminate is checked for failure. If there is no failure then procedure is continued until failure. As soon as any of the failure criteria is satisfied, failure of the material occurs. The corresponding material properties are reduced to zero in accordance with the failure mode.

The four failure criteria, incorporated into the material model MAT_22, are characterised by seven material parameters, namely:

- X_T - longitudinal tensile strength
- Y_T - transverse tensile strength
- Z_T - normal tensile strength

- S_{xy} - shear strength in XY plane
- S_{xz} - shear strength in XZ plane
- Y_C - transverse compressive strength
- α - nonlinear shear stress parameter

All the strength properties of the material have to be determined experimentally. The nonlinear shear stress parameter is calculated from the stress strain relation. Strains in the material are described by the following equations:

$$\varepsilon_x = \frac{1}{E_x}(\sigma_x - \nu_x \sigma_x) \tag{3.4}$$

$$\varepsilon_y = \frac{1}{E_y}(\sigma_y - \nu_y \sigma_y) \tag{3.5}$$

$$2\gamma_{xy} = \frac{1}{G_{xy}}\tau_{xy} + \alpha\tau_{xy}^3 \tag{3.6}$$

The failure criterion for matrix cracking is given by Equation 3.7:

$$\left(\frac{\sigma_y}{Y_T}\right)^2 + \frac{\frac{\tau_{xy}^2}{2G_{xy}} + \frac{3}{4}\alpha\tau_{xy}^4}{\frac{S_{xy}^2}{2G_{xy}} + \frac{3}{4}\alpha S_{xy}^4} = e_M^2 \tag{3.7}$$

If $e_M^2 > 1$, failure occurs and the following material properties E_y, G_{xy}, ν_x, ν_y are reduced to zero.

Failure in compression is described by Equation 3.8

$$\left(\frac{\sigma_y}{2G_{xy}}\right)^2 + \left[\left(\frac{Y_C}{2G_{xy}}\right)^2 - 1\right]\frac{\sigma_y}{Y_c} + \frac{\frac{\tau_{xy}^2}{2G_{xy}} + \frac{3}{4}\alpha\tau_{xy}^4}{\frac{S_{xy}^2}{2G_{xy}} + \frac{3}{4}\alpha S_{xy}^4} = e_C^2 \tag{3.8}$$

If $e_C^2 > 1$, failure occurs and the following material properties E_y, ν_x, ν_y are reduced to zero.

Failure caused by fibre breakage is assumed to be the final failure mode and is given by Equation 3.9

$$\left(\frac{\sigma_x}{X_T}\right)^2 + \frac{\frac{\tau_{xy}^2}{2G_{xy}} + \frac{3}{4}\alpha\tau_{xy}^4}{\frac{S_{xy}^2}{2G_{xy}} + \frac{3}{4}\alpha S_{xy}^4} = e_F^2 \tag{3.9}$$

If $e_F^2 > 1$, failure occurs and the following material properties E_x, E_y, G_{xy}, ν_x, ν_y are reduced to zero.

Delamination failure, in the case of $\sigma_z \geq 0$, is described with Equation 3.10

$$\left(\frac{\sigma_z}{Z_t}\right)^2 + \frac{\tau_{xz}^2 + \tau_{yz}^2}{S_{xz}^2(d_{ms}d_{fs} + \delta)} = e_l^2 \tag{3.10}$$

If $e_l^2 \geq 1$, delamination failure occurs due to tensile and shear stresses.

The above criteria can be simplified for linear elastic laminates when the nonlinear shear stress parameter α is equal to zero.

3.3.2.2.2 MAT_59 - Material Composite Failure Option

Material MAT_59 is an elasto-plastic material model for modelling orthotropic composites with solid and shell elements (Schweizerhof et al., 1998). According to Gemkow (2013), the failure model implemented in MAT_59 for the two dimensional case is based on the Chang and Chang (1987) theory, while for the three dimensional case failure is based on the Cheng and Hallquist (2004) failure criteria. The equations for the stress based failure (Peng et al., 2011) for the corresponding failure modes in a three dimensional case are given below:

Fibre failure under longitudinal tension (fibre rupture) is given by Equation 3.11:

$$\left(\frac{\sigma_x}{X_t}\right)^2 + \left(\frac{\tau_{xy}}{S_{xy}}\right)^2 + \left(\frac{\tau_{xz}}{S_{xz}}\right)^2 \geq 1, \ \sigma_x > 0 \tag{3.11}$$

Matrix failure under transverse tension (matrix cracking) is given by Equation 3.12:

$$\left(\frac{\sigma_y}{Y_t}\right)^2 + \left(\frac{\tau_{xy}}{S_{xy}}\right)^2 + \left(\frac{\tau_{yz}}{S_{yz}}\right)^2 \geq 1, \ \sigma_y > 0 \tag{3.12}$$

Longitudinal shear failure is given by Equation 3.13:

$$\left(\frac{\sigma_x}{X_t}\right)^2 + \left(\frac{\tau_{xz}}{S_{xz}}\right)^2 \geq 1, \ \sigma_x > 0 \tag{3.13}$$

Transverse shear failure is given by Equation 3.14:

$$\left(\frac{\sigma_y}{Y_t}\right)^2 + \left(\frac{\tau_{yz}}{S_{yz}}\right)^2 \geq 1,\ \sigma_y > 0 \tag{3.14}$$

Delamination failure is given by Equation 3.15:

$$\left(\frac{\sigma_z}{Z_t}\right)^2 + \left(\frac{\tau_{xz}}{S_{xz}}\right)^2 + \left(\frac{\tau_{yz}}{S_{yz}}\right)^2 \geq 1,\ \sigma_z > 0 \tag{3.15}$$

Fibre failure under longitudinal compression (fibre buckling and kinking) is given by Equation 3.16:

$$\left(\frac{\sigma_x}{X_c}\right)^2 \geq 1,\ \sigma_x < 0 \tag{3.16}$$

Matrix failure under transverse compression (matrix cracking) is given by Equation 3.17:

$$\left(\frac{\sigma_y}{S_{xy}+S_{yz}}\right)^2 + \left[\left(\frac{Y_c}{S_{xy}+S_{yz}}\right)^2 - 1\right]\frac{\sigma_y}{Y_c} + \left(\frac{\tau_{xy}}{S_{xy}}\right)^2 + \left(\frac{\tau_{yz}}{S_{yz}}\right)^2 \geq 1,\ \sigma_y < 0 \tag{3.17}$$

Failure in through thickness compression is given by Equation 3.18:

$$\left(\frac{\sigma_z}{S_{xz}+S_{yz}}\right)^2 + \left[\left(\frac{Z_c}{S_{xz}+S_{yz}}\right)^2 - 1\right]\frac{\sigma_z}{Z_c} + \left(\frac{\tau_{xz}}{S_{xz}}\right)^2 + \left(\frac{\tau_{yz}}{S_{yz}}\right)^2 \geq 1,\ \sigma_z < 0 \tag{3.18}$$

In comparison to material model MAT_22, material model MAT_59 exceeds the capabilities of the former, as it allows for modelling of the longitudinal and out of plane compression for solid elements, which is the restriction of MAT_22.

The Performance and accuracy of MAT_59 are validated and compared to other material models further in this chapter.

3.3.2.3 Damage models in LS-DYNA

3.3.2.3.1 MAT_54 - Material Enhanced Composite Damage

Material MAT_54 is a composite material damage model, which allows for modelling of anisotropic, linear elastic behaviour of undamaged and damaged composite structures. Different material orientations are defined in the material with the parameter $MANGLE$ for each integration point which define a single layer of a laminate. The nonlinearity in the material model is introduced through various damage criteria after damage in the laminate occurs. Degradation of the material properties in MAT_54 is controlled by the damage parameters. Material MAT_54 allows for complete and partial reduction of mechanical properties of the material. In addition to stress based failure criteria, strain limiting parameters can be defined to describe the onset of the damage and reduction of material parameters (Schweizerhof et al., 1998). This material model is applicable only to shell elements.

For this material model, the following material properties are necessary: Young's modulus, poissons ratio and shear modulus in every direction. Moreover, material strengths in fibre and matrix directions for compression and tension are needed. Failure of the material is governed by the Chang-Chang failure criteria (Chang and Chang, 1987), and is described with the following equations:

Fibre failure in tension (fibre rupture) is given by Equation 3.19:

$$\left(\frac{\sigma_x}{X_T}\right)^2 - 1 = e_F^2 \tag{3.19}$$

If $e_F^2 < 0$, the behaviour of the material is elastic. If $e_F^2 \geq 0$, failure occurs and the following material properties are set to zero: E_x, E_y, G_{xy}, ν_{yx}, ν_{xy}.

Fibre failure in compression (fibre buckling and kinking) is given by Equation 3.20:

$$\left(\frac{\sigma_x}{X_C}\right)^2 - 1 = e_C^2 \tag{3.20}$$

If $e_C^2 < 0$, the behaviour of the material is elastic. If $e_C^2 \geq 0$, failure occurs and the following material properties are set to zero: E_x, ν_{yx}, ν_{xy}.

Matrix failure in tension (matrix cracking under transverse tension and shearing) is given by Equation 3.21:

$$\left(\frac{\sigma_y}{Y_T}\right)^2 + \left(\frac{\tau_{xy}}{S_C}\right)^2 - 1 = e_M^2 \tag{3.21}$$

If $e_M^2 < 0$, the behaviour of the material is elastic. If $e_M^2 \geq 0$, failure occurs and the following material properties are set to zero: E_y, ν_{yx}, G_{xy}

Matrix failure in compression (matrix cracking under transverse compression and shearing) is given by Equation 3.22:

$$\left(\frac{\sigma_y}{2S_C}\right)^2 + \frac{\sigma_y}{Y_C}\left[\frac{Y_C^2}{4S_C^2} - 1\right] + \left(\frac{\tau_{xy}}{S_C}\right)^2 - 1 = e_D^2 \tag{3.22}$$

If $e_D^2 < 0$, the behaviour of the material is elastic. If $e_D^2 \geq 0$, failure occurs and the following material properties are set to zero: ν_{yx}, ν_{yx}, G_{xy}.

Table 3.1: Strain limiting parameters for MAT_54 (LSTC, 2013a).

Parameter	Definition
DFAILT	maximum strain for fibre tension
DFAILC	maximum strain for fibre compression
DFAILM	maximum strain for matrix (tension and compression)
DFAILS	maximum shear strain
EFS	effective strain

As mentioned before, material model MAT_54 has an option to define the strain limits, despite the failure controlled by stress based criteria. The strain limiting parameters are given in Table 3.1 (Hallquist, 2006, LSTC, 2013a).

Furthermore, the failure of the material can be controlled with a time step size criteria. This criterion is controlled with a parameter TFAIL, which allows for deletion of the element when a time step for the element reaches the critical value (Hallquist, 2006, LSTC, 2013a).

Therefore, there are four different ways for failure to be defined in the MAT_54, namely:

Table 3.2: Damage parameters for MAT_54 (LSTC, 2013a).

Parameter	Definition
SOFT	softening reduction factor for material strength in crashfront elements
FBRT	softening reduction factor for fibre tensile strength
YCFAC	softening reduction factor for compressive strength
SOFTG	softening reduction factor for transverse shear moduli in crashfront elements
SLIMT1(2)	factor for minimum stress limit after maximum stress is reached for fibre(matrix) tension
SLIMC1(2)	factor for minimum stress limit after maximum stress is reached for fibre(matrix) compression

- For $DFAILT = 0$, the failure is controlled with Chang Chang failure criteria
- For $DFAILT > 0$, the failure of the material is controlled by maximum (or minimum) strain defined with $DFAILT$ and $DFAILC$
- For $EFS > 0$, the failure of the material occurs when the effective strain(EFS) is exceeded
- For $TFAIL > 0$, the failure of the material is controlled with the element time step.

In addition to different methods of failure, this material model allows for the definition of damage parameters, which control material softening after failure. Damage of the element is not restricted only to the material which failure criterion was satisfied. MAT_54 enables the use of a "crashfront" zone, which is defined by the elements sharing the nodes with the element deleted due to the complete failure (failure has occurred in all integration points). To enable the crashfront definition, $TFAIL$ needs to be greater than zero. The softening parameters available in MAT_54 are given in Table 3.2.

3.3.2.3.2 MAT_58 - Material Laminated Composite Fabric

Material MAT_58 is a composite material model based on a damage mechanics model formulated by Matzenmiller et al. (1995). It allows to model damage in orthotropic materials under in-plane tensile, compressive or shear loading conditions. It can be used to model the behaviour of complete laminates with unidirectional (UD) and woven fabrics layers. This material is restricted to plate and shell problems as it is formulated for the plane stress conditions only.

Failure criteria implemented into the material model 58 are based on the Hashin (1980) failure criteria and are given by the following equations:

Fibre failure in tension (fibre rupture) is given by Equation 3.23:

$$\left(\frac{\sigma_x}{X_T}\right)^2 - 1 = e_F^2 \tag{3.23}$$

If $e_F^2 < 0$, the behaviour of the material is elastic. If $e_F^2 \geq 0$, failure occurs.

Fibre failure in compression (fibre buckling and kinking) is given by Equation 3.24:

$$\left(\frac{\sigma_x}{X_C}\right)^2 - 1 = e_C^2 \tag{3.24}$$

If $e_C^2 < 0$, the behaviour of the material is elastic. If $e_C^2 \geq 0$, failure occurs.

Matrix failure in tension (matrix cracking under transverse tension and shearing) is given by Equation 3.25:

$$\left(\frac{\sigma_y}{Y_T}\right)^2 + \left(\frac{\tau_{xy}}{S_C}\right)^2 - 1 = e_M^2 \tag{3.25}$$

If $e_M^2 < 0$, the behaviour of the material is elastic. If $e_M^2 \geq 0$, failure occurs.

Matrix failure in compression (matrix cracking under transverse compression and shearing) is given by Equation 3.26:

$$\left(\frac{\sigma_y}{Y_C}\right)^2 + \left(\frac{\tau_{xy}}{S_C}\right)^2 - 1 = e_D^2 \tag{3.26}$$

If $e_D^2 < 0$, the behaviour of the material is elastic. If $e_D^2 \geq 0$, failure occurs.

The above failure criteria define the threshold for damage onset. The stresses considered in the failure criteria are the effective stresses referred to the net area rather than the nominal stress. Matzenmiller et al. (1995) described the relation between the nominal and effective stresses in the form of Equation 3.27.

$$\hat{\sigma} = \begin{bmatrix} \hat{\sigma_x} \\ \hat{\sigma_y} \\ \hat{\tau_{xy}} \end{bmatrix} = \begin{bmatrix} \frac{1}{1-\omega_x} & 0 & 0 \\ 0 & \frac{1}{1-\omega_y} & 0 \\ 0 & 0 & \frac{1}{1-\omega_{xy}} \end{bmatrix} \begin{bmatrix} \sigma_x \\ \sigma_y \\ \tau_{xy} \end{bmatrix} \tag{3.27}$$

Where ω_x and ω_y are damage parameters which have different values for tension and compression, and ω_{xy} is a damage parameter for shear and it's value is independent of the sign of the shear stress. Considering the material stiffness tensor as a function of the damage, it can be described with Equation 3.28:

$$C(\omega) = \frac{1}{D} \begin{bmatrix} (1-\omega_x)E_x & (1-\omega_x)(1-\omega_y)\nu_{yx}E_y & 0 \\ (1-\omega_x)(1-\omega_y)\nu_{xy}E_x & (1-\omega_y)E_y & 0 \\ 0 & 0 & D(1-\omega_{xy})G \end{bmatrix} \tag{3.28}$$

where $D = 1 - (1-\omega_x)(1-\omega_y)\nu_{xy}\nu_{yx}$

As soon as the limit stresses are exceeded by the stresses developed in the material, the damage evolution is triggered. At that point the elastic response of the material is finished and the material behaviour is represented by the damage evolution law given by equation Equation 3.29:

$$\omega = 1 - exp\left[-\frac{1}{m_i e}\left(\frac{\varepsilon_i}{\varepsilon_{fi}}\right)^{m_i}\right] \tag{3.29}$$

Where e is Euler's number, m_i is the parameter responsible for the control of the stress-strain response of the material after damage is triggered, ε_i is the strain in the material, ε_{fi} is the nominal failure strain of the material, and index the i denotes the direction of the applied loading.

The nominal failure strains are given as follows:

- Longitudinal failure: $\varepsilon_{f1} = \frac{X_{t,c}}{E_1}$
- Transverse failure: $\varepsilon_{f2} = \frac{Y_{t,c}}{E_2}$

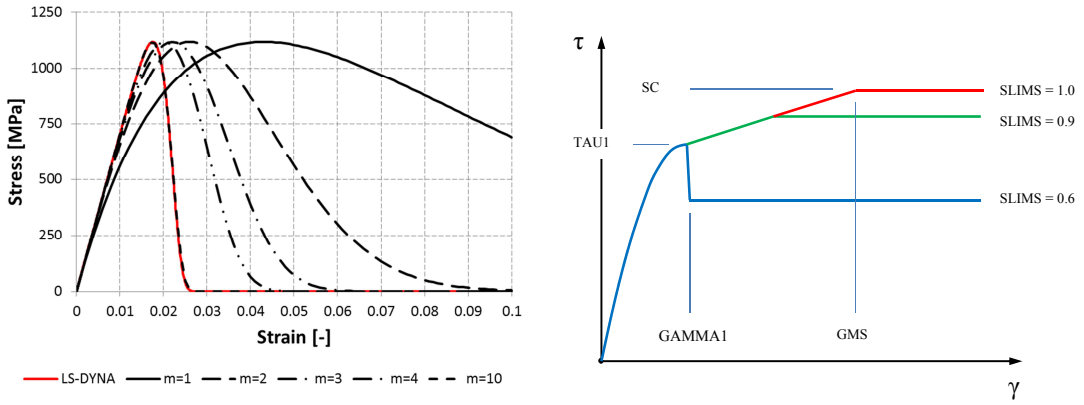

(A) (B)

FIGURE 3.4: (A) Influence of parameter *m* on the tensile stress-strain relationship (Gemkow, 2013), (B) Visualisation of shear stress limit parameters *TAU*1 and *GAMMA*1.

- Shear failure: $\varepsilon_{f12} = \frac{S}{G_{12}}$

The strain-softening parameter m_i present in the damage evolution law given with Equation 3.29 cannot be defined in LS-DYNA. According to Gemkow (2013), the default value of the parameter m in LS-DYNA is equal to 10. This value defines the quasi brittle response of the material (see Figure 3.4 A). LS-DYNA allows for definition of additional parameters used to limit the stress in the softening part of the material response. Moreover, two parameters (TAU1 and GAMMA1) can be defined to control the slope of the shear stress-strain curve (see Figure 3.4 B).

Similarly to MAT_54, MAT_58 allows for definition of a crashfront zone through a definition of TSIZE parameter.

The parameters available in LS-DYNA to control the damage of the material are presented in Table 3.3.

3.3.2.3.3 MAT_221 - Material Orthotropic Simplified Damage

Material model MAT_221 is an orthotropic material model, which allows for definition of simplified damage and failure. The elastic behaviour of MAT_221 is based on the material model 22 (LSTC, 2013a). This composite material model is implemented only for three dimensional elements.

Table 3.3: Parameters describing damage in MAT_58 (LSTC, 2013a).

Parameter	Definition
TAU1	stress limit in the shear stress-strain controlling the slope of the stress-stress curve after damage intiation
GAMMA1	strain limit in the shear stress-strain controlling the slope of the stress-stress curve after damage intiation
SLIMT1	factor for minimum stress limit after fibre tensile failure
SLIMC1	factor for minimum stress limit after fibre compression failure
SLIMT2	factor for minimum stress limit after matrix tensile failure
SLIMC2	factor for minimum stress limit after matrix compression failure
SLIMS	factor for minimum stress limit after shear failure
FS	type of failure surface
TSIZE	time step for automatic element deletion (triggers the crashfront zone in the material)

Failure of the material can be defined based on the failure strains in the elements for nine loading cases - tension and compression in each of the main directions and shear failure in three parallel planes, defined by the fibre and transverse to fibre directions. An additional parameter (NERODE) controls the erosion of the elements after failure and allows for deletion of elements after different combinations of failure, based on the failed integration points.

Similarly, nine damage parameters are available to be defined: six to control the degradation of the Young's modules for tension and compression, and three to control the degradation of the shear modules. In order to define damage of the material, in addition to the damage parameters, the damage thresholds need to be defined by the user. LS-DYNA enables to illustrate damage in the material with the history variables in DATABASE_EXTENT_BINARY output.

Definition of the damage and failure parameters can be found in Table 3.4.

3.3.3 Delamination modelling

Section 3.2.3 defines the damage modes of composite structures under impact loading. Except in-plane failure related to the matrix cracking or fibre rupture, another

Table 3.4: Failure and damage parameters in MAT_221 (LSTC, 2013a). Variable x defines direction (a, b or c direction) and xx defines plane (ab, bc or ac plane).

Parameter	Definition
EPSxTF	Tensile failure strain along x-direction
EPSxCF	Compressive failure strain along x-direction
EPSxxF	Shear failure strain in xx plane
EPSDxT	Damage threshold in tension along x direction
EPSCxT	Critical damage threshold in tension along x direction
CDAMxT	Critical damage in tension along x direction
EPSDxC	Damage threshold in compression along x direction
EPSCxC	Critical damage threshold in compression along x direction
CDAMxC	Critical damage in compression along x direction
EPSDxx	Damage threshold in shear in xx plane
EPSCxx	Critical damage threshold in shear in xx plane
CDAMxx	Critical damage in shear in xx plane

form of damage can arise between the plies of the composite material. It is a delamination. This paragraph describes the delamiantion failure mode and presents the available modelling techniques for prediction of delamination initiation and propagation.

3.3.3.1 Literature review

According to Wisnom (2012), delamination is one of the most dangerous failure modes in composite materials. Due to its internal occurrence, between the plies of the laminate, it is extremely difficult to detect during the inspection. Despite invisibility of this internal damage its occurrence can significantly reduce structure stiffness and strength. Therefore, ability to model and predict delamination, during the design stage of the components, is a crucial task for the designers and FE analysts.

Delamination in the structure arises due to the interlaminar longitudinal and transverse shear stresses, transverse in-plane stresses (Choi and Chang, 1992), and is characterised by the separation of the adjacent plies. Although it is known what

causes delamination, this failure mechanism is not fully understood yet (Rajbhandari et al., 2002) and its onset and propagation are extremely difficult to predict (Leung et al., 2011).

Few different methods were established to predict the initiation and development of delamination between the composite plies. Their implementation into explicit FE code, was more difficult than it was in case of the in-plane failure criteria. This difficulty is related to the fact that after delamination occurrence, the composite structure behaves in different manner and delamination strongly affects the damage progression within a structure. Separation of the plies causes formation of sublaminates with considerably lower stiffness, than in the case of the intact structure. Therefore, delaminated structure subjected to dynamic loading can fail in different way than undamaged laminate (Rajbhandari et al., 2002).

Different methods for predicting delamination damage in the composites were developed. Choi and Chang (1992) proposed a model for prediction of the matrix cracking and delamination, in the graphite/epoxy laminates, based on a double failure criterion. They inferred that delamination is a damage mode resultant from the matrix cracking, which is an initial failure mode in the composite laminates subjected to impact loading. They obtained a results with good agreement with the experimental results. However, the results obtained with this approach are dependent on the empirical parameter in the failure criteria. This parameter is a limitation of Choi and Chang (1992) approach as it can only be obtained experimentally.

Delamination between two thick plates under low velocity impact was studied by Zheng and Sun (1995). They used Mindlin plate finite element model, with contact constraints applied to the interface between plates to predict the delamination. Numerical results obtained with this method showed good agreement with the experimental results. Zheng and Sun (1995) concluded that their approach to model dalemination is computationally efficient and accurate for calculation of strain energy release rate at delamination front.

Luo et al. (1999) modelled and tested the damage onset and propagation under impact loading in the composite plates. They incorporated three stress based failure criteria (fibre breakage, interlaminar delamination and matrix failure) into ABAQUS composite model. Three layers of 20-noded solid elements were used in their research to model the symmetrical composite laminate. Luo et al. (1999) approach

treated fibre breakage as the final failure mode and simulations were terminated after fibre failure. In case of the interlaminar delamination and matrix failure the corresponding material properties were reduced to 1% of their initial value. Authors identified delamination and matrix cracking as the main damage modes for the impacted composite, moreover, they observed good agreement between the numerical and experimental results.

Hou et al. (2000) enhanced the existing DYNA3D composite material model, based on the Chang Chang failure criterion. The approach proposed by the authors was based on the implementation of improved failure criteria to the composite failure model. Failure criteria used by the authors is presented with equations 3.30 - 3.33 and damage evolution law is given with Equation 3.34. Hou et al. (2000) used their model for prediction of the impact damage in the composite plate under low velocity impact. Moreover, Hou et al. (2000) considered interaction between the damage modes by implementation of corresponding stress update schemes. Composite plate modelled with stack of solid elements successfully represents the experimental results, however, the delamination free region under the impactor was larger in case of numerical simulation. Authors suggested further studies on the influence of the interaction between through-thickness compression and shear stresses on the delamination onset and propagation.

Fibre failure:

$$e_f^2 = \left(\frac{\sigma_x}{X_t}\right)^2 + \left(\frac{\sigma_{xy}^2 + \sigma_{xz}^2}{S_f^2}\right) \geq 1 \tag{3.30}$$

Transverse matrix cracking

$$e_m^2 = \left(\frac{\sigma_y}{T_t}\right)^2 + \left(\frac{\sigma_{xy}}{S_{xy}}\right)^2 + \left(\frac{\sigma_{yz}}{S_{myz}}\right)^2 \geq 1 \tag{3.31}$$

Matrix crushing, for $\sigma_y < 0$:

$$e_d^2 = \frac{1}{4}\left(\frac{\sigma_y}{S_{xy}}\right)^2 + \frac{Y_c^2 \sigma_y}{4 S_{xy}^2 Y_c} - \frac{\sigma_y}{Y_c} + \left(\frac{\sigma_{xy}}{S_{xy}}\right)^2 \geq 1 \tag{3.32}$$

Delamination, for $\sigma_z \geq 0$:

$$e_l^2 = \left(\frac{\sigma_z}{Z_t}\right)^2 + \left(\frac{\sigma_{yz}}{S_{lyz}}\right)^2 + \left(\frac{\sigma_{zx}}{S_{zx}}\right)^2 \geq 1 \tag{3.33}$$

where, S_f is shear strength involving fibre failure, S_m shear strength for matrix cracking in the transverse and through thickness plane and S_l is shear strength for delamination in the transverse and through thickness plane.

Damage evolution law:

$$\{d\} = \{d(t)\}\,(0 < d_{ij} < 1) \tag{3.34}$$

where d_{ij} is a damage parameter for corresponding load direction.

Further work of Hou et al. (2001), on the delamination problem in the composite plates under impact, succeed in the implementation of more realistic delamination criterion into LS-DYNA (see Equations 3.36 - 3.38). This modification in the failure criterion took into account the out of plane compression as the load case which influence delamination onset. Therefore, Hou et al. (2001) concluded that delamination can develop in the area where interlaminar shear stresses are high and the out-of-plane compression is relatively low. This approach is an improvement to Hou et al. (2000) model, where the delamination under compressive loading was restricted. The new delamination criteria developed by Hou et al. (2001) were implemented into LS-DYNA MAT_22 composite model and are given with Equations 3.36 - 3.38.

Collombet et al. (1996) proposed a three dimensional damage model for the impact on the composite laminates. Authors used a stack of solid elements to represent the laminate plies. Separate plies were tied together by the contact algorithm based on the Lagrangian multiplier technique. Delamination occurs when the contact between two corresponding nodes of the adjacent plies was broken. Collombet et al. (1996) obtained good agreement between the experimental results and numerical simulation for modelling damage in the glass-epoxy composite plates.

Similar approach to model delamination with solid elements connected together by tied contact was used by Hoof et al. (1999) and Hung et al. (1995). Each ply of the composite laminate was modelled with the layer of solid elements and contact tied was implemented between each interface. When dalamination occurred, the tied contact was broken based on the delamination failure criteria, implemented into the contact algorithm (see Equation 3.35). This solution for modelling delamination between composite lay-ups shows good correlation between the numerical and experimental results.

$$F_{delam} = \left(\frac{\sigma_n}{S_n}\right)^2 + \left(\frac{\sigma_s}{S_s}\right)^2 \tag{3.35}$$

where, σ_n and σ_s are the interface normal and shear stresses, respectively, and S_n and S_s are the normal and shear strengths of the interface, respectively.

Lammerant and Verpoest (1996) investigated the influence of the matrix cracks on delamination in composite plates under impact loading. In their approach the composite laminate was modelled as a solid structure. The interface between adjacent plies was modelled with spring elements, which controlled damage development base on the nodal displacement. In their research, Lammerant and Verpoest (1996) considered structure with and without initial cracks in the laminate. Initial cracks were modelled as nodes without spring connection in between the adjacent plies. Moreover, no spring connection was modelled between the nodes of a single ply to represent initial matrix cracks between the fibres. The results obtained with the numerical analysis were in correspondence to the experimental results. Authors concluded that the initial matrix cracks cannot be neglected in modelling delamination onset and development. Similar conclusion regarding the influence of the initial matrix cracks on the delamination initiation was drown by other authors (Abrate, 1998, Choi and Chang, 1992, Joshi and Sun, 1985).

Recently, the attention in delamination modelling was drawn by the techniques based on the linear elastic fracture mechanics, such as the stiffness derivative (Parks, 1974), the J-integral (Rice, 1968), virtual crack extensions (Hellen, 2005) or virtual crack closure methods (Raju, 1987, Rybicki and Kanninen, 1977). These techniques allows for prediction of single and multiple cracks propagation, however, the initial position of the crack as well as propagation paths need to be known and specified in advance. Crack propagation in above methods is based on the Griffith (1921) criteria, which assumes that the crack propagates when the critical value of fracture toughness is exceeded by the energy release rate at the crack tip. Nevertheless, as mentioned before, above methods are restricted to the structures where position of the initial crack is known. Therefore, these modelling techniques are not suitable to model the onset of delamination in the structure under impact loading.

Restriction of the fracture mechanics based models, namely, the inability to predict delamination onset, can be overcame with the methods based on damage mechanics and/or softening plasticity, combined with an indirect application of fracture mechanics (Gordnian et al., 2008). One of these techniques is the Cohesive Zone Model (CZM), which applied together with interface elements allows for modelling of

delamination initiation and propagation without specifying an initial crack location (Aymerich et al., 2008, Turon et al., 2007). CZM assumes existence of a process zone in front of the physical crack tip. This process zone, referred to as a cohesive zone, is delimited by the cohesive surfaces that are held together by cohesive tractions. The strength of the interface (traction) is related to the relative displacement of the cohesive surface through the traction separation law, which also takes into account the progressive softening of the interface after damage onset (Aymerich et al., 2008, Camanho and Davila, 2002, Mi et al., 1998).

Three of the delamination modelling techniques described above are available in LS-DYNA, namely:

- delamination failure criterion incorporated into material models MAT_22 and MAT_59
- delamination through contact tiebreak implemented between the layers of solid elements (delamination based on failure criteria or CZM)
- delamination modelled with the interface elements, of zero or finite thickness, implemented between the composite plies

The three delamination modelling approaches are discussed further in next section of this chapter. Deeper insight is provided for the delamination modelling with cohesive elements due to its ability to predict onset and propagation of delamination.

3.3.3.2 Delamination modelling techniques in LS-DYNA

3.3.3.2.1 Failure criterion for delamination

Delamination based on failure criteria is available in two different LS-DYNA material models.

First of these models is Material Composite Damage (MAT_22 - described in 3.3.2.3). The delamination criterion was implemented into MAT_22 by Hou et al. (2001) and is based on the modified Brewer and Lagace (1988) delamination failure criterion. This delamination criterion takes into account the interaction between

the interlaminar shear and through thickness compression, and is defined by the following expressions:

In the case of $\sigma_z \geq 0$,

$$\left(\frac{\sigma_z}{Z_t}\right)^2 + \frac{\tau_{xz}^2 + \tau_{yz}^2}{S_{xz}^2(d_{ms}d_{fs} + \delta)} = e_l^2 \tag{3.36}$$

If $e_l^2 \geq 1$, delamination failure occurs due to tensile and shear stresses.

In the case of $-\sqrt{\tau_{xz}^2 + \tau_{yz}^2/8} \leq \sigma_z < 0$

$$\frac{\tau_{xz}^2 + \tau_{yz}^2 - 8\sigma_z^2}{S_{xz}^2(d_{ms}d_{fs} + \delta)} = e_l^2 \tag{3.37}$$

If $e_l^2 \geq 1$, delamination failure occurs due to shear and low compressive stresses.

Finally in the case of $\sigma_z < -\sqrt{\tau_{xz}^2 + \tau_{yz}^2/8}$

$$e_l^2 \equiv 0 \tag{3.38}$$

no delamination failure occurs.

The following parameters were introduced in Equations 3.36 to 3.38: e_l is a delamination indicator; d_{ms} is a matrix damage coefficient ($0 \leq d_{ms} \leq 1$); d_{fs} is a fibre damage coefficient ($0 \leq d_{fs} \leq 1$); and δ is the ratio between the interlaminar shear stresses before and after occurrence of matrix or fibre failure (Hou et al., 2001).

In order to display the delamination failure in MAT_22, an additional card for history variables need to be defined in DATABASE_EXTENT_OPTION keyword in LS-DYNA. History variable number 7 is related to delamination failure in MAT_22.

The second of the material models to predict delamination in composite materials is Material Composite Failure (MAT_59 - described in 3.3.2.2). The delamination failure criterion for this model is given by Equation 3.39:

For $\sigma_z > 0$

$$\left(\frac{\sigma_z}{Z_t}\right)^2 + \left(\frac{\tau_{xz}}{S_{xz}}\right)^2 + \left(\frac{\tau_{yz}}{S_{yz}}\right)^2 \geq 1 \tag{3.39}$$

The above failure criterion does not consider delamination failure in compression, hence the delamination in this material model occurs only due to the tensile and shear stresses.

To visualise the delamination failure in MAT_59, additional card history variables need to be defined in the DATABASE_EXTENT_OPTION keyword in LS-DYNA. History variable number 4 is related to visualisation of the delamination failure in MAT_59.

Delamination failure criteria in material models are the easiest approaches to model delamination as they only require definition of additional history variables in LS-DYNA. However, these approaches do not allow for modelling of separation of the adjacent plies in the laminate. Therefore, the delamination propagation in composite structures cannot be modelled with failure based delamination criteria only.

3.3.3.2.2 Delamination modelled with contact tiebreak

Another approach to model delamination in composite materials is using the tiebreak contact algorithm. This method allows to define a contact which ties separate layers of the composite and can be broken after a certain criterion is fulfilled.

Contact implemented between the interface of layers of elements gives good approximation of the real structures. In this case, a single layer of elements represents the composite ply and delamination can be modelled as a loss of contact between two adjacent plies of the material.

There are two different ways of modelling delamination with a contact tiebreak. The first one is based on the delamination failure criterion implemented in the contact algorithm and the second one is equivalent to the cohesive zone modelling. The latter approach will be discussed and described in a separate section dedicated to the interface elements.

According to the LS-DYNA keyword manual (LSTC, 2013b), the following failure criterion was implemented into the tiebreak contact algorithm:

$$\left(\frac{|\sigma_n|}{NFLS}\right)^2 + \left(\frac{|\sigma_s|}{SFLS}\right)^2 \geq 1 \tag{3.40}$$

Where, σ_n is a normal stress, $NFLS$ is a normal failure stress, σ_s is a shear stress and $SFLS$ is a shear failure stress.

The above failure criterion is implemented into contact tiebreak options 2, 3 and 6. Contact tiebreak option 4 is limited only to the normal stress component of the

failure criterion and is represented with Equation 3.41. For contact tiebreak option 5, the stress is limited by the perfectly plastic yield criterion, which takes different form in the case of tension (see Equation 3.42) and compression (Equation 3.43)

$$\frac{|\sigma_n|}{NFLS} \geq 1 \tag{3.41}$$

$$\frac{\sqrt{\sigma_n^2 + 3|\sigma_s|^2}}{NLFS} \leq 1 \tag{3.42}$$

$$\frac{\sqrt{3|\sigma_s|^2}}{NLFS} \leq 1 \tag{3.43}$$

In addition to the above failure criteria, contact tiebreak options 5 and 6 allow for the modelling of damage of the interface. The damage is triggered when the failure criterion is satisfied. For option 5, the damage of the interface is a function of the crack width opening and can be defined by the user with a load curve. For option 6, the damage is a linear function of the distance between two points, which were initially in contact. After the damage is fully developed, the failure of the interface occurs and the contact algorithm behaves as surface to surface contact.

3.3.3.2.3 Delamination modelled with interface elements

The last approach available in LS-DYNA to model delamination in composites is by introducing interface elements between two adjacent layers of elements. This technique allows to model the delamination with fracture mechanics based separation laws incorporated into the cohesive element formulation.

The general idea of the delamination modelled with the CZM is illustrated in Figure 3.5. This figure shows bilinear softening constitutive law for pure delamination modes (Mode I, Mode II or Mode III). The applied load causes development of the interlaminar stresses in the interface elements. The first line represents the linear elastic response of the material, where the high value of initial stiffness of the interface holds the top and bottom faces together. At this stage, the material is not damaged and it behaves in an elastic manner (point 1 on the curve). Point 2 on the curve represents the point where the interlaminar stresses, developed inside

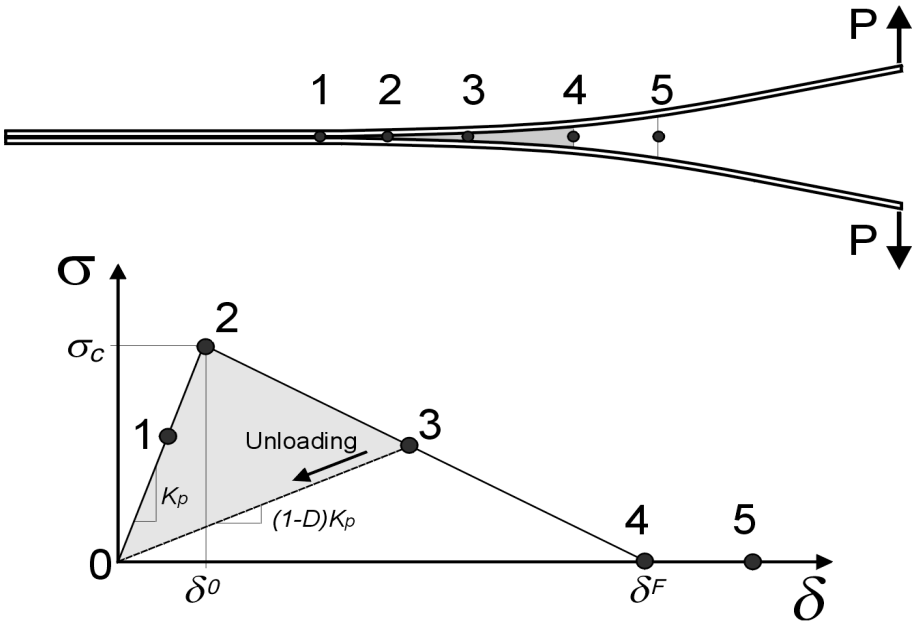

Figure 3.5: Bilinear traction separation law (LSTC, 2012).

the interface, reach the corresponding material strength. From this moment, the material softening process begins. As a consequence, the stiffness of the material is reduced gradually to zero. Point 3 on the curve indicates that the damage of the material progressed, however, the plies of the laminate have not separated yet. This means, that in the case of structure unloading, the stresses and strains in the interface would decrease to zero, following a straight line toward the origin. The triangle formed within the points 0, 2 and 3 of the constitutive law, determines the energy dissipated for the partial damage of the interface. If unloading of the structure does not happen, the stiffness of the interface is further reduced until it reaches zero, which corresponds to a complete separation of the laminate plies. At this stage, the damage parameter reaches unity and the structure is not able to carry any further load. Failure of the interface occurs and the corresponding cohesive element is removed from the analysis (point 5 on the curve).

The area under the traction-relative displacement curve corresponds to the fracture toughness (energy release rate) of the interface material for adequate delamination mode.

LS-DYNA provides a number of cohesive material models which enable for modelling

of delamination with a CZM approach. The formulation of interface elements allows for implementation of zero or finite thickness solid cohesive elements between two layers of composite material for modelling the interface prone to delamination.

In addition to interface elements, contact tiebreak options 7, 9 and 11 allow for introduction of cohesive zone modelling for delamination between composite layers. For these contact options, a traction separation laws were incorporated into a definition of contact algorithm.

Delamination modelling with cohesive zone approach is a powerful tool for modelling delamiantion in composite materials as it allows for modelling both onset and propagation of delamination. Hence, it was decided that further insight into this modelling technique is necessary for full understanding of the behaviour of cohesive elements. The underlying theory for the cohesive material models is presented further in this section.

Literature review on cohesive elements

The Cohesive Zone Model approach was first introduced by Dugdale (1960) and Barenblatt (1959, 1962). In their research they used the concept of cohesive traction in the plastic deformation zone in front of the crack tip. Dugdale (1960) assumed that the cohesive strength of the interface is equal to the yield strength of the material and is constant within the cohesive zone. The Barenblatt (1959) model is very similar to the model presented by Dugdale (1960), however, the stresses within the cohesive zone are not constant but they vary with the deformation.

The approach of the deformation zone in front of the crack tip was later implemented into a FE code by Hillerborg et al. (1976), who employed it into an analysis of the crack formation and growth in concrete. Fast crack growth in brittle solids was investigated with the CZM approach by Needleman (1987). He concluded that modelling the interface with CZM is very suitable for structures with relatively weak interfacial strengths in comparison to the adjoining material, such as composite structures.

Later, the improvement of CZM was achieved by introduction of more realistic cohesive models (Camacho and Ortiz, 1996, Tvergaard and Hutchinson, 1992, 1993).

In comparison to the model presented by Dugdale (1960), in these models the initial elastic behaviour is followed by a softening process for the damaged interface. In the softening zone, the traction is decreased with a separation of the interface. Moreover, the onset of crack propagation is controlled with the critical separation parameter.

Further improvement of the cohesive zone approach was done by Schellekens and DeBorst (1994) who introduced separate elements to model the interface.

Following DeBorst, different element types have been proposed for the modelling of the cohesive interfaces. In general, the existing cohesive elements can be divided into point interface elements and continuous cohesive elements (Camanho and Davila, 2002, Elmarakbi et al., 2009).

The point cohesive elements are nonlinear spring elements. Cui and Wisnom (1993) used point decohesion elements to model delamination onset and growth in glass/epoxy composites. Nonlinear springs were also used by Shahwan and Waas (1997) for the analysis of delaminated structures under compressive load.

The choice of element types for the continuous cohesive elements is considerably wider. Finite thickness elements were employed to model delamination of composite shell structures by Reedy et al. (1997). Line decohesion elements were used by Petrossian and Wisnom (1998) for delamination prediction in discontinuous plies. Chen (1999) also used line cohesive elements to predict the progressive delamination in composites. Chen's approach was further applied to ABAQUS (SIMULIA, 2013) FE software. Finally, zero thickness volumetric elements were used to bond layers of solid elements by DeMoura et al. (1997), Elmarakbi et al. (2009), Goncalves et al. (2000), Mi et al. (1998) and many others.

As mentioned before, the main advantage of using cohesive elements for modelling delamination in composite structures is the possibility to model delamination onset and growth without specifying the initial crack location. Moreover, the direction of delamination propagation does not need to be specified before the analysis.

Despite the advantages of using cohesive elements, like every numerical approach, the CZM suffers from numerical instabilities. One of the main issues related to modelling delamination with CZM is the elastic snap back (Gao and Bower, 2004, Goncalves et al., 2000, Hu et al., 2007, Mi et al., 1998). This problem occurs after the interface strength is reached by the stresses generated in the element, and is

characterised by high oscillations in the simulation of damage progression. The elastic snap back problem is especially evident for interfaces with high initial stiffness and high strength, modelled with coarse meshes (Hu et al., 2007).

The problem can be addressed using some direct techniques. For instance, application of very fine meshes can mitigate high oscillations in the softening zone, however, this solution leads to significant increase in computational time. Another solution is to decrease the strength and initial stiffness of the cohesive zone. However, this results in a lower slope of the load displacement curve before damage onset. Alfano and Crisfield (2001) performed parametric studies on the variation of the maximum strength of the interface with a constant fracture toughness. They concluded that lower cohesive strength can increase the stability of the results and improve the convergence of the solution with negligible influence on the predicted results. A decrease in the interfacial strength leads to an increase of the cohesive zone length and number of elements in the interface separation zone. The accuracy of the softening response ahead of the crack tip is increased, although the stress distribution in the crack tip neighbourhood can be affected (Alfano and Crisfield, 2001). Similar approach of lowering the interface strength while keeping a constant energy release rate was proposed by Bazant and Planas (1997) in their crack band model.

Riks (1979) proposed an incremental method, which follows an equilibrium path after instability. Recently, other methods were developed to overcome the elastic snap back instability without mesh refinement, namely, an artificial damping method (Gao and Bower, 2004), a move-limit method (Hu et al., 2007) and finally, a new adaptive cohesive element proposed by Elmarakbi et al. (2009).

Despite some numerical issues with the CZM, this method remains a useful approach for modelling delamination in composite structures.

Element formulation

The interface between the composite plies can be modelled with zero thickness cohesive elements as it was stated in the previous sections. The interpolation shape functions for the bottom and top faces of cohesive elements are compatible with the kinematics of the adjoining elements (Davila et al., 2001). The formulation of cohesive elements employs the relation between traction and relative displacement.

This relationship is given in the form of a constitutive law, which combines strength of the interface with relative displacement, taking into account the softening process of the interface after delamination onset.

So far many different traction separation laws have been proposed and investigated by researchers, for instance: linear softening (bilinear) (Camacho and Ortiz, 1996, Geubelle and Baylor, 1998), bilinear softening (Petersson, 1981, Wittmann et al., 1988), cubic polynomial (Tvergaard, 1990), trapezoidal (Tvergaard and Hutchinson, 1993), smoothed trapezoidal (Scheider and Brocks, 2003) and exponential (Ortiz and Pandolfi, 1999) traction separation law.

Single mode delamination

The simplest from the above strain softening constitutive laws and the most often used in modelling delamination of composite structures (Camanho et al., 2003, De-Moura et al., 1997, Pinho et al., 2004) is a bilinear constitutive model. Therefore, the cohesive element formulation shown in this section is based on the bilinear cohesive law (see Figure 3.5).

In general, the traction separation law can be expressed in the form given by Equation 3.44:

$$\int_0^{\delta_i^f} \tau_i d\delta_i = G_{iC} \tag{3.44}$$

where, $i = 1,\ 2,\ 3$ corresponds to the delamination mode, δ_i^f and τ_i are respectively, the ultimate relative displacements and ultimate interface tractions for the corresponding delamination mode, and G_{iC} is a critical energy release rate, equal to the fracture toughness of the material for the corresponding delamination mode.

The onset displacement for different delamination modes can be calculated using Equation 3.45

$$\delta_i^o = \tau_{ui}/K_i \tag{3.45}$$

where $i = 1,\ 2,\ 3$ corresponds to the delamination mode, τ_{u1} is the interface normal strength (traction in normal direction), τ_{u2} and τ_{u3} are the interface shear strengths (tractions in tangential direction), and K_i are the corresponding stiffnesses.

In order to complete the description of the cohesive element formulation, the unloading condition needs to be specified. To do so, it is necessary to introduce a

maximum relative displacement variable, δ^{max}. The unloading behaviour is defined in terms of maximum relative displacement of the point:

$$Mode\ I: \qquad \delta_1^{max} = max\{\delta_1^{max}, \delta_1\}, \qquad \delta_1^{max} \geq 0 \tag{3.46}$$

$$Mode\ II\ or\ III: \qquad \delta_i^{max} = max\{\delta_i^{max}, \delta_i\}, \qquad i = 2,3 \tag{3.47}$$

It is described using a loading function, F:

$$Mode\ I: \qquad F\left(|\delta_1| - \delta_1^{max}\right) = \frac{\langle |\delta_1| - \delta_1^{max} \rangle}{|\delta_1| - \delta_1^{max}}, \qquad \delta_1^{max} \geq 0 \tag{3.48}$$

$$Mode\ II\ or\ III: \qquad F\left(|\delta_i| - \delta_i^{max}\right) = \frac{\langle |\delta_i| - \delta_i^{max} \rangle}{|\delta_i| - \delta_i^{max}}, \qquad i = 2,3 \tag{3.49}$$

where, the following operator is used:

$$\langle |\delta_1| - \delta_1^{max} \rangle = \begin{cases} 0 & \Leftarrow \quad |\delta_1| - \delta_1^{max} \leq 0 \\ |\delta_1| - \delta_1^{max} & \Leftarrow \quad |\delta_1| - \delta_1^{max} > 0 \end{cases}$$

The irreversibility of the damaged material is taken into account by implementation of maximum relative displacement into the constitutive equation. After damage onset, if the relative displacement decreases, the material unloads toward the origin with a degraded stiffness. Therefore, the bilinear constitutive law, which takes into account the irreversibility of the damage and the material softening, can be defined with Equation 3.50 (Alfano and Crisfield, 2001, Camanho and Davila, 2002, Chen, 1999, Davila et al., 2001):

$$\tau_i = \begin{cases} K\delta_i & \Leftarrow \quad \delta_i^{max} \leq \delta_i^o \\ x(1-d_i)K\delta_i & \Leftarrow \quad \delta_i^o < \delta_i^{max} < \delta_i^f \\ 0 & \Leftarrow \quad \delta_i^{max} \geq \delta_i^f \end{cases} \tag{3.50}$$

Where, $d_i = \frac{\delta_i^f(\delta_i^{max} - \delta_i^o)}{\delta_i^{max}(\delta_i^f - \delta_i^o)}$, $i = 1,2,3;\ d \in [0,1]$, is the damage parameter.

To prevent interpenetration of the faces after crack occurrence, the following condition is applied:

$$\tau_1 = K\delta_1 \quad \Leftarrow \quad \delta_1 \leq 0 \tag{3.51}$$

The above condition reassigns the penalty stiffness to the model after penetration of the newly created surfaces is detected.

Taking into account the above considerations, a cohesive element is fully defined by the energy release rate, the cohesive traction and the initial stiffness (Lee et al., 2010). However, research results have shown that the key parameter controlling the behaviour of cohesive elements is the critical energy release rate (LSTC, 2012, Mi et al., 1998). The slope of the traction - relative displacement curve (elastic stiffness) and the peak traction do not cause significant change in the final results of the analyses. Therefore, the values of stiffness and traction of the interface can be changed within the analysis as far as the energy release rate is kept constant. The values of the fracture toughness have to be determined experimentally for the corresponding delamination mode.

Mixed mode delamination

The wide application of composite materials is related to different types of load acting on these structures in their lifecycle. Therefore, the delamination created in the structure usually arises under complex loading and the delamination propagation needs to be described in terms of multi mode delamination. Hence, the interface element constitutive model is required to take into account delamination onset and propagation under mixed mode conditions.

Delamination onset

In the case of single modes of delamination, the damage onset can be determined by comparison of the traction and the strength of the material. Nevertheless, for more complex types of loading the delamination onset and related softening behaviour can occur before any of the ultimate traction values is reached. Cui and Wisnom (1993) emphasised the significance of the interactions of interlaminar stresses on delamination predictions. Since the maximum stress criteria, used for prediction of delamination onset under single type of loading, do not consider the interaction between the interlaminar stresses, the results obtained with this approach were unrealistic.

Accordingly, Chen (1999) proposed a quadratic failure criterion for prediction of delamination onset under mixed mode loading conditions. This criterion accounts for the interaction between normal and in-plane stress components and it was successfully used by Camanho and Matthews (1999), Cui and Wisnom (1993), Davila and

Johnson (1993). Assuming that the compressive normal traction does not influence delamination initiation, the delamination failure criterion is given by Equation 3.52:

$$\left(\frac{\langle\tau_1\rangle}{\tau_{u1}}\right)^2+\left(\frac{\tau_2}{\tau_{u1}}\right)^2+\left(\frac{\tau_3}{\tau_{u1}}\right)^2=1 \tag{3.52}$$

Total mixed mode relative displacement, δ_m is defined with Equation 3.52:

$$\delta_m=\sqrt{\langle\delta_1^2\rangle+\delta_2^2+\delta_1^2}=\sqrt{\langle\delta_1^2\rangle+\delta_{shear}^2} \tag{3.53}$$

where, δ_{shear} represents the combined tangential relative displacement for delamination Modes II and III.

Assuming that $\tau_{u2}=\tau_{u3}$, and combining it with Equation 3.45 for relative displacements for an onset of single mode delamination, the combined tangential relative displacement can be described as:

$$\delta_2^o=\delta_3^o=\delta_{shear}^o=\frac{\tau_{u2}}{K_2} \tag{3.54}$$

Hence, the ratio of mode mixity, β, for an opening displacement δ_1 greater than zero is given as:

$$\beta=\frac{\delta_{shear}}{\delta_1} \tag{3.55}$$

Substituting Equations 3.45 and 3.53 - 3.55 into Equation 3.52, the relation for the mixed mode relative displacement in the softening zone is given as:

$$\delta_m^o=\begin{cases}\delta_1^o\delta_2^o\sqrt{\frac{1+\beta^2}{\left(\beta\delta_1^o\right)^2+\left(\delta_2^o\right)^2}} & \Leftarrow \quad \delta_1>0\\ \delta_{shear}^o & \Leftarrow \quad \delta_1\leq 0\end{cases} \tag{3.56}$$

For the proposed mixed mode formulation the pure mode loading is a particular case:

Mode I :	$\delta_m^o=\delta_1^o$	$\beta=0$
Mode II or III :	$\delta_m^o=\delta_{shear}^o$	$\beta\to\infty$

Delamination propagation

Similarly to the delamination onset, the delamination propagation needs to be defined separately for the mixed mode loading conditions. The softening response of

the material is obtained in terms of the fracture toughness and energy release rates of the material. Most of the existing failure criteria for delamination growth are established only for mixed modes I and II due to the lack of reliable method for the prediction of fracture toughness for the mode III delamination. However, some methods have been proposed to determine the mode III fracture toughness such as the Edge Crack Torsion (Lee, 1993, Ratcliffe, 2004). Camanho and Davila (2002) used the approach proposed by Li and O'brien (1996), where $G_{shear} = G_{II} + G_{III}$.

In order to properly describe the mixed mode behaviour of the cohesive element the fracture toughness dependency on the mixity ratio needs to be considered. Several different mixed mode delamination criteria have been proposed to describe damage propagation in composite materials. One of the most frequently used among these criteria is the power law criterion defined with Equation 3.57:

$$\left(\frac{G_I}{G_{IC}}\right)^{\alpha} + \left(\frac{G_{II}}{G_{IIC}}\right)^{\alpha} = 1 \tag{3.57}$$

where, α is a mixity ratio.

The mixed mode I and II interface fracture toughness for composites was obtained by Reeder (1992). He performed mixed mode bending (MMB) tests and obtained valuable results, which enable to assess numerous available mixed mode failure criteria. Utilising data collected by Reeder (1992), a power law criterion was assessed for the mixed model delamination prediction. The analysis results performed with the power law criterion gave good agreement to the experimental results for the PEEK matrix composites for $\alpha = 1$, but at the same time, it failed to predict delamination growth in the epoxy based composites.

Another criterion to predict delamination propagation under mixed mode loading conditions was proposed by Benzeggagh and Kenane (1996). It was defined as a function of the fracture toughness for the corresponding load condition and parameter η, responsible for the mode mixity (see Equation 3.58).

$$G_{IC} + (G_{IIC} - G_{IC}) \left(\frac{G_{II}}{G_T}\right)^{\eta} = G_C \tag{3.58}$$

where $G_T = G_I + G_{II}$.

Incorporating mode III delamination, the criterion takes the form given with Equation 3.59:

$$G_{IC} + (G_{IIC} - G_{IC}) \left(\frac{G_{shear}}{G_T} \right)^{\eta} = G_C \tag{3.59}$$

where $G_T = G_I + G_{shear}$.

The application of failure criterion established by Benzeggagh and Kenane (1996) to predict delamination growth gave good agreement to the experimental results for a wide range of mode mixity values for both thermoplastic (PEEK) and brittle epoxy resins (Camanho and Davila, 2002).

Both criteria are implemented into the cohesive element formulation in LS-DYNA. However, according to Camanho and Davila (2002), it is recommended to use the Benzeggagh-Kenane failure criterion for prediction of delamination propagation in thermoplastic and epoxy based composites. For thermoplastic composites, the power law criterion also gives reasonably good results.

The energy release rates for complete separation can be calculated using Equation 3.60:

$$\int_0^{\delta_m^{if}} \tau_i d\delta_i = G_{iC} \tag{3.60}$$

where $i = 1,\ 2,\ 3$ correspond to the delamination mode.

Substituting equations 3.50, 3.54, 3.55 into 3.60 and further into 3.57 or 3.59, the expression for the ultimate mixed mode displacement for total decohesion can be established.

Therefore, the mixed mode ultimate displacements for the power law and for the Benzeggagh-Kenane failure criterion are given by Equations 3.61 and 3.62 respectively:

$$\delta_m^f = \begin{cases} \frac{2(1+\beta^2)}{K\delta_m^o} \left[\left(\frac{1}{G_{IC}} \right)^2 + \left(\frac{\beta^2}{G_{IIC}} \right)^{\alpha} \right]^{-\frac{1}{\alpha}} & \Leftarrow \quad \delta_1 > 0 \\ \sqrt{\left(\delta_2^f \right)^2 + \left(\delta_3^f \right)^2} & \Leftarrow \quad \delta_1 \leq 0 \end{cases} \tag{3.61}$$

$$\delta_m^f = \begin{cases} \frac{2}{K\delta_m^o}\left[G_{IC} + (G_{IIC} - G_{IC})\left(\frac{\beta^2}{1+\beta^2}\right)^{\eta}\right] & \Leftarrow \quad \delta_1 > 0 \\ \sqrt{\left(\delta_2^f\right)^2 + \left(\delta_3^f\right)^2} & \Leftarrow \quad \delta_1 \leq 0 \end{cases} \tag{3.62}$$

Similarly to the delamination onset, the pure mode loading is a particular case of the above criterion:

$$\begin{array}{lll} Mode\ I: & \delta_m^f = \delta_1^f & \beta = 0 \\ ShearMode: & \delta_m^f = \delta_{shear}^f & \beta \to \infty \end{array}$$

Constitutive equation for mixed mode delamination

Combining the penalty stiffness K, the mixed mode relative displacement for delamination initiation and complete separation, δ_m^o and δ_m^f, and the damage function d, the constitutive relation for the mixed mode delamination can be defined with Equation 3.63

$$\tau_s = D_{sr}\delta_r \tag{3.63}$$

where

$$D_{sr} = \begin{cases} K\bar{\delta}_{sr} & \Leftarrow \quad \delta_m^{max} \leq \delta_m^o \\ \bar{\delta}_{sr}\left[(1-d_m)\,K + Kd\bar{\delta}_{s1}\frac{\langle -\delta_1\rangle}{-\delta_1}\right] & \Leftarrow \quad \delta_m^o < \delta_m^{max} < \delta_m^f \\ \bar{\delta}_{s1}\bar{\delta}_{1r}\frac{\langle -\delta_1\rangle}{-\delta_1}K & \Leftarrow \quad \delta_m^{max} \geq \delta_m^f \end{cases} \tag{3.64}$$

where $d_m = \frac{\delta_m^f(\delta_m^{max}-\delta_m^o)}{\delta_m^{max}(\delta_m^f-\delta_m^o)}$, $d \in [0,1]$, is the mixed mode damage parameter.

The unloading conditions are defined by incorporating a maximum mixed mode relative displacement,δ_m^{max}, and a loading function F as follows:

$$\delta_m^{max} = max\{\delta_m^{max}, \delta_m\} \tag{3.65}$$

$$F\left(\delta_m - \delta_m^{max}\right) = \frac{\langle \delta_m - \delta_m^{max}\rangle}{\delta_m - \delta_m^{max}} \tag{3.66}$$

According to equations 3.65 and 3.66, the damage of the interface is tracked by only one variable, namely the maximum mixed mode relative displacement δ_m^{max}. The interface elements mixed mode constitutive behaviour for delamination mode I and II is shown in Figure 3.6.

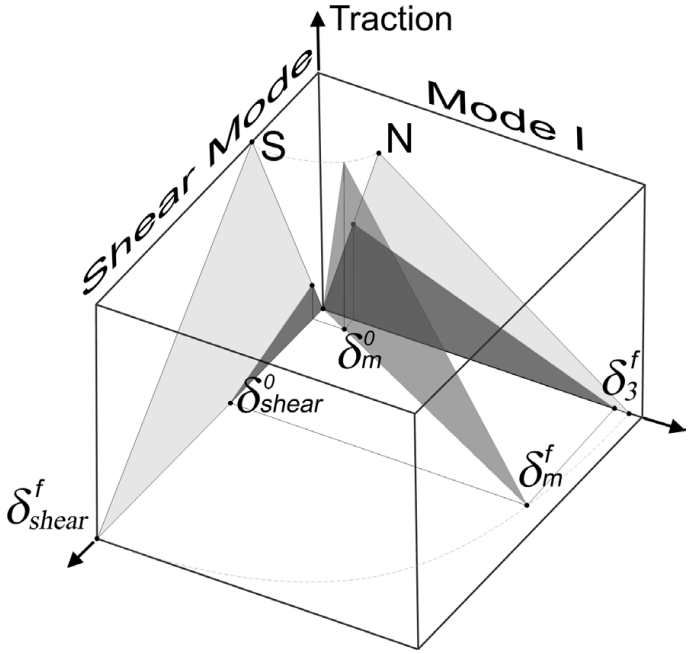

Figure 3.6: Mixed mode bilinear constitutive law (Camanho and Davila, 2002).

3.4 Validation of modelling techniques

3.4.1 Evaluation of failure composite models - single element tests

LS-DYNA provides a number of composite material models applicable to shell and solid elements. Modelling of impact response of the structure requires to account for the through thickness stresses developed within the structure. Since shell elements do not take into account the normal stresses, it was decided that these elements would not be considered in this thesis. Therefore, LS-DYNA composite material models available only for shell elements would be neglected in the material models evaluation (MAT_54 and MAT_58).

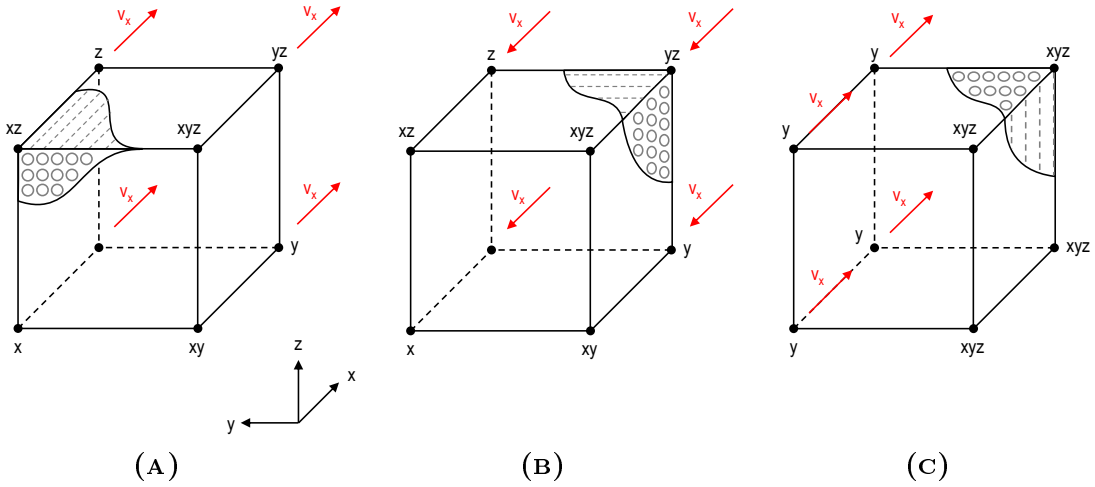

Figure 3.7: Single solid element test conditions: (A) Tension in AB plane, (B) Compression in BC plane, (C) Shear in AC plane.

Three LS-DYNA material models allow for modelling of composite material with solid elements, namely: MAT_22, MAT_59 and MAT_221. These three material models were evaluated based on single element tests under tensile, compressive and shear loading. Finally, the results obtained in the single element tests were compared with analytical results.

A single three dimensional solid element was loaded with a strain rate of $\dot{\varepsilon} = 0.1\frac{mm}{s}$. This quasi-static loading was modelled by applying velocity to the nodes. The load cases and boundary conditions are illustrated in Figure 3.7. The constrained degrees of freedom are denoted in the figure with a capital letter. Composite material properties available within the "Crashowrthiness, Impact and Structural Mechanics Group" were used for the evaluation of the composite material models (see Table 3.5).

Nine different fibre orientations were investigated under three different loadings, namely: 0°, 45° and 90° in the AB, AC and BC planes. This gives 81 individual test cases conducted within nine separate simulations (three different load cases for three different material orientation planes).

Results of the single element tests, performed in LS-DYNA, were compared to the analytical failure calculations based on the failure criteria for the corresponding

Table 3.5: Composite material properties for LS-DYNA.

Property	**Notation**	**Value**
Density	ρ	$1.55 \frac{g}{cm^3}$
Young's modulus, a-direction	E_a	70800 MPa
Young's modulus, b-direction	E_b	42700 MPa
Young's modulus, c-direction	E_c	8000 MPa
Poisson's ratio, ba-plane	ν_{ba}	0.125
Poisson's ratio, ca-plane	ν_{ca}	0.037
Poisson's ratio, cb-plane	ν_{cb}	0.062
Shear modulus, ab-plane	G_{ab}	10600 MPa
Shear modulus, ac-plane	G_{ac}	4400 MPa
Shear modulus, bc-plane	G_{bc}	2600 MPa
Longitudinal tensile strength, a-direction	X_T	1119 MPa
Transverse tensile strength, b-direction	Y_T	617 MPa
Normal tensile strength, c-direction	Z_T	60 MPa
Longitudinal compressive strength, a-direction	X_C	768 MPa
Transverse compressive strength, b-direction	Y_C	463 MPa
Normal compressive strength, c-direction	Z_C	45 MPa
Shear strength, ab-plane	S_{ab}	146 MPa
Shear strength, ac-plane	S_{ac}	93 MPa
Shear strength, bc-plane	S_{bc}	53 MPa
Ultimate longitudinal tensile strain	ε_{XT}	0.0158
Ultimate transverse tensile strain	ε_{YT}	0.0144
Ultimate normal tensile strain	ε_{ZT}	0.0075
Ultimate longitudinal compressive strain	ε_{XC}	0.0108
Ultimate transverse compressive strain	ε_{YC}	0.0108
Ultimate normal compressive strain	ε_{ZC}	0.0056
Ultimate shear strain, ab-plane	γ_{ab}	0.0138
Ultimate shear strain, ac-plane	γ_{ac}	0.0211
Ultimate shear strain, bc-plane	γ_{bc}	0.0204

material model. The comparison of failure strengths for the longitudinal, transverse and normal directions was straightforward, while for 45° orientations the stress state was transformed to the principal axis system. The results comparison for each material model is shown in the corresponding table together with the identification of the failure mode responsible for failure of the element.

The failure criteria governing the failure modes for materials MAT_22 and MAT_59 were defined for different material orientations using a custom-written MATLAB script. The script enabled for the transformation of the stresses from the load axes to the material axes, the calculation of the failure strengths in accordance with the fibre directions and the differentiation between failure in compression and tension. The script code is given in Appendix A.

The shear failure due to a combination of tensile and compressive stresses, generated in the material, was also illustrated with history variables and was verified analytically.

3.4.1.1 MAT_22

As described in section 3.3.2.2.1, the 3D Chang-Chang failure criteria are implemented into material model MAT_22. In addition to in-plane criteria, a delamination failure criterion is available within the material model. Comparison of the failure strengths obtained with LS-DYNA to the analytical results shows very good agreement, which is an evidence that failure in MAT_22 is governed by the Chang-Chang failure criteria.

The results for material orientation in the AB-plane for all three loading cases are shown in Figure 3.8. The ultimate failure strengths with the corresponding failure modes for MAT_22 are shown in Table 3.6 and Table 3.7.

From the results presented below, it can be seen that MAT_22 does not take into account compressive failure. The lack of compressive failure in longitudinal and normal direction was expected due to the lack of an option to define these parameters on the material input card. The absence of transverse compressive failure was not expected as this parameter is specified in the material control card. The absence

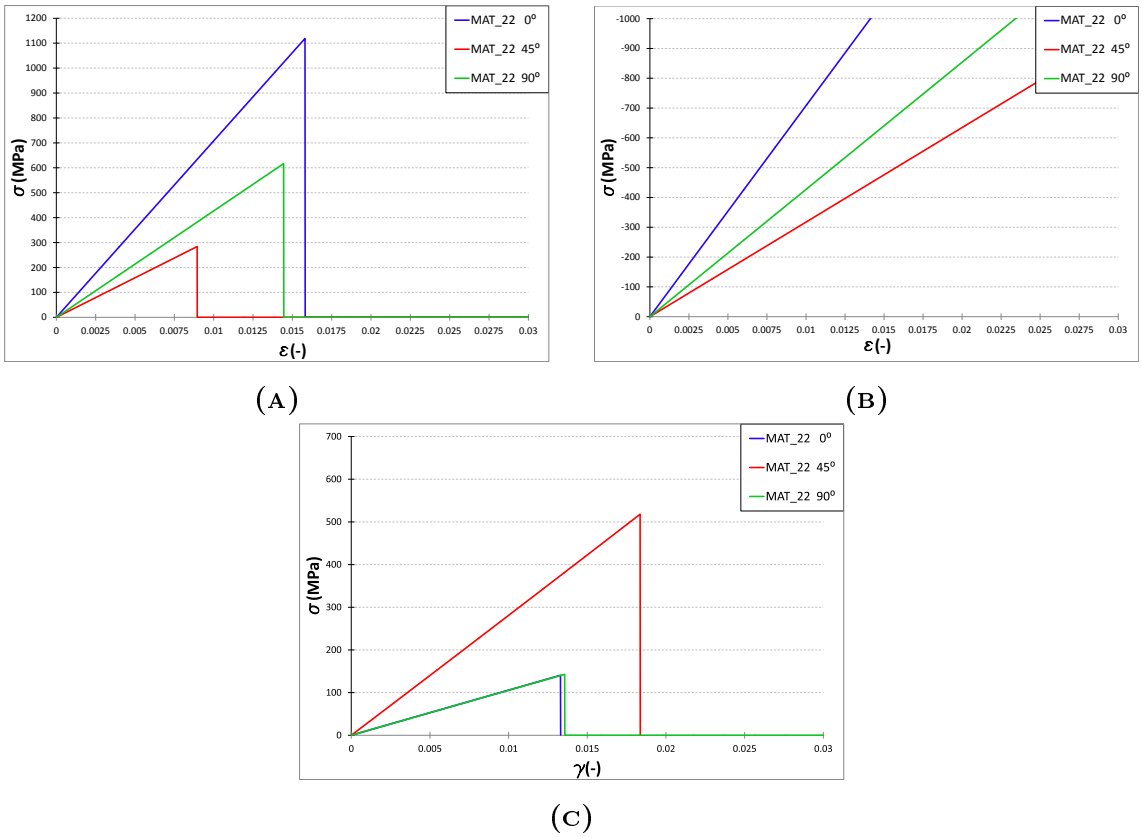

Figure 3.8: MAT_22 single element test results for 0°, 45° and 90° material orientation in AB-plane: (A) tension, (B)compression, (C) shear.

of the compressive failure criteria in MAT_22 is a significant shortcoming for this material model and it restricts its application in impact analyses.

Results for the remaining load cases in the AC and BC planes, together with the corresponding failure strengths and strains, are presented in Appendix B.

3.4.1.2 MAT_59

As described in Section 3.3.2.2.2, the 3D Cheng-Hallquist failure criteria govern the failure of composite in material model MAT_59. This statement needs to be checked and confirmed as the LS-DYNA theory manual does not provide exact information on the failure criteria implemented into the material model.

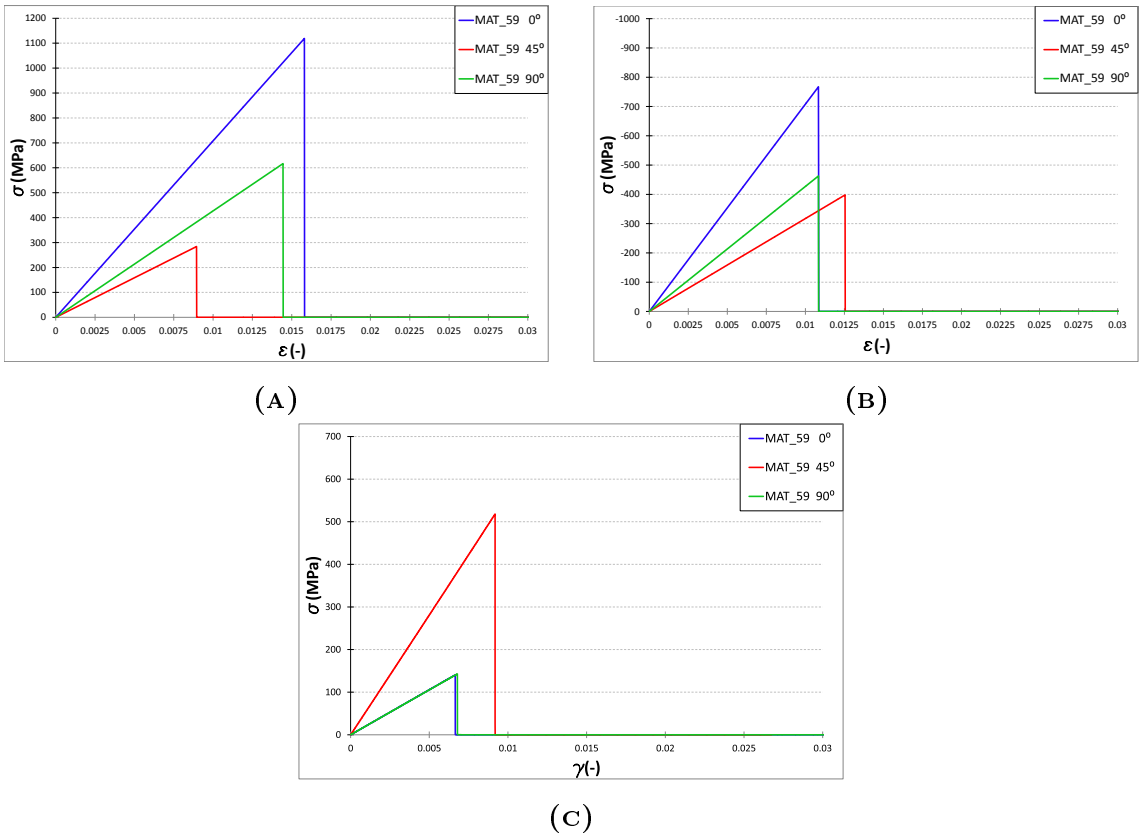

FIGURE 3.9: MAT_59 single element test results for 0°, 45° and 90° material orientation in AB-plane: (A) tension, (B)compression, (C) shear.

Results for 0°, 45° and 90° material orientations in the AB-plane for all three loading cases are shown in Figure 3.9. The ultimate failure strengths and strains with the corresponding failure modes for MAT_59 are presented in Table 3.7 and Table 3.8. The results for the remaining load cases are presented in Appendix B.

The results presented in Table 3.8 and Figure 3.9 show excellent agreement between the failure strengths calculated analytically using the Cheng-Halquist failure criteria and the results obtained from the LS-DYNA analyses. This proves that the Cheng-Hallquist failure criteria govern failure in MAT_59. There are eight failure criteria implemented into MAT_59 which take into account fibre, matrix and delamination failure of the composite material depending on the load case.

MAT_59 allows for removal of failed elements from the analysis. The erosion of elements occurs as soon as all three normal stresses (σ_x, σ_y and σ_z) are reduced to

zero due to failure in the respective failure mode (LSTC, 2014).

From the results obtained with MAT_59 it can be seen that this material model takes into account failure under tensile, compressive and shear load. This is a significant improvement to MAT_22, which does not take into account compressive failure. The incorporation of compressive failure makes this material model suitable for modelling of impact on composite structures.

3.4.1.3 MAT_221

Failure in MAT_221 is based on the ultimate strain specified for the material input card. The maximum strains can be calculated using a simple expression based on the elastic or shear moduli and the ultimate strength of the material for the corresponding load case. According to LSTC (2013a), MAT_221 takes into account

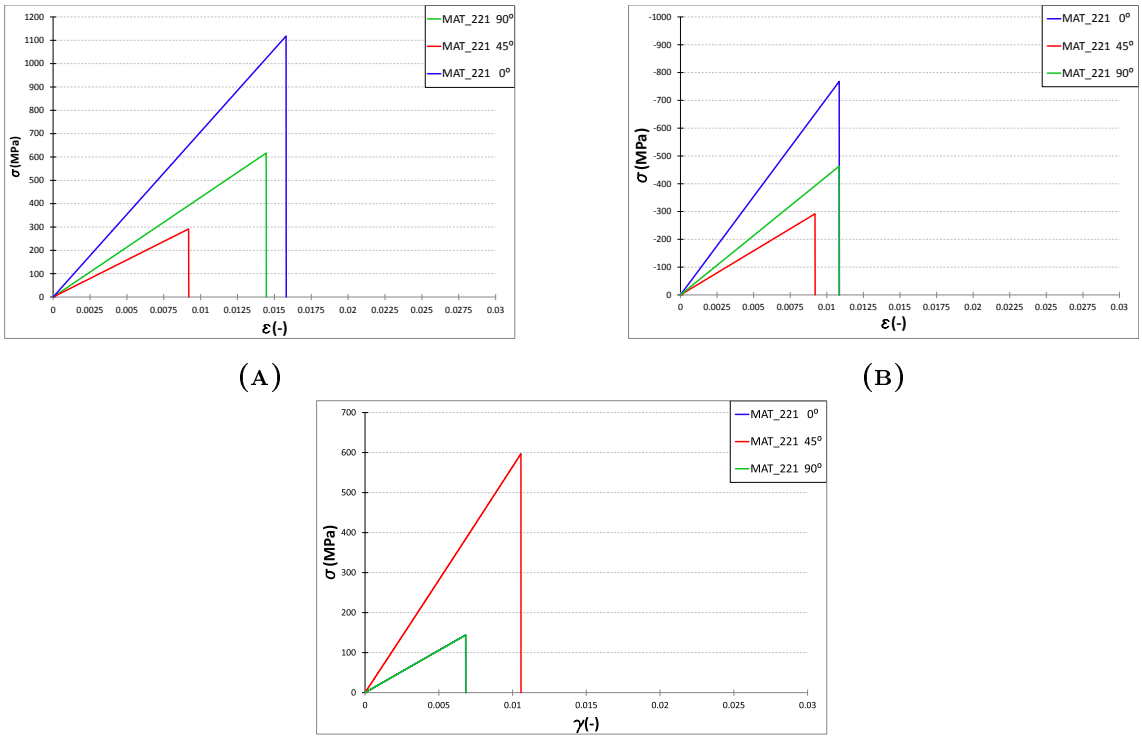

Figure 3.10: MAT_221 single element test results for 0°, 45° and 90° material orientation in AB-plane: (A) tension, (B)compression, (C) shear.

nine load cases, namely: tension and compression in fibre and transverse to fibre directions and shear failure in three parallel planes defined by the main axes.

Results for 0°, 45° and 90° material orientations in the AB-plane for all three loading cases are shown in Figure 3.10. The ultimate failure strengths and strains obtained in analyses with the material model MAT_221 are presented in Tables 3.10 and 3.11. The results of the remaining load cases are presented in Appendix B.

As evident from the stress-strain graphs, the results for the tensile failure strengths for MAT_221 are exactly the same as for MAT_22 and MAT_59. In addition, the results for shear and compression for the load along the material axes showed perfect agreement with MAT_59. The results for 45° differ from the results obtained with the other material models. This difference showed that the failure of the material in this direction is controlled by different failure mode compared to of MAT_22 and MAT_59.

MAT_221 allows for element deletion when the material failure strain is reached. The erosion of elements is controlled with the NERODE parameter and it allows for accumulation of few failure modes before the element is deleted.

Table 3.6: Failure strengths for MAT_22.

MAT_22 AB					
	LAYUP	LS-DYNA INPUT	LS-DYNA OUTPUT	Error	FC
TENSION	0°	1119	1118.95	0.00%	CC1
	45°	284	284.07	-0.02%	CC3
	90°	617	616.806	0.03%	CC3
COMPRESSION	0°	-	-	-	-
	45°	-	-	-	-
	90°	-	-	-	-
SHEAR	0°	146	145.957	0.03%	CC1
	45°	-	860.368	-	CC1
	90°	146	145.957	0.03%	CC3

Table 3.7: Failure strains for MAT_22.

MAT_22 AB					
	LAYUP	LS-DYNA INPUT	LS-DYNA OUTPUT	Error	FC
TENSION	0°	0.015805	0.015804	0.01%	CC1
	45°	0.0089	0.008956	-0.63%	CC3
	90°	0.01445	0.014455	-0.04%	CC3
COMPRESSION	0°	-	-	-	-
	45°	-	-	-	-
	90°	-	-	-	-
SHEAR	0°	0.013774	0.01377	0.03%	CC1
	45°	-	0.034992	-	CC1
	90°	0.013774	0.01377	0.03%	CC3

Table 3.8: Failure strengths for MAT_59.

MAT_59 AB					
	LAYUP	LS-DYNA INPUT	LS-DYNA OUTPUT	Error	FC
TENSION	0°	1119	1118.95	0.00%	CH1
	45°	284	284.07	-0.02%	CH2
	90°	617	616.806	0.03%	CH2
COMPRESSION	0°	-768	-767.366	0.08%	CH6
	45°	-402	-397.922	1.02%	CH7
	90°	-463	-462.804	0.04%	CH7
SHEAR	0°	146	145.957	0.03%	CH1
	45°	-	654.672	-	CH1
	90°	146	145.957	0.03%	CH2

Table 3.9: Failure strains for MAT_59.

MAT_59 AB					
	LAYUP	LS-DYNA INPUT	LS-DYNA OUTPUT	Error	FC
TENSION	0°	0.015805	0.015804	0.01%	CH1
	45°	0.00895	0.008956	-0.63%	CH2
	90°	0.01445	0.014455	-0.04%	CH2
COMPRESSION	0°	0.010847	0.010869	-0.20%	CH6
	45°	-	0.012539	-	CH7
	90°	0.010843	0.010849	-0.05%	CH7
SHEAR	0°	0.013774	0.01377	0.03%	CH1
	45°	-	0.033974	-	CH1
	90°	0.013774	0.01377	0.03%	CH2

Table 3.10: Failure strengths for MAT_221.

MAT_221 AB					
	LAYUP	LS-DYNA INPUT	LS-DYNA OUTPUT	Error	FC
TENSION	0°	1119	1118.25	0.07%	
	45°	-	291.621	-	
	90°	617	616.806	0.03%	
COMPRESSION	0°	-768	-768.077	-0.01%	
	45°	-	-291.733	-	
	90°	-463	-462.804	0.04%	
SHEAR	0°	146	145.957	0.03%	
	45°	-	533.003	4.82%	
	90°	146	145.957	0.03%	

Table 3.11: Failure strains for MAT_221.

MAT_221 AB					
	LAYUP	LS-DYNA INPUT	LS-DYNA OUTPUT	Error	FC
TENSION	0°	0.015805	0.015804	0.01%	
	45°	-	0.008956	-	
	90°	0.01445	0.014455	-0.04%	
COMPRESSION	0°	0.010847	0.010849	-0.01%	
	45°	-	0.009193	-	
	90°	0.010843	0.010839	0.04%	
SHEAR	0°	0.013774	0.01377	0.03%	
	45°	-	0.021678	-	
	90°	0.013774	0.01377	0.03%	

3.4.2 Evaluation of delamination modelling techniques - DCB delamination mode I test

In order to evaluate the existing delamination modelling techniques, the double cantilever beam (DCB) analyses of delamination mode I were performed using LS-DYNA. The analyses were performed based on the ASTM D 5528 standard test method for mode I delamination. The setup of the test is shown in Figure 3.11.

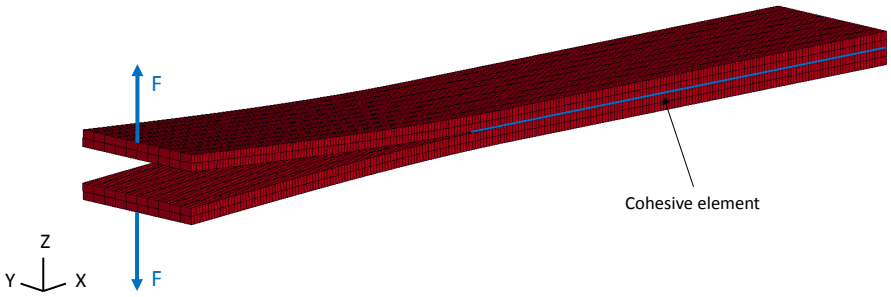

Figure 3.11: Double cantilever beam delamination mode I test setup.

In the real test, the sample was made out of 24 plies of a unidirectional carbon fibre reinforced composite with a ply thickness of 0.18 mm. The dimensions of the specimen are $l = 120\ mm$ in length, $w = 20\ mm$ in width and $t = 4.32\ mm$ in thickness. The initial crack length for the DCB specimen was equal to $l_c = 50\ mm$. A constant displacement rate of $\dot{\varepsilon} = 10\ \frac{mm}{s}$ was applied to the corresponding end of the sample. The material properties of the composite layup are given in Table 3.5. The load curve obtained during the DCB delamination mode I test is shown in Figure 3.12. The energy released rate for mode I delamination obtained within the test was $G_{IC} = 418\ \frac{J}{m^2}$, the maximum load was $P^{max} = 95\ N$ and the opening displacement of the sample at the delamination onset $\delta_o = 4.8\ mm$. The data for the DCB delamination mode I test were available within the "Crashworthiness, Impact and Structural Mechanics Group".

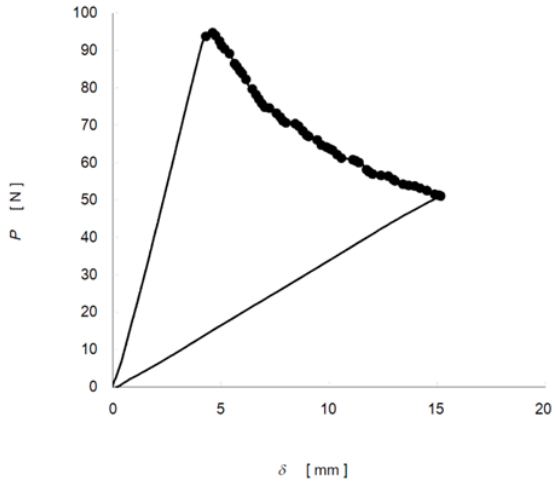

Figure 3.12: Double cantilever beam delamination mode I test results.

This section presents the parametric studies on the delamination mode I modelled in LS-DYNA. They include mesh sensitivity studies, where the most appropriate mesh density of the cohesive zone is determined in terms of the interface elements stability and computational cost of the analysis. In addition, the sensitivity of the cohesive zone on the input parameters was analysed. Both the mesh and material parameters sensitivity studies were performed for the cohesive zone modelled with material model MAT_138. This material model was chosen due to its simplicity related to the bilinear traction separation law used for cohesive element formulation. Finally, the interface was modelled with different cohesive material models and con-

tact algorithms for comparison and assessment of the performance of all delmination modelling techniques available in LS-DYNA. Delamination modelled with the failure criteria implemented in the composite material models was not within the scope of this work and consequently was not shown in this section.

The numerical model was based on the DCB specimen used for the test of delamination mode I (described in the beginning of this section). The supported end of the DCB was restricted with the constraints for all degrees of freedom, while the end with the initial crack was loaded with a constant displacement rate of 100 mm/s. The displacement rate in the numerical analysis was increased in order to decrease the computational cost of the analysis and it did not have an influence on the final response of the interface elements. The input parameters for MAT_138 used for the cohesive zone modelling are: energy release rate G_{IC}, peak traction in normal direction T and stiffness in normal direction EN. The initial values used for the analyses are: $G_{IC} = 0.418\ \frac{J}{mm^2}$, $T = 95\ MPa$ and $EN = 1 \cdot 10^5 \frac{N}{mm}$.

All the results presented in the following subsections were filtered with the 2000 Hz SAE filter to remove the numerical oscillations.

3.4.2.1 Delamination modelled with cohesive elements

3.4.2.1.1 Mesh sensitivity

The analysis of the performance of the cohesive zone modelling began with the mesh sensitivity studies. According to Benzeggagh and Kenane (1996) and Turon et al. (2007), at least three elements are necessary in the cohesive zone to appropriately represent the interface and adequately capture the fracture toughness. Therefore, the element size in the crack growth direction shall not be greater than 0.5 mm.

In order to confirm the above statement, four separate analyses with different mesh densities were performed. The meshes used in the analyses vary in the number of elements used in the crack growth direction, as well as through the thickness of the DCB. Number of elements through the thickness has an influence on the bending response of the cantilever beam, hence it was decided to investigate the influence of the increased numbers of elements in the thickness direction. The number of elements across the width was kept constant as it does not affect the results of the

analysis. The differences between the models are shown in Table 3.12, together with the computational cost, the resulting opening displacement and the peak force for delamination onset.

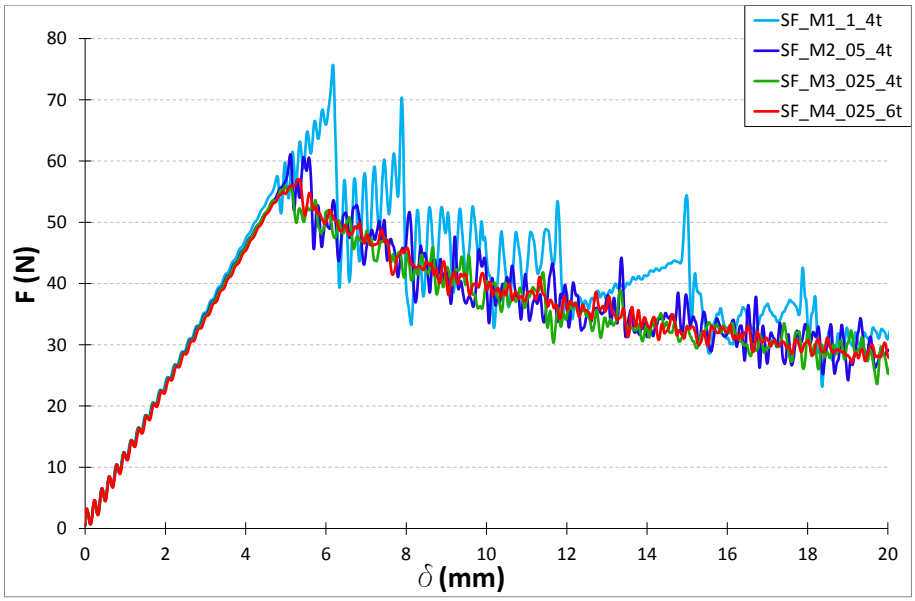

Figure 3.13: Section forces comparison for different meshes of DCB delamination mode I. Legend explanation: SF denotes section force, M1 states the mesh sensitivity analysis number 1, 1-025 denotes the size of the mesh in millimetres, and 4t denotes the number of elements through the thickness of the sample.

Figure 3.13 shows the force-opening displacement curve for the mesh sensitivity studies. It can be seen directly that the results of the delamination mode I test modelled with cohesive elements are highly mesh dependent. The interface element length of 1 mm in the crack direction is not adequate to model the cohesive zone appropriately. The results for this coarse mesh show high oscillations related to the elastic snap back. Moreover, the load peaks visible in Figure 3.13 do not represent the real behaviour of the interface (see Figure 3.12). Increasing the number of elements in the cohesive zone improves the convergence of the results and reduces the problem related with the elastic snap back. However, it significantly increases the computational cost of the calculations. As it can be seen from Table 3.12, the analyses with the cohesive element size of 0.25 mm have very long computational time.

Table 3.12: Mesh sensitivity cases.

Sample	Nr of elements in crack direction	Element size in crack direction (mm)	Nr of elements through the thickness	Peak force (N)	Opening displacement (mm)	CPU time (h)
DCB_M1	120	1	4	57.4	4.78	0.18
DCB_M2	240	0.5	4	60.9	5.10	0.41
DCB_M3	480	0.25	4	55.9	4.98	2.67
DCB_M4	480	0.25	6	57.0	5.30	7.85

The average peak load for all the numerical cases is $F_{av}^{max} = 57.8\ N$ while for the experiment the load of $P^{max} = 95\ N$ was obtained. The opening displacement for the numerical results was varying from $\delta_o = 4.6\ mm$ to $\delta_o = 5.3\ mm$. This results agreed with the opening displacement measured during the experiment, $\delta_o = 4.8\ mm$.

Based on the results presented above, it was decided that in further analyses the cohesive zone would be modelled with the element size of $l_{el} = 0.5\ mm$ in the crack growth direction. This element size gives adequate results with relatively low oscillations and is computationally efficient.

3.4.2.1.2 Traction influence

The second studies on the performance of cohesive zone modelling were based on the variable value of the cohesive traction. As mentioned before, the cohesive traction does not change the response of the cohesive zone as far as the energy release rate is kept constant during the analysis (Alfano and Crisfield, 2001, Bazant and Planas, 1997).

For the following analyses, the value of the traction was changed from $T_1 = 95\ MPa$ to $T_5 = 15\ MPa$ with a constant negative increment of 20 MPa. As mentioned before, the cohesive element length in the crack direction is equal to $l_{el} = 0.5\ mm$. All remaining parameters were kept the same, as defined in the model description in the beginning of this section. Table 3.13 shows all the study cases with the corresponding traction values, resultant peak forces and opening displacement for delamination onset.

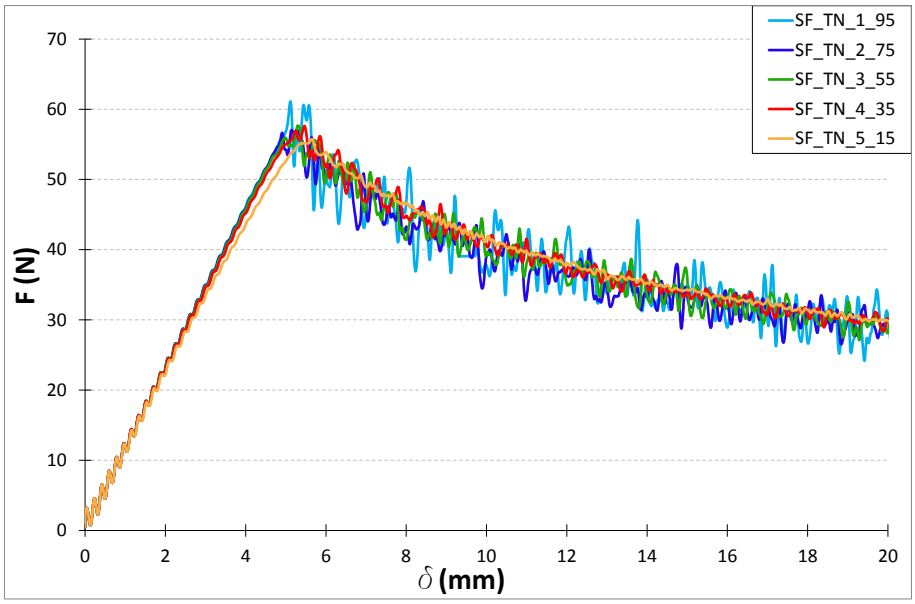

Figure 3.14: Section forces comparison for different traction values of the cohesive zone for DCB delamination mode I test. Legend explanation: SF denotes section force, TN1 denotes traction sensitivity analysis number 1, 95-15 denotes the traction value, e.g. 95 MPa.

Figure 3.14 shows the section force versus opening displacement curve for the traction sensitivity studies. It can be seen that the amplitude of the oscillations decreases with decreasing traction value. The lower the traction of the cohesive elements, the more stable response can be observed on the force - displacement curve. Figure 3.14 and Table 3.13 show that the traction value does not have an influence on the maximum load carried by the interface before the crack propagation onset. This finding agrees with the observations of Alfano and Crisfield (2001) and Bazant and Planas (1997) observations. The slight difference between the peak load of the first case is related to the high oscillations of the solution, in comparison to the lower oscillations response of the interface elements with lower traction. It is worth to mention that the lowest tested value of the cohesive traction slightly changes the slope of the force displacement curve.

As it was shown with the results above, the value of the traction specified for the cohesive material model does not have an influence on the maximum load carried by the interface. Therefore, it was decided to use the value of the traction equal to

Table 3.13: Cohesive traction sensitivity cases.

Sample	Normal traction (MPa)	Peak force (N)	Opening displacement (mm)
DCB_T1	95	60.9	5.10
DCB_T2	75	56.2	4.88
DCB_T3	55	55.6	4.92
DCB_T4	35	56.9	5.21
DCB_T5	15	56.9	5.23

$T_4 = 35\ MPa$ for further sensitivity studies. This value of the traction enables for the stable response of the interface and does not affect the slope (stiffness) of the interface.

3.4.2.1.3 Stiffness influence

The subsequent studies investigate the response of the interface to changes in stiffness. As mentioned before, the cohesive element length in the crack direction was equal to $l_{el} = 0.5\ mm$ and the traction in normal direction was equal to $T_4 = 35\ MPa$.

Table 3.14: Stiffness sensitivity cases.

Sample	Normal stiffness $\left(\frac{N}{mm}\right)$	Peak force (N)	Opening displacement (mm)
DCB_K1	$1 \cdot 10^5$	56.9	5.21
DCB_K2	$5 \cdot 10^5$	56.2	5.14
DCB_K3	$1 \cdot 10^6$	56.9	5.21
DCB_K4	$5 \cdot 10^6$	57.1	5.22
DCB_K5	$1 \cdot 10^7$	57.0	5.23

From Figure 3.15 and Table 3.14 it can be seen that the value of the interface stiffness does not have a significant influence on the response of the interface. Slight improvement on the results stability can be noticed for the highest value of the interface stiffness.

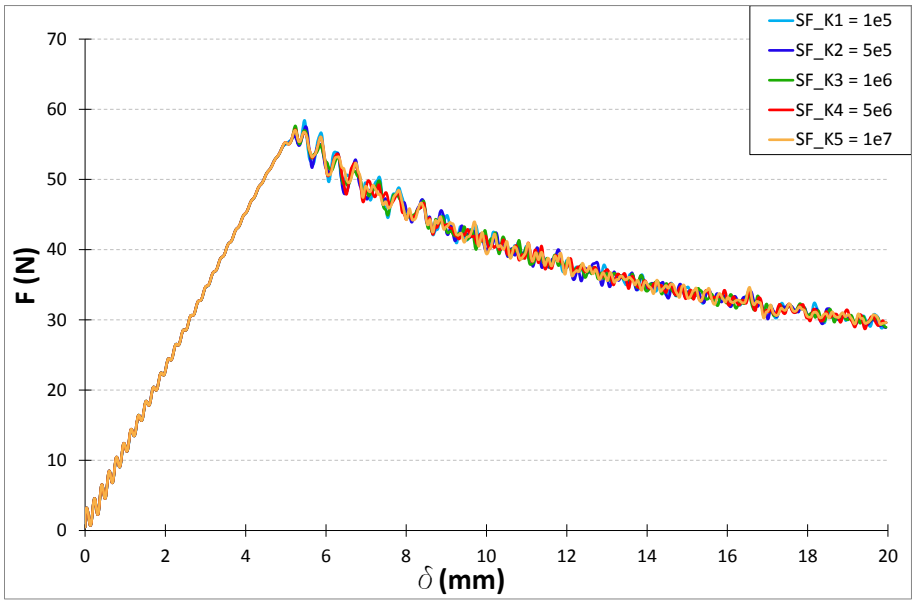

Figure 3.15: Section forces comparison for different stiffness values of the cohesive zone for DCB delamination mode I test. Legend explanation: SF denotes section force, K1 denotes stiffness sensitivity analysis number 1, 1e5 denotes the actual value of stiffness expressed in $\frac{N}{mm}$.

The values of the peak force and opening displacement varied by less than 1 N and 1 mm from the average peak force $F_{av}^{max} = 56.84\ N$ and average opening displacement $\delta_{av} = 5.206\ mm$ respectively. Similarly to the previous parametric studies, the maximum load carried by the interface in the numerical analysis was lower than in the case of the experiment.

The value of the stiffness has negligible influence on the results and response of the cohesive zone. Therefore, it was decided to use the initial value of stiffness ($K_1 = 1 \cdot 10^5 \frac{N}{mm}$) for all remaining analyses.

3.4.2.1.4 Energy release rate influence

The last and the most important parameter required for the definition of the interface element was the energy release rate, i.e. the fracture toughness of the interface. This material property was determined experimentally. The response of the cohesive zone

to changes in the energy release rate was investigated by performing a sensitivity study.

The values of the energy release rate investigated within these studies are shown in Table 3.15. The cohesive element length in the crack direction was equal to $l_{el} = 0.5\ mm$, the traction in normal direction was equal to $T_4 = 35\ MPa$ and the stiffness in normal direction was $K_1 = 1 \cdot 10^5 \frac{N}{mm}$.

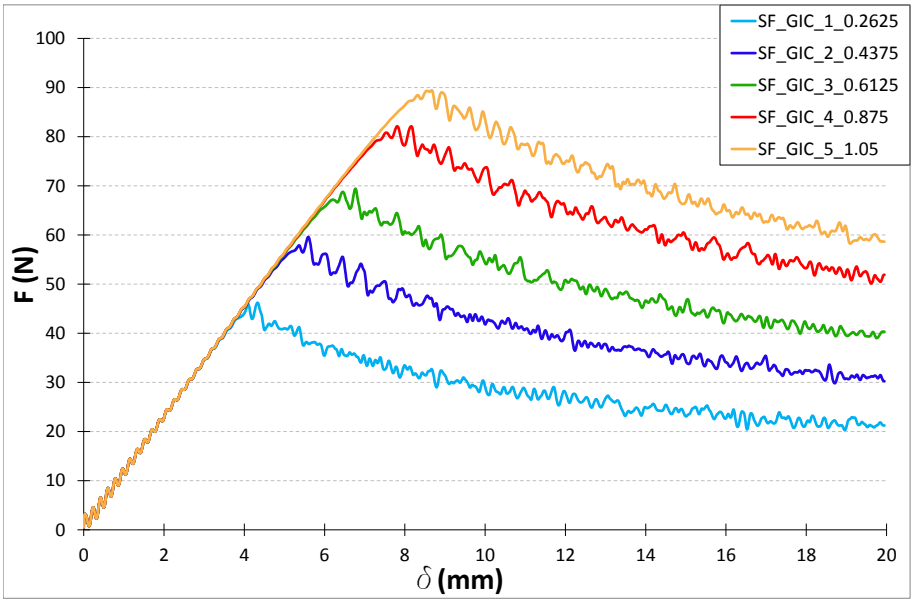

Figure 3.16: Section forces comparison for different energy release rate values of the cohesive zone for DCB delamination mode I test. Legend explanation: SF denotes section force, GIC1 denotes the energy release rate sensitivity analysis number 1, and the last digit denotes the actual value of the energy release rate expressed in $\frac{J}{mm^2}$.

Figure 3.16 shows the section force versus opening displacement curve for the energy release rate sensitivity studies. It can be seen that before the delamination onset the force increases along the same line, which shows that the elastic stiffness of the interface did not change. Increase of the energy release rate causes increase of the maximum load in the interface. The increase of the load bearing capability of the interface resulted in an increased opening displacement of the DCB specimen.

The case studies presented in this section proved the conclusion of Alfano and Crisfield (2001) and LSTC (2012), that the energy release rate is the most important

Table 3.15: Mode I energy release rate sensitivity cases.

Sample	Energy release rate GIC $\left(\frac{J}{mm^2}\right)$	Peak force (N)	Opening displacement (mm)
DCB_GIC_1	0.2625	45.9	4.09
DCB_GIC_2	0.435	57.9	5.29
DCB_GIC_3	0.6125	67.2	6.19
DCB_GIC_4	0.875	80.8	7.56
DCB_GIC_5	1.05	88.4	8.33

parameter controlling the behaviour of the interface modelled with the cohesive elements.

3.4.2.1.5 Other cohesive zone formulations

Finally, the performance of different cohesive material models was compared. Four cohesive material models available in LS-DYNA (MAT_138, MAT_184, MAT_85 and MAT_186) were used to model the interface of the DCB specimen.

There are four cohesive material models available in LS-DYNA for modelling delamination initiation and propagation, namely:

- MAT_138 - Material Cohesive Mixed Mode
- MAT_184 - Material Cohesive Elastic
- MAT_184 - Material Cohesive TH (Tvergaard-Hutchinson)
- MAT_184 - Material Cohesive General

Each of these material models differ slightly in the formulation of the cohesive element, hence different input parameters are required to model the cohesive zone. Material model MAT_138 has a bilinear traction separation law implemented into the interface element formulation. MAT_184 is a simple cohesive elastic material model, where normal traction defines the strength of the interface. This material model does not provide softening of the interface after delamination. Material

model MAT_185 allows to use a trapezoidal traction separation law. Material model MAT_186 allows for any type of traction separation law to be defined, as in this material model the traction separation law is specified with a load curve.

Table 3.16 shows the input parameters necessary for the definition of the interface element with different cohesive material models in LS-DYNA. The parameters for the analyses were chosen in a way, which enables direct comparison of the results.

Table 3.16: Parameters necessary to define the interface element with different LS-DYNA material models.

Material model	Input parameters
MAT_138	normal and tangential: energy release rate, traction and stiffness
MAT_184	tangential stiffness; normal stiffness; normal traction
MAT_185	peak traction; maximum normal and tangential separations; scaled distances to: peak traction, beginning of softening, for failure
MAT_186	type of effective separation; load curve with normalised traction separation law; fracture toughness in normal and tangential direction; peak traction in normal and tangential direction

Figure 3.17 shows the section force versus opening displacement curves for the analyses with different cohesive material models. From this figure it can be seen that three material models have almost identical responses for the corresponding input parameters, namely: MAT_138, MAT_185 and MAT_186. For these material models the maximum force and the opening displacement for the delamination onset are almost the same (see Table 3.17). It is important to notice, that the results obtained with MAT_138 show the lowest amplitude of the oscillations among these three materials models. The results obtained with the simplest cohesive material model - MAT_184 do not match the experiment results. The resultant force - opening displacement curve for MAT_184 does not follow the realistic behaviour of the interface.

Furthermore, the results show that the cohesive material model MAT_184 is not relevant for modelling delamination propagation. This material model does not predict correctly the strength of the interface. The high discrepancy of the numerical and experimental results can be related to the lack of damage model within MAT_184.

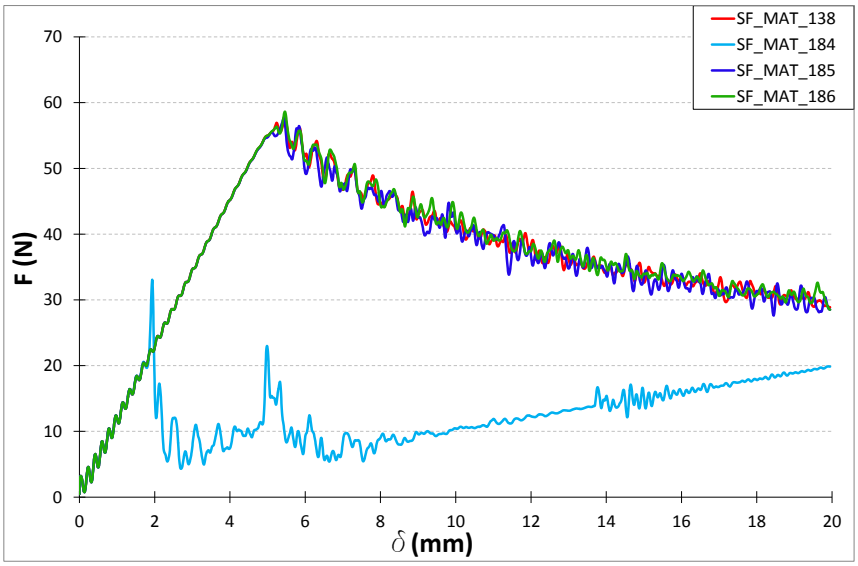

Figure 3.17: Section forces comparison for different cohesive material models for DCB delamination mode I test. Legend explanation: SF denotes section forces, MAT_138 denotes the cohesive material model used in the analysis.

Instantaneous reduction of the load bearing capability of the interface causes instability and has a significant influence on the material response. Therefore, it is not recommended to model delamination with MAT_184. The remaining three material models show good correlation of the predicted force-opening displacement curve for the delamination mode I test. Similarly to the other analyses shown before, the load bearing capability of the interface modelled with a cohesive zone was lower than the one measured during the experiment. Material models MAT_138, MAT_185 and MAT_186 can be used to model delamination onset and propagation in composite structures under mode I loading.

3.4.2.1.6 Delamination modelled with contact algorithm

As mentioned in section 3.3.3.2.2, delamination in composite materials can be modelled with the contact tiebreak option available in LS-DYNA. In this case, the interface between two laminates is modelled with a contact algorithm instead of interface elements. This solution was much easier to utilise into existing FE model, as it does not require implementation of separate elements between two layers of existing el-

ements. Instead, the master and slave segments are defined for the neighbouring layers of elements and the adequate contact algorithm is chosen to model the interface.

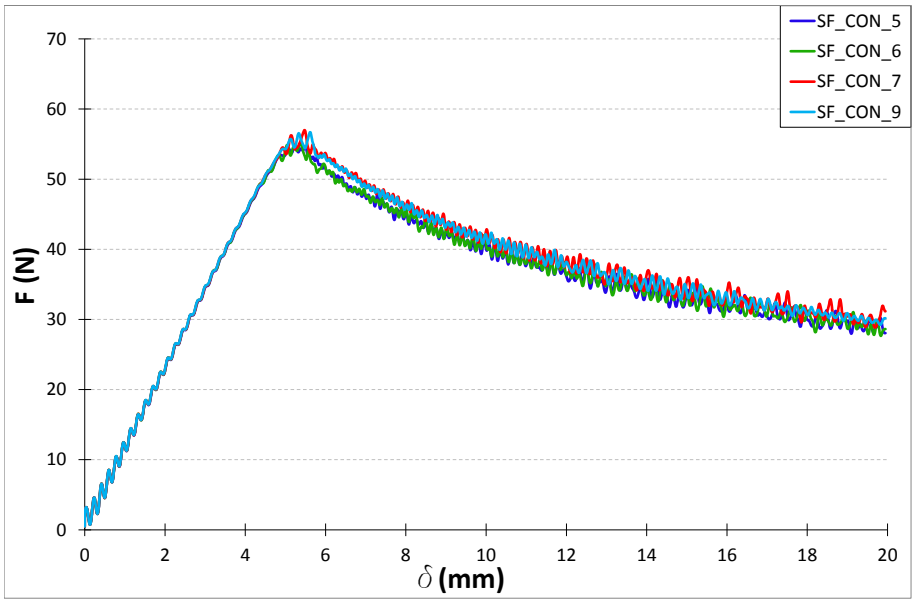

Figure 3.18: Section forces comparison for different tiebreak contact algorithms used for modelling of DCB delamination mode I test. Legend explanation: SF denotes section forces, CON_5 denotes contact tiebreak option 5.

There are four contact algorithms implemented in LS-DYNA, which allow for modelling of delamination onset and softening response of the interface after failure. These contact algorithms are listed below:

- Contact Tiebreak Option 5 - stress limit by a perfectly plastic yield condition. Damage is a function of the crack width opening,
- Contact Tiebreak Option 6 - delamination onset modelled with a failure stress. Damage is a linear function of the distance between two points,
- Contact Tiebreak Option 7 - Dycoss Discrete Crack Model,
- Contact Tiebreak Option 9 - delamination model equivalent to MAT_138.

The interface modelled with contact algorithms use the same model set-up and input parameters as the interface modelled with cohesive elements.

Figure 3.18 shows resultant force - opening displacement curves for the DCB delamination mode I. From this figure, it can be seen that the results obtained with different contact algorithms are very similar. Table 3.17 shows that the opening displacement at the delamination onset and maximum load carried by the interface do not differ significantly between the contact algorithms. However, a slight difference between the curves can be seen in Figure 3.18 after delamination onset. Except the higer peak force also the trajectory of the force - opening displacement curve indicates that the interface modelled with the contact algorithms with a built in traction separation law (contact options 7 and 9) is slightly stronger.

Similarly to the interface modelled with cohesive elements, the interface strengths obtained within the numerical analyses are compared to the interface strengths measured during the experiment. Except the differences in the load bearing capability, the force - opening displacement curves obtained within the numerical analyses reflect the curve obtained during the test.

3.4.2.2 Comparison of delamination modelled with cohesive elements and contact algorithm

In this subsection, the results of the interface modelled with cohesive elements are compared to the results of the interface modelled with the contact algorithm.

Table 3.17 shows the maximum load carried by the interface and the opening displacement for the delamination onset, for the DCB delamination mode I analyses. In addition, it presents the number of parameters required for the full description of the interface and the computational time of the analyses. The force - opening displacement curves for the corresponding modelling techniques are shown in Figures 3.17 and 3.18.

Direct comparison between the results was possible thanks to the corresponding input parameters. In the case of MAT_185, the trapezoidal traction separation law was reduced to a bilinear curve by an appropriate selection of material input parameters. In the case of the MAT_186, the bilinear traction separation law was

Table 3.17: Comparison of different delamination modelling approaches.

Sample	No of parameters to define	Peak force (N)	Opening displacement (mm)	CPU time (h)
MAT_138	6	56.9	5.21	0.41
MAT_184	3	20.6	1.72	0.36
MAT_185	6	55.4	5.13	0.39
MAT_186	6	56.2	5.22	0.63
CON_5	2	54.9	5.23	0.23
CON_6	3	54.8	5.05	0.22
CON_7	4	56.3	5.14	0.21
CON_9	6	55.7	5.13	0.22

implemented into the model via a load curve. The remaining delamination modelling approaches utilise data obtained from the experimental test as input parameters.

The results obtained with MAT_184 are omitted in the further comparison, as they deviate significantly from the results obtained with the remaining approaches. Moreover, the response of this material model does not reflect the actual behaviour of the interface observed during the experiment.

From the force - opening displacement curves shown in Figures 3.17 and 3.18, it can be seen that all the delamination modelling approaches give similar results in terms of the interface response. The results vary slightly in the maximum load carried by the interface and opening displacement for the delamination onset between the cases. The maximum average peak load for all of the approaches was equal to $F_{av}^{max} = 55.74\ N$ and the average opening displacement was $\delta_{av}^{o} = 5.16\ mm$. The standard deviation for the peak load at the delamination onset was $\sigma_{F_{av}^{max}} = 0.77$ and for the opening displacement $\sigma_{\delta_{av}^{o}} = 0.06$, which shows very low discrepancy of the results.

Benchmark studies were performed on 16 processors of a high performance computer available at Cranfield University for the number of elements corresponding to the number of elements in the case study denoted as DCB_M2. The last column of Table 3.17 clearly shows that the analyses performed with the contact algorithms are more effective in terms of computational cost. Shorter computational times are highly appreciated for analyses of complicated models with high number of elements.

Therefore, in terms of computation cost efficiency it is recommended to model the interface with the contact algorithm.

To sum up, the results obtained with different delamination modelling approaches show good agreement between the cases except the interface modelled with MAT_184. The results obtained with MAT_184 show that this material model is not suitable to model delamination in composite materials under mode I loading condition.

3.5 Conclusions

- Composite material model MAT_22 does not allow for modelling of the compressive failure in any of the fibre directions.
- The numerical results obtained with a single element of MAT_22, MAT_59 and MAT_221 showed good accuracy to the analytical results.
- None of the composite material models have the Equation of State (EOS) incorporated into the code, hence it does not take into account the shock wave creation and propagation in the material. The lack of EOS in the composite material models result in not accurate modelling of the impact phenomenon on composite materials.
- The fracture toughness of the interface is crucial parameter, which governs the behaviour and load carrying capacity of the modelled interface.
- The cohesive traction does not influence the strength of the interface, however, its value has a significant influence on the numerical stability of the solution.
- The results of the numerical analyses are highly dependent on the mesh density along the crack growth direction.
- Cohesive elements described by the bilinear traction separation law are not stable. It is related to the strain energy stored in the damaged material. This causes situation in which the undamaged material load capacity is lower than the load capacity of the damaged material.

Chapter 4

Composite sandwich panels

4.1 Introduction

Composite materials provide superior stiffness and strength to weight ratio in comparison to metallic alloys. This allows for a significant reduction of the structural weight of components manufactured from composite materials. Further mass reduction can be achieved with the introduction of sandwich structures where low density cores are embedded between the composite face sheets. The use of low density cores in composite structures aims to increase the momentum of inertia of the structure and improve its bending stiffness without increasing the overall weight.

This chapter provides an introduction to composite sandwich structures, followed by a literature review on the impact resistance of composite sandwich panels and techniques for modelling of the core materials in LS-DYNA. For better understanding, the structure of the chapter is illustrated in Figure 4.1.

In the first part of the chapter, a literature review on the impact on sandwich composites is presented. The emphasis was put on sandwich structures with additional through thickness reinforcement and its influence on the impact resistance of composite sandwich panels. The subsequent section introduces foam materials for sandwich cores. At this stage, morphology and properties of low density foams were described.

The subsequent section introduces techniques for modelling of foam materials. Four foam material models were selected and their theoretical background was described.

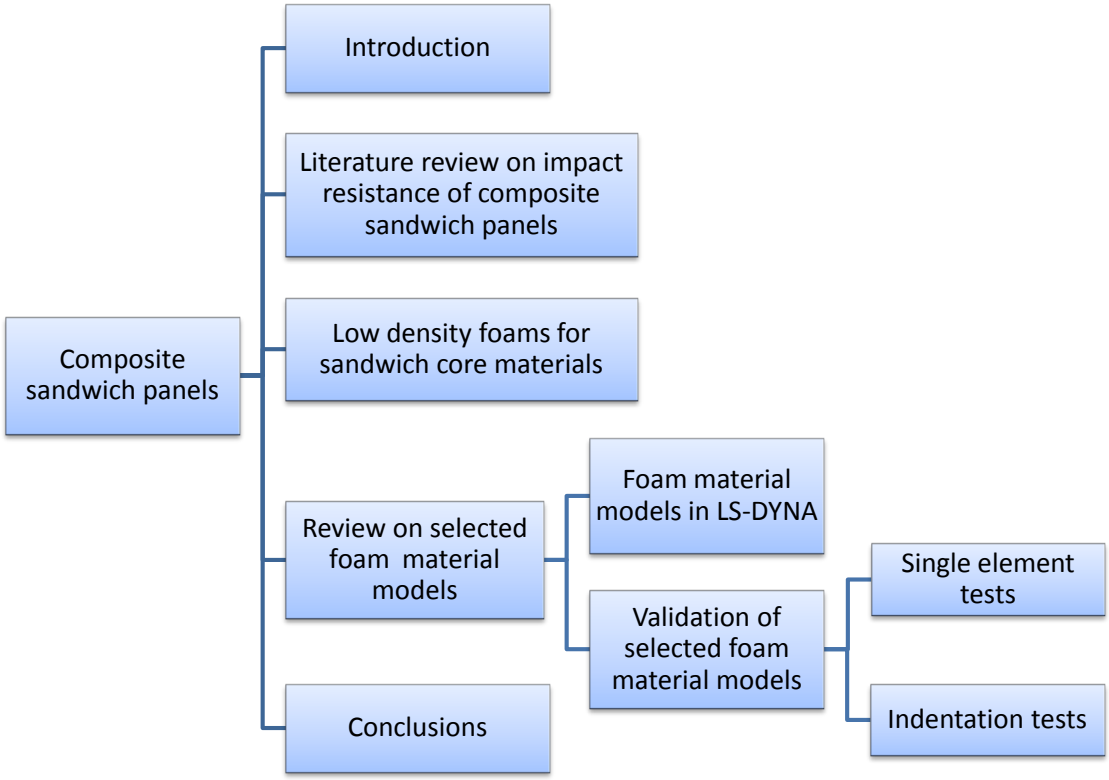

FIGURE 4.1: Chapter 4 structure.

Furthermore, the performance of selected material models was investigated through the single element tests and indentation tests.

The last section of the chapter describes the conclusions drawn from foam material models validation tests.

4.2 Impact resistance of sandwich panels

Composite sandwich structures are a subclass of composite materials which are manufactured through the attachment of stiff composite skins to a lightweight core. The core materials are characterised by low density and low material strength. However, the combination of these two relatively weak components - thin composite skins and low density core - results in a structure with very high bending stiffness and low structural weight.

A range of different materials can be used as a core of a sandwich composite. The most common are: honeycombs, balsa wood, open and closed cell foams (e.g. polyurethane (PUR), polystyrene, polyvinylchloride (PVC)) or metal foams (e.g. aluminium). For the sandwich skins the glass or carbon laminates are the most popular, however, metal face sheets can also be used.

Usage of sandwich structures has increased recently in the aerospace, marine and offshore applications (Hazizan and Cantwell, 2002) due to the advantages offered in terms of bending stiffness, stability and weight reduction (Raju et al., 2008). Despite the enhanced stability and stiffness properties of the structures, sandwich panels have a weak impact resistance (Abrate, 1997, Horrigan et al., 2000, Raju et al., 2008, Wang et al., 2012). Therefore, extensive research has been done in the field of the impact resistance of sandwich structures.

Horrigan et al. (2000) investigated the impact of soft and hard projectiles on a honeycomb core sandwich structure with glass fibre skin panels. They concluded that the investigated sandwich panels suffered from shallow core crushing when impacted by a soft projectile, while a hard projectile caused deeper damage of the core corresponding to the shape of the projectile. Moreover, in the case of the impact with hard projectiles the damage of the skin panel was more extensive. Charles and Guedra-Degeorges (1991) demonstrated that the dent depth is proportional to the impact energy until a maximum value is reached. Rhodes (1975) performed a number of impact tests on a range of different sandwich systems and concluded that the increase of the core crush strength can improve the impact resistance of the sandwich structure.

Raju et al. (2008) investigated the impact resistance of sandwich plates with honeycomb cores. They observed that the impact response of the sandwich panels, characterised in terms of peak impact force, was dependent on the core thickness, the size of the impactor and the type of face sheet, but it was independent of the boundary conditions.

Flores-Johnson and Li (2011) conducted quasi-static indentation tests on foam core sandwich panels with carbon fibre face sheets. They investigated the influence of different impactor shapes on the indentation of the sandwich panels. They concluded that the foam core density and the nose shape of the impactor had significant influence on the energy absorption, as well as, on the damaged area and indentation

failure of the carbon fibre sandwich panels. Moreover, they observed that the boundary conditions influence the indentation load of the panels.

The impact resistance of sandwich panels with a range of PVC/PUR foam cores was investigated by Hazizan and Cantwell (2002). Their research showed that the damage of PVC/PUR systems with brittle core material is characterised by a shear fracture, while for intermediate modulus system the samples failed in buckling of the impacted composite skin. High modulus PVC/PUR systems failed in delamination of the top skin. Therefore, they concluded that the dynamic response of the foam-based sandwich structures is controlled by the elastic properties of the core material.

Wang et al. (2012) examined the impact resistance of PUR foam based sandwich panels with plain weave carbon fibre facings. They investigated the influence of face and core thickness, and impactor size at different energy levels. They found that the thickness of the foam core material did not have any influence on the impact response and damage extent of the investigated sandwich panels. Increasing the face thickness resulted in increased peak load and decreased contact duration. The ratio of absorbed energy to impact energy decreased together with increasing face thickness. In addition, the thickness of the face sheets influenced the damage diameter and indentation depth of the samples. Increase of the impact energy caused an increase of the absorbed/impact energy ratio and contact duration. Moreover, it increased the indentation depth and damage diameter. Finally, increase of the peak load and decrease of the contact duration and absorbed/impact energy ratio was observed with the increase of impactor size.

Mines et al. (1998) studied the perforation of two different composite sandwich panels. The panels were made out of woven glass epoxy prepreg skins with a honeycomb core and woven glass vinyl ester skins with a Coremat core. They found that energy absorption is controlled by the core crush and it increases with increasing impact velocity. The increase of the perforation energy was caused by the increase of skin failure stress and core strength at high strain rates. Additionally, they concluded that the failure progression is influenced by the core density.

Mahfuz et al. (1992) used a Split Hopkinson bar method to investigate the strain rate sensitivity of sandwich panels in the through thickness direction. They studied the influence of different core properties on the failure modes under impact conditions.

Mahfuz et al. (1992) observed increased strain rate sensitivity for structures with higher density of the core. Furthermore, they demonstrated that the crushing of the core material plays significant role in the energy absorption process. In their studies, initial delamination did not influence the failure process of the sandwich structures and it did not reduce load bearing capacity in the case of a dynamic, through thickness load.

The type and extent of the damage of graphite/epoxy sandwich panels with foam and honeycomb cores under low velocity impact was studied by Anderson and Madenci (2000). They concluded that increasing the foam density and thickness of the face sheets improves the energy absorption of sandwich panels. Moreover, they found that the internal damage of the sandwich panels with both, foam and honeycomb cores is quite severe, without any significant indication of damage on the impacted surface.

Gustin et al. (2005) investigated the influence of added Kevlar and hybrid (Kevlar-carbon) fibres to the carbon fibre face sheets on the impact resistance and compression after impact of carbon sandwich panels. They concluded that adding of Kevlar fibres to the carbon face sheets improved the energy absorption and average maximum impact force of the sandwich structure by 10%. Furthermore, 5% improvement in the absorbed energy and 14% in the average maximum contact force was observed for the sandwich panels with hybrid face. The utilisation of Kevlar or hybrid layers in the impacted skin minimised the reduction of compressive strength after impact of sandwich panels. Moreover, it improved the impact resistance of the sandwich panels, however, it reduced their overall stiffness and compressive strength.

Mohmmed et al. (2013) performed numerical and experimental studies on the impact damage of sandwich panels with different ply angle face sheets subjected to low velocity impact. In their studies, sandwich panels with unidirectional, cross ply, angle ply and quasi-isotropic face sheets were subjected to a drop weight impact with three different energies. They also carried out a numerical impact analysis in ABAQUS using a finite element model of the corresponding sandwich panels. Good agreement between the numerical and experimental results was obtained in terms of energy absorption and peak load. However, Mohmmed et al. (2013) were not able to model correctly the debonding between the face sheets and the core material.

Moreover, the damage size and shape did not correspond to the damage obtained during the experiment.

The above researches show that the impact resistance of composite sandwich structures is influenced by many different factors. The main factors which control the energy absorption, damage extent and damage mode are:

- material used for composite skins (material type and layup)
- face sheet thickness
- core material (density and crush properties)
- core thickness
- size and shape of the impactor

Except changes in the face sheet materials and properties of the core, many researchers started to look into improving the sandwich structures impact resistance by improvement of the core materials. This could be achieved by introduction of additional structures within the core of the sandwich panels. The aim of such reinforcement was to increase the strength of the core material, and therefore the energy absorption, with the smallest possible mass increase of the sandwich component.

Torre and Kenny (2000) compared the impact resistance of novel corrugated sandwich panel with fibre-phenolic matrix composite faces and a foam core with an additional corrugated panel, to a standard sandwich panel with glass fibre-polyester matrix composite and a foam core. They proved that the corrugated design has increased the energy absorption properties and strength in comparison to the standard sandwich panels.

Vaidya et al. (2008) performed an experimental investigation on the impact resistance of novel 3D sandwich composites under a range of impact energies. Moreover, they compared the impact performance of hollow and PUR foam filled 3D sandwich panels. The novel composited design consisted of E-glass fabric face sheets bonded together with vertical piles, which were woven to the faces to form an integral sandwich structure. Low velocity impact tests on the novel 3D composite panel showed no delamination failure in the structure. The modes of failure observed in the hollow

samples were dominated by rupture of the face sheets and buckling of the core, while only core crushing together with piles failure was observed in the case of the foam filled sandwich samples. Filling of the samples with polyurethane foam increased the impact load carrying capacity of the sandwich panels by 250%.

Lascoup et al. (2010) performed experimental studies on the influence of stitches introduced within the foam core on the impact resistance of glass/foam sandwich structures. They concluded that the impact performance of the stitched sandwich panels was significantly improved. The initial impact energy was absorbed for degradation of the stitches rather than core crushing. The introduction of stitches in the core material significantly limit the delamination between the foam and the face sheet interface. Moreover, it was found that the geometrical parameters of the stitches influence the global response of the sandwich panel.

Baral et al. (2010) compared the soft body impact resistance of a honeycomb sandwich panel and a foam based sandwich panel with through thickness reinforcement. The first sandwich panel was manufactured with a Nomex honeycomb core and carbon fibre prepreg face sheets. The second panel was manufactured with the same face sheets system and a Rohacell foam core reinforced in through thickness direction by pultruded carbon fibre pins. The comparison of these two sandwich panels revealed that the reinforced design had twice as high impact energy until damage as the honeycomb design.

The research performed on the impact resistance of reinforced sandwich panels is not extensive. It shows that implementation of additional structures within the core material can highly increase the impact resistance of sandwich composites. Nevertheless, this research field needs further investigation.

Little research has been done on the high velocity impact on composite sandwich structures. Wang et al. (2014) studied the impact resistance of carbon fibre composite lattice core sandwich structures subjected to high velocity impact. They compared the energy absorption efficiency of the carbon fibre composite sandwich structure to steel and aluminium lattice core sandwich structures for a range of velocities. Results of the analysis revealed that for a specific range of velocities the composite sandwich panel had better energy absorption efficiency than the steel and aluminium panels of the same weight.

Buitrago et al. (2010a) performed experimental studies on the perforation of glass/polyester structures under high velocity impact conditions. They compared the ballistic limit and damage extent of different composite structures. The structures taken into investigation were: monolithic glass/polyester laminate of different thickness, sandwich panels with glass/polyester face sheets and PVC foam core, and finally two separated glass/polyester laminates which correspond to sandwich structure facings separated with a core thickness but with no core in between the faces. Monolithic laminates showed increased impact resistance in terms of ballistic limit with increasing thickness, however, the damage area was also increased in these cases. The ballistic limit of the sandwich structure was similar to the ballistic limit of the separated plates. Moreover, it was similar to the ballistic limit of the monolithic composite structure of the same thickness. Buitrago et al. (2010a) observed that the sandwich structure had greater damage on the back surface of the panel, while in the case of the structure with separated panels the bigger damage was observed on the impacted face.

Ivanez et al. (2011) performed numerical analysis of high velocity impact on sandwich structures and separated composite plates in ABAQUS. The numerical results were validated against the investigation of Buitrago et al. (2010a). Ivanez et al. (2011) modelled the composite face sheets of the sandwich panel with a progressive damage model implemented into ABAQUS by user subroutine. The foam was modelled with a crushable foam plasticity model. The results obtained from the numerical analysis showed good agreement to the experimental results in terms of ballistic limit and residual velocity.

Vaidya et al. (2001) investigated the response of a novel design of sandwich panels, with a number of through thickness reinforcements, subjected to high velocity impact. The structures used for this study consisted of hollow Z-pin core panels, honeycomb and foam core sandwich structures reinforced with steel, glass/epoxy and titanium Z-pins. The application of Z-pins in sandwich panels showed considerable improvement in the impact resistance of the sandwich panels with a small increase in weight.

Villanueva and Cantwell (2004) studied the failure modes of novel aluminium core sandwich structures with unidirectional (UD), woven glass and fibre-metal composite face sheets under high velocity impacts. In the case of UD glass face sheets,

delamination and longitudinal face sheet splitting were the predominant modes of failure. Impact tests on the sandwich structure with woven skins showed reduced delamination area in comparison to the sandwich panels with UD skins. Villanueva and Cantwell (2004) concluded that the implementation of fibre-metal laminates for the skins of sandwich structures increases their perforation energy by approximately 23% in comparison to composite facings, while maintaining comparable volume fractions.

Velmurugan et al. (2006) studied the response of glass fibre sandwich panels with thin polyurethane foam cores under a range of velocities (30-100 m/s). Three sets of glass fibre facings were used for the facings of the sandwich structure: low and high modulus glass fibres and a hybrid of both. The thickness of the foam core was kept as small as possible, therefore the energy absorption and improvement in stiffness of the foam core were neglected. The hybrid structures had a higher ballistic limit than the sandwich panel with low modulus fibre facings, and a lower ballistic limit than the sandwich panel with high modulus fibre facings.

Buitrago et al. (2010b) performed numerical and experimental studies on the perforation of honeycomb sandwich structure with honeycomb core and carbon/epoxy facings under high velocity impact. The numerical analysis was performed with a three dimensional finite element model implemented into ABAQUS/Explicit. The results were compared to the experimental results and showed good agreement. Buitrago et al. (2010b) concluded that for impact velocities of 250 $\frac{m}{s}$ approximately 40% and 45% of the impact energy was absorbed by the top and bottom facings respectively, while for velocities close to the ballistic limit almost 60% of the impact energy was absorbed by the top face sheet. The energy absorbed by the honeycomb core varied between 10% and 20% depending on the impact velocity. Fibre breakage was the dominant failure mechanism of the composite facings, while for the honeycomb core it was plastic deformation of the aluminium walls. Moreover, it was observed that the damage of the sandwich structures was highly localised.

The above research shows there is great potential in the reinforced composite sandwich panels. However, additional research is required in this field, especially on the impact performance of reinforced sandwich structures subjected to high impact velocities, as it can be crucial for improvement of safety in aerospace.

The research presented in this thesis is focused on the impact resistance of reinforced composite sandwich panels under high velocity impact loading caused by a soft projectile. The core of the investigated sandwich panel was manufactured from low density polyurethane foam. Therefore, the subsequent sections of this chapter are dedicated to the description of low density foams, their modelling techniques and material models used for representation of foams in LS-DYNA.

4.3 Low density foams as core materials

Foams are multi-phase materials built from the pockets of gas trapped within the solid matrix. The manufacturing of the foams through an expansion process results in a porous microstructure of foams. Due to the rise of the matrix material during the expansion process, gas particles are formed and enclosed within the matrix, forming the porous microstructure of foams. The size of the gaseous pores controls the foam behaviour as it is responsible for the compressive properties of the foam (Croop and Lobo, 2009).

Based on the morphology of the gas phase, foams can be characterised as open or closed cell foams. In addition to the distinction of open and closed cell, foams can be divided into crushable and elastomeric. This distinction is based on the properties of the matrix used for manufacturing of the foam.

Crushable foams are manufactured from rigid matrices and their behaviour can be characterised by brittle or ductile deformation of the foam walls. In the case of brittle foams, the walls of the foam fail and they do not recover after the load is removed. In the case of ductile foams, the walls of the cells undergo plastic deformation and small or no recovery can be observed after the load removal. Examples of brittle foams are rigid polyurethane foams and examples of ductile foams are metallic foams.

The application of flexible materials as foam matrices results in elastomeric foams. These foams are characterised by high flexibility and high level of recovery. Most of the elastomeric foams are open cell, however, closed cell elastomeric foams do also exist. An example of flexible foams with good recoverability is the flexible polyurethane foam.

High compressibility and bending stiffness, which goes together with zero or very low Poisson's effects, are the main mechanical characteristics of foam materials (Du Bois, 2009). Their low strength properties in tension and shear are balanced with a good energy absorption in compression.

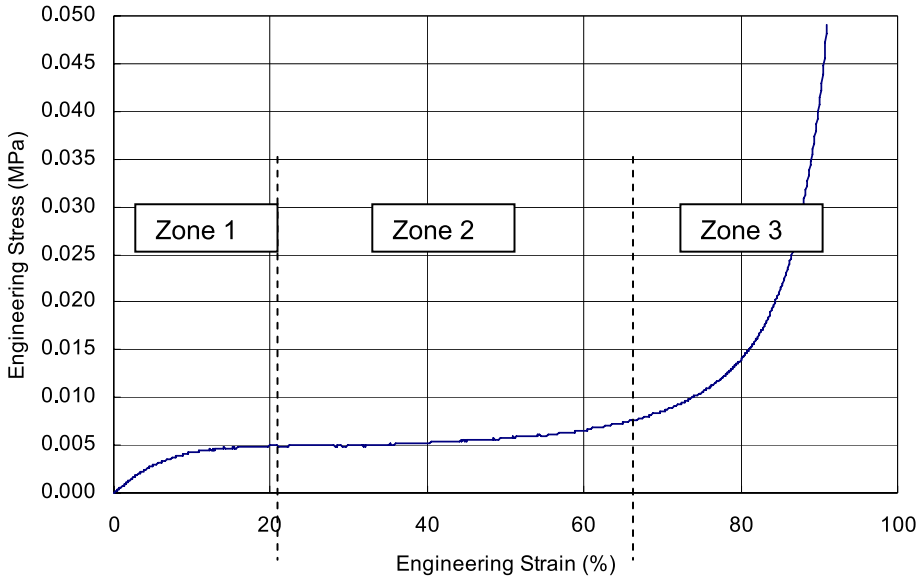

Figure 4.2: Typical zones in foam compressive stress-strain curve (Croop and Lobo, 2009).

The compressive behaviour of foams is characterised by a particular stress-strain response, common for all foam materials. The compressive stress-strain relation can be divided into three zones, shown in Figure 4.2. In Zone 1, the stress increases until it reaches the strength of the matrix material. At that point, the curve changes its slope and becomes flat - Zone 2. This part of the stress-strain curve is called the plateau compaction region. At this stage, the matrix material yields and the walls of the foam cells start to collapse or fail due to the gas movement. If the matrix material strength is exceeded by the gas pressure, the cells are ruptured by the exiting gas, releasing it to the atmosphere. If the matrix strength is higher than the pressure of the compressed gas, the cells collapse. Following the collapse or rupture of the foam cells, the densification of the foam begins - Zone 3. At the densification stage, the foam stress-strain relationship is similar to the stress-strain relationship of the matrix material. The above behaviour can be observed for most foam materials,

however, the size of the zones can vary depending on the morphology and matrix of the foam (Croop and Lobo, 2009).

It is worth to mention, that foams are rate dependent materials (Kolling et al., 2007). It is related to the escape of the gas from the porous structure. When a foam sample is loaded at a low strain rate, the gas has enough time to escape from the structure. When a higher strain rate is applied, the gas does not have enough time to escape from the structure and provides an additional cushioning effect to the structure, thus a higher load is required to compress the sample. The rate dependency can increase the load necessary to compress the sample up to 100% for higher strain rates.

4.4 Review on selected LS-DYNA foam material models

Different core materials require different modelling approaches to appropriately represent the response of the particular core material. The foam behaviour varies due to differences in the porous microstructure and matrices type, as well as discrepancies in the manufacturing process. Moreover, the physics of foams related to their viscosity, which causes the rate dependency, damping, hysteresis and stress relaxation (Du Bois, 2009), makes the numerical modelling of foams a challenging task.

Plenty of material models have been developed to represent the behaviour of the foam materials. In general, the foam material models available in LS-DYNA allow for definition of a stress-strain curve to predict the response of the foam. Some of the material models are designed for recoverable or non-recoverable foams, some take into account rate dependency and others enable to model failure of the material due to tension or shear. However, it needs to be borne in mind that each model has some limitations.

In order to determine the most relevant foam material model for impact application, four material models were chosen and their capabilities were assessed. The foam material models taken under investigation were:

- MAT_57 - Material Low Density Foam
- MAT_63 - Material Crushable Foam

- MAT_83 - Material Fu Chang Foam
- MAT_154 - Material Deshpande Fleck Foam

Further in this section, the theoretical background and LS-DYNA definition of the chosen material models is presented.

4.4.1 Foam material models in LS-DYNA

4.4.1.1 MAT_57

Material MAT_57 is an urethane foam material model designated for modelling of low density, highly compressible elastic foams (LSTC, 2006, Slik et al., 2006). For this material model, the compressive behaviour is defined with a load curve input, defined in terms of nominal stress versus strain. The compression of the foam is one dimensional and do not couple with the transverse direction. The unloading behaviour of the foam can be modelled by changing the SHAPE and HU parameters (see Figure 4.3). In addition to the shape factor, an optional decay factor can be defined. This parameter is responsible for the reload behaviour of the foam. MAT_57 allows for modelling fully elastic recovery of the foam material.

In addition, this material model allows for definition of the tensile cut off pressure, which governs the tensile failure of the foam material. If tension failure is defined, the material behaves linearly until tearing occurs (LSTC, 2013a). Although failure of the material can be defined, it does not result in material deletion. In case of failure, the pressure in the material stays at the value of the cut off pressure or it is brought back to zero (depending on the value of the FAIL parameter).

According to Croop and Lobo (2009), soft open cell polyurethane foams can be modelled with high fidelity with material model MAT_57. Additionally, MAT_57 can be used for modelling of seat cushions and paddings for Side Impact Dummies (LSTC, 2013a).

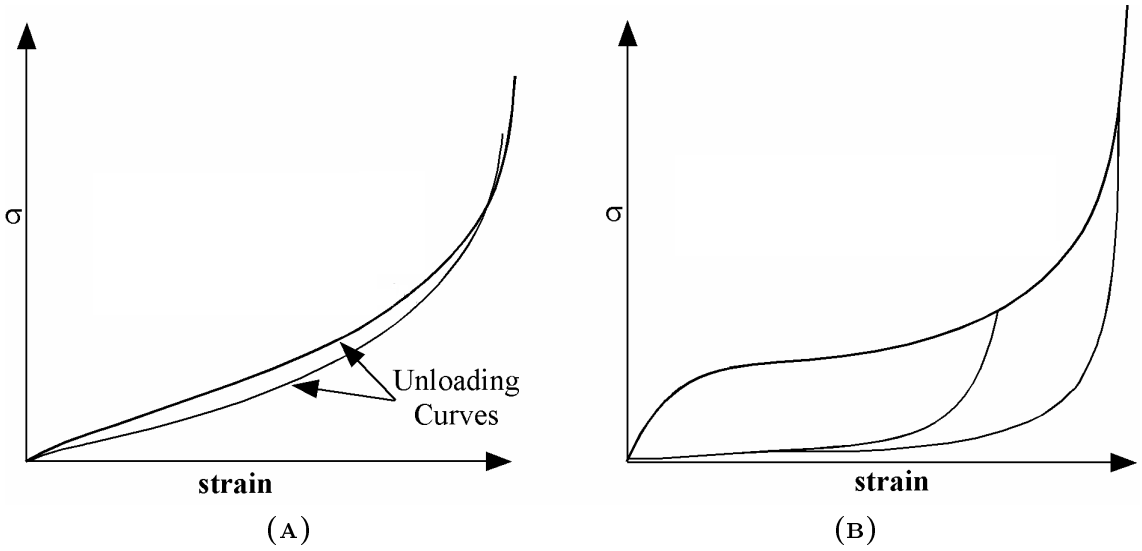

Figure 4.3: Compressive behaviour of low density foam model: (A) Typical unloading curves for shape factor equal to unity, (B) Typical unloading curves for a high value of shape factor (5-7) and for low shape factor (0.1) (LSTC, 2013a).

4.4.1.2 MAT_63

MAT_63 is an isotropic foam material model where the compression of the material is one dimensional with zero Poisson's effects. In addition to the compression behaviour defined by the load curve, damping and tension cut off stress can be defined for more realistic behaviour of the material. Rate sensitivity can be taken into account via the damping coefficient. However, to include the strain rate effects, it is recommended to use MAT_163 - MODIFIED_CRUSHABLE_FOAM, which is a modified version of MAT_63. The crushable foam material model was designed for modelling of crushable foams which show low elastic recovery and do not require cyclic loading and unloading behaviour.

The compressive behaviour of the foam is defined through a load curve in terms of yield stress versus volumetric strain. Unloading in this material model is fully elastic. Figure 4.4 presents the loading and unloading behaviour of the material. The sample is unloaded from point a to the cut off stress denoted as b. Furthermore, the sample is unloaded to point c and reloaded to point d. From point d, the reloading of the material continues along the defined load curve. In order to prevent failure of

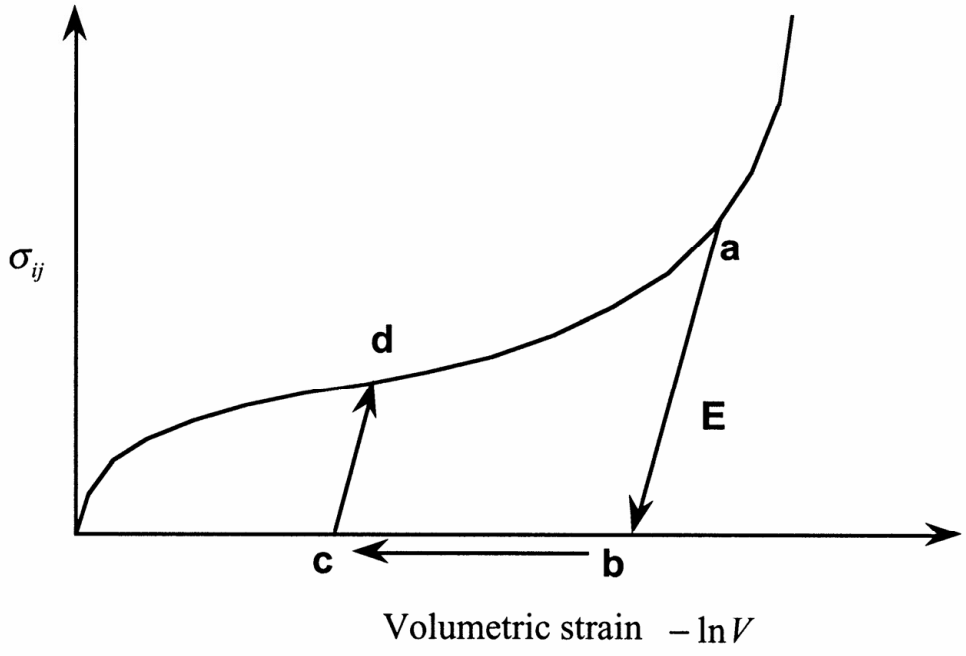

FIGURE 4.4: Yield stress - volumetric strain curve for crushable foam (LSTC, 2013a).

the material under low tensile loads, the non zero value for the tensile cut-off needs to be defined. A high value of the tensile cut off changes the tensile behaviour of the material and makes it similar to the compressive behaviour.

The volumetric strain for the stress-strain curve definition in MAT_63 is defined in terms of the relative volume:

$$\gamma = 1 - V \tag{4.1}$$

Where γ is the volumetric strain and V is the relative volume, defined as the ratio of the current volume to the initial volume.

4.4.1.3 MAT_83

MAT_83 is a foam material model which allows for modelling the rate sensitive response of the elastomer foams. This material model is based on the constitutive foam material model developed by Fu Chang et al. (1998). In Fu-Chang's material model a tabulated formulation is proposed instead of the viscous description of the

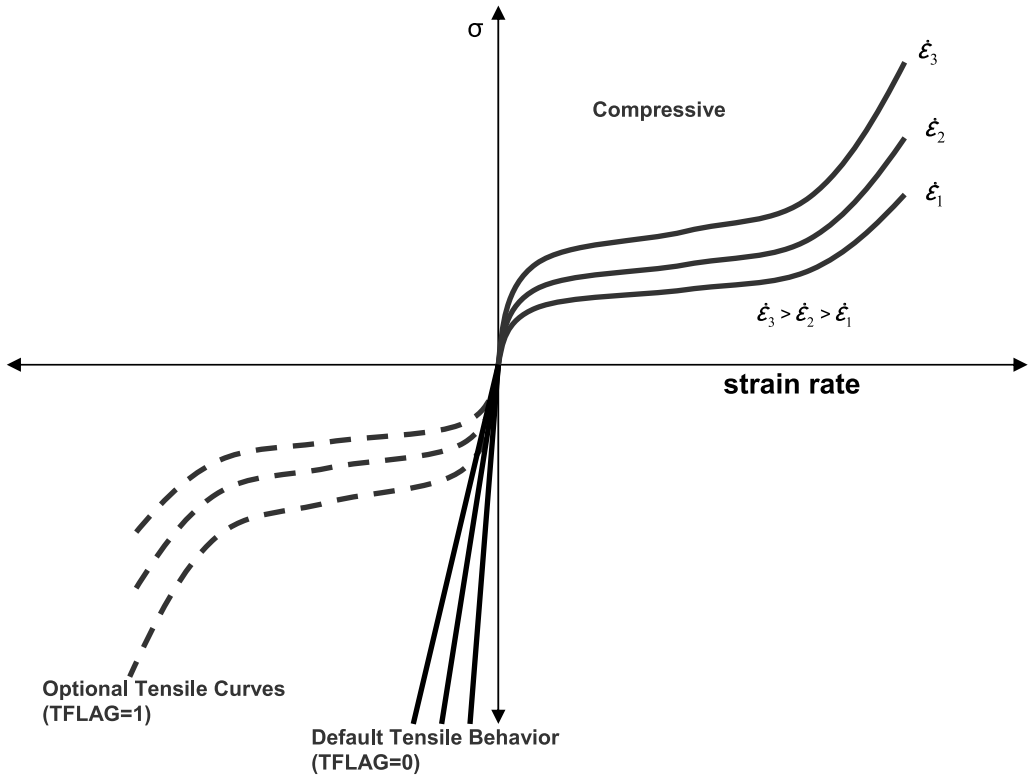

FIGURE 4.5: Fu Chang's foam model rate effects in tension and compression (LSTC, 2013a).

foam material (Kolling et al., 2009). The main assumption of MAT_83 is that there is no coupling between the material axes (Poisson's ratio equal to zero). Therefore, Fu-Chang's material model is a one dimensional material law where the stress strain relation, obtained at different strain rates from the uniaxial static and dynamic tests, is a direct input (Kolling et al., 2009, Serifi et al., 2003).

The material stress-strain relation is defined through a load curve in terms of nominal stress versus strain. Different strain rates corresponding to different behaviour are defined in a table as a function of strain rate. Figure 4.5 presents the input stress-strain curves for different strain rates. Linear interpolation is used by LS-DYNA for prediction of the stress-strain values for the applied strain rate. In case the strain rates are higher than specified, no extrapolation is done and LS-DYNA uses the curve defined for the highest specified strain rate.

The unloading behaviour based on a tabulated principle was added to MAT_83

by Kolling et al. (2007). Definition of the unloading path allowed for modelling of Mullin's effect (reload follows the unloading curve after material first loading and unloading). For correct definition of the material model no unloading curve needs to be specified. If the unloading curve is not specified, the unloading follows the lowest strain rate curve. Nevertheless, this can cause a stiffer response of the foam material (Serifi et al., 2003). In addition to the unloading curve and unloading along the lowest strain rate curve, LS-DYNA allows to control the unloading behaviour with HU (hysteretic unloading factor) and SHAPE (shape factor for unloading) factors.

MAT_83 also allows for definition of cut off stress and damping through the viscous coefficient. Similarly to MAT_57, definition of cut off stress triggers material failure when the cut off stress is reached. After failure occurrence, the stress in the material remains at the value of the cut off stress or is reset to zero depending on the parameter FAIL. Failure of the material is not followed by element deletion.

4.4.1.4 MAT_154

Material model MAT_54 is an isotropic, continuum based constitutive model for crushable foams (Reyes et al., 2003), based on the Deshpande and Fleck (2000) foam model. This material model is an extension of the von Mises yield criterion, which combines the hydrostatic stresses into an equivalent stress. The hydrostatic stress term was implemented into the yield function of the material model to take into account the changes in the foam volume. The Deshpande-Fleck foam material model was implemented into LS-DYNA as MAT_154 by Reyes et al. (2003).

In Reyes et al. (2004) it is mentioned that the statistical variation of the density together with two fracture criteria (stress and strain based fracture criteria) were implemented into their material model. However, MAT_154 existing in LS-DYNA does not include the statistical variation of the density and only a strain based fracture criterion is available for users. Therefore, MAT_154 allows for element deletion when the critical value of volumetric strain is reached in the element. The fracture criterion is given by Equation 4.2:

$$If\ \varepsilon_m \geq \varepsilon_{cr} => element\ erosion \tag{4.2}$$

Where ε_m is the actual volumetric strain and ε_{cr} is the critical volumetric strain.

In MAT_154 the compressive stress strain relation is controlled through the input parameters shown in Table 4.1.

Table 4.1: MAT_154 parameters definitions (LSTC, 2013a, Rajaneesh et al., 2009).

Parameter	Definition	Unit
ALPHA	controls shape of the yield surface	-
GAMMA	curve fit parameter	MPa
EPSD	densification strain	-
ALPHA2	curve fit parameter	GPa
BETA	curve fit parameter	-
SIGP	yield stress	MPa
CFAIL	volumetric failure strain	-
DERFI	defines type of derivation used in material subroutine	-

MAT_154 material model was designed to model aluminium foams used in energy absorption structures. However, since this material model is a curve fitting model, it was decided to investigate its capabilities in the application for polyurethane foam.

4.4.2 Validation of selected foam material models

The LS-DYNA foam material models introduced in the previous subsection were chosen to be validated in order to assess their capabilities in modelling of foam behaviour. The assessment of the compressive properties of the corresponding material models was performed with single element tests. In addition to the compression tests, the ability to capture failure of the core material was investigated in an indentation test of foam blocks.

4.4.2.1 Single element tests

The constant stress solid element with a single integration point was chosen for the single element tests of the foam material models. The cubic element of 1 mm side length was supported as shown in Figure 4.6. Foam materials are assumed to be

isotropic, therefore the material properties of the foam are the same in all directions and only one set of single element tests is necessary for the assessment of the foam response.

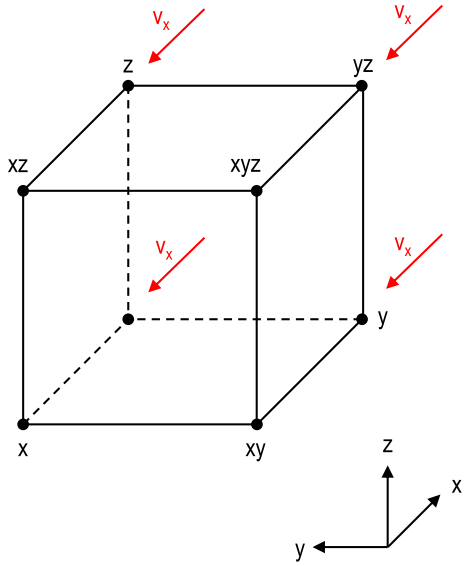

Figure 4.6: Single element test setup.

Although most of the foam material models allow for a direct input of experimentally obtained stress-strain curves, the straight input of compressive properties might not be relevant for crashworthiness applications. It is related to the fact that compression tests of the foam material are performed only up to 70-80% of the sample's height, while in crash analysis the element might be compressed up to nearly 100% of strain. The significant reduction in the length of the element results in a considerable increase of the computational time and in worst cases, the termination of the analysis due to the negative volume. In the case of maximum strain transgression, LS-DYNA extrapolates the stress strain curve for higher strains based on the last slope of the compressive input curve. However, in most of the cases the LS-DYNA extrapolation is insufficient and the model can still fail with negative volume. A possible solution for the excessive compression issue is a manual exponential extension of the compressive stress strain curve up to 95-99% of strain (Bala, 2006, LSTC, 2012).

The stress-strain curve assigned to the foam material models is shown as a black

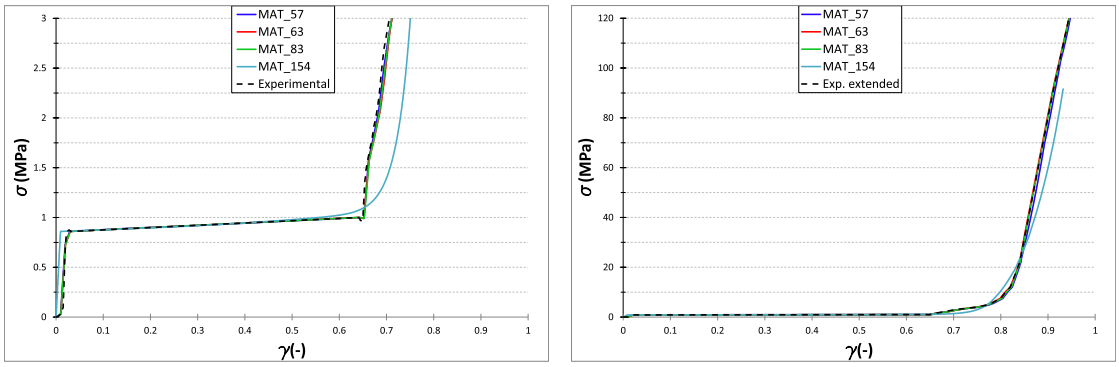

(A) (B)

Figure 4.7: Compressive behaviour of chosen material models: (A) Experimental curve, (B) Extended curve.

dashed line in Figure 4.7. This curve corresponds to the curve obtained from a compression test of PVC Rohacell foam performed by Mohmmed et al. (2013). After the single element tests, the compressive curves of the material models were compared to the experimental curve. The compressive stress-strain responses for the exact and extended compressive behaviour of the foam material models are presented in Figures 4.7 A and 4.7 B respectively.

For material models MAT_57, MAT_63 and MAT_83, the obtained stress-strain curves followed exactly the input curve. Therefore, these material models are able to represent accurately the compressive behaviour of the foam.

In the case of material model MAT_154 the compressive stress-strain curve does not follow exactly the curve obtained from the experiment (see Figure 4.7 A). For this foam material model the initial slope of the curve is steeper compared to the experimental curve. Steeper slope of the curve is related to the stiffer response of the foam material. The plateau stress value is the same as the experimental value, and finally, the densification response slightly differs from the experimental densification curve. The transition between the plateau region and the densification zone is smooth for MAT_154, which results in a slower increase of the stress in the material. The densification of the material occurs for higher values of strain, which results in slightly softer behaviour of the foam at the strain value of 65%. A comparison of the extended curves, illustrated in Figure 4.7 B, shows very good agreement between the stress-strain curves.

Considering the fact that the Deshpande-Fleck foam material model is not based on an input curve but on curve fitting material parameters, the compressive behaviour of the PVC foam was represented very well. Therefore, material model MAT_154 can be used for modelling of compression of PVC with good accuracy.

To sum up, the single element compression tests of the foam material models showed good capabilities of the chosen material models for the prediction of the compressive behaviour of the foam.

4.4.2.2 Indentation tests

Indentation tests on a block of foam were performed in order to investigate the capabilities of the foam material models to capture the material shear failure under a localised impact loading. In addition to the failure of the material, the energy absorption of the different material models was compared.

The cuboidal block of foam was impacted with the steel intender at the energy of 50 J. The dimensions of the foam sample were: length $l = 100\ mm$, width $w = 80\ mm$ and height $h = 40\ mm$. The bottom of the foam sample was simply supported and the side surfaces of the sample were free to deform. The setup of the analysis is shown in Figure 4.8.

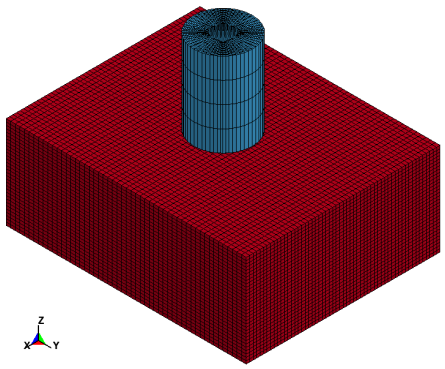

FIGURE 4.8: Indentation test setup.

In order to prevent the issue related to the negative volume, the compression stress strain curve was extended in accordance with the recommendations of Bala (2006).

In addition to the extended load curve, the deletion of the elements due to the negative volume was turned on (PFAIL parameter on the CONTROL_SOLID card). Eroding contact between the impactor and the foam block was defined to prevent the loss of contact in case if elements were deleted.

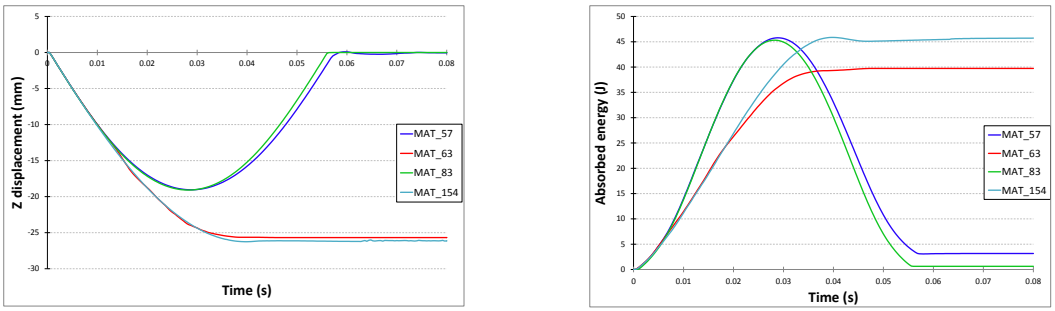

(A) (B)

FIGURE 4.9: Comparison of different foam material models: (A) Foam block centre displacement, (B) Foam block energy absorption.

Figure 4.9 A shows the indentation depth measured as displacement of the foam block centre point. The displacement curves show that materials MAT_57 and MAT_83 are suitable to model fully recoverable foams, which is also confirmed in Figure 4.10 B and Figure 4.10 F. Both material models showed the same level of indentation depth and very similar path of elastic recovery for the same values of the HU and SHAPE parameters ($HU = 0$ and $SHAPE = 0$).

The displacement curves for material models MAT_63 and MAT_154 showed exactly the same level of indentation depth. Moreover, the indentation of the foam blocks was permanent in both of the cases, which proves that MAT_63 and MAT_154 are suitable for modelling of crushable foams. Figures 4.10 D and 4.10 H show that the indentation of the foam samples is permanent and stays on the maximum level, which indicates that there is no elastic recovery of the material. However, the difference in behaviour of these two materials is evident in the plots of the indentation process. The deformation of the foam for MAT_63 is rather smooth and does not show any failure of the foam material (see Figures 4.10 C and 4.10 D), while the indentation of the foam block modelled with MAT_154 is characterised with mate-

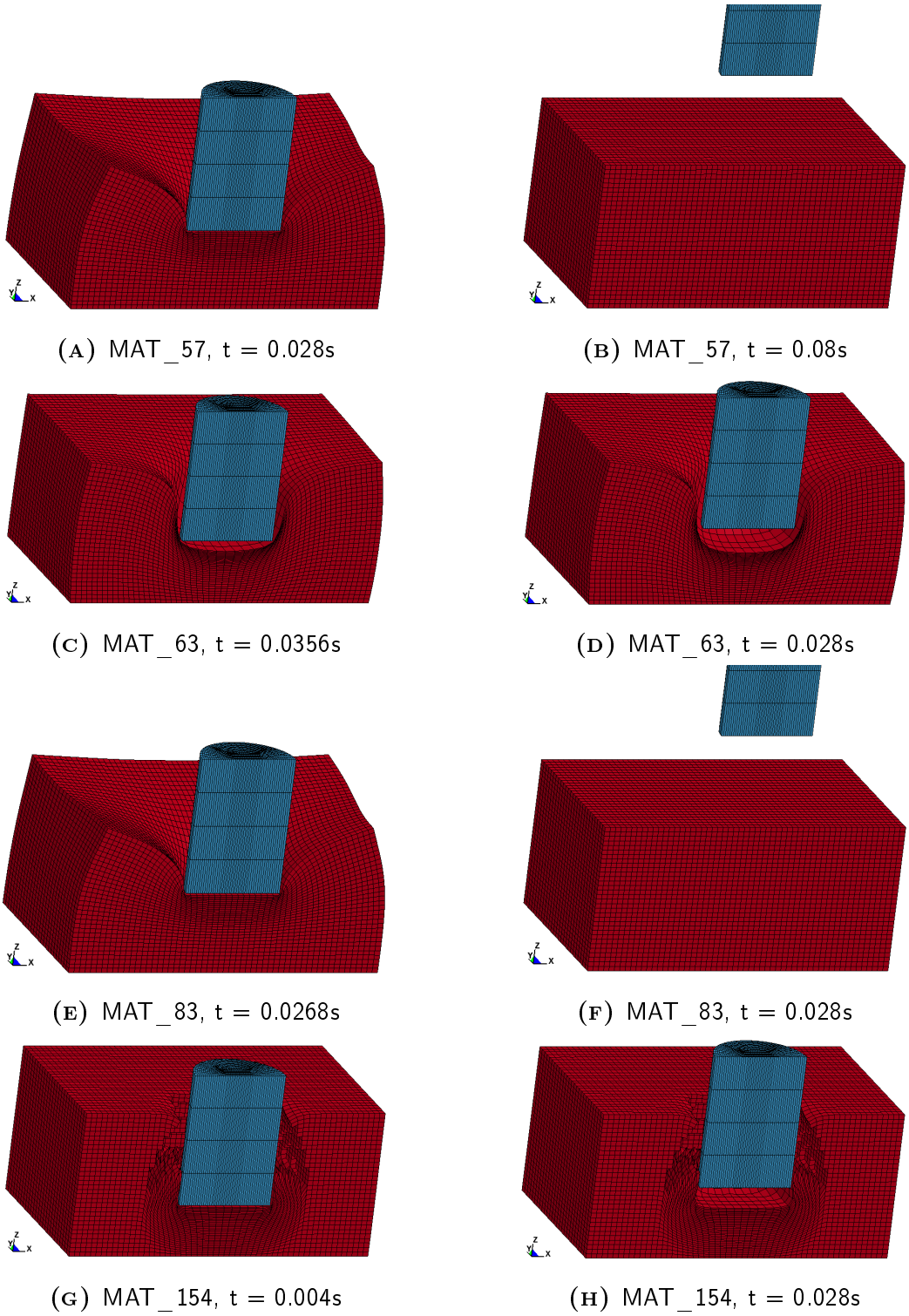

(A) MAT_57, t = 0.028s

(B) MAT_57, t = 0.08s

(C) MAT_63, t = 0.0356s

(D) MAT_63, t = 0.028s

(E) MAT_83, t = 0.0268s

(F) MAT_83, t = 0.028s

(G) MAT_154, t = 0.004s

(H) MAT_154, t = 0.028s

FIGURE 4.10: Comparison of foam materials response at the time of maximum penetration and in the end of analysis for materials: MAT_57 ,MAT_63 ,MAT_83, MAT_154.

rial failure and formation of a conical crater in the material (see Figures 4.10 G and 4.10 H).

Figure 4.9 B shows the energy absorption of the foam block in the indentation analysis with different foam material models. The energy absorbed with MAT_57, MAT_83 and MAT_154 was on the same level and was equal to $E_{A57} = 45.8\ J$, $E_{A83} = 45.3\ J$ and $E_{A154} = 45.9\ J$ respectively. For MAT_63 the absorbed energy was slightly lower and was equal to $E_{A63} = 39.7\ J$. The energy curves show that all the absorbed energy in the case of material MAT_57 and MAT_83 was used for the elastic recovery of the material. This also confirms the same recovery characteristics visible on the displacement graph (see Figure 4.9 A). In the case of the foam block modelled with MAT_63 and MAT_154, the absorbed energy stays on the same level, which is related to the crushable behaviour of these two material models.

To sum up, material models MAT_57 and MAT_83 are suitable for modelling elastic foams with full recovery. They are suitable for analyses where only the absorption properties of the foam are investigated and the recovery is either desired or does not influence the final results. However, due to the fully recoverable characteristics of the foam these material models are not suitable for modelling crushable foams. On the other hand, MAT_63 and MAT_154 are appropriate material models for modelling of crushable foams. However, there are significant differences between these two material models. MAT_63 is a simple material model where the foam behaviour is described by the input curve and the basic material parameters, while MAT_154 can reproduce the behaviour of crushable foams only using curve fitting. Furthermore, MAT_63 does not allow for failure of the foam material, while MAT_154 is able to represent material failure resulting in element deletion. Both of these material models gave comparable results in terms of indentation depth, however, the difference in the absorbed energy was quite significant.

4.5 Conclusions

- Composite sandwich panels with through thickness reinforcement have superior impact resistance and energy absorption over standard sandwich structures,

- LS-DYNA foam material models MAT_57 and MAT_83 are suitable to represent fully recoverable elastomeric foams,
- LS-DYNA foam material models MAT_63 and MAT_154 are suitable to represent crushable foams,
- Deshpande-Fleck (MAT_154) foam material model is the only one from the investigated foam material models which allows for modelling of foam material failure,
- Indentation analysis of the composite sandwich panel proved that MAT_154 is able to correctly reproduce the energy absorption and failure of the foam core under impact conditions.

Chapter 5

Experiment preparation

5.1 Introduction

This chapter provides a full description of all actions taken to prepare the bird impact experiment. For better understanding, the structure of the chapter is illustrated in Figure 5.1.

The first part of the chapter introduces the concept of the novel composite panels design. In this section, the corrugated and tubular sandwich panel designs are introduced. This is followed by the selection of the materials for manufacturing of the composite panels.

The subsequent section presents the manufacturing process of the corrugated and tubular sandwich panels. The consecutive steps were described in order to illustrate the complexity of the manufacturing process. In addition, the manufacturing of the gelatine birds and the foam samples was described.

The subsequent section contains a description of the compression tests performed on the foam samples.

The following section provides a description of the gas gun system used for the bird impact experiment. The description contains specifications of the gas gun itself, the measurement velocity system and the gun calibration. Moreover, in this section the design process for the bird release system is explained.

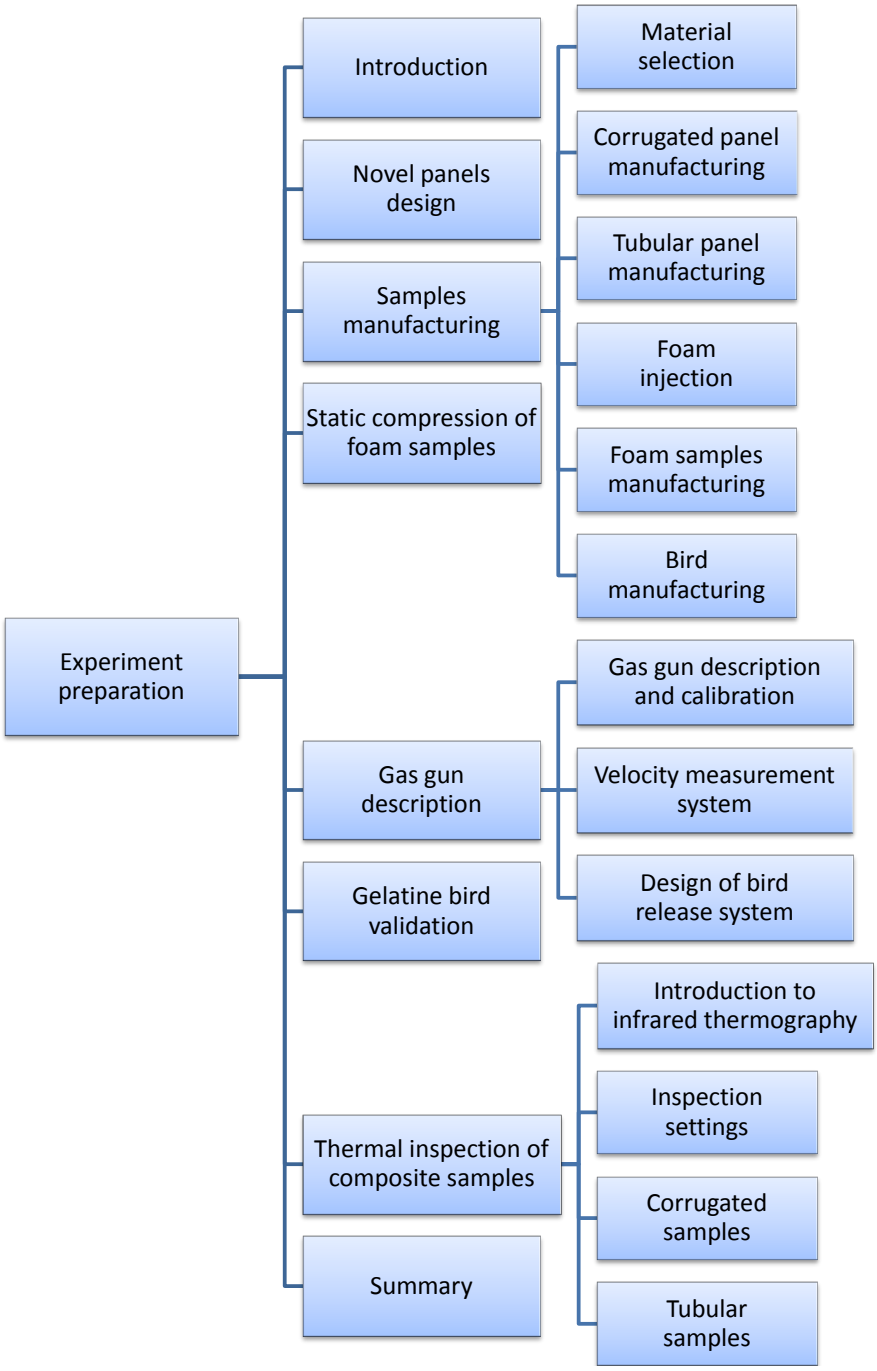

FIGURE 5.1: Chapter 5 structure.

In the subsequent section the pre-impact inspection of the manufactured samples is described. This contains an introduction to thermography, as one of the non-destructive techniques (NDT) for investigation of composite materials and explains why this NDT method was chosen. Furthermore, the inspection of the novel sandwich panels is presented.

In the last section, a summary of the whole chapter is presented.

5.2 Novel panel design

The literature review on the composite sandwich panels revealed that improvement of the impact resistance and energy absorption capabilities of these structures can be achieved by reinforcement of the sandwich core. Therefore, two novel sandwich structures were proposed and their design is presented in this section.

The first structure is based on the standard sandwich panel with a foam core. The panel was reinforced with a corrugated composite panel bonded between the two carbon fibre face sheets, as shown in Figure 5.2 A. The corrugated sheet contained four layers of [0°/ 90°] woven carbon fibre prepreg material. The application of the corrugated panel was intended to improve the through thickness strength and stiffness of the sandwich structure. For terminology simplification, the corrugated sandwich structure is referred to as a corrugated panel, or CSP, in the subsequent sections of the thesis.

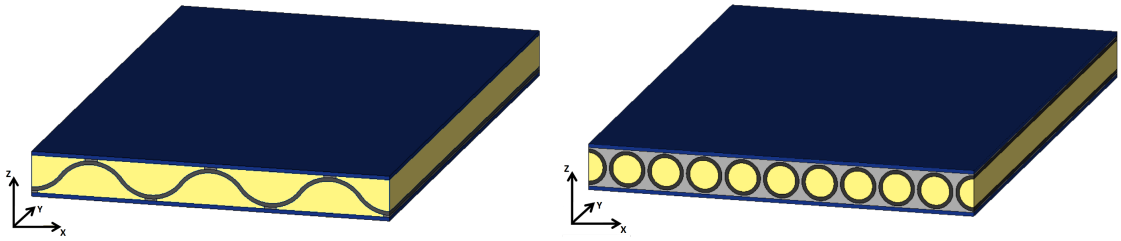

(A) (B)

Figure 5.2: New composite design: (A) Corrugated sandwich panel, (B) Tubular sandwich panel.

The second of the proposed structures was a composite sandwich panel with a tubular reinforcement incorporated between the sandwich face sheets. In this case, the core of the sandwich panel consisted of aligned composite tubes bonded to the carbon fibre sheets with polyurethane adhesive. The empty core of the tubes was filled with low density foam. The design of the structure is shown in Figure 5.2 B. For terminology simplification, the tubular sandwich structure is referred to as a tubular panel, or TSP, in the subsequent sections of the thesis.

5.2.1 Material selection

Pre-preg carbon fibre flat sheets bought from Easy Composites Ltd were used as face sheets of the novel sandwich structures. According to the manufacturer's description (Easycomposites, 2010), the carbon fibre sheets were produced in an autoclave from three layers of carbon fibre Twill pre-preg. The exact layup schedule and ply orientations of the material are shown in Table 5.1 and the material properties are shown in Table 5.2.

For the sandwich core filler, two part polyurethane liquid foam, supplied by CFS Fibreglass Supplies, was chosen. The CFS two part foam is a rigid, low density foam system. It was suitable to choose this material due to the ease of filling cavities and availability on the market. Solidified foam has a density of $48 - 50\ \frac{kg}{m^3}$ which fulfils the requirements for a low density core of the sandwich materials. The foam is produced by mixing of two liquid components, namely, Tripor 227 Component A and Tripor Component B at a ratio 1 to 1.13 by weight or 1:1 by volume. The compressive properties of the foam were not provided by the manufacturer. Therefore, compression tests of the foam samples were conducted in order to determine the compressive stress-strain relation for the polyurethane foam used for manufacturing of the sandwich panels. The procedure and compression test are described in Section 5.3.4.

The tubular sandwich panel was manufactured from 10 *mm* Roll Wrapped Carbon Fibre Tubes supplied by Easy Composites. The tubes were manufactured from high modulus Toray T700 unidirectional carbon fibre prepreg and E-Glass UD (80/20). The tube fibres were oriented in 0° and 90° directions which ensures superior mechanical properties in comparison to the pultruded tubes, the fibres of which are

Table 5.1: Layup schedule for Easy Composites prepreg carbon fibre sheet.

Schedule	Ply Orientation
204g 2/2 Twill 3k Prepreg Carbon Fibre	0°, 90°
430g 2/2 Twill 12k Prepreg Carbon Fibre	0°, 90°
204g 2/2 Twill 3k Prepreg Carbon Fibre	0°, 90°

Table 5.2: Vari-prepreg material properties.

Property	Test method	Value
Flexural strength	EN2562	850 MPa
Flexural modulus	EN2562	59000 MPa
Tensile strength	ISO 527	650 MPa
Tensile modulus	ISO 527	59000 MPa
ILSS - Short Beam Shear	EN2563	65 MPa

Table 5.3: Layup schedule for Easy Composites carbon fibre roll wrapped tubes.

Schedule	Ply Orientation
300gsm Toray T700	0°
300gsm E-Glass UD	90°
300gsm Toray T700	0°
300gsm E-Glass UD	90°
300gsm Toray T700	0°

Table 5.4: Carbon fibre roll wrapped tube material properties.

Property	Value
Density	$1.6\frac{g}{cm^3}$
Young's Modulus 0°	70000 MPa
Young's Modulus 90°	70000 MPa
Ultimate tensile strength 0°	600 MPa
Ultimate compressive strength 0°	570 MPa
Ultimate tensile strength 90°	600 MPa
Ultimate compressive strength 90°	570 MPa

Table 5.5: MTM 46 EL material properties.

Property	Test method	Value
Tensile modulus	D3039	55800 MPa
Compressive modulus	D3410	53300 MPa
Transverse tensile modulus	D3039	56400 MPa
Transverse compressive modulus	D3410	51900 MPa
Tensile strength	D3039	497 MPa
Compressive strength	D3410	698 MPa
Transverse tensile strength	D3039	513 MPa
Transverse compressive strength	D3410	706 MPa
Tensile strain to failure	D3039	0.9 %
Compressive strain to failure	D3410	1.3 %
Transverse tensile strain to failure	D3039	0.92 %
Transverse compressive strain to failure	D3410	1.37 %
In-plane shear modulus	D3518	3510 MPa
In-plane shear strength	D3518	113.4 MPa
Min. tensile Poisson's ratio	D3039	0.04
Max. compressive Poisson's ratio	D3410	0.04
Min. tensile Poisson's ratio	D3039	0.05
Max. compressive Poisson's ratio	D3410	0.05
ILSS (WARP)	D2344	71.8 MPa
ILSS - Short Beam Shear	EN2563	65 MPa

Table 5.6: Permabond PT326 material properties.

Property	Test method	Value
Shear strength	ISO 4587	$9 - 11$ MPa
Tensile strength	ISO 37	$16 - 25$ MPa
Elongation at break	ISO 37	$< 15\%$ MPa
Hardness	ISO 868	$65 - 75$ $Shore\ D$
Coefficient of thermal expansion	ASTM D-696	$85 \times 10^{-6} \frac{1}{K}$
Peel strength		$150 - 170$ $N/$ 25 mm

oriented only in one direction. The layup schedule of a single tube is shown in Table 5.3 and its material properties are presented in Table 5.4.

The corrugated panels were manufactured from ACG MTM46EL prepreg material purchased from the Advanced Composites Group Umeco Composites. MTM46EL prepreg is a medium temperature, toughened epoxy system intended for aerospace applications. The mechanical properties of MTM46EL are shown in Table 5.5. The mould for the corrugated shape was manufactured based on a PVC corrugated sheet.

In order to bond all components together, Permabond PT326 polyurethane adhesive was purchased from Easy Composites Ltd. Permabond PT326 is a high performance, rigid polyurethane adhesive suitable for bonding a wide variety of materials including plastics, composites and metals. The material properties of the cured adhesive are shown in Table 5.6. Permabond PT326 is a two part adhesive with a 4-7 minutes pot life. The handling strength of the adhesive is achieved after 90-120 minutes. The full bond strength of the adhesive is reached after 4-5 days curing at room temperature.

5.3 Samples manufacturing

5.3.1 Corrugated panel manufacturing

The first step in the manufacturing process of correct the composite sandwich panel with corrugated reinforcement was to manufacture the corrugated tool. The corrugated sheet was cut to dimensions of 400 $mm \times 250$ mm. Subsequently, a wooden frame was assembled around the cut panel and placed on a metal base around the corrugated panel. Thin film was spread on the top of the corrugated sheet and sealed to prevent any unwanted leakage. The assembled structure was placed on the heated vacuum curing and debulking table, ready for the mixture to be poured, as shown in Figure 5.3 A.

The next step was the preparation of the mixture, from which the corrugated tool was made. For this purpose, 400 g of epoxy resin was mixed with 66 g of hardener. Then, the filler was added to the mixture of epoxy and hardener, and mixed thoroughly until the compound obtained a uniform, dark violet colour. Subsequently,

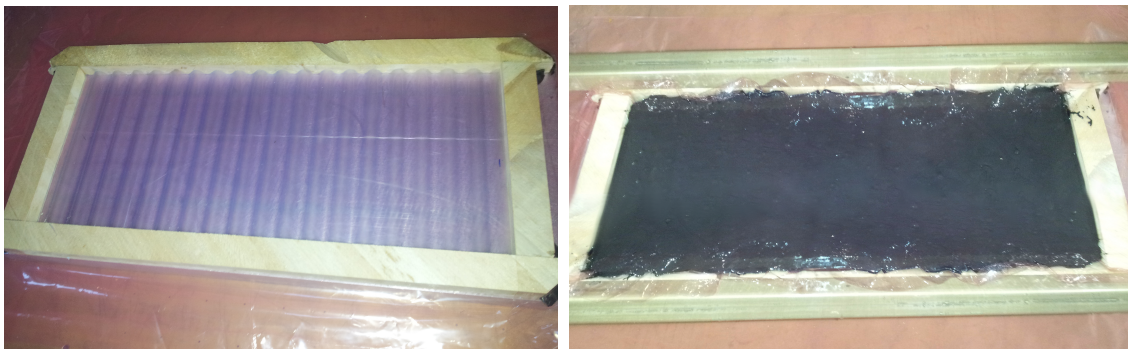

(A) (B)

Figure 5.3: Corrugated panel manufacturing process: (A) Wooden frame around the corrugated sheet, (B) Form filled with with the epoxy mixture.

the mixture of epoxy resin, hardener and the filler was poured slowly into the sealed form.

The pouring process was combined with application of pressure and equalisation of the compound to ensure uniform and precise distribution of the material across the corrugated shape. The pressure application and equalization was performed manually with a wooden slat. After the form was filled with the material, see Figure 5.3 B, it was covered with a cling film and the vacuum curing table was heated up to a temperature of $60°C$ to accelerate the curing process. The form was left on the vacuum curing table to fully cure for 12 hours. When the curing process was completed, the fully cured corrugated tool was removed from the form and the cling film was separated.

The second step was to manufacture the corrugated composite panel. Due to the difficulties with the precise distribution of the carbon fibre prepreg on the corrugated shape, it was decided to manufacture a corrugated panel separately for each sample rather than manufacturing one big corrugated panel and then cut it into smaller dimensions. Therefore, to improve the distribution control over the corrugated waves, the tool was cut to a size of 200 $mm \times 250$ mm.

The MTM46EL carbon fibre prepreg was cut into rectangular samples of 200 $mm \times$ 160 mm and stacked into four 0° / 90° layers to form a 1 mm thick panel.

Subsequently, the stacked panel was wrapped in protective cloth and cling film to facilitate the separation of the panel from the tool. Then, the secured panel was

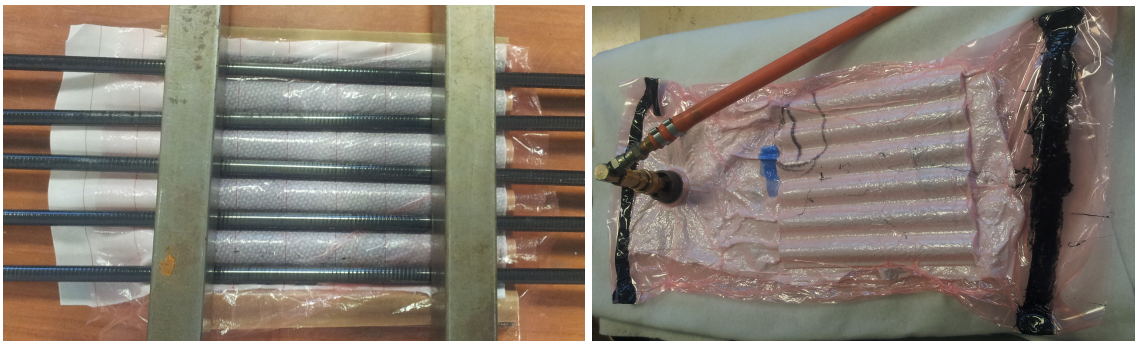

(A) (B)

FIGURE 5.4: Corrugated panel manufacturing process: (A) Loading of the prepreg to fit the corrugated shape, (B) Air removal from the sealed bag with corrugated prepreg.

enclosed in the vacuum curing table in order to remove the air and heat up the resin present in the prepreg. For this purpose, the vacuum curing table was set to a temperature of 60° C. After the resin was heated, the prepreg was placed on the corrugated tool and fit to the corrugated shape. To improve the fitting of the prepreg to the tool, the composite tubes were placed over the corrugated waves and loaded with steel ingots as shown in Figure 5.4 A. After fitting the prepreg over the corrugated shape, the tool with the panel was enclosed in a foil bag and sealed. Next, the air was removed from the bag using a vacuum pump as shown in Figure 5.4 B. Subsequently, the sealed bag with the tool and the prepreg panel was put into an autoclave for 5 minutes at a pressure of $3bar$, to consolidate the composite. After autoclave consolidation, the tool with the corrugated panel was left on the heated plate to cure. The curing process was performed at a temperature of $90°C$ and was supported by a vacuum pump to maintain the constant air removal.

After 12 hours of curing, the corrugated panel was removed from the sealed bag. The manufactured panel is shown in Figure 5.5. The production process was repeated twice in order to produce three corrugated panels. Another step in the manufacturing process of the corrugated sandwich panel was the bonding of the corrugated reinforcement with the composite sheets.

The fully cured prepreg face sheet was delivered in the size of 600 $mm \times 600$ mm. The face sheet panel was cut into smaller samples, 200 $mm \times 160$ mm, to ease the assembly process of the corrugated panels. The surface of the face sheet panels was

(A) (B)

Figure 5.5: Corrugated panel: (A) top side view, (B) front side view.

very glosy. Therefore, it was necessary to polish the surface with a sandpaper to make it rough and improve the bonding properties. Afterwards, the prepreg sheets and corrugated panels surfaces were cleaned with acetylene in order to remove any organic contaminants and prepare the surfaces for bonding.

The ready for assembling face sheets were placed on a table. A thin layer of the adhesive was placed on the top of every wave of the corrugated panel on one side of the panel, as shown in Figure 5.6 A. Subsequently, every single wave was covered with the adhesive and the face sheet was placed on top of the corrugated panel, see Figure 5.6 B. After the face sheets were placed on both sides of the corrugated panel, the metal ingots were used to equal the samples from each side. Subsequently, before initial bond, the samples were covered in thin foil and loaded from the top with steel blocks to assure good matching between the corrugated reinforcement and the prepreg face sheets.

Permabond PT326 polyurethane adhesive was used to bond the composite parts together. A twin tube cartridge gun dispenser was used to assure the appropriate mixing of the adhesive. One sample was bonded at a time to assure high precision of manufacturing.

After the adhesive was fully cured, the corrugated sandwich panels were ready for the injection of the polyurethane foam. The injection process was performed after the corrugated and tubular sandwich panels were manufactured, and is described in detail in Section 5.3.3.

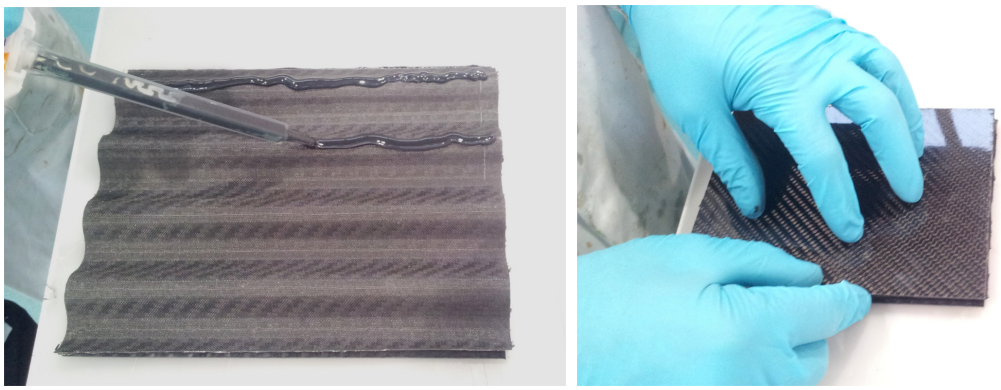

(A) (B)

Figure 5.6: Corrugated sandwich panel: (A) Adhesive injection, (B) Assembly of the corrugated sandwich structure.

5.3.2 Tubular panel manufacturing

The manufacturing process of the tubular sandwich panel was much simpler than the manufacturing of the corrugated sandwich structure. The ease of manufacturing was related to the fact that the reinforcement in form of 1000 mm long tubes was delivered directly from the manufacturer.

Each of the tubes was sanded manually to prepare the external surface for bonding and then cut into shorter tubes of 160 mm length. After the tubes were cut, both ends of each tube were polished with sandpaper to remove the sharp edges. Subsequently, all tubes were cleaned with acetylene to remove any organic contaminants and prepare the surface for bonding.

As a first step, the prepreg sheets for the faces of the tubular sandwich panels were cut to the dimensions 160 $mm \times 110$ mm. Subsequently, one surface of each sample was sanded with a sandpaper to prepare the surface for bonding. Afterwards, the surfaces were cleaned once again with acetylene.

When everything was prepared for the assembly of the tubular structure, the gun dispenser was loaded with the Permabond adhesive and the assembly process of the tubular sandwich panel begun.

The bottom sheet was placed on the thin foil on the table and the adhesive was distributed in form of a thick line on the prepared surface, directly afterwards the

tube was placed on the adhesive. However, before the tube was placed on the line of the adhesive, the layer of adhesive was dispensed on the side of the tube to prepare the bonding surface for the subsequent tubes.

The procedure was repeated until the panel contained ten tubes across its width. After all the tubes were in place, the adhesive was distributed on the top of every tube and the carbon fibre face sheet was placed on top of the tubes. Next, the sample was equalised with steel ingots and kept in position for $5-7$ min as this was the initial bonding time indicated by the adhesive manufacturer. Subsequently, the panel was loaded with the steel block on the top and the whole process was repeated until three samples were assembled.

The full cure of the adhesive was achieved after 24 hours and the samples were unloaded. Outflows of the adhesive were removed from the samples using a razor and the samples were ready for the foam injection.

Due to the relatively short time for initial cure of the adhesive and the large number of tubes, the whole process required quick assembly and therefore pictures of the process were not taken.

5.3.3 Foam injection

After all the composite samples were assembled, they were ready for the last stage of the manufacturing process, namely, the foam injection. Before the foam injection, the samples were sealed from the bottom with adhesive tape to prevent leakage of the foam. Next, the adhesive tape was used to create flanges on both sides of the samples to prevent the panel surfaces from foam leakage.

As described in the material selection Section (5.2.1), a two part liquid polyurethane CFS foam was used to fill the cavities in the panels. The foam containers were placed in a fume cupboard in order to prevent exposure to hazard substances. Subsequently, 10 ml of the Component A and 10 ml of the Component B were mixed thoroughly. Afterwards, the mixture was poured into the cavities in the corrugated panel. Half of the corrugated panel cavities were filled at a time, due to the short cream time (from start of mixing to start of rise) of the CFS foam. Following the foam rise, the surplus of the foam was removed. After the rise process was completed,

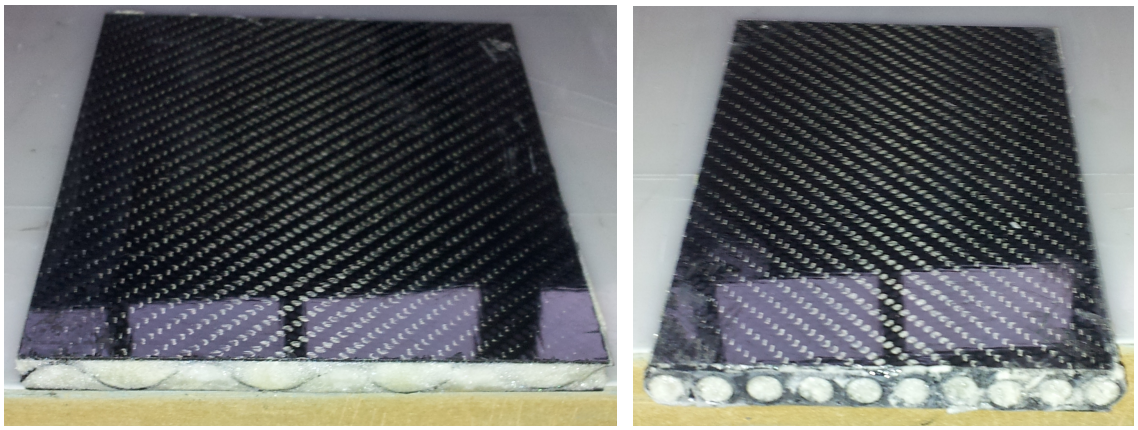

(A) (B)

FIGURE 5.7: Panels after foam injection: (A) Corrugated panel, (B) Tubular panel.

the remaining cavities were filled with the mixture of CFS components. The tubular panel cavities were filled with foam in the same way. Images of the samples after foam injection are shown in Figure 5.7

Finally, after the foam was completely cured, the samples were cut to the final dimensions of 150 $mm \times 100$ mm.

5.3.4 Foam samples manufacturing

The compressive properties of the polyurethane foam, used for the core of the sandwich panels, was essential for building an accurate numerical model of the sandwich structure in LS-DYNA. Therefore, it was important to investigate the foam material behaviour under compressive loading.

Quasi-static compression tests were conducted using the Instron 1000RD compression test rig in the Department of Applied Mechanics at Cranfield University. The tests were conducted according to the ASTM C365/C365M-05 standard, which determines the test methods for flat-wise compressive properties of sandwich cores.

In order to manufacture the foam samples, it was necessary to design the mould. The foam mould consisted of 5 rectangular metal plates, which assembled together formed a cuboidal cavity. Disassembly of the walls allowed for easy removal of the foam from the mould.

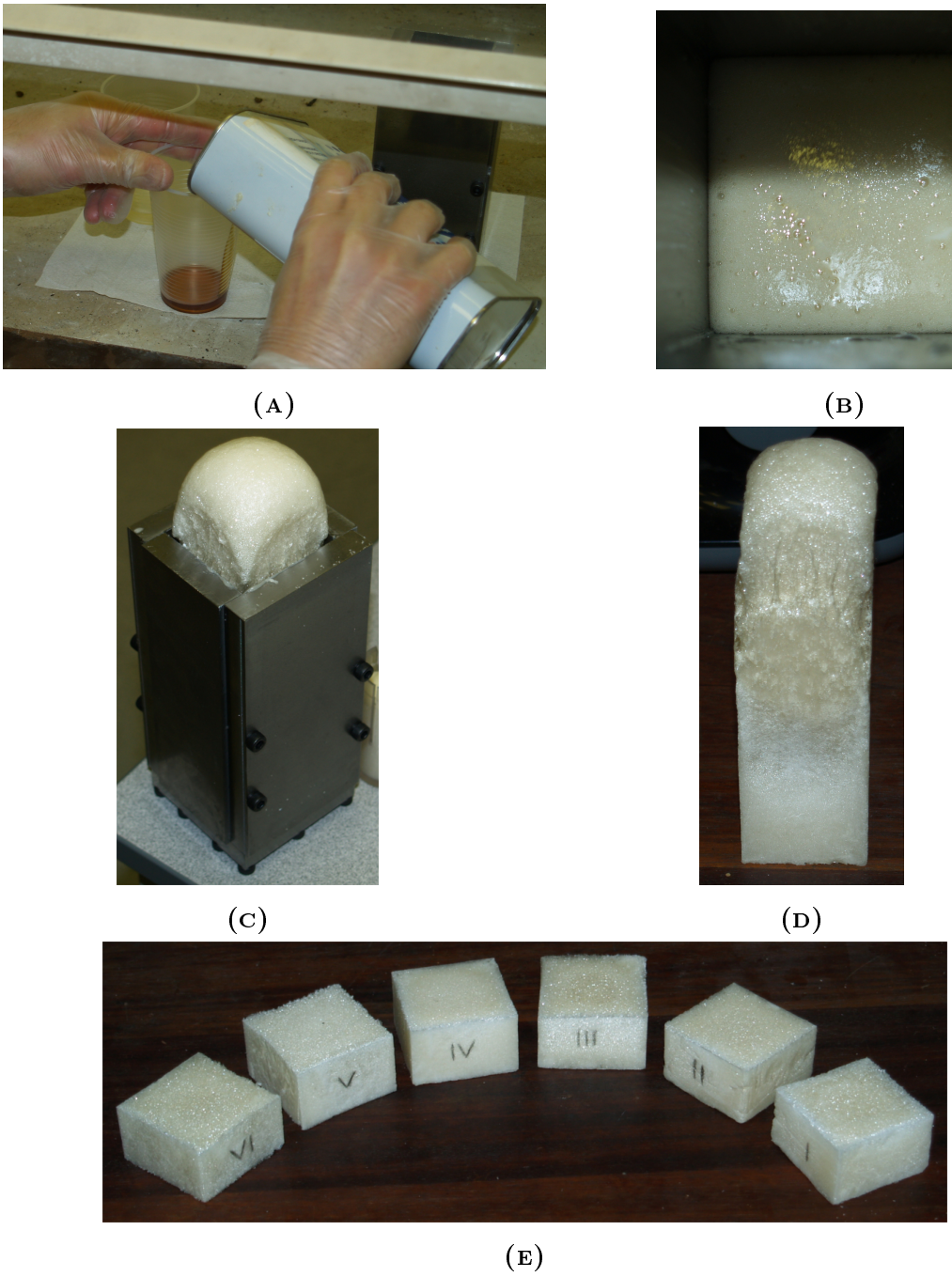

(A) (B) (C) (D) (E)

Figure 5.8: Manufacturing of foam samples: (A) Measurements of foam compounds, (B) Expansion process, (C) Fully expanded foam in the form, (D) Foam block removed from the mould, (E) Foam samples cut to the desired dimensions.

It was decided to test the cuboidal foam sample. The base of the sample was a square with a side of 50 mm, which corresponded to the size of the mould cross section. Before assembly of the mould, each of the internal surfaces was covered with a wax release agent to support the removal process of the sample. The assembled structure was sealed before the foam mixture was prepared. Subsequently, the foam ingredients were mixed at volume ratio of 1:1, as described in the material safety data sheet. 20 ml of Component A and 20 ml of Component B mixed thoroughly before the liquid mixture was poured into the mould. The mixing process and foam rising was performed in the fume cupboard. After the expansion of the foam was completed, the mould was disassembled and the sample was removed. The test coupons were cut to a height of 30 mm. The consecutive steps of the foam samples manufacturing process are shown in Figure 5.8.

5.3.5 Bird manufacturing

As mentioned before, artificial birds are desired in the process of aircraft certification to substitute the real birds used during the tests. However, there are no specifications regarding manufacturing of artificial birds. Therefore, the birds used for the purpose of this thesis were manufactured following the recipe proposed by Lavoie et al. (2009). This recipe was chosen due to the good representation of the real bird, confirmed by Lavoie et al. (2009), as well as, due to the relatively simple manufacturing process. The bird recipe of Lavoie et al. (2009) does not require the use of rotating moulds during the solidification process. This was the case in the procedures used by Wilbeck (1978), who used ballistic gelatine with phenolic micro-balloons for bird manufacturing.

The procedure of Lavoie et al. (2009) fulfils four criteria: the density of the mixture must be approximately $\rho = 950\frac{kg}{m^3}$ (Airoldi and Cacchione, 2006, Wilbeck, 1978); the mixture needs to be liquid in order to be poured to the mould; the texture of the solidified mixture needs to be uniform; and the fully solidified bird needs to be stiff enough to be launched from a gun.

The receipe of Lavoie et al. (2009) was intended for manufacturing of a 1 kg bird. The bird used in this experiment was of a mass of 40 g, therefore, the quantities of the constituents were scaled accordingly and are shown in Table 5.7. However,

Table 5.7: Gelatine bird ingredients.

Ingredient	Quantity
Cold water	85 g
Ballistic gelatine powder	8.0 g
Sodium carboxymethylcellulose	2.0 g
Aluminium acetate basic	0.5 g
Cinnamomum zeylanioum	1 *drop*

it needs too be highlighted that the simple scaling down of the proportions did not result in the correct density of the bird. According to Lavoie et al. (2009), the density of gelatine birds can be controlled by the amount of cinnamomum zeylanioum. This observation was confirmed during the manufacturing process. A single drop of cinnamomum zeylanioum added to the gelatine mixture resulted in a bird of a density above $\rho = 1000\frac{kg}{m^3}$. Two drops, resulted in a bird of density of approximately $\rho = 950\frac{kg}{m^3}$. Three drops added to the gelatine resulted in a bird of density around $\rho = 920\frac{kg}{m^3}$.

It was observed that the amount of cinnamomum zeylanioum controlled the time of gelatine mixture solidification. The shorter the time of initial solidification the more air bubbles, formed during the mixing, were enclosed within the gelatine mixture and the lower the density of the bird.

Therefore, it was decided that all birds should be manufactured with two drops of cinnamomum zeylanioum.

The steps of the bird manufacturing process are described below:

1. Mix the gelatine powder with cold water and leave it for 5 minutes,
2. Heat up the mixture to temperature of $45°C$,
3. While the mixture is heated, mix the aluminum acetate basic and the sodium carboxymethylcellulose,
4. Pour heated gelatine mix into a blender and add two drop of the cinnamomum zeylanioum,

5. Run the blender at the lowest rotational speed for $1-3$ s, in order to minimise bubbles formation,
6. Add premixed aluminum acetate basic and the sodium carboxymethylcellulose, and mix for $3-5$ s,
7. Using a syringe, pour the gelatine mixture into the bird mould,
8. Seal the mould and put it in a refrigerator, at a temperature of $5°C$, for 3 hours,
9. After 3 hours, remove the bird from the mould and wrap it with a cling film,
10. Put the bird back into the refrigerator.

A mould was designed to manufacture birds of 25 mm diameter and up to 88.6 mm length. It consisted of four separate parts, two lids and two middle parts with cylindrical groove. Half of the form with the manufactured bird is shown in Figure 5.9.

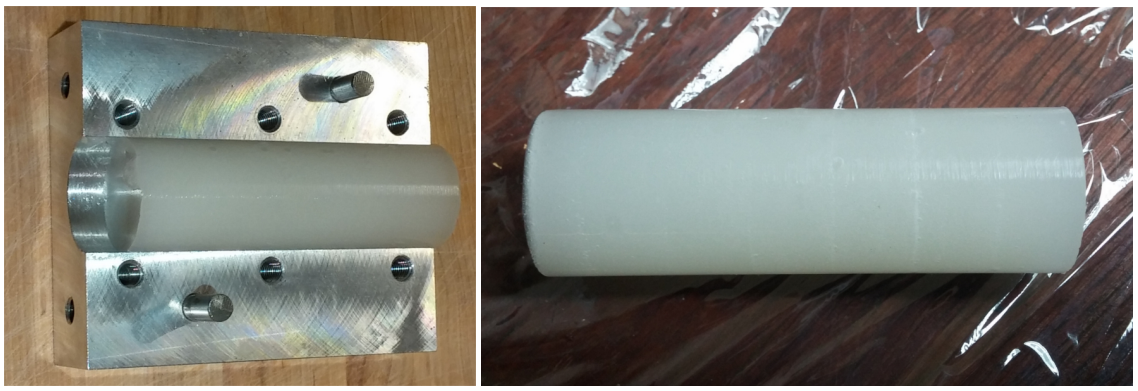

(A) (B)

Figure 5.9: Bird manufacturing: (A) Bird in the form, (B) Solidified bird.

Six straight-ended cylindrical birds were manufactured using the procedure described above. The bird diameter was 25 mm and the length was 75 mm, however, the birds were cut to 50 mm in order to achieve the length to diameter ratio of 2:1 suggested by Budgey (2000). Each of the birds was wrapped in cling film and put into a sabot.

The specifications of the manufactured birds are given in Section 6.2.1.

5.4 Static compression of foam samples

Static foam compression tests were performed in order to investigate the compressive properties of the polyurethane foam used for manufacturing of the corrugated and tubular sandwich samples.

Six foam samples were manufactured and tested according to the ASTM C365/C365M-05 standard. The foam samples were numbered from 1 to 6 as shown in Figure 5.8 E. The sample dimensions were $50\ mm \times 50\ mm \times 30\ mm$. Due to the variable density of the foam specified by manufacturer, it was decided to calculate the average density of the polyurethane foam, based on the density of the foam samples. Therefore, the weight of the samples was measured and the density for each sample was calculated. The average density was $\rho = 60.78 \frac{kg}{m^3}$.

The Instron 1000RD was used for testing. The rig was connected to a data acquisition system delivered by Instron, which recorded the load-displacement characteristics for the head of the compressive platens.

The compression of the samples was conducted at a constant head displacement rate of $\dot{\delta_h} = 0.5\ \frac{mm}{s}$ in accordance with the ASTM standard. The maximum possible compressive load was $F_{max} = 5000\ N$, however, it was decided to perform the test up a the load of $F_{max} = 4700\ N$. The sample and the testing rig are shown in Figure 5.10.

Based on the recorded displacements of the head, the volumetric strains for each foam sample were calculated. The volumetric strain was calculated with Equation 5.1:

$$\gamma = 1 - V \tag{5.1}$$

Where γ is the volumetric strain and V is the relative volume, defined as the ratio of the current volume to the initial volume.

Similarly, the stresses in the foam material were calculated based on the recorded load characteristics. The simple relationship between applied force and cross sectional area of the sample was used for stress calculations. The compressive stress-volumetric strain curves are presented in Figure 5.11 A. Finally, a mean stress-strain

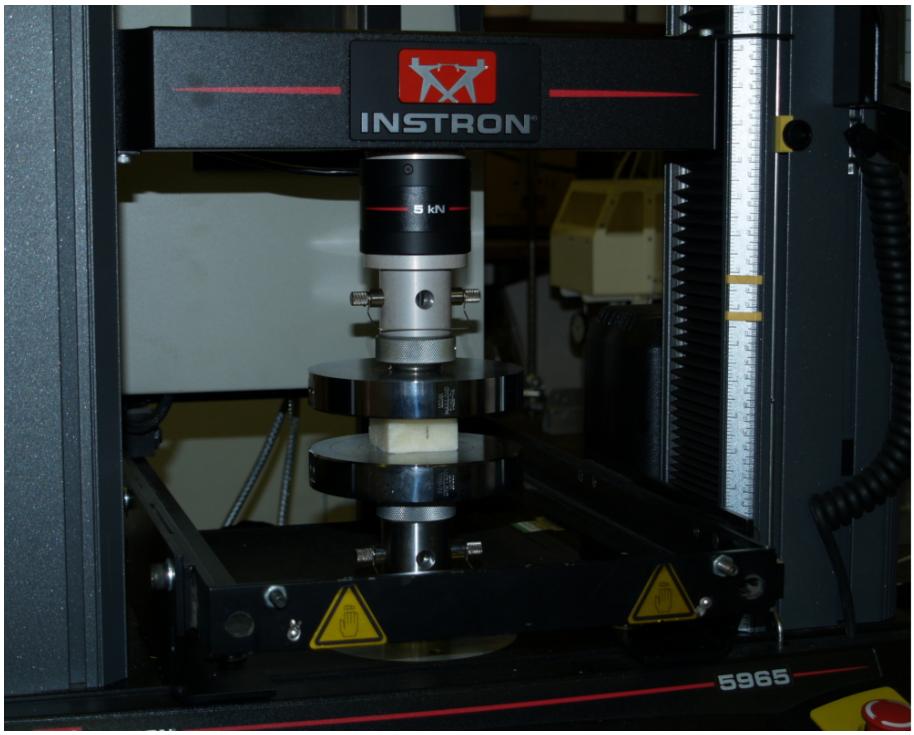

FIGURE 5.10: Foam compression test.

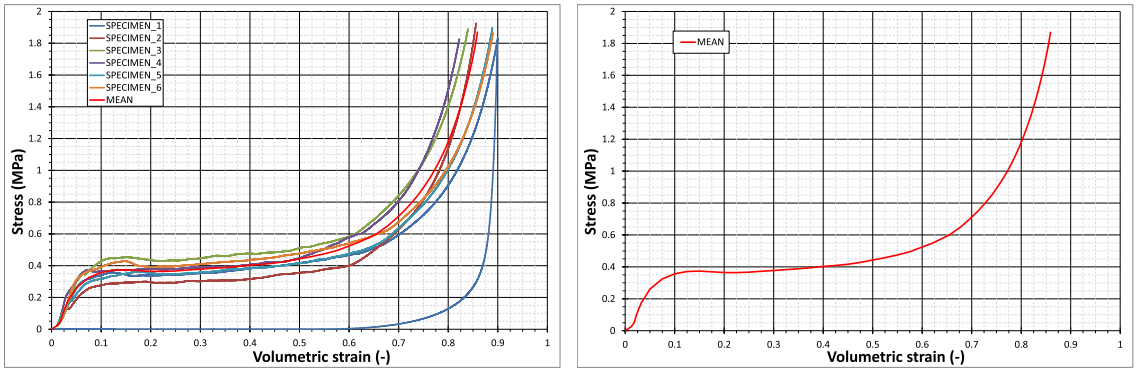

(A) (B)

FIGURE 5.11: Stress strain curves obtained from foam compression tests: (A) Stress strain curves for six samples and average values, (B) Mean stress-strain curve from all compression tests.

curve was obtained combining the results of all six samples and was used as input curve for the numerical analyses (see Figure 5.11 B).

Based on the mean stress-strain curve, the plateau stress was $\sigma_p = 0.39\ MPa$ and the maximum stress for the maximum measured volumetric displacement of $\gamma_{max} = 0.85$ was $\sigma_{max} = 1.9\ MPa$.

The mean stress-volumetric strain relationship together with the density and the value of the plateau stress are the necessary input parameters for all investigated foam material models.

5.5 Gas gun description

5.5.1 Gas gun

A single stage nitrogen gas gun (SSNGG) available in the Crashworthiness, Impact and Structural Mechanics Group (CISMG) at Cranfield University was used to perform the bird impact experiment. It was decided to use the 2 m barrel with the gas gun, which gave a capability to launch projectiles up to 340 $\frac{m}{s}$ at a pressure of 50 bar. The range of impact velocities allows to cover high velocity impacts (bird strike), as well as low velocity impacts (split Hopkinson pressure bar) (Seidl et al., 2013). The gas gun with its components is shown in Figure 5.12.

5.5.2 Velocity measurement system

The velocity measurement system (VMS) for the single stage nitrogen gas gun was designed and developed at the Department of Applied Mechanics at Cranfield University. The velocity measurement was based on the time measurement between two LED light beam sensors (see Figure 5.13 B). The sensors are located along the barrel in a casing mounted at the muzzle of the barrel (see Figure 5.13 A). The distance between the sensors is equal to $l_s = 15.25\ mm$. Each sensor detects the presence of an object and sends a signal to the counter (see Figure 5.13 C) where the time difference is measured.

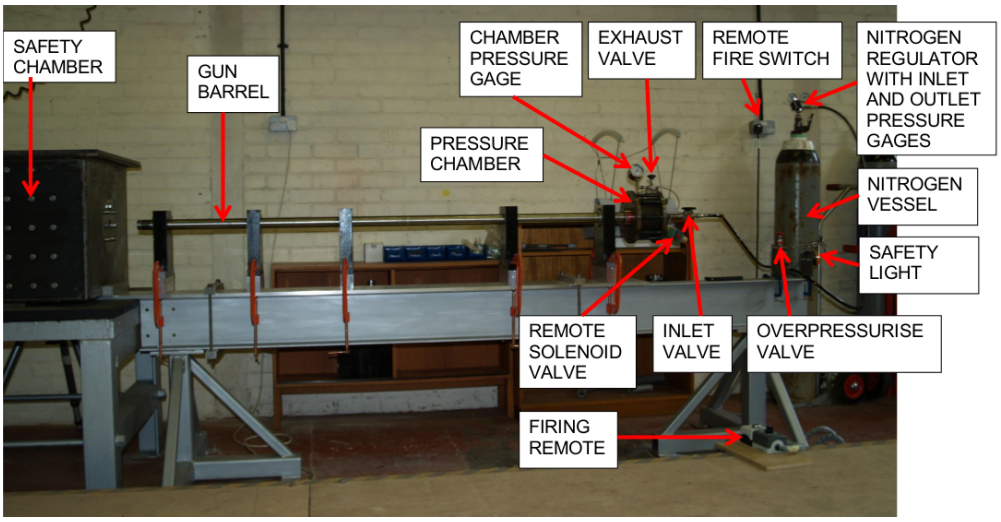

Figure 5.12: Single nitrogen gas gun system, with two meter barrel.

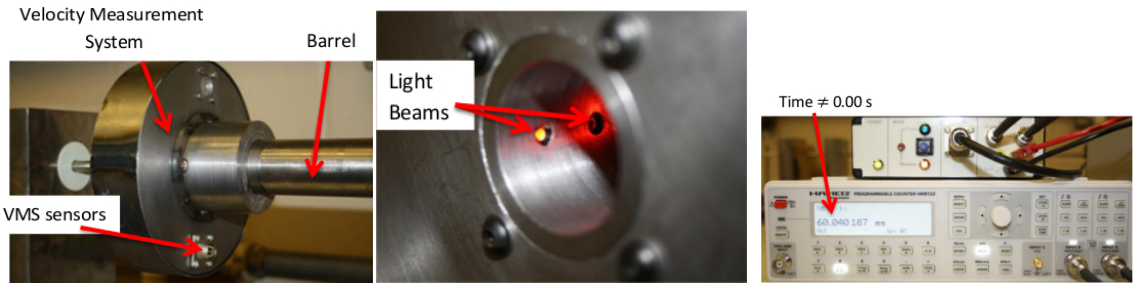

(A) (B) (C)

Figure 5.13: Velocity measurement system: (A) Head of the VMS mounted to the end of the barrel, (B) LED light beam sensors, (C) VMS counter.

After the projectile passes between the two sensors the time is measured and displayed on the counter. Based on the distance and the measured time, the velocity of the projectile can be calculated, under the assumption that there is no acceleration within the casing of the velocity measurement system. The components of the velocity measurement system are shown in Figure 5.13.

5.5.3 Gun calibration

In order to assure the repeatability of the results, a number of acetal projectiles of different mass were launched with the gun, at a range of different pressures, and

their velocity were measured. It was decided to use projectiles with three different masses for the gas gun calibration. Projectiles of 25 g, 50 g and 100 g were chosen, which correspond to the half weight, weight and double weight of the bird with the sabot.

The velocity of the projectiles was measured using two different velocity measurement systems, namely, the velocity measurement system described in the previous section, mounted on the barrel muzzle, and a chronograph, placed in the safety chamber. The chronograph was used to check and confirm the accuracy of the measurements obtained with the main VMS. The error of the measured velocity was 0.1% for the VMS and 0.5% for the chronograph. The highest discrepancy between the measured velocities was $3\frac{m}{s}$.

The results of the calibration shots for a projectile of mass equal to $m_p = 50g$ are shown in Table 5.8. These results were chosen due to the similar masses of the cylindrical projectile and the sabot with a bird.

The velocity measurements presented in Table 5.8 show very close agreement between the shots at the same pressure. For the lowest pressure measured, the average velocity was $V_{av1} = 100\ \frac{m}{s}$, while for the highest pressure the average velocity was $V_{av5} = 260\ \frac{m}{s}$. The discrepancy between the measured velocities at the same pressure increased with increasing pressure. The standard deviation for the lowest pressure measured was $\sigma_1 = 0.391$ and for the highest $\sigma_5 = 1.587$, which indicates that the gas gun can shoot with repeatable velocity for the same pressure values. However, it needs to be highlighted that the pressure is not the only factor influencing the resultant velocity of the projectile. The surface finish of the projectiles has a significant influence on the traction inside the barrel, therefore, to obtain the comparable velocities, the finish of the projectile needs to be of high quality.

In addition, the calibration shots confirmed that the VMS measured the velocities with very good accuracy. The average difference between the velocities measured with the chronograph and the VMS was $\Delta V_{VMS} = 1.93\frac{m}{s}$. The VMS is the preferred measurement system.

Based on the velocity measurements, a quadratic regression curve relating the gun pressure and the projectile velocity was determined and is described with Equation 5.2. The velocity measurements and the regression curve are shown in Figure 5.14.

TABLE 5.8: Velocities measured with VMS and chronograph.

Sample	Mass (g)	Pressure (bar)	VMS time (μs)	VMS velocity (m/s)	Chron. velocity (ft/s)	Chron. velocity (m/s)	VMS mean velocity (m/s)	Chron. Mean velocity (m/s)	VMS velocity Standard deviation	Chron. velocity Standard deviation
1	51	5	151.457	100.689	331	100.889				
2	51	5	151.867	100.417	315	96.012	100.288	98.958	0.391	2.117
3	51	5	152.870	99.758	328	99.974				
4	51	10	111.262	137.064	460	140.208				
5	51	10	110.722	137.732	460	140.208	137.627	140.411	0.423	0.287
6	51	10	110.440	138.084	462	140.818				
7	51	20	81.093	188.056	626	190.805				
8	51	20	80.632	189.131	629	191.719	188.965	191.313	0.684	0.380
9	51	20	80.387	189.707	628	191.414				
10	51	30	68.707	221.957	731	222.809				
11	51	30	68.990	221.047	730	222.504	221.071	222.504	0.713	0.249
12	51	30	69.252	220.210	729	222.199				
13	51	40	58.040	262.750	866	263.957				
14	51	40	58.515	260.617	860	262.128	260.745	262.230	1.587	1.371
15	51	40	58.910	258.869	855	260.604				

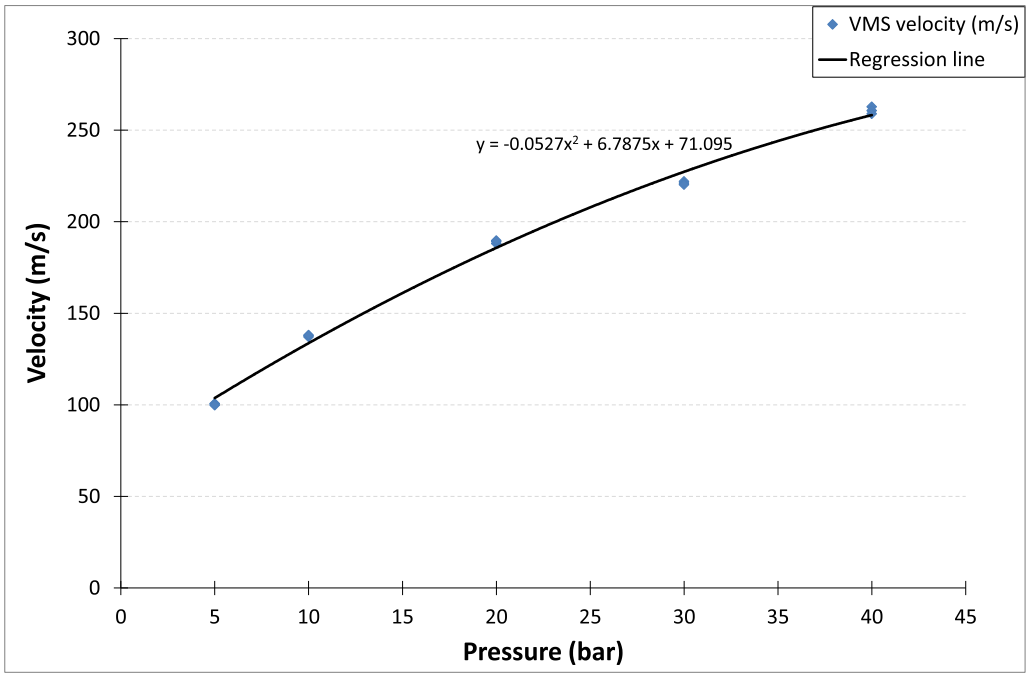

Figure 5.14: Calibration shots velocities for 50 g projectile at different pressures. Regression line based on the velocity measurements.

The regression curve allows for calculation of the velocity of the 50 g projectile for different pressures with reasonable accuracy.

$$V(p) = -0.0527p^2 + 6.7875p + 71.095 \tag{5.2}$$

The regression curve describes the velocity $V(p)$ as a function of the pressure (p) in the gun chamber.

5.5.4 Design of bird release system

The bird impact on the composite panels was performed with a gelatine bird. In order to launch the gelatine bird with the gas gun, it was necessary to design a mechanism to protect and safely release the bird.

The protection of the bird was necessary during the projectile launch. Release of the pressure from the chamber causes rapid change in the pressure in the barrel which leads to explosion of the gelatine when no protection is used. To assure the bird's

integrity and shape conservation after the shot, it was decided to enclose the bird in a plastic sabot.

Solving the problem of the bird integrity during the pressure release phase caused another problem related to the bird release from the sabot and the preservation of the bird shape and integrity at the moment of release. Therefore, it was necessary to design a mechanism, called a sabot splitter, which destroyed the sabot in a certain way and enabled safe release of the bird. The following conditions needed to be fulfilled by the sabot and splitter designs to assure safe release of the bird:

- the sabot material should split progressively and symmetrically on the splitter surface to avoid any misalignment and consequently bird damage
- the bird should not be compressed by the sabot walls after the beginning of the splitting process
- the diameter of the splitter channel should be bigger than the bird diameter
- no debris or parts of the sabot should travel through the sabot splitter channel
- the conical part and the channel entrance of the splitter need to withstand the sabot impact and remain undamaged

Easy opening initiation and progression was the main requirement for the sabot design. Therefore, six symmetrical grooves along the sabot were designed in equal distances along the sabot circumference to trigger the split process and facilitate the symmetrical opening of the sabot. The length of the grooves was 40 mm from the head of the sabot, and the depth was 2.2 mm. The length of the sabot grooves was optimised to reduce the necking of the sabot, which occurred just after the collision between the sabot and the splitter. An additional feature facilitating the opening initiation was the increased diameter of the sabot hole at a distance of 10 mm from the head of the sabot. The draft of the sabot design is shown in Figure 5.15.

Two different materials were considered for the sabot, namely: acetal and polycarbonate. Acetal is a brittle copolymer, which is easy to machine and it offers excellent surface finish (DirectPlastics, 2015, Products, 2003a) - this material was used for manufacturing of the gas gun calibration projectiles. Polycarbonate is a

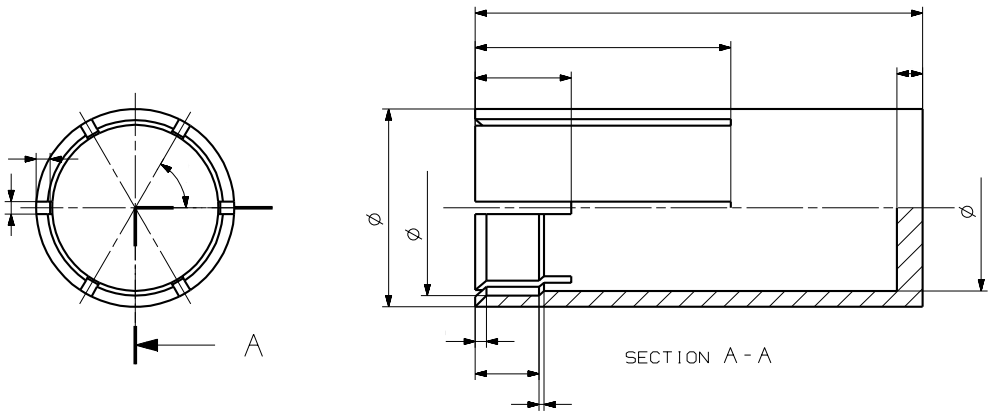

Figure 5.15: Sabot drawing.

thermoplastic polymer which offers very high impact resistance and high modulus of elasticity (GoodFellow, 2008, Products, 2003b). However, polycarbonate does not offer such excellent surface finish as acetal. One of the requirements for safe release of the bird was the ability of the sabot material to fail progressively. Therefore, it was decided to use a polycarbonate due to its higher ductility.

Finally, the new sabot splitter was designed. The splitter needed to be mounted inside the safety chamber, preferably as close to the barrel exit as possible. The easiest way to achieve that, was to enclose the sabot splitter within the casing, mounted at the back of the safety chamber front wall.

The sabot splitter was designed to work for two sabot sizes corresponding to the two gun barrels available in the Department of Applied Mechanics, namely $d_1 = 31\ mm$ and $d_2 = 62\ mm$. Therefore, it was necessary for the splitter to have a modular structure, which allows for the exchange of the splitter parts depending on the size of the barrel.

In order to assure complete opening of the sabot for the bigger barrel, it was necessary to ensure enough space for the opening of the bigger sabot. Therefore, the inner diameter of the casing was given 170 mm. The casing was joined with the sabot splitter base. The base was designed in a way which enabled holding of the splitter for both diameters. Further, only the sabot splitter for the barrel of 31 mm was described as this barrel was used for the bird impact on the composite samples.

The sabot splitter takes part in the initiation and progressive opening of the sabot. The highest loads are acting in the vicinity of the entrance to the splitter channel, as this part is the first to get in contact with the sabot. The sharp edge of the channel entrance and the very high impact loads make the entrance of the sabot extremely vulnerable to damage. The high probability of getting damage was the main reason for designing the modular structure of the splitter. It was decided to design a system with two separate components - the splitter base and the insert, which can be easily replaced in case of damage. The small dimensions and the simple machining process of the splitter insert make it easy and cheap to replace. The splitter insert and the splitter base are shown in Figure 5.16 as parts 1 and 2, respectively.

Another important aspect of the design process was to assure enough clearance between the bird and the channel walls in order to prevent damage of the bird. The diameter of the splitter channel was designed to be 26.5 mm which gives 1.5 mm of clearance. Further enhancement of the clearance between the bird and the splitter channel walls was possible by increasing the diameter of the channel hole by $1 - 2$ mm at a distance of 25 mm from the back of the insert. In addition to the design requirements, it is necessary to highlight the importance of the very precise alignment between the gun barrel and the sabot splitter.

Splitter components were manufactured from Steel EN45. However, it is highly recommended to use hardened steel for manufacturing of the splitter insert to prevent damage of this part. The material properties of Steel EN45 are presented in Table 5.10.

In order to assure correctness of the sabot and sabot splitter designs, the bird release analysis was performed using LS-DYNA. During this analysis the progressive collapse of the polycarbonate sabot and bird integrity were assessed.

The bird was modelled with SPH particles. The elastic-plastic-hydrodynamic material model, with Grunaisen equation of state, was used to model the bird. The sabot was modelled with constant stress solid elements and a plastic-kinematic material model. Strain failure criterion was used to erode the failed elements and reproduce the failure of the material during the impact. The polycarbonate material properties, used in the simulation, are shown in Table 5.9. Hourglass control option 5 was used with solid elements to prevent numerical instabilities. In addition, elements

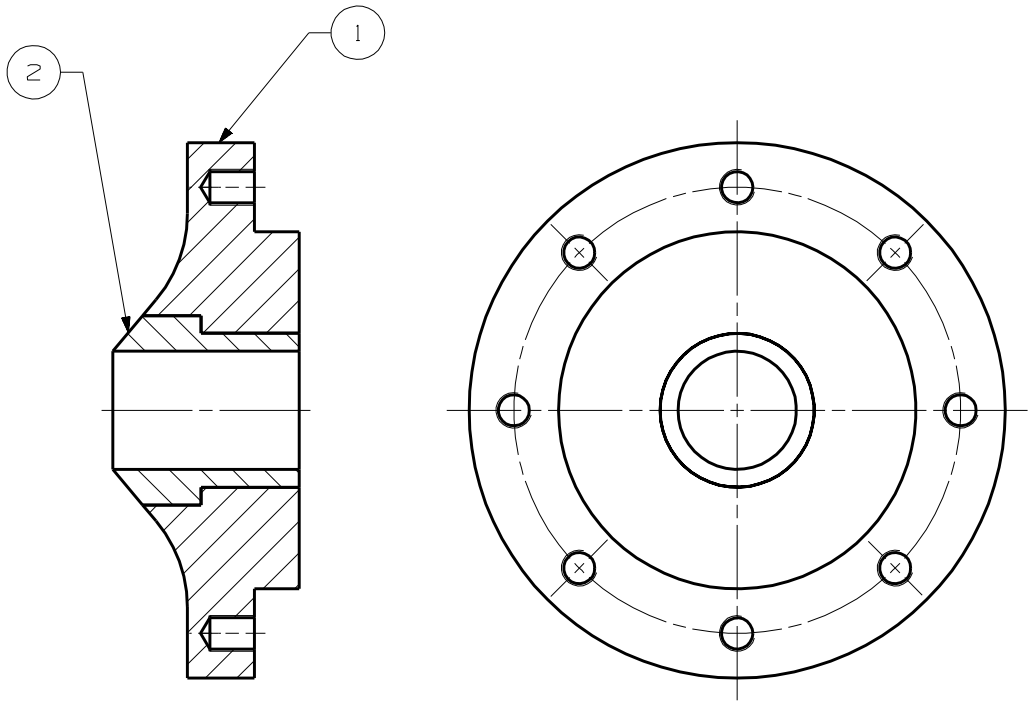

Figure 5.16: Splitter assembly drawing.

with negative volume were eroded from the analysis (PSFAIL in LS-DYNA CONTROL_SOLID option). The sabot and the bird were assigned a velocity of 115 $\frac{m}{s}$, which corresponds to the velocity of the bird impact tests on the composite samples.

The sabot splitter was modelled with solid elements and a plastic-kinematic material model with steel material properties (see Table 5.10). The rear surface of the splitter was fixed in the Z direction and all the rotations were blocked, which corresponded to the constrains in the real experiment. In the analysis, the centre lines of the sabot and sabot splitter were coincident.

The initial configuration of the sabot impact is shown in Figure 5.17 A. Figures 5.17 B-5.17 D show the failure propagation of the sabot material. From the figures it could be seen that the sabot opens progressively along the grooves, forming an opening flower. Moreover, there are no debris flying through the sabot channel. Figure 5.17 D shows the final stage of the sabot opening and the separation of the sabot walls from the bottom.

To investigate the behaviour of the sabot floor, the velocity of the sabot floor centre

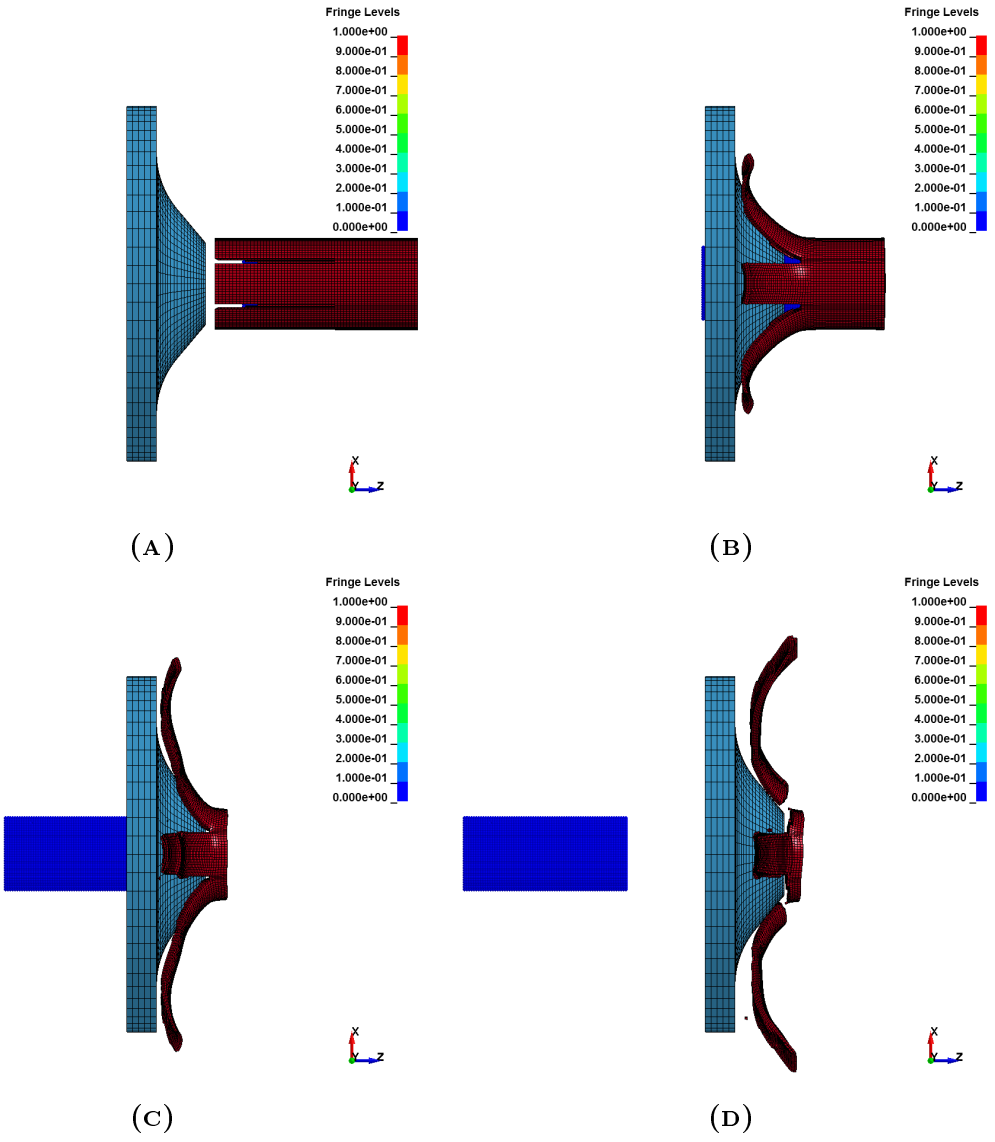

Figure 5.17: Sabot split process: (A) $t = 0\ s$, (B)$t = 0.00035\ s$, (C) $t = 0.0007\ s$, (D) $t = 0.00105\ s$.

Table 5.9: Polycarbonate material properties (Products, 2003b).

Parameter	Value
Density	$1.83 \times 10^3 \ \frac{kg}{m^3}$
Young's modulus	2400 MPa
Poisson's ratio	0.3
Yield stress	70 MPa
Elongation at break	$> 50\%$

Table 5.10: Steel material properties (KVSteel, 2009).

Parameter	Value
Density	$7.85 \times 10^3 \ \frac{kg}{m^3}$
Young's modulus	210000 MPa
Poisson's ratio	0.3
Yield stress	420 MPa
Elongation at break	25%

node was plotted and is shown in Figure 5.18. From the velocity graph it could be seen how the velocity of the sabot floor was changed during the impact event. The sabot collapse can be divided into three stagese. In the very beginning, the velocity is constant when the sabot approaches the splitter. As soon as the splitter and the sabot get in contact, the velocity of the sabot starts to decrease. The initial drop of velocity is caused by the initial contact and the initiation of the sabot walls opening. As soon as the opening begins, the velocity becomes constant (see flat part of the curve between response time $t = 0.0002 - 0.0004$ s). At the response time $t = 0.0004$ s, the opening of the sabot along the grooves is finished and the crack propagation is stopped by the lower part of the sabot, where there are no grooves to simplify the opening. At this stage the velocity drastically drops and the sabot floor slows down until it is stop. At $t = 0.0085$, the sabot floor is completely stopped and it bounces back from the sabot splitter.

In addition to the sabot opening process, the displacement of the bird particles in the XY plane was plotted, to investigate any changes in the bird shape. Figures 5.17 C and 5.17 D show no displacement of the bird, therefore the bird is not expected to be affected during the release process.

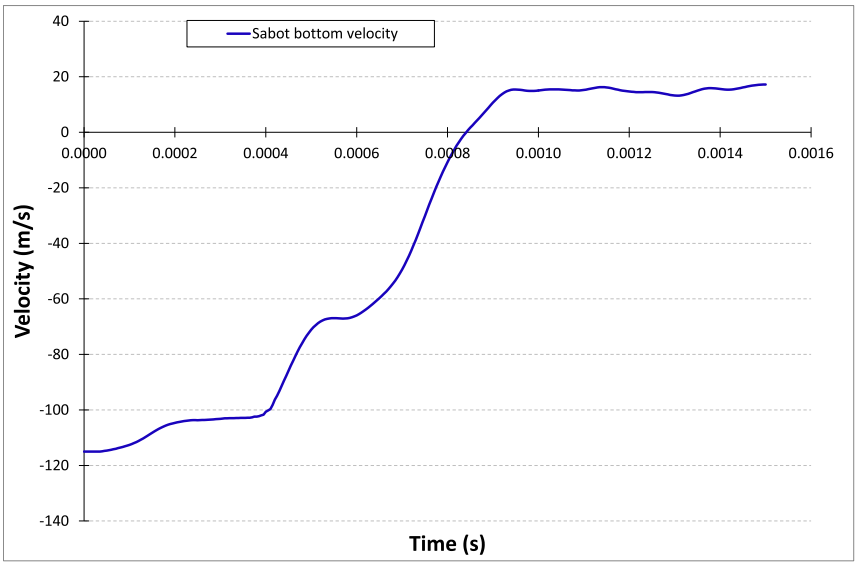

FIGURE 5.18: Time history of the sabot bottom velocity during the impact.

Time history plots (Figure 5.17) and the sabot floor velocity graph (Figure 5.18) confirmed that the sabot floor did not propagate through the channel. Moreover, it was confirmed that there was no damage of the bird. Therefore, all the conditions imposed to the bird release system design were fulfilled.

Finally, after the successful numerical analysis, the sabot design was examined experimentally. However, before the experiment, an additional change in the sabot design was made. Namely, small holes were drilled along the sabot circumference, close to the bottom. This change was done in order to prevent vacuum formation behind the bird at the moment of bird release.

For the experiment, the bird was wrapped in a thin layer of cling film to prevent deformation of the bird. To facilitate the release from the sabot and decrease friction, the external surface of the bird was lubricated with vaseline. The mass of the bird with sabot was $m_{bs} = 46.8g$. The pressure chamber of the gas gun was pumped to $p = 6\ bar$ which resulted in a bird velocity of $V_i = 116.35\frac{m}{s}$. An Olympus high speed camera was used to record the impact event. The settings of the camera are described further in Section 6.2.3.

The bird shape behind the sabot stripper is shown in Figure 5.19 A and the final shape of the sabot after bird release experiment are shown in Figure 5.19 B.

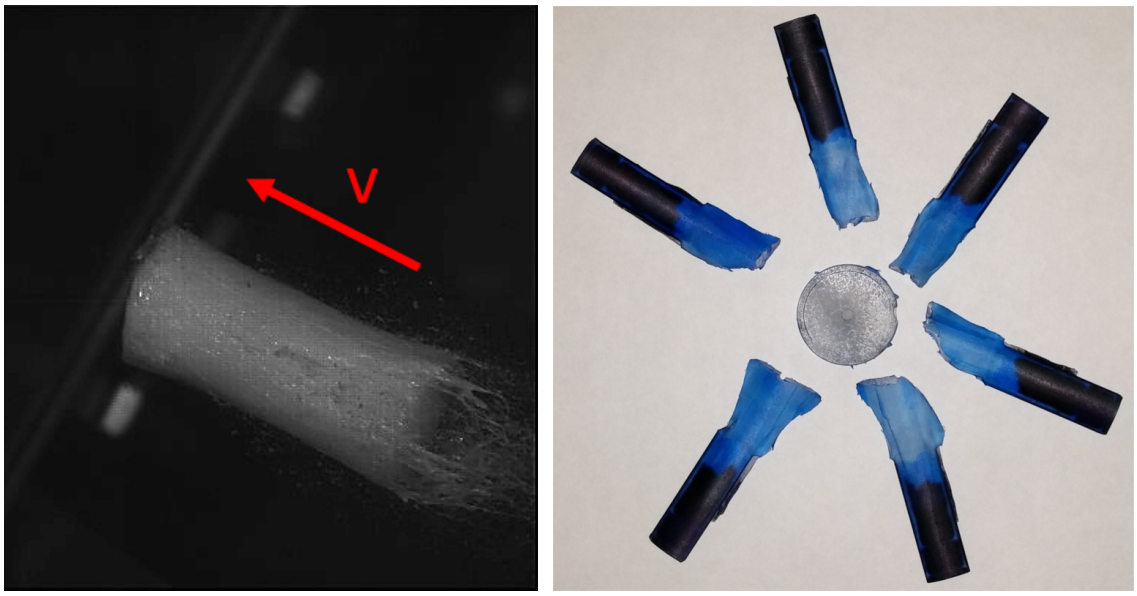

(A) (B)

Figure 5.19: Bird release system investigation: (A) Conservation of bird shape behind the splitter, (B) Final form of the sabot after bird release experiment.

Figure 5.19 A illustrates the shape of the bird behind the sabot splitter. From the figure, no significant change in the bird shape was observed. The bird conserved its initial cylindrical shape. There is a "tail" visible behind the bird. Since the back of the bird is flat, it is believed that the "tail" is the residual of the vaseline used for bird lubrication. Figure 5.19 B illustrates pieces of the sabot gathered after the experiment. The residuals of the sabot indicate that sabot behaved as modelled. The sabot walls opened along the grooves and the floor was separated from the walls. All the pieces of the sabot stayed within the sabot splitter casing as no debris were visible in the video from the high speed camera.

Figures 5.19 A and Figure 5.19 B prove the correctness of the bird release system design. All the requirements imposed to the bird release system were met and the system was ready to be used for the tests on the composite samples.

5.6 Thermography inspection of composite samples

The last stage of the experiment preparation was the thermography inspection on the quality of the manufactured composite samples. The inspection enabled for a comparison between the initial and post impacted state of the composite samples.

Two different methods of Non-Destructive Inspection (NDI) were considered to investigate the novel sandwich samples, namely, C-scanning and thermal imaging.

First considered method was a phased array C-scanning, which is based on the utilisation of high frequency sound waves to examine the internal structure of the samples. This method was not appropriate to examine foam filled samples due to the presence of cavities within the foam material. The waves bundle emitted by the probe of the phased array C-scanner was not able to propagate through the foam. The foam layer was treated as a free surface, and the waves reflected from the back surface of the composite face sheet.

The second considered technique was a thermal wave imaging, also known as thermography. This non-destructive technique is based on thermal analysis of the preheated samples. Inspection of the novel composite sandwich panels was possible using thermography, however, the complex structure of the samples enabled only for single sided images of the samples. Therefore, all the samples were scanned from both sides to assess the entire structure.

The basics of the thermal imaging together with the inspection of the novel composite panels are described further in this section.

5.6.1 Introduction to infrared thermography

Infrared thermography is a non-destructive inspection technique, which employs infrared and thermal measurements to determine the structure quality. This technique allows for identification of thermo-physical properties of the structure, detection of initial subsurface defects or damage formed during the life cycle of the machine components (Avdelidis et al., 2004, Maldague, 2000), as well as, identification of material loss due to corrosion (Shepard, 1997). Moreover, this technique is not only relevant

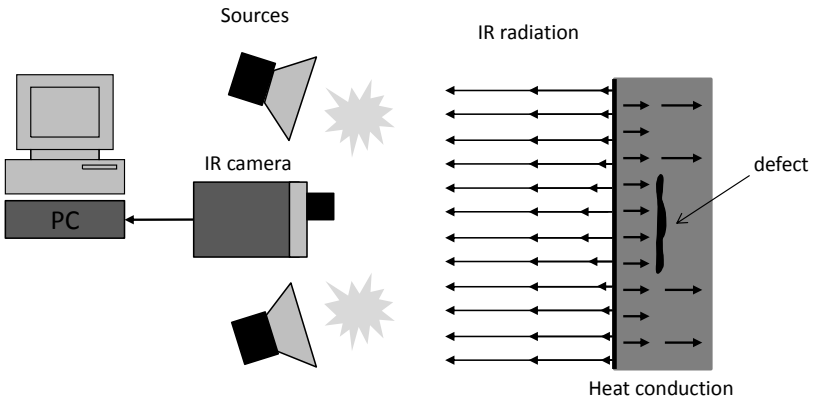

Figure 5.20: Schematic picture of infra-red thermography.

to detect the damage after impact, but also to monitor the dynamic response of the structure during the impact event (Meola and Carlomagno, 2010).

There are two different infrared thermography approaches, namely, passive (Avdelidis and Moropoulou, 2004) and active approach (Shepard, 1997). The passive approach is commonly used for inspecting structures and buildings in civil engineering. In the passive approach, structures with different thermal characteristics than ambient are inspected. The inspection is based on the comparison of the thermal contrast of the structure and the surroundings. In the active thermography approach, the thermal contrast is induced by an external thermal source (Avdelidis et al., 2004), e.g. strong light. Two different methods are recognised within the active thermography approach, namely, pulsed thermography (PT) and pulsed-phase thermography (PPT).

Since pulsed thermography was used for the inspection of the sandwich composite samples, only this technique is described in this section.

In the PT technique, the surface of the sample is heated with a brief (usually few millise-conds) uniform light pulse, which can be generated with a flash lamp array (Shepard, 2007) or other source of heat. The thermal response of the sample is recorded with an infrared camera connected to the data acquisition system. The schematic outline of the pulsed thermography technique is shown in Figure 5.20.

The infrared camera captures the thermal contrast of the sample heated with the flash lamp array. The acquisition of data from the camera usually starts before

the sample is heated and continues for a few seconds after the flash. For a perfect sample, i.e. manufactered from homogeneous material, the heat propagates into the sample, starting from its surface, at a constant rate. The rate of heat propagation is determined by the thermal diffusivity of the sample material. Any discontinuity in the material changes the heat diffusion rate which disrupts the heat flow within the structure. A change in the cooling rate is visible in the thermal characteristics measured for defect and uniform material (Shepard, 1997). Besides a thermal characteristics graph, the data acquisition system captures a stack of infrared images from different depths of the sample. Inspection of the infrared images enables for detection and measurements of defects. Current thermography systems are equipped with the newest infrared cameras, which allows for data acquisition quicker than every 15 ms. High data acquisition rate is especially important for materials with high heat propagation rate, where return to the equilibrium state (state before heating up) takes only few hundred milliseconds.

5.6.2 Characterisation of the inspection system and inspection settings

ThermoScope II is an active thermography system used for the thermal inspection of the novel sandwich samples. The components of the ThermoScope system are shown in Figure 5.21. The system consist of an infrared camera enclosed in a portable casing together with the flash lamps (the box on the right hand side). The flash lamps provide pulse light energy of approximately 25 kJ within a fraction of a second to heat up the sample. The box on the far left is the power supply for the flash lamps, which generates high voltage of 15 kV. Computer used for the control and processing of the thermal images is located in the middle of the figure. The performance assessment of the ThermoScope system was described by Widjanarko et al. (2012).

A long wave length infrared camera XENICS GOBI 384 was used for recording of thermal images from the thermography inspection. This camera enables for capturing images with resolution of 384×512 $pixels$. The sensitivity of the camera was 50 mK.

The inspection was performed at 61% humidity and ambient temperature of $T = 25.8°C$. The settings used for thermography analysis are shown in Figure 5.22.

FIGURE 5.21: Components of thermography system ThermoScope II (Widjanarko et al., 2012).

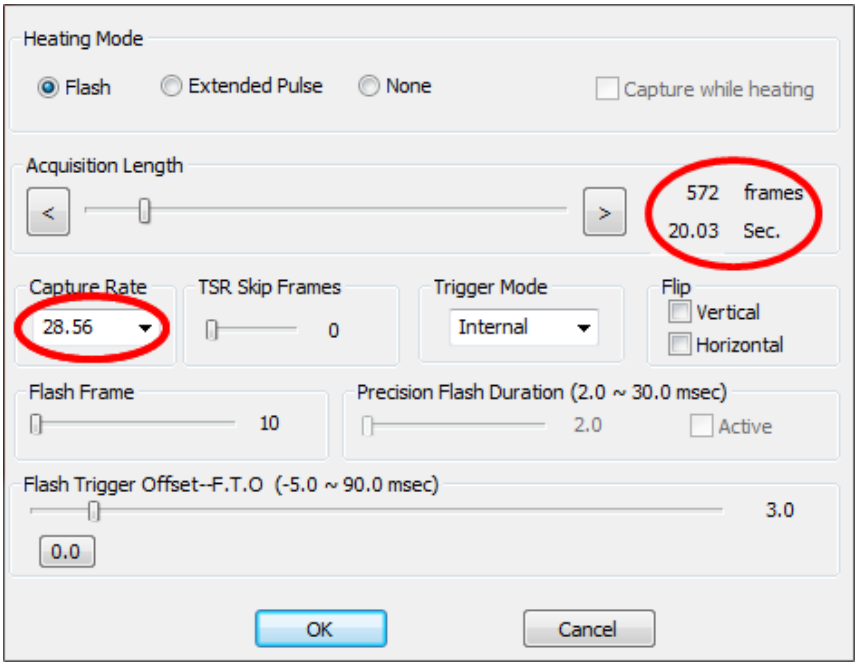

FIGURE 5.22: Thermal inspection settings.

The acquisition time was set to $t = 20\ s$ and the acquisition rate was set to 28.56 frames per second. This corresponds to an acquisition length equal to 572 frames. The same settings were used for each side of the samples. A thermographic signal reconstruction system, MOSAIQ, was used to post process the raw thermography data acquired during the analysis.

The results of the inspection are presented and described in the following sections of this chapter.

5.6.3 Corrugated sandwich panels thermal inspection

Three corrugated samples were scanned using infrared thermography. Each of the samples was numbered and its sides (top and bottom) were labelled accordingly. Labelling of the sample helped in identification of the same side for the inspection after impact. Moreover, it enabled direct comparison of the inspection analyses results.

All samples were scanned from both sides. Due to the complex design, the heat could not propagate from the top surface to the bottom surface. The images of both inspected sides are shown together in order to simplify the visualisation and discussion of the results. For each sample, infrared images are presented together with the corresponding intensity graphs. The intensity graphs illustrate the heat characteristics, read at the locations of the placed markers, which were chosen to show in the best way the differences in heat propagation within the materials and their existing defects. Based on the results of the thermography analysis, a decision was made on which side the samples would be impacted to ensure the best quality of the impacted composite and repeatability of the results.

5.6.3.1 Corrugated sandwich panel CSP_1

Figure 5.23 shows the infrared images of CSP_1. Two sets of images were taken for the bottom and top face of the sample. For each of the images, three markers (red, blue and purple) were placed on the top of the corrugated panel wave, where the composite prepreg sheet is bonded to the corrugated panel, and additional two were located on the bonding between the prepreg sheet and the foam. Figure 5.23 A

shows the bonding surface between the top face sheet and the corrugated panel and foam, further referred to as *separation* or *separation point*. The top face separation is well visible in the thermal characteristics graph shown in Figure 5.24 A, indicated as the first vertical dashed line. The colours of the curves in the graph correspond to the colours of the markers. The separation occurred at time $t = 0.77\ s$ of the inspection, which corresponds to the 22^{nd} plot frame. Red colour in the image depicts the location of the carbon fibres, yellow/orange represents the foam and black represents the adhesive bond or resin/adhesive rich layers.

The separation image (see Figure 5.23 A) shows that the corrugated waves were not perfectly symmetrical. It can be seen that the two top waves were of equal height (two red stripes) and the bottom wave was shorter, so that there was more adhesive required to bond the faces together (black stripe on the bottom). Moreover, the adhesive bond in the case of the lowest wave was not spread uniformly. The black colour vanishes on the left side of the sample and the adhesive bond area is smaller than the ones on the middle and right side of the sample. In addition, there is some adhesive blob visible on the line representing the lowest wave. No air bubbles or other initial defects are visible from the image of the separation points.

The second image of the top side, taken at time $t = 7\ s$ (200^{th} frame), is shown in Figure 5.23 B. The inspection time corresponds to the second vertical dashed line of the thermal characteristics graph, shown in Figure 5.24 A. The image was taken at a location corresponding to the cross-section close to the middle plane across the sample thickness. At this point, the foam and the corrugated panel are completely separated from the face sheet. From the infrared image and the corresponding thermal characteristics graph it is evident that the material was free of any initial defects. However, some imperfections in the form of uneven distribution of the adhesive were present within the internal structure of CSP_1.

Figure 5.23 C shows the separation of the bottom face sheet of CSP_1. The top edge of the sample is not visible due to the limitations of the inspection equipment. Three markers (red, blue and purple) were placed on the top of the corrugated panel wave and additional two (green and cyan) were located on the bonding between the face sheet and the foam. The separation occurred at time $t = 0.735\ s$ of the inspection, which corresponds to the 21^{st} plot frame. The separation point image confirms that the corrugated panel is not perfectly symmetric. Two top red stripes depict the

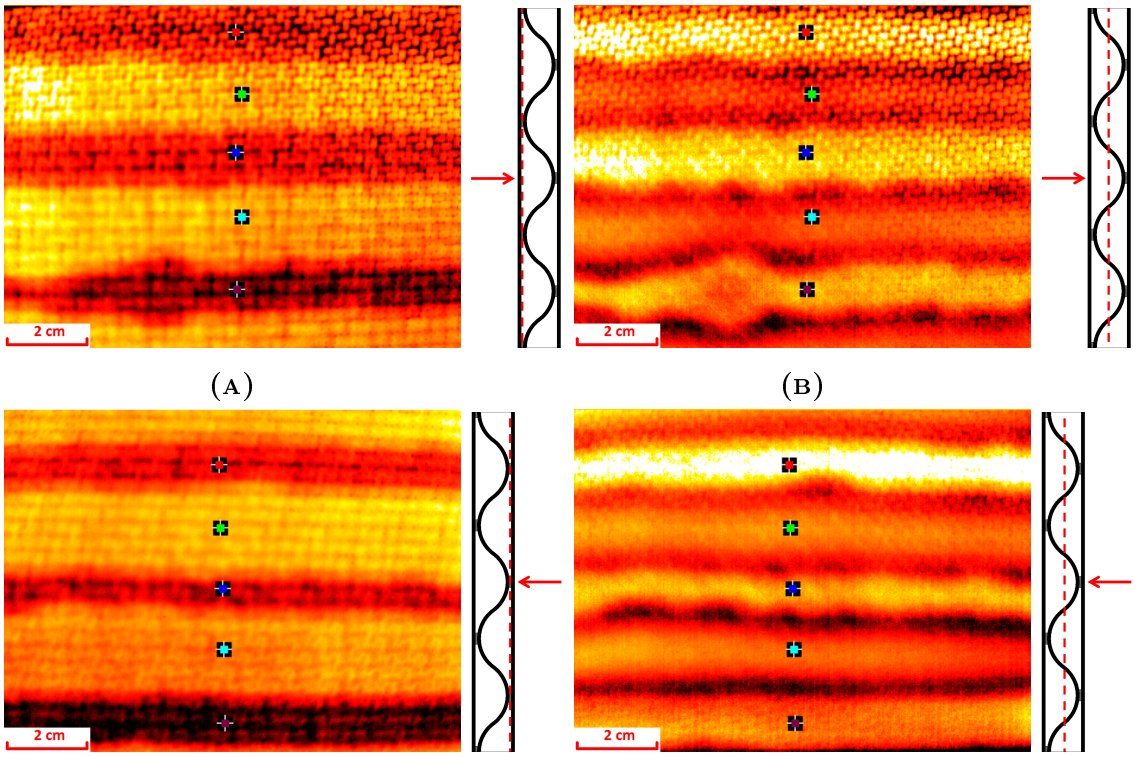

(A) (B)

(C) (D)

FIGURE 5.23: Infrared images of CSP_1, with markers location: (A) Top surface $t = 0.77\ s$, (B) Top surface $t = 7\ s$, (C) Bottom surface $t = 0.735\ s$, (D) Bottom surface $t = 7\ s$.

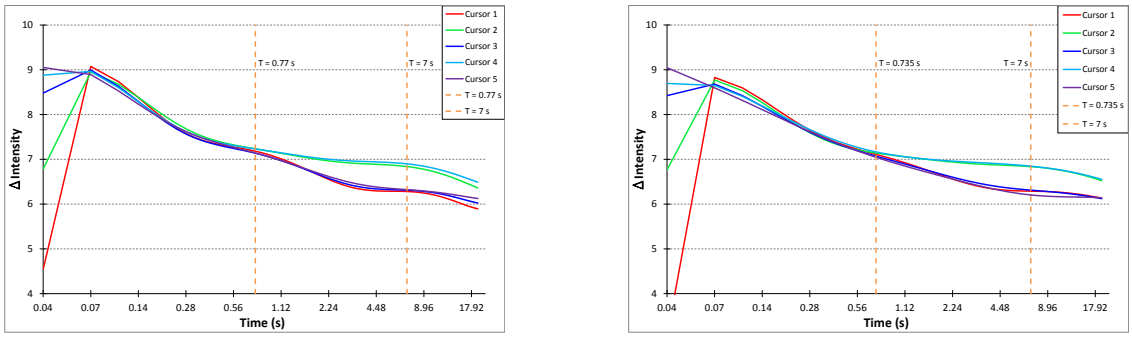

(A) (B)

FIGURE 5.24: Thermal characteristics of CSP_1: (A) top surface, (B) bottom surface.

edge of the wave of the corrugated panel and the black stripe in the bottom of the image illustrates the adhesive rich layer. All the stripes are of different width, which shows that the top parts of the waves are at different locations across the thickness of the sample. The separation point is also shown in the thermal characteristics graph in Figure 5.24 B as the first vertical dashed line. The thermal characteristics graph shows that except the imperfections related to the non-uniform distribution of adhesive and unevenness of the corrugated panel, there was no initial defects within the sample.

Figure 5.23 D shows the vicinity of the middle plane of CSP_1. The complete separation of the thermal characteristics is shown in Figure 5.24 B as the second vertical dashed line. The infrared image and the corresponding thermal characteristics graph prove that no defects were present within the internal structure of the sample.

To summarise the above findings, the first corrugated sample was of good quality, with clearly visible borders between the core material and the reinforcement. There were no voids or initial defects present within the sample. However, some imperfections were identified, e.g. uneven distribution of the adhesive, unsymmetrical corrugated panel.

Based on the thermography inspection of CSP_1, the bottom face of the panel was chosen for the bird impact.

5.6.3.2 Corrugated sandwich panel CSP_2

Figure 5.25 A shows the separation of the CSP_2 top face sheet. The separation occurred at time $t = 0.7\ s$ of the inspection which corresponds to the 20^{th} plot frame (first dashed line in Figure 5.26 A). The infrared image shows that the corrugated panel was uneven. The two top red stripes represents the transition between the adhesive and the corrugated panel, and the black stripe visible in the bottom of the image depicts the adhesive layer. Despite the imperfections, no defects were detected within the structure.

Figure 5.25 B shows the middle plane of CSP_2. It is also visible in the thermal characteristics graph, shown in Figure 5.26 A, as the second vertical dashed line. The infrared image shows adhesive blobs in the vicinity of the blue marker, which

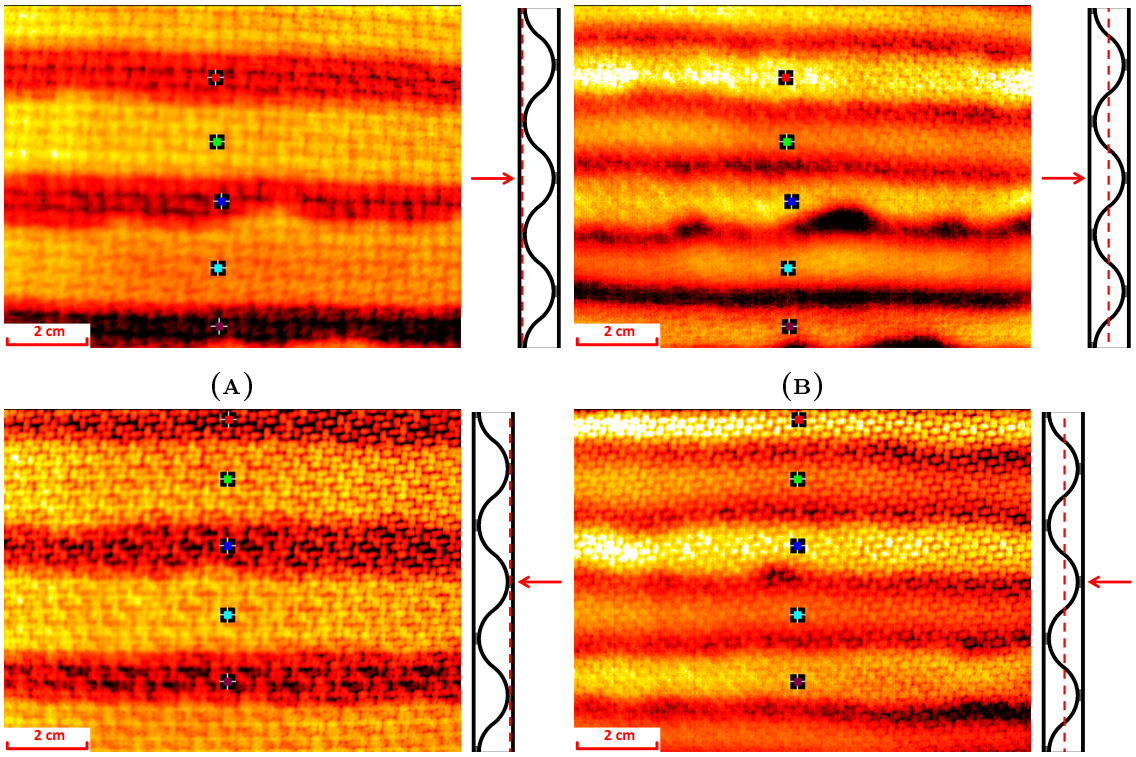

(A) (B)

(C) (D)

FIGURE 5.25: Infrared images of CSP_2, with markers location: (A) Top surface $t = 0.7\ s$, (B) Top surface $t = 7\ s$, (C) Bottom surface $t = 0.7\ s$, (D) Bottom surface $t = 7\ s$.

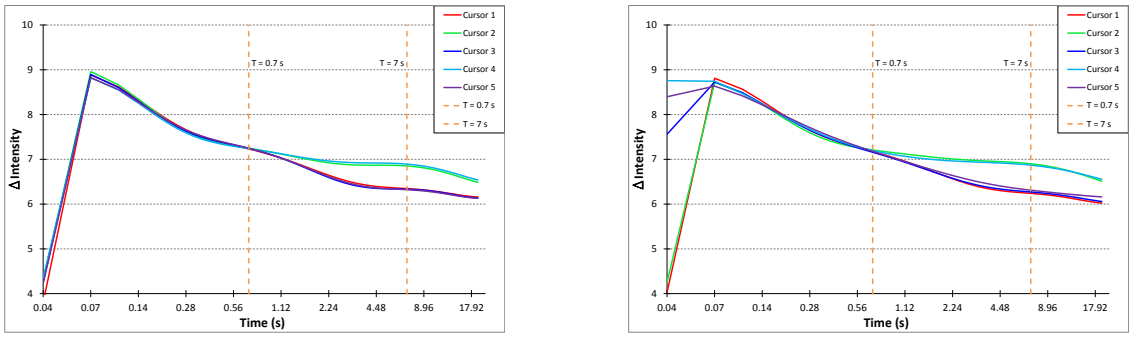

(A) (B)

FIGURE 5.26: Thermal characteristics of CSP_2: (A) top surface, (B) bottom surface.

resulted from uneven distribution of adhesive and uneven height of the corrugated waves. The thermal characteristics for the corresponding markers coincide together which indicates that no defects exists at the locations of the markers. Therefore, despite uneven distribution of the adhesive and inequality of the corrugated panel, the sample internal structure was free from initial defects.

Figure 5.25 C shows the separation of the bottom face sheet of CSP_2. The even distribution and thickness of the red/black stripes indicates uniform bond between the face sheet and the corrugated panel. This also proves that the corrugated waves on the bottom side were even. From the thermal characteristics shown in Figure 5.26 B, it can be seen that there was no initial defects at the locations of the markers.

The image of the middle plane of the CSP_2 bottom side is shown in Figure 5.25 D. The state captured is shown as the second vertical dashed line in Figure 5.26 B. The red/black stripes corresponding to the fibre reinforcement are evenly distributed, which indicates that the corrugated waves were even. Figure 5.26 B shows that the thermal characteristics measured at the locations of the markers are coincident for the corresponding materials. This indicates that there was no subsurface defects within the internal structure of CSP_2.

The quality of CSP_2 and CSP_1 was similar, with clearly visible borders between the corrugated panel and the foam core. Despite some imperfections, such as uneven distribution of the adhesive and not symmetric corrugated reinforcement, the structure of the sample was uniform and free from initial defects.

Based on the thermography inspection of CSP_2, the bottom face of the panel was chosen for the bird impact.

5.6.3.3 Corrugated sandwich panel CSP_3

The separation of the CPS_3 top side is shown in Figure 5.27 A. It is evident that the corrugated panel was not even in terms of wave height. Moreover, the uneven distribution of the adhesive is clearly visible in the image. The separation point is also indicated as the first vertical dashed line in the corresponding thermal characteristic graph, shown in Figure 5.28 A. Before the separation point all the thermal characteristics curves remain coincident until the separation point is reached. At

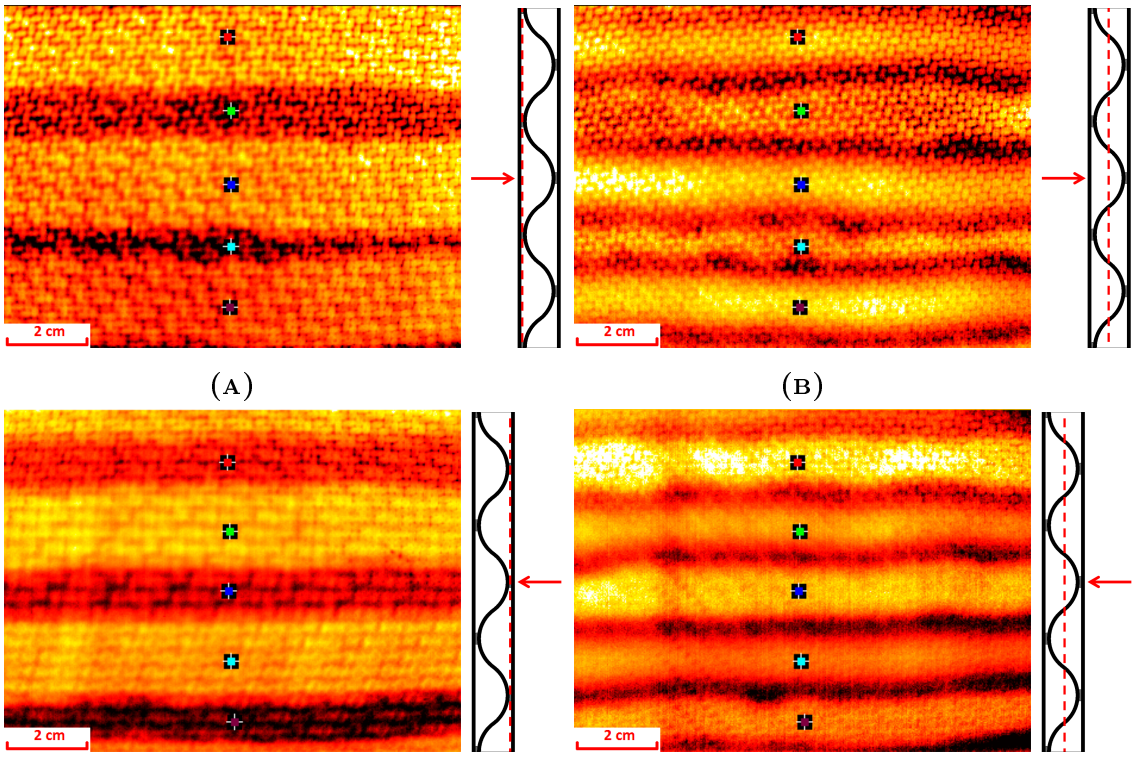

(A) (B)

(C) (D)

FIGURE 5.27: Infrared images of CSP_3, with markers location: (A) Top surface $t = 0.7\ s$, (B) Top surface $t = 7\ s$, (C) Bottom surface $t = 0.7\ s$, (D) $t = 7\ s$.

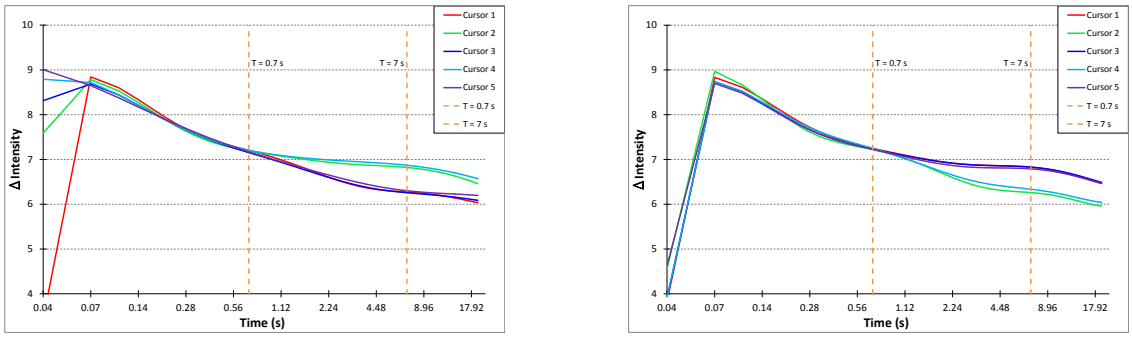

(A) (B)

FIGURE 5.28: Thermal characteristics of CSP_3: (A) top surface, (B) bottom surface.

the separation point, the bottom surface of the face sheet is reached and the green and cyan curves (corresponding to green and cyan markers located on the foam) split from the curves bunch due to the different heat propagation of the foam and the carbon fibres. From the infrared image and the thermal characteristics graph it can be seen that the sample did not have any initial defects underneath the top face sheet.

The middle plane image of the top face of CSP_3 is shown in Figure 5.27 B. The infrared image confirms differences in the corrugated pattern - the red lines showing the carbon fibre reinforcement have an uneven spatial distribution. The state captured in the infrared image corresponds to the second vertical dashed line in Figure 5.28 A, where the thermal characteristics are presented. Both figures show that no internal delaminations or other defects were present within the sample.

Figure 5.27 C shows the separation point of the CSP_3 bottom side. It indicates inequality of the corrugated waves distribution, which is reflected in the different intensity levels of the red stripes. The black stripe represents the adhesive rich layer and indicates that this corrugated wave was the lowest. Despite the inequality of the corrugated waves, the bond between the corrugated panel and the face sheet did not have any visible defects. The stripes are straight and their thicknesses are comparable.

Figure 5.27 D shows the infrared image of the middle plane of CPS_3. It is evident that the distribution of the adhesive was not uniform. No initial defects can be seen in the image, which was confirmed with the thermal characteristics graph, shown in Figure 5.28 B.

The thermographic inspection of CPS_3 showed that the quality of the sample was very similar to the quality of the remaining corrugated panels. Despite small imperfections, e.g. uneven distribution of the adhesive, the sample interior was free from initial defects.

Based on the thermography inspection of CSP_3, the bottom face of the panel was chosen for the bird impact.

5.6.4 Tubular sandwich panels thermal inspection

The internal structure of three tubular sandwich samples was assessed based on the thermographic inspection. Each of the samples was numbered and its sides (top and bottom) were labelled accordingly. Labelling of the sample helped in identification of the same side for the inspection after impact. Moreover, it enabled direct comparison of the inspection analyses results.

All samples were scanned from both sides. Due to the complex design, the heat could not propagate from the top surface to the bottom surface. The images of both inspected sides are shown together in order to simplify the visualisation and discussion of the results. For each sample, infrared images are presented together with the corresponding intensity graphs. The intensity graphs illustrate the heat characteristics, read at the locations of the placed markers, which were chosen to show in the best way the differences in heat propagation within the materials and their existing defects. Based on the results of the thermography analysis, a decision was made on which side the samples would be impacted to ensure the best quality of the impacted composite and repeatability of the results.

Infrared images of the tubular samples show the separation point of the top and bottom face sheets and the middle plane of the sample. For the tubular samples, separation occurs at the bond between the composite tubes and the foam filling the composite tubes. In the case of the tubular panels, the separation point is not clearly visible. The difficulties in the detection of separation are related to the manner in which the samples were manufactured. The carbon tubes were bonded to the face sheets with strong polyurethane adhesive. Its thermal characteristic after full cure is very close to the characteristic of the carbon fibre laminate. Moreover, in the tubular panel, the adhesive fills much bigger volume in comparison to the corrugated samples. Hence, the distinction between the materials is more difficult.

5.6.4.1 Tubular sandwich panel TSP_1

The separation of the top side of TSP_1 is shown in Figure 5.29 A. The image was taken at time $t = 0.841\ s$, which corresponds to the 24^{th} plot frame. The separation is also shown in the thermal characteristic plots (see Figure 5.30 A) as

the first vertical dashed line. Four markers were located on the composite panel - two at the locations of the composite tubes (red and green), one on the void (blue) and one on the adhesive rich layer (cyan).

Due to the very similar thermal characteristics of the carbon fibre and the Permabond adhesive, it was quite difficult to distinguish these two components in the infrared image shown in Figure 5.29 A. However, the white spots visible in the images are clearly showing the voids within the adhesive. Based on this observation, it can be noticed that the adhesive layers are represented by dark orange/yellow colours and the composite tubes as the red stripes. The black regions visible in the infrared image correspond to the adhesive rich bond between the composite tube and the top face sheet. This adhesive rich layer is also visible in the thermal characteristics plot as cyan curve (see Figure 5.30 A). As it can be seen from the graph, the thermal characteristic of the adhesive rich layer separates slightly from the remaining curves. From the graph it also can be seen that the void surrounding the blue marker does not influence the thermal characteristic - the blue curve is coincident with the remaining curves. Based on this observation it was concluded that the void had a small volume and did not propagate deeply into the adhesive. Nevertheless, each void is an existing imperfection arisen during the manufacturing process and could influence the impact resistance of the sample.

The image corresponding to the middle plane of TSP_1 is shown in Figure 5.29 B. The red and yellow stripes represent the carbon fibre tubes and the foam respectively. The black spots represent the adhesive rich bond between the tubes. From the infrared image it can be seen that the tubes and the foam are distributed evenly across the sample width. Moreover, there are no voids or air bubbles within the foam material. The darker orange stripe representing the foam material can be related to the coupling induced by the adhesive rich layer shown in the bottom of Figure 5.29 A.

Separation point of the TSP_1 bottom side is shown in Figure 5.29 C. The infrared image was taken at time $t = 0.87\ s$ (25^{th} plot frame). Four markers were located on the sample in order to measure the thermal characteristics from the desired points - two markers were located on the adhesive layer (green and blue) and two markers on the top of the composite tubes (green and cyan). The location of the blue marker was chosen to measure the thermal characteristics of the void in the adhesive and

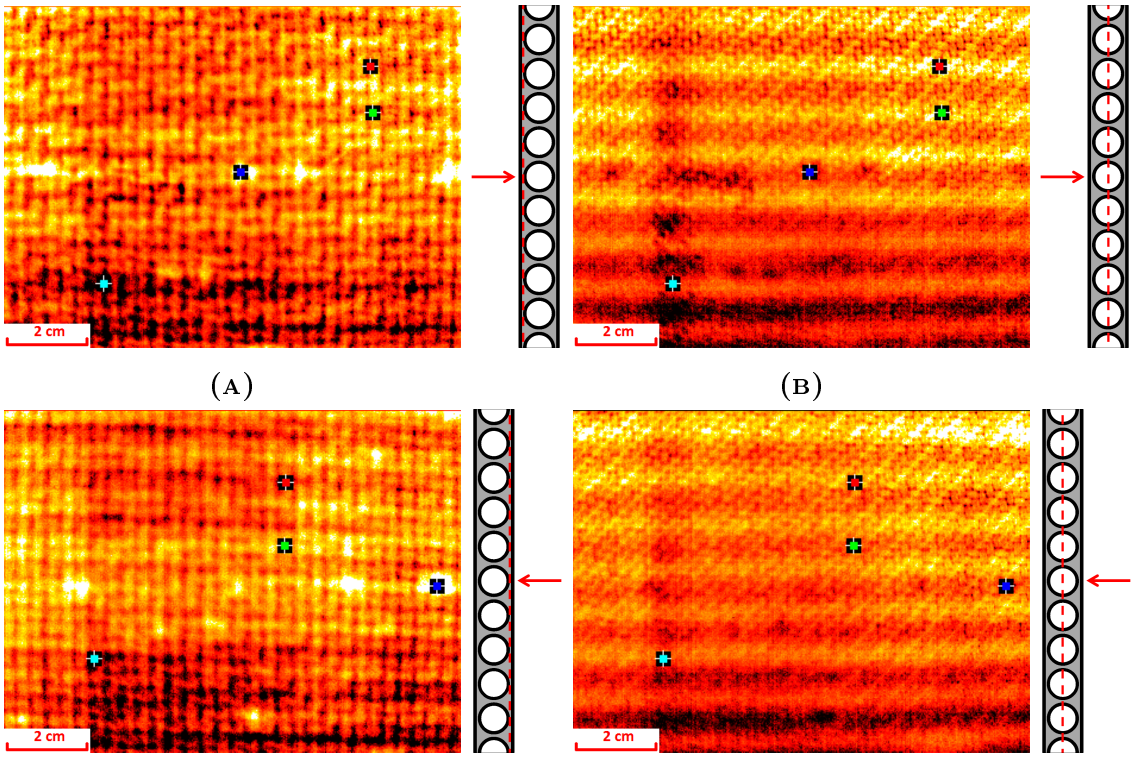

FIGURE 5.29: Infrared images of TSP_1, with markers location: (A) Top surface $t = 0.841\ s$, (B) Top surface $t = 4.2\ s$, (C) Bottom surface $t = 0.876\ s$, (D) $t = 4.3\ s$.

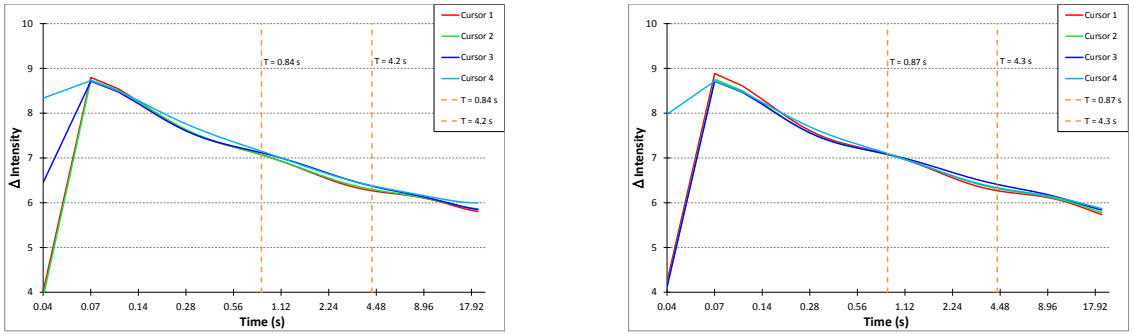

FIGURE 5.30: Thermal characteristics of TSP_1: (A) top surface, (B) bottom surface.

the location of the cyan marker was chosen to measure the thermal characteristic of the adhesive rich layer. The separation point is visible in the thermal characteristics graph shown in Figure 5.30 B, as the first vertical dashed line. The infrared image shows few white spots corresponding to the voids within the adhesive bond. From the thermal characteristics graph it can be seen that the curve, corresponding to the blue marker located on the air bubble, did not change its slope significantly. Therefore, the void had low volume and it was located only below the face sheet panel. In addition to the voids, the infrared image shows the adhesive rich layer in the bottom of the sample. This can be confirmed with the characteristics graph - the light blue curve splits slightly from the remaining curves.

Figure 5.29 D shows the middle plane of TSP_1. The state, at which the image was taken, is marked in the thermal characteristics plot (see Figure 5.30 B) as the second vertical dashed line. The infrared image was taken from the bottom side of the sample, hence the are slight differences in the infrared images between Figures 5.29 B and 5.29 D. However, there are some similarities between the images. The vertically distributed spots, corresponding to the adhesive rich layers, are visible in both images. In addition, there is an adhesive rich connection between the composite tubes visible as a black stripe in the bottom of the images. The bottom side image shows an even distribution of the composite tubes. Moreover, there were no voids within the foam material. Some coupling with the adhesive rich layer can be observed in the bottom of the sample, as the foam colour is much darker than in the remaining part of the panel.

To summarise the inspection, the first tubular sample was of reasonably good quality. The composite tubes and the foam material were distributed uniformly across the sample. However, slight differences in the distance between the composite tubes can be noticed. The distribution of adhesive was not even across the sample. This resulted in adhesive rich regions. Moreover, there were clearly visible air bubbles or voids within the adhesive bond, which may become the starting point for the damage progression or debonding within the panel after impact.

Based on the infrared images of TSP_1, the bottom face of the sample was chosen for the bird impact. The infrared image of the bottom side of the sample showed equal distribution of the adhesive in the middle part of the sample where the bird

would impact. Moreover, the central area of the sample was free of voids below the face sheet.

5.6.4.2 Tubular sandwich panel TSP_2

The separation at the top face of TSP_2 is shown in Figure 5.31 A. White spots visible in the adhesive layers are air bubbles or voids in the adhesive bond. The infrared image shows two significant air bubbles of approximately $20 - 25\ mm$ underneath the top face sheet. These defects are the result of the uneven distribution of the Permabond adhesive. In addition, the infrared image reveals presence of few smaller bubbles within the adhesive material. The separation point is also illustrated in the thermal characteristics graph (see Figure 5.32 A) as the first vertical dashed line. From the characteristics graph it can be seen that the dark blue curve, corresponding to the dark blue marker placed in the location of the air bubble, splits slightly from the remaining curves. This indicates that the depth of the void was quite significant.

The middle plane of TSP_2 is shown in Figure 5.31 B. The state at which the plot was taken is marked as the second vertical dashed line in the thermal characteristics graph presented in Figure 5.32 A. The red lines visible in Figure 5.31 B correspond to the composite tubes and the adhesive bonding the tubes together. In the bottom of the sample, these lines become dark red/black, which is a result of the coupling with the adhesive rich layer visible in the bottom of Figure 5.31 A. The distribution of the foam is uniform across the sample. The darker colour of the foam in the bottom of the sample is a result of coupling with the adhesive rich layer. The thermal characteristics graph, shown in Figure 5.32 A, clearly illustrates the change in the heat propagation rate within the void. The dark blue curve is clearly separated from the remaining curves, which indicates that the void propagates deeper into the adhesive.

The separation of the bottom side of TSP_2 is shown in Figure 5.31 C. In this case, five markers were located on the sample - two on the top of the composite tubes (green and cyan), one on the foam (red) and two on the voids under the face sheet (blue and violet). The separation is also shown in the thermal characteristics graph (see Figure 5.32 B) as the first vertical dashed line. The infrared image reveals a

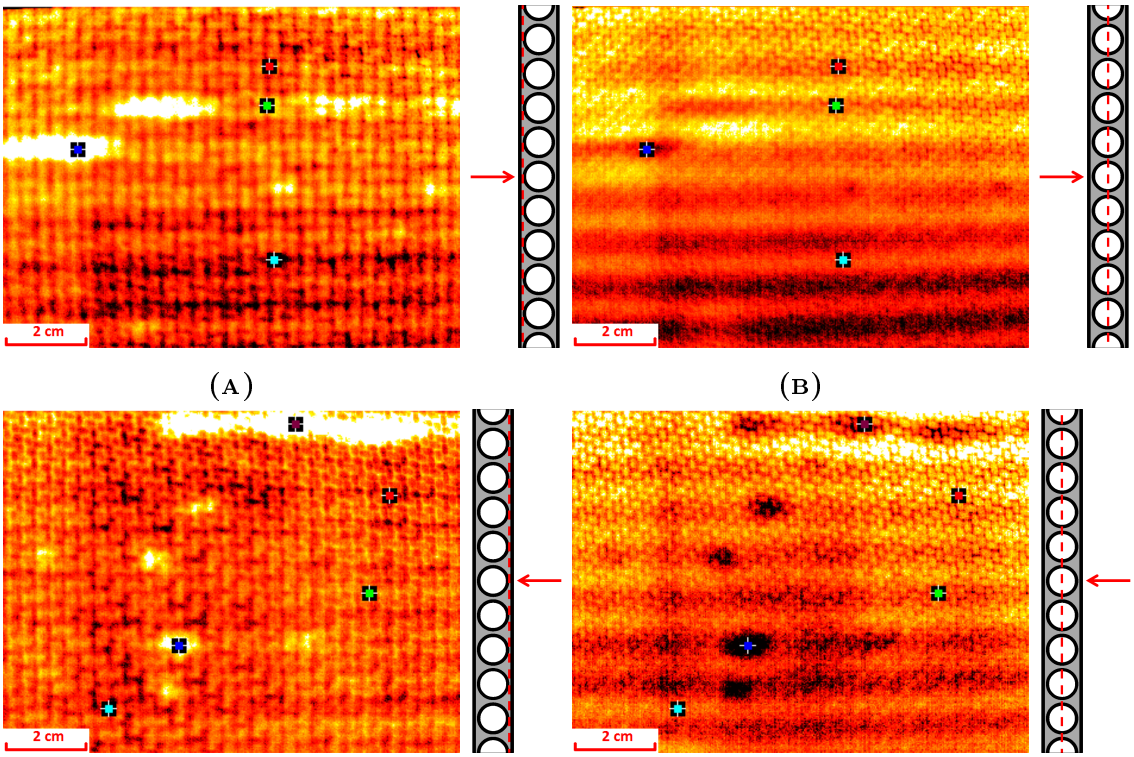

(A) (B)

(C) (D)

FIGURE 5.31: Infrared images of TSP_2, with markers location: (A) Top surface $t = 0.893\ s$, (B) Top surface $t = 4.6\ s$, (C) Bottom surface $t = 1.015\ s$, (D) $t = 7.87\ s$.

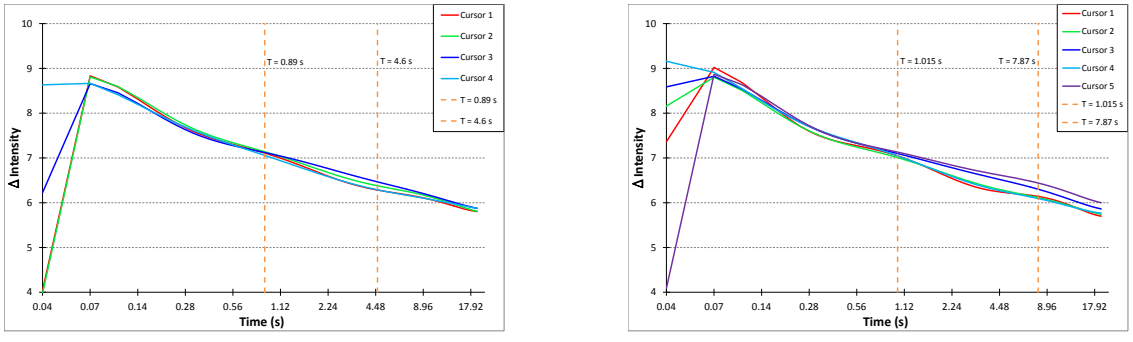

(A) (B)

FIGURE 5.32: Thermal characteristics of TSP_2: (A) top surface, (B) bottom surface.

significant void of approximately 5.5 *cm* close to the edge of the sample. Moreover, some smaller voids trapped within the adhesive are visible. Figure 5.32 B shows that the thermal characteristics read from the voids (dark blue and violet curves) separate significantly from the remaining curves. It is a result of different heat propagation rate within the voids. With the exception of the well visible voids, the distribution of the adhesive across the sample bottom face was uniform.

Figure 5.31 D shows the middle plane of TSP_2. The corresponding thermal characteristics graph is shown in Figure 5.32 B. The foam is equally distributed between the tubes which are visible in the infrared image as yellow/orange lines. The longitudinal void, visible in the top of Figure 5.31 C, strongly interferes with the infrared image of the middle plane (longitudinal black spot near the top edge of the image). This indicates that the void had a significant depth. In addition to the longitudinal spot, there are four other black spots, corresponding to the locations of the voids. The interference with the voids reduced the accuracy of the inspection results in the vicinity of the voids.

To summarise, the results of the infrared thermography of TSP_2 showed many initial defects of the panel. Two voids of approximately 2.5 *cm* were present in the middle part of the sample below the top skin. In addition, one void of approximately 5.5 *cm* was present in the adhesive material below the bottom face panel. Moreover, some smaller air bubbles were detected within the adhesive material. With the exception of defects resulting from the hand manufacturing process of the samples, the foam distribution within the composite tubes was uniform. Furthermore, the tubes were bonded to the face panel along the entire length (the air bubbles and voids were present in the adhesive between the tubes).

Based on the thermography results, the bottom face of the sample was chosen for the bird impact. Although the bottom side of the sample was not free from imperfections, the centre part was of reasonably good quality with even adhesive distribution. Moreover, large void detected during the inspection was located at the edge of the sample and its influence on the impact results should be negligible.

5.6.4.3 Tubular sandwich panel TSP_3

The separation of the top side of TSP_3 is shown in Figure 5.33 A. White spots visible in the image correspond to the locations of air bubbles or voids. From Figure 5.33 A it can be seen that the sample is uniform underneath the top skin. There are only two small air bubbles. The adhesive rich layers are visible in the bottom of the panel. The separation is also indicated in the thermal characteristics graph (see Figure 5.34 A) as the first vertical dashed line. Both the image and the thermal characteristics show a uniform distribution of the foam and the adhesive. Therefore, the sample was of good quality.

The middle plane of TSP_3 is shown in Figure 5.33 B and the corresponding thermal characteristics are shown in Figure 5.34 A. From both figures it is evident that the internal structure of the sample was intact and no defects were present. The black spots visible in the infrared image correspond to the adhesive rich layers.

The separation of the bottom side of TSP_3 is shown in Figure 5.33 C. The corresponding thermal characteristics graph is presented in Figure 5.34 B. Two voids of considerable size, approximately 60 mm and 30 mm, can be identified within the sample internal structure. The shape of the longer void indicates that one or two tubes were not fully bonded with the composite face sheet. In addition, smaller voids can be seen as bright spots within the material. The thermal characteristics graph shows clear separation of the red and green curves, corresponding to the markers placed in the locations of the voids.

Figure 5.33 D shows the midplane of TSP_3. The strong interference with the large voids visible in Figure 5.33 C reduces the accuracy of the middle plane inspection results. Strong interference indicates that the voids were of considerable depth.

To summarise, the results of the infrared thermography inspection of TSP_3 showed significant differences in the quality of the top and the bottom sides of the sample. The top of the sample showed uniform distribution of adhesive and foam material with good bonding between the face panel and the composite tubes. There were only few small air bubbles visible below the face sheet panel. The quality of the bottom side of the sample was in contradiction to the top of the sample. The inspection images showed two significant voids in the adhesive material which affects also the bonding between the composite tubes and the face sheet.

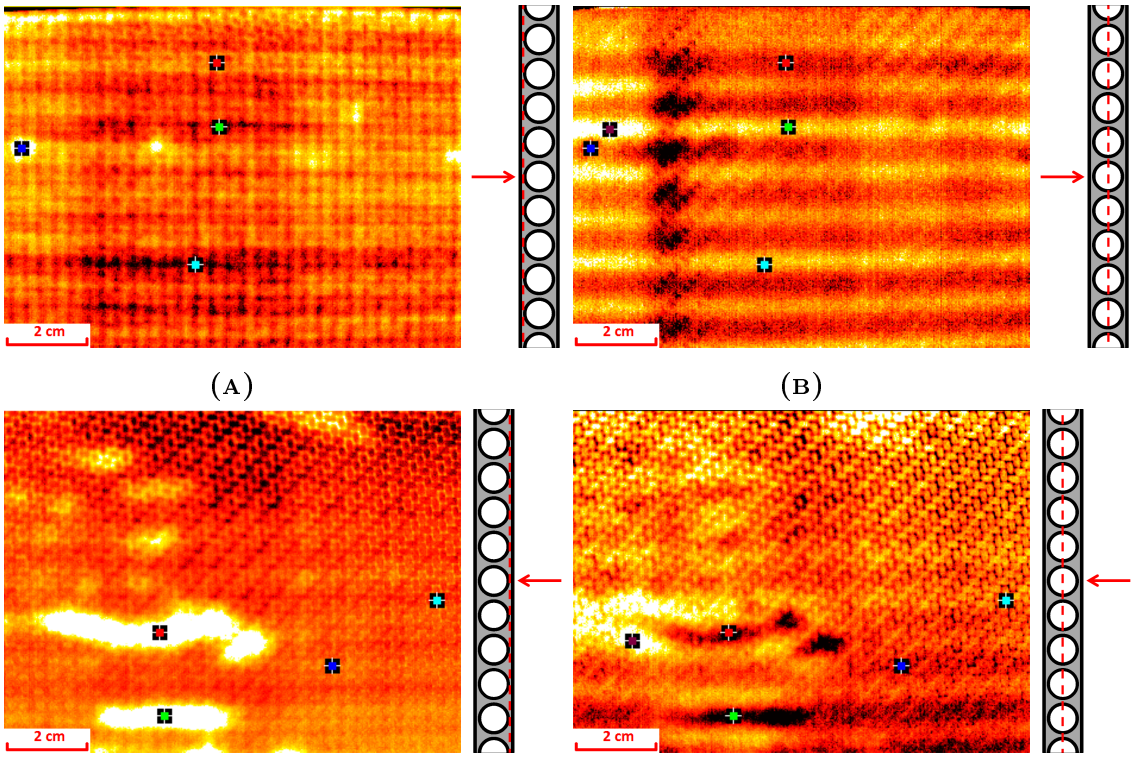

(A) (B)

(C) (D)

FIGURE 5.33: Infrared images of TSP_3, with markers location: (A) Top surface $t = 0.876\ s$, (B) Top surface $t = 3.5\ s$, (C) Bottom surface $t = 1.26\ s$, (D) $t = 4.387\ s$.

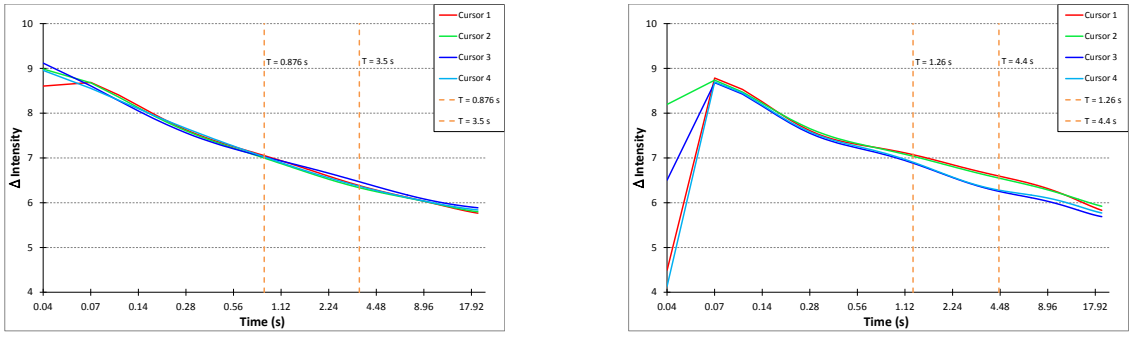

(A) (B)

FIGURE 5.34: Thermal characteristics of TSP_3: (A) top surface, (B) bottom surface.

Based on the thermography results, the top face of TSP_3 was chosen for the bird impact due to the uniform distribution of the materials showing only minor imperfections. The presence of two large voids could have a significant influence on the impact resistance of TSP_3.

5.7 Summary

In this chapter all the preparations for the bird impact experiment were presented.

The first part of the chapter described the manufacturing process of the novel composite sandwich panels, the foam samples and the gelatine birds. It included the process of material selection and the consecutive steps of the composite panels manufacturing.

Subsequently, the compression test on the foam samples was performed in order to determine the compressive properties of the low density foam, used for manufacturing of the novel composite panels. The compressive stress-strain relation, necessary to perform reliable numerical analysis, was determined within these tests.

Afterwards, the description of the gas gun used for the bird impact experiment was provided. The calibration of the gas gun, performed with acetal projectiles was performed. The calibration shots proved that the gun was capable of shooting with the repeatable velocities for a given gun pressure. Based on the velocity measurements, a regression curve was determined to enable calculation of the projectile velocity for the bird impact tests. Furthermore, a bird release system was designed to enable safe release of the birds during the impact test. The design process included material selection and numerical optimisation of the bird release system. Finally, bird release tests were performed to verify the design. The tests proved the accuracy of the numerical analysis. The sabot enclosing the bird failed in the same manner as predicted within the numerical analysis. Moreover, the bird remained intact and its shape was conserved after the release.

Finally, a non-destructive technique i.e. infrared thermography was chosen for assessment of the internal structure quality of the manufactured samples. The results of the thermography inspection were presented with the corresponding discussion.

The inspection of the internal structure revealed small imperfections and initial defects of the manufactured samples. Moreover, it enabled for a direct comparison of the results between the samples before and after impact. Eventually, the impact side for the bird strike experiment was chosen for each of the samples, based on the infrared inspection results.

Chapter 6

Bird strike experiments

6.1 Introduction

This chapter provides a description of the experimental procedure used for the bird impact test. Furthermore, the results of the bird impact tests were described together with the post impact inspection of the impacted samples. For better understanding, the structure of the chapter is illustrated in Figure 6.1.

In the first part of the chapter the experimental arrangement is described. This section contains a description of the samples preparation, the boundary conditions used during the test and the data acquisition system used to record the bird impact on the panels.

In the subsequent section, the results of the bird impact experiment were presented. Images acquired throughout the bird impact are shown together with other data captured during the test. This is followed by a description of the visual and thermographic inspections of the composite samples after the bird impact test.

In the last part of the chapter, a discussion of the experimental results and conclusions are presented.

6.2 Experiment arrangement

In this section, the final preparations for the bird impact experiment are described.

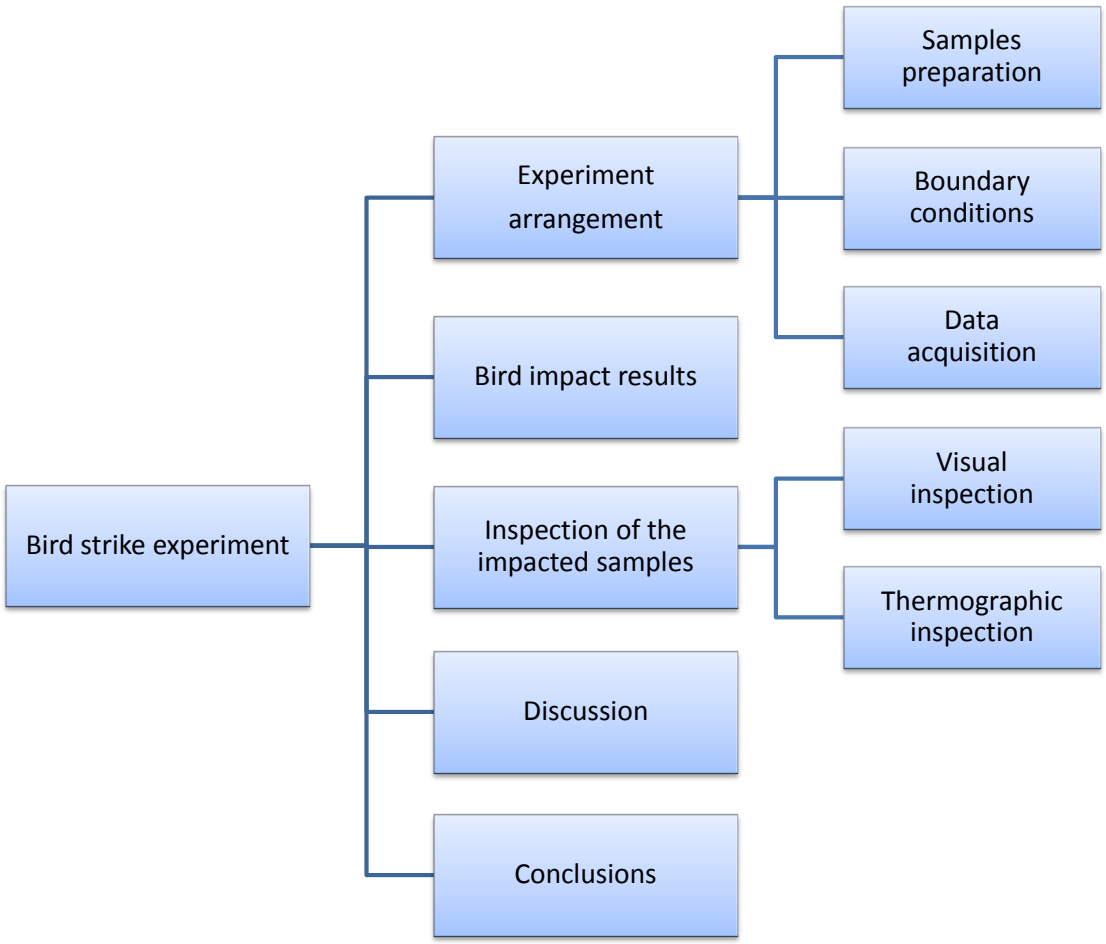

FIGURE 6.1: Chapter 6 structure.

6.2.1 Samples preparation

Six samples were divided into two groups containing three corrugated and three tubular sandwich panels. As described in Section 5.6, all the samples were numbered and their top and bottom faces were marked accordingly. The samples numbering and side designation was necessary for the identification of the impacted side after the test. Furthermore, the mass of the composite samples was measured. Based on the initial thermography inspection of the samples, the impact side was chosen for each sample. After this decision was made, the impact sides were marked with a cross at the left top corner of the sample and the centre of impact was determined and marked with a dot.

The birds were manufactured one day before the test. They were wrapped in a thick layer of cling film to prevent the bird from loss of moisture. Afterwards, the birds were placed in a fridge to assure their solidification. Three hours before the experiment, the birds were removed from the fridge to heat up to room temperature. Afterwards, the thick layer of cling film was removed and the birds were measured and weighed. In between measurements, the birds were wrapped in a very thin layer of cling film and numbered. Further, the bird were covered in vaseline and placed in the sabot. The bird with a sabot is further referred as a projectile.

Before the birds were inserted into the sabots, the sabots were painted with a black marker. This procedure was necessary to assure correct measurements of the velocity measurement system (VMS). Trial shots revealed that the polycarbonate sabots containing the birds were not always detected with the LED sensors of the VMS due to the sabot transparency. Therefore, it was decided to paint the sabots before the test to assure correct measurements. Furthermore, the projectiles were weighed in order to determine the mass of the projectile and the pressure for the gas gun.

The bird measurements together with the impact side for the samples are presented in Table 6.1. Figure 6.2 shows the numbered birds and sabots ready to be fired.

Table 6.1: Bird and sample measurements.

Sample No.	Sample type	Sample mass (g)	Impacted side	Bird No.	Bird length (mm)	Bird mass (g)	Bird density ($\frac{g}{cm^3}$)	Projectile mass (g)
1C	Corrugated	90	Bottom	1	51	25.7	0.987	46.8
2C	Corrugated	89	Bottom	2	53	25.4	0.976	46.1
3C	Corrugated	92	Bottom	3	53	24.4	0.955	45.5
1T	Tubular	180	Top	4	52	24.7	0.967	45.9
2T	Tubular	181	Top	5	51	24.7	0.977	45.8
3T	Tubular	183	Bottom	6	51	24.4	0.975	45.9

The highest probability of a bird strike on aircraft is during take off and landing. Hence, it was decided to perform the bird impact tests with a velocity slightly higher than the take off safety speed for most operating aircraft. Such velocity is even higher than the velocity required for the take-off of the biggest commercial aircraft - the take-off safety speed is in the range $130 - 190\ kn$ ($240.8 - 333.4\ \frac{km}{h}$)

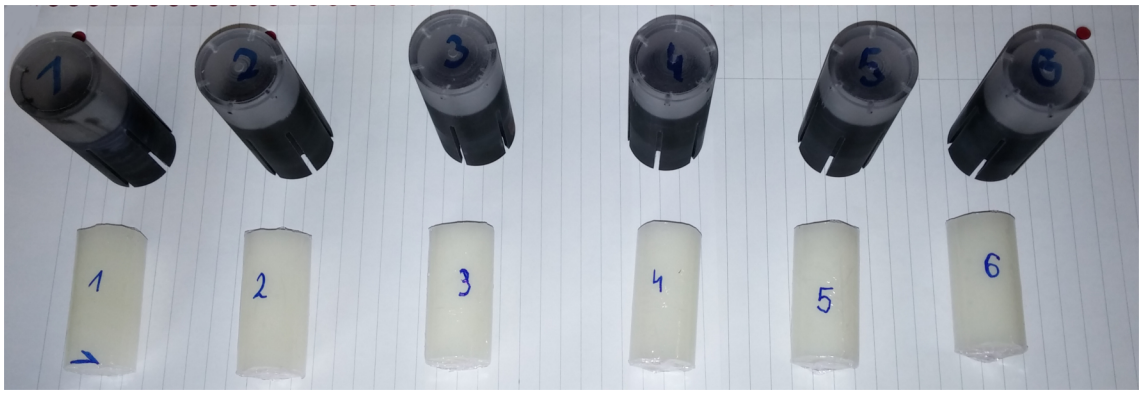

Figure 6.2: Birds and sabots prepared for the test.

for Boeing 747 (DVA, 2009) and $140 - 160\ kn$ ($259.3 - 296.3\ \frac{km}{h}$) for Airbus A380 (Air France, 2010). The higher velocity used for the bird impact tests ensures the safety of the structure after impact. Therefore, the birds were aimed to be fired at approximately velocity of $V_i = 120\ \frac{m}{s}(430\ \frac{km}{h})$.

After the decision on the bird impact velocity was made, it was crucial to determine the pressure necessary for firing the birds at the desired velocity. Based on the regression line determined for a 50 g projectile, a pressure of 7.66 bar was calculated. However, none of the projectiles had a mass of exactly 50 g (see Table 6.1), therefore it was decided to pump the gun to a pressure of $6 - 7\ bar$. Finally, the trial shot to confirm the bird impact velocity at the corresponding pressure was performed. The projectile of 46 g was shot at a pressure of 6 bar what resulted in velocity of $115.7\ \frac{m}{s}$.

6.2.2 Boundary conditions

One of the most important steps in the experimental procedure was to assure the alignment between the gun and bird release system. The alignment was checked once again, with a special alignment bar, before firing the trial shot. The alignment bar consisted of two acetal cylinders mounted on both ends of a straight aluminium rod. The diameter of the first acetal cylinder was equal to the internal barrel diameter ($31mm$) and the diameter of the second acetal cylinder was equal to the diameter of the channel in the bird release system ($26.5mm$).

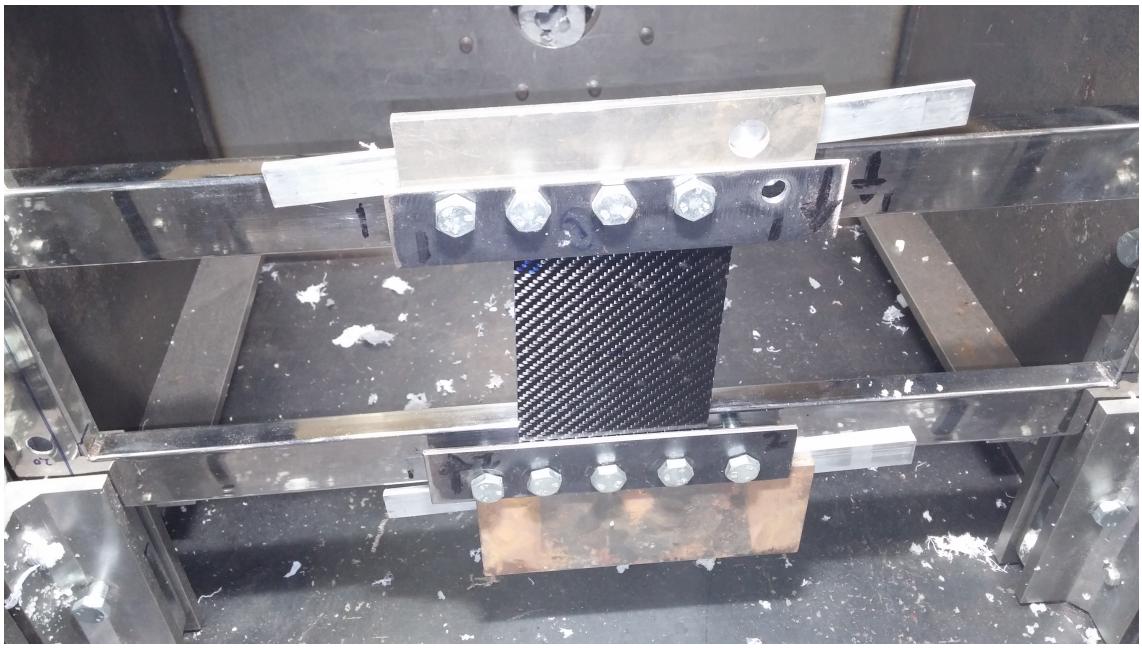

Figure 6.3: The boundary conditions used during the test.

Subsequently, the VMS was mounted on the barrel muzzle and all the sensors were connected to the counter. The sensors were checked with a voltmeter and calibrated accordingly to the Statement of Procedure (SOP) for the VMS. Afterwards, the VMS was ready to measure the velocity of the shots.

In the next step, the holding frames were set to the appropriate height for mounting the sample. The span between the frames was equal to 110 mm. Subsequently, the sample was placed and fixed within the holding frames, as shown in Figure 6.3. Fixing of the sample correspond to the fixed boundary conditions. The dot on the impact surface of the sample was aligned with the centre line of the barrel and bird release system, after which, the sample was ready for testing.

6.2.3 Data acquisition

In order to record the bird impact sequence, an OLYMPUS $I-SPEED3$ high speed camera was used. The camera was put on the top of the safety chamber to record the bird impact on the composite samples. The safety chamber was covered with a plexiglass plate to assure the transparency of the chamber lid.

The high speed camera was set to record at a sampling rate of 10000 frames per seconds (fps). This allowed to capture enough images of the bird hitting the sample. However, increasing the number of fps up to such high value required very strong light. Therefore, three very strong lights were put on the top of the transparent lid and the light rays were focused on the sample. The high speed camera was synchronised to the VMS. As soon as the projectile activated the velocity measurement, the high speed camera recording was triggered. The synchronisation between the camera and the VMS allowed to reduce the recording time, which was set to 5 seconds.

Due to the lack of pressure gauges, no pressure distribution was measured during the test.

6.2.4 Experiment procedure

After all set-up preparations were finished, the following experimental procedure was executed for the bird impact test:

1. Open the over-pressurisation valve to remove remaining pressure from the system,
2. Close the over-pressurisation valve and the exhaust valve,
3. Open the lid of the gas gun pressure chamber,
4. Make sure that both ends of the sabot fit inside the barrel and it is not too tight on either end,
5. Place the sabot in the barrel so that it is flush with the end of the barrel,
6. Close the pressure chamber by re-attaching the back plate and tightening the bolts,
7. Evacuate people from the building,
8. Reset the VMS,
9. Pump the corresponding pressure into the gun pressure chamber,

10. Turn on the lights,
11. Turn on the fire remote system,
12. Leave the building with the firing remote,
13. Proceed with the test,
14. Come back to the building,
15. Switch off the fire remote and the light,
16. Open the over-pressurisation valve to remove the remaining pressure from the system,
17. Open the exhaust valve to relieve the remaining pressure from the chamber,
18. Note the projectile velocity,
19. Save the data from the camera,
20. Wait until the safety chamber is clear of any visible debris and slowly remove the lid of the chamber with the assistance of a vacuum pump (only for composite samples),
21. Clean up the sabot debris,
22. Verify that the bird release system is undamaged,
23. Wearing gloves, remove the sample from the fixing frame and clean it up from the bird debris
24. Verify the sample for visible damage and place it in the grip seal bag

The above procedure was repeated for all the composite samples.

6.3 Bird impact results

In this section only the results of the bird impact experiment are presented. The discussion and analysis of the results is presented in Section 6.5.

The tests were conducted in the Applied Mechanics Department laboratory at Cranfield University. The ambient air temperature and relative humidity on the day of the experiment were $T = 25°C$ and 60% respectively.

The results from the bird impact tests are shown in Table 6.2. The impact energy for each test was calculated with the measured velocity and bird mass. The evaluation of the samples internal damage was based on the infrared thermography inspection presented in the following section.

Table 6.2: Results of the bird impact test.

Sample No.	Impacted side	Pressure (bar)	Impact velocity ($\frac{m}{s}$)	Impact energy (J)	Surface damage	Internal damage	Back surface damage
1C	Bottom	6	116.35	174	Yes	No	No
2C	Bottom	6	114.63	167	Yes	No	No
3C	Bottom	6	116.28	165	No	No	No
1T	Top	6	115.95	166	No	No	No
2T	Top	6	116.51	167	No	No	No
3T	Bottom	6	119.74	175	No	No	No
1T	Top	14	160.55	317	No	No	No
2T	Top	15	172.14	346	No	No	No
3T	Bottom	18	210.43	547	No	No	No
1T	Top	38	235.72	714	Yes	Yes	Yes
2T	Top	40	254.09	783	Yes	Yes	Yes
3T	Bottom	38	242.31	755	Yes	Yes	Yes

The sequence of the bird impact, recorded with the high speed camera at 10000 fps, is shown in Figure 6.4. The complete sequence of the bird impact on a composite sandwich panel is shown in Appendix C.1. A composite sample just after bird impact test is shown in Figure 6.5.

Since the initial set of tests did not lead to any damage of the tubular sandwich panels, additional tests were performed to investigate their damage threshold for

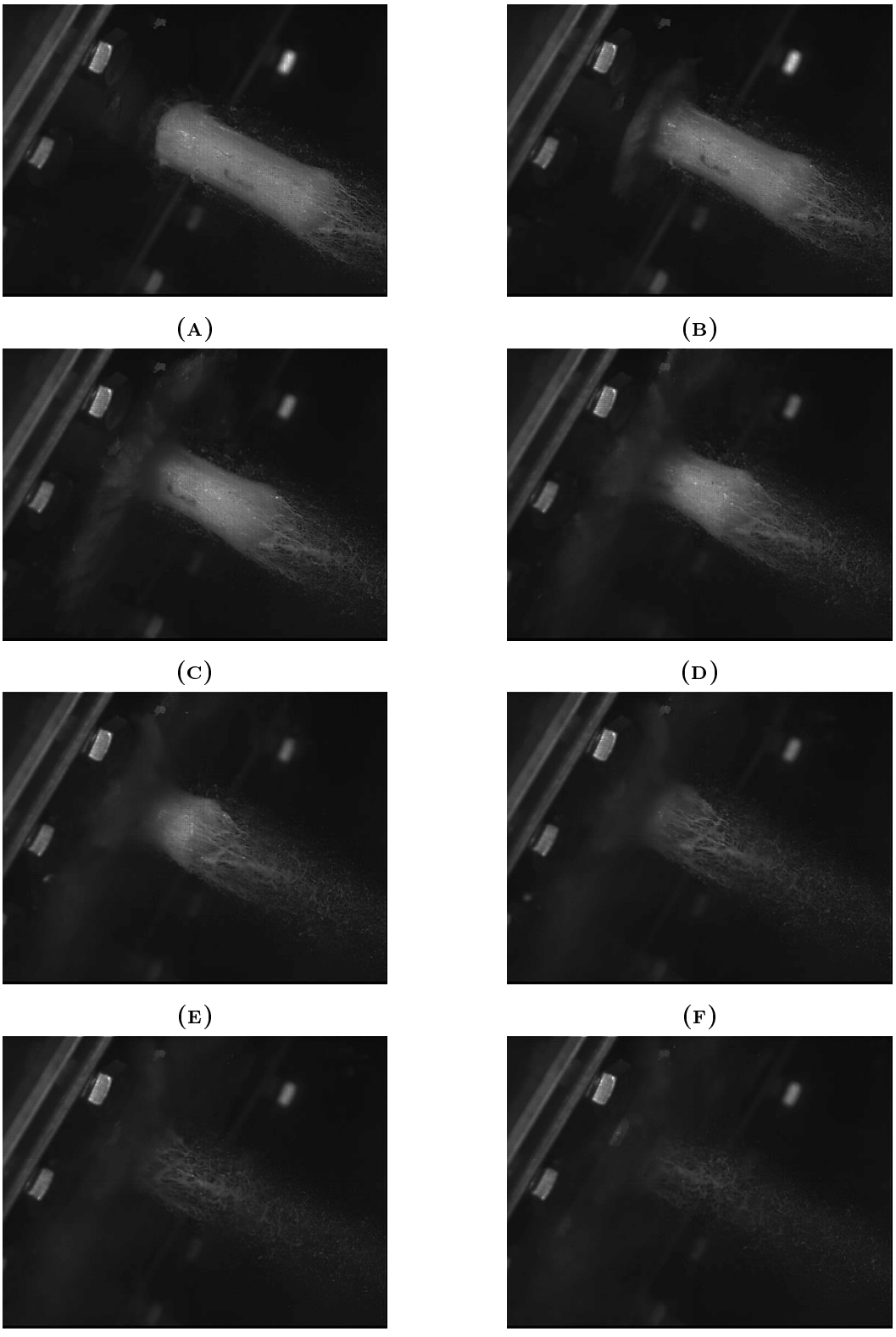

(A) (B) (C) (D) (E) (F) (G) (H)

FIGURE 6.4: Bird impact sequence images at time intervals of 0.8 *ms*.

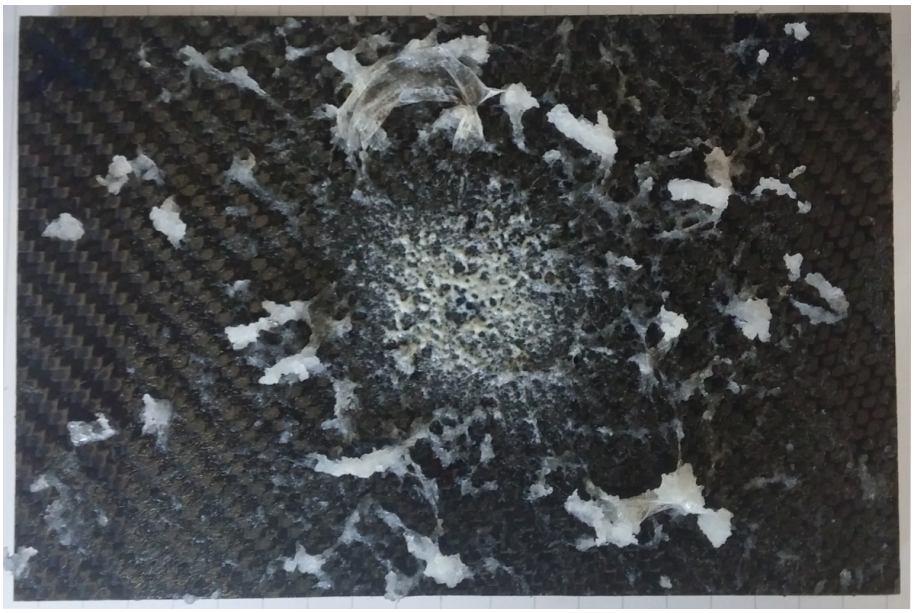

Figure 6.5: Composite sandwich panel just after bird impact.

soft body impact. The obtained results showed that damage of the tubular sandwich panels occurred within the impact velocity range $V_i = 235 - 255\ \frac{m}{s}$, which corresponds to a pressure of $p_i = 38 - 40\ bar$.

6.4 Inspection of the impacted samples

This section presents the results of the visual and thermographic inspections performed on the testes samples.

The corrugated sandwich panels are denoted as CSP and the tubular sandwich panels as TSP.

6.4.1 Visual inspection of the impacted samples

After the impact tests, the tested samples were subjected to a visual inspection. Images of the impacted samples are shown in Figures 6.6, 6.7 and 6.8. Due to the very high gloss of the samples surfaces, there might be light reflections visible in the images. A measuring tape was placed along the length of the samples in order to

visualise the size of the damage. In the results description, the directions along the length and the width of the sample are referred to as longitudinal and transverse directions respectively.

The initial inspection of CSP_1 revealed a small spall visible on the impacted surface (see Figure 6.6 A). The spall size was 2 $mm \times 3$ mm and it was located near the location of the bird impact. The spall was surrounded by a visible delamination area of triangular shape. There were no visible signs of damage on the rear face sheet of the sample. Visual inspection of the sample edges did not reveal any delaminations between the foam and the carbon fibre panels.

The surface damage of CSP_2 is shown in 6.6 B. From this figure it can be seen that the damage was very pronounced. There were two significant spalls visible on the impacted face sheet. The spalls were located longitudinally on both sides of the impact centre. In addition to the spalls, there was a longitudinal crack between the spalls at a distance of 10 mm from the impact location. Despite very pronounced damage of the impacted surface of the sample, no damage indication was found on the rear surface of CSP_2. The inspection of the edges did not show any separation between the polyurethane foam and the carbon fibre panels.

The visual inspection of CSP_3 did not show any form of visible damage on any of the sample face sheets (see Figure 6.6 C). Moreover, the edges of the sample were free from any separations between the foam and the face sheets.

After the first set of tests, performed at an impact velocity of approximately 116 $\frac{m}{s}$, there was no indication of visual damage of tubular sandwich panels (see Figure 6.7). The same results were observed after the impact tests with a velocity range $160 - 210$ $\frac{m}{s}$. Finally, the last set of impact tests, performed for impact velocities corresponding to a pressure of $p = 40$ bar, led to damage of the tubular samples. Such pressure resulted in a velocity range of $V_i = 235 - 255$ $\frac{m}{s}$ and an impact energy range of $715 - 785$ J.

TSP_1 was impacted by the bird at an impact velocity of $V_i = 235$ $\frac{m}{s}$, which resulted in three longitudinal cracks of 10 mm, 15 mm and 10 mm in the vicinity of the bird impact location. There was no other form of damage visible on the impacted surface of the sample TSP_1. The inspection of the rear surface did not show any visible damage. Moreover, no debonding was visible on the samples edge.

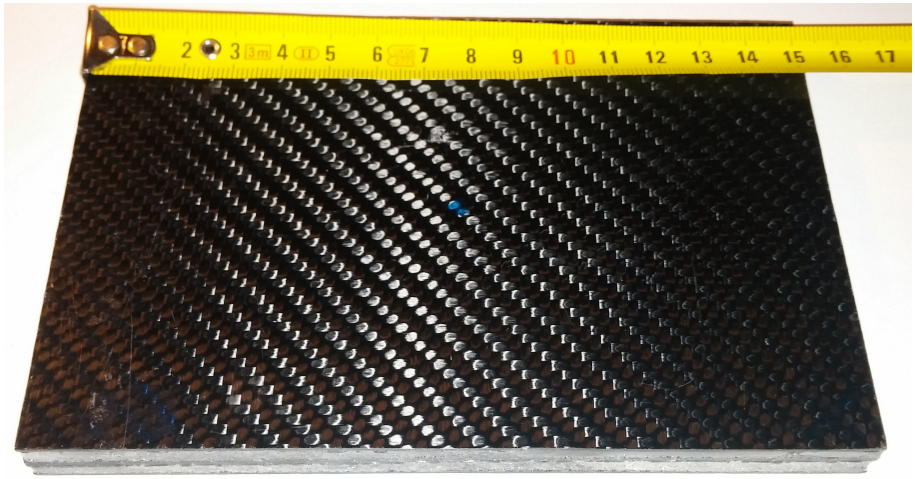

(A) CSP_1

(B) CSP_2

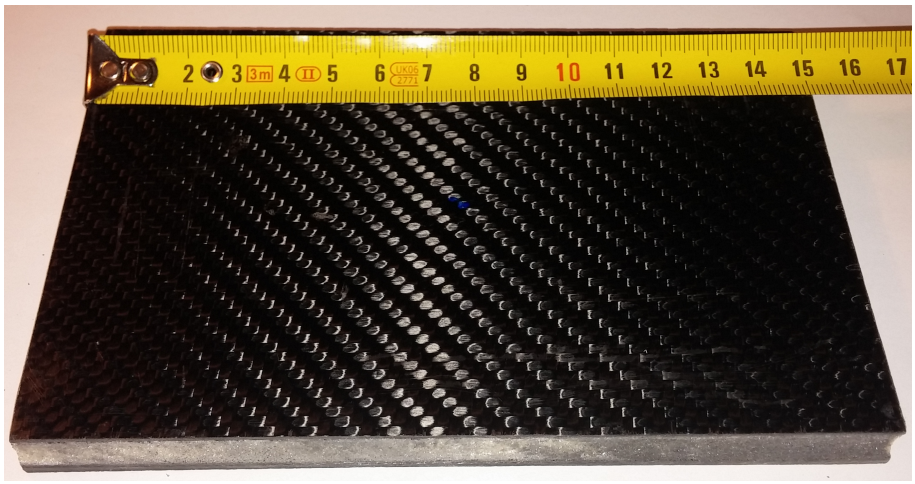

(C) CSP_3

FIGURE 6.6: Visual inspection of corrugated sandwich panels after bird impact test.

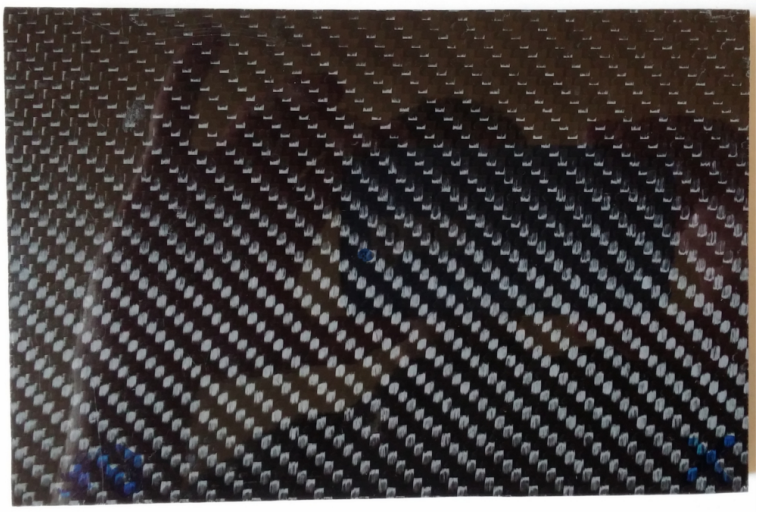

(A) TSP_1

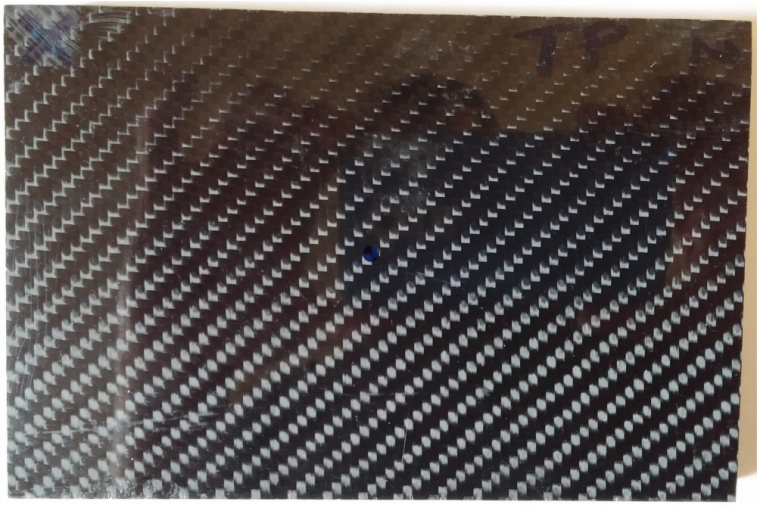

(B) TSP_2

(C) TSP_3

FIGURE 6.7: Visual inspection of tubular sandwich panels after first of impact test.

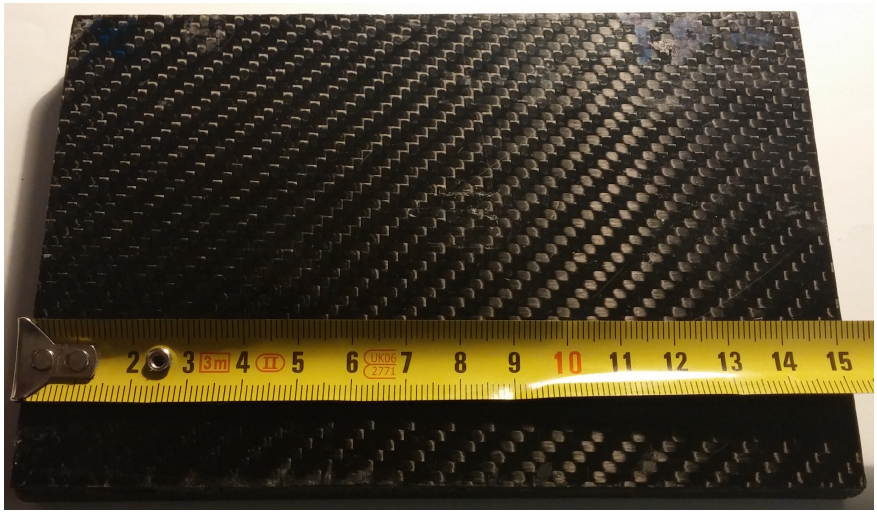

(A) TSP_1

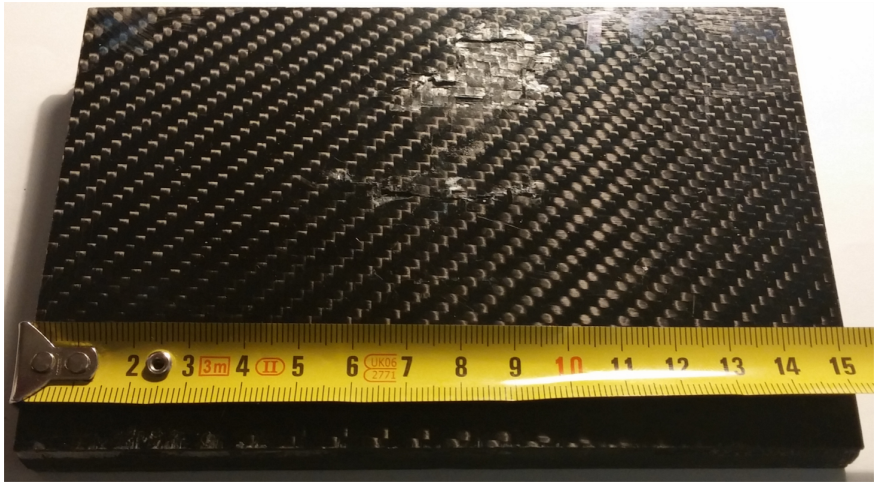

(B) TSP_2

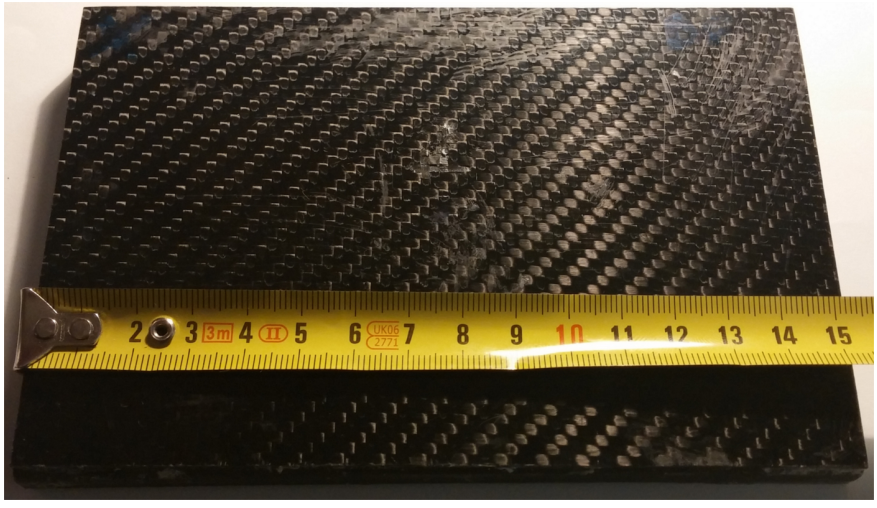

(C) TSP_3

FIGURE 6.8: Visual inspection of tubular sandwich panels after damage threshold impact test.

TSP_2 was impacted at a velocity of $V_i = 254\ \frac{m}{s}$. Such high impact velocity resulted in very pronounced damage of the sample. The visual inspection of the impacted surface showed three longitudinal cracks in the vicinity of the bird impact location. A 24 mm long crack was visible 16 mm away form the centre of the sample, while 10 mm and 40 mm long cracks were located at a distance of 2 mm from the impact centre. Careful examination of the impacted surface revealed subsurface damage in the vicinity of cracks. Moreover, there was a spall of approximately 370 mm^2 visible at a distance of 20 mm above the longest crack. In addition to the impacted surface damage, there was a 16 mm long, transverse crack on the rear surface of TSP_2. Careful examination of the rear surface revealed that the sample suffered from extensive subsurface damage underneath the rear face sheet. Furthermore, one of the edges of the sample showed separation between the composite tube and the carbon fibre face sheets.

TSP_3 was impacted at a velocity of $V_i = 242\ \frac{m}{s}$. This impact velocity resulted in a small spall in close vicinity of the centre of. The size of the spall was approximately $10\ mm \times 12\ mm$. Moreover, there was a 10 mm long longitudinal crack at a distance of 3 mm from the centre of impact. No visual damage in the form of cracks or spalls was visible on the rear surface of the sample. However, the unevenness of the rear surface could be identified from careful examination of the surface. The visual inspection of the sample edges revealed debonding of the composite tube from the face sheet along the length of the sample of approximately 55 mm.

6.4.2 Thermographic inspection of the impacted samples

In this section the, thermography inspection of the impacted samples iss presented. Due to the change in the hardware, the thermographic inspection of the impacted samples was performed with a different infrared camera than the initial thermographic inspection of the samples. This change led to differences in the heat characteristics of the samples which are visible in the thermal characteristics graphs. Moreover, significant improvement in the quality of the images was noticed. However, the change in the resolution of the images led to differences between the infrared images from the initial and post impact inspections. The new camera used was FLIR SC7600 INSBMB mid wave length cooled quantum detector based infrared camera.

This camera enables for capturing images with a resolution of 640×512 $pixels$. The sensitivity of the camera was 15 mK (the old camera had sensitivity of 50 mK).

For easier comparison, the images of the impacted and non-impacted samples of each inspection were plotted together, e.g. see Figure 6.9 for CSP_1. The left hand side of each plot illustrates the non-impacted samples (BI), while the right hand side illustrates the samples after the impact (AI). The schematic representation of the sample was add to the figures to highlight the inspected cross section. In addition to the infrared images, the thermal characteristics are presented. These were measured at the point locations illustrated as markers on the images. The location of the markers was chosen to show in the best way the state of the impacted samples.

The inspection was performed at a relative humidity of 40% and an ambient temperature of $27°C$. The settings used for the thermography analysis were the same as the ones of the initial inspection. The acquisition time was set to $t = 20$ s at an acquisition rate of 28.6 fps. The acquisition time corresponds to an acquisition length of 572 frames. The same settings were used for the analysis of each side of the samples. The thermographic signal reconstruction system MOSAIQ was used to post process the raw thermography data acquired during the analysis.

Due to the differences in resolutions of the infrared cameras used for the initial and after impact inspection, there are small differences between the infrared images. Therefore, the images were cut in a way which allows for a direct comparison of the inspection results. Due to the change in the hardware, the clamp used to hold the sample is visible on the left hand side of the images.

Thermographic inspection results of all corrugated and tubular sandwich panels are presented in the following sections for the impact velocity of $V_i = 115\frac{m}{s}$. Furthermore, the thermographic analysis of the tubular sandwich panel impacted at the damage threshold velocity of $V_{DTV} = 235\frac{m}{s}$ is presented as the most representative case from the last set of impact tests.

6.4.2.1 Corrugated sandwich panel CSP_1

Figure 6.9 shows the infrared images of the non-impacted (left hand side) and impacted samples (right hand side). The corresponding thermal characteristics graphs are shown in Figure 6.10. Figures 6.9 A - 6.9 D illustrate the impact side and Figures 6.9 E - 6.9 H illustrate the rear side of the sample. The location of the markers was chosen to show in the best way the differences in the heat characteristics. The locations of markers in the images on the left hand side correspond to the locations of the markers in the images of the impacted samples. This allows for a comparison of the heat characteristics of the samples before and after impact.

Figures 6.9 A and 6.9 B show the separation point of the impacted side of CSP_1. From Figure 6.9 B, some damage on the composite panel can be identified. The most pronounced damage can be seen as a black spot around the pink marker. The damage is also indicated very well on the heat characteristics graph (Figure 6.10 B). The pink line corresponding to the pink marker is completely separated from other lines which confirms the damage in the material.

Figures 6.9 C and 6.9 D show middle plane images of the impact side. It is evident that the damage of the impacted sample was only on the impacted surface, since there are no changes visible in the infrared image of the sample before and after the impact. The restriction of damage to the impacted surface is confirmed on the thermal characteristics graph, shown in Figure 6.10 B. The separated pink curve coincide to the remaining curves behind the separation point.

Figures 6.9 E - 6.9 H show the images taken of the rear side of the sample. Figures 6.9 E and 6.9 F show the separation point for the rear face of the panel and Figures 6.9 G and 6.9 H show the mid plane of the panel for the inspection of the rear side. These sets of images indicate that there was no damage on the rear face sheet of CSP_1. Moreover, there were no visible changes in the images of the sample middle plane. The lack of internal damage was also confirmed on the thermal characteristics graph for the impacted sample, shown in Figure 6.10 D. From this graph it can be seen that the curves for the corresponding marker locations remain together, similarly to the thermal characteristics before the impact (see Figure 6.10 C).

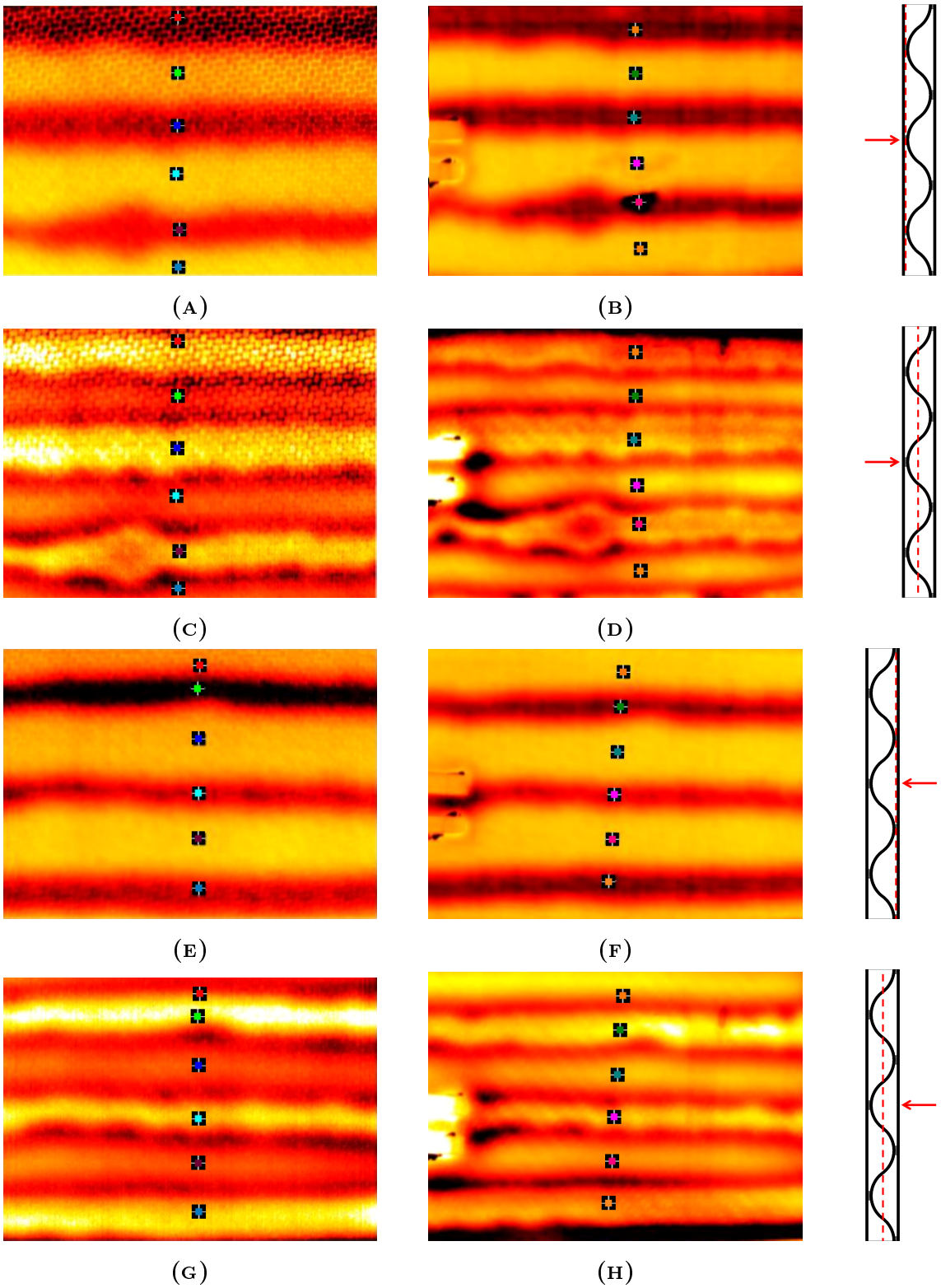

(A) (B)

(C) (D)

(E) (F)

(G) (H)

Figure 6.9: Thermography inspection of CSP_1 before (BI) and after (AI) bird impact test: (A) Impact side BI, (B) Impact side AI, (C) Impact-mid side BI, (D) Impact-mid side AI, (E) Rear side BI, (F) Rear side AI, (G) Rear-mid side BI and (H) Rear-mid side AI.

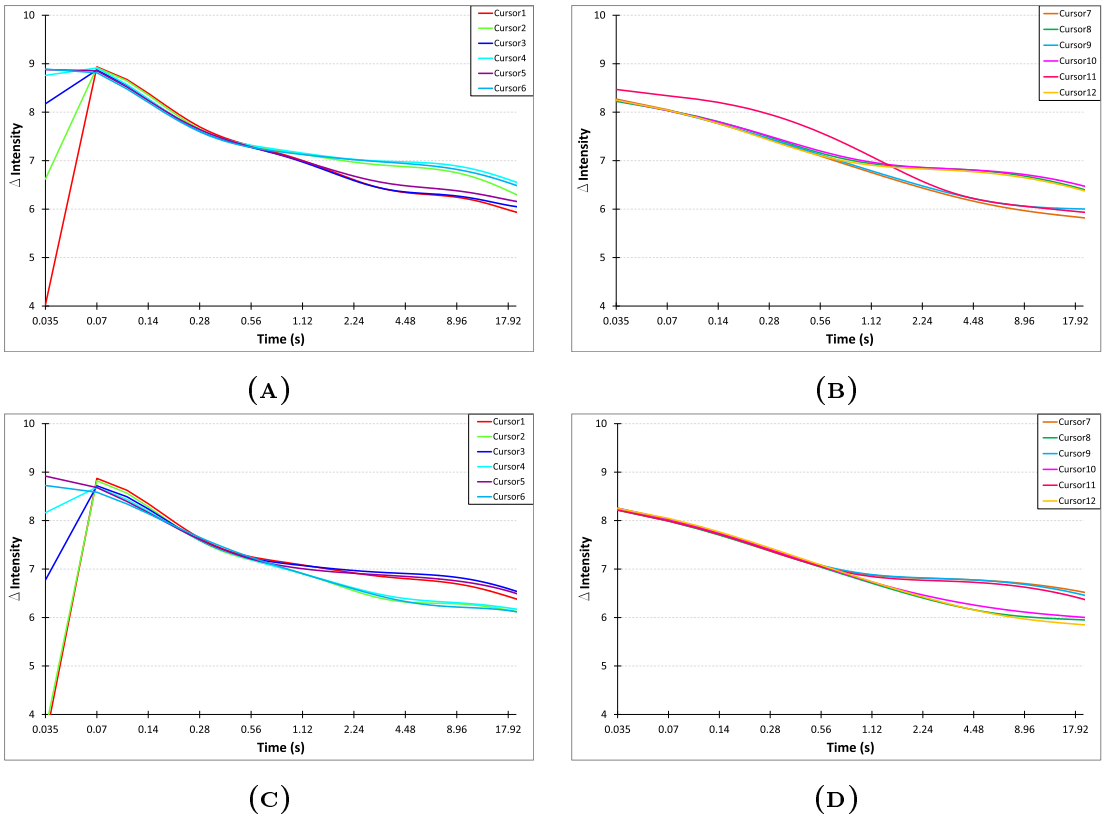

Figure 6.10: Thermal characteristics for CSP_1 before (BI) and after (AI) bird impact test: (A) Impact side BI, (B) Impact side AI, (C) Rear side BI and (D) Rear side AI.

6.4.2.2 Corrugated sandwich panel panel CSP_2

The infrared inspection images of CSP_2 are shown in Figure 6.11. The corresponding thermal characteristics graphs are shown in Figure 6.12. Figures 6.11 A-6.11 D and 6.12 A-6.12 B illustrate the inspection of the impact side of the panel and Figures 6.11 E-6.11 H and 6.12 C-6.12 D illustrate the rear side of the panel. The locations of markers was chosen to show in best way the differences in the heat characteristics. The locations of markers in the images on the left hand side correspond to the locations of the markers in the images of the impacted samples. This allows for a comparison of the heat characteristics of the samples before and after impact.

Figures 6.11 A and 6.11 B show the separation point of the impacted face of CSP_2. It is evident that the impacted surface was severely damaged. Figure 6.11 B shows

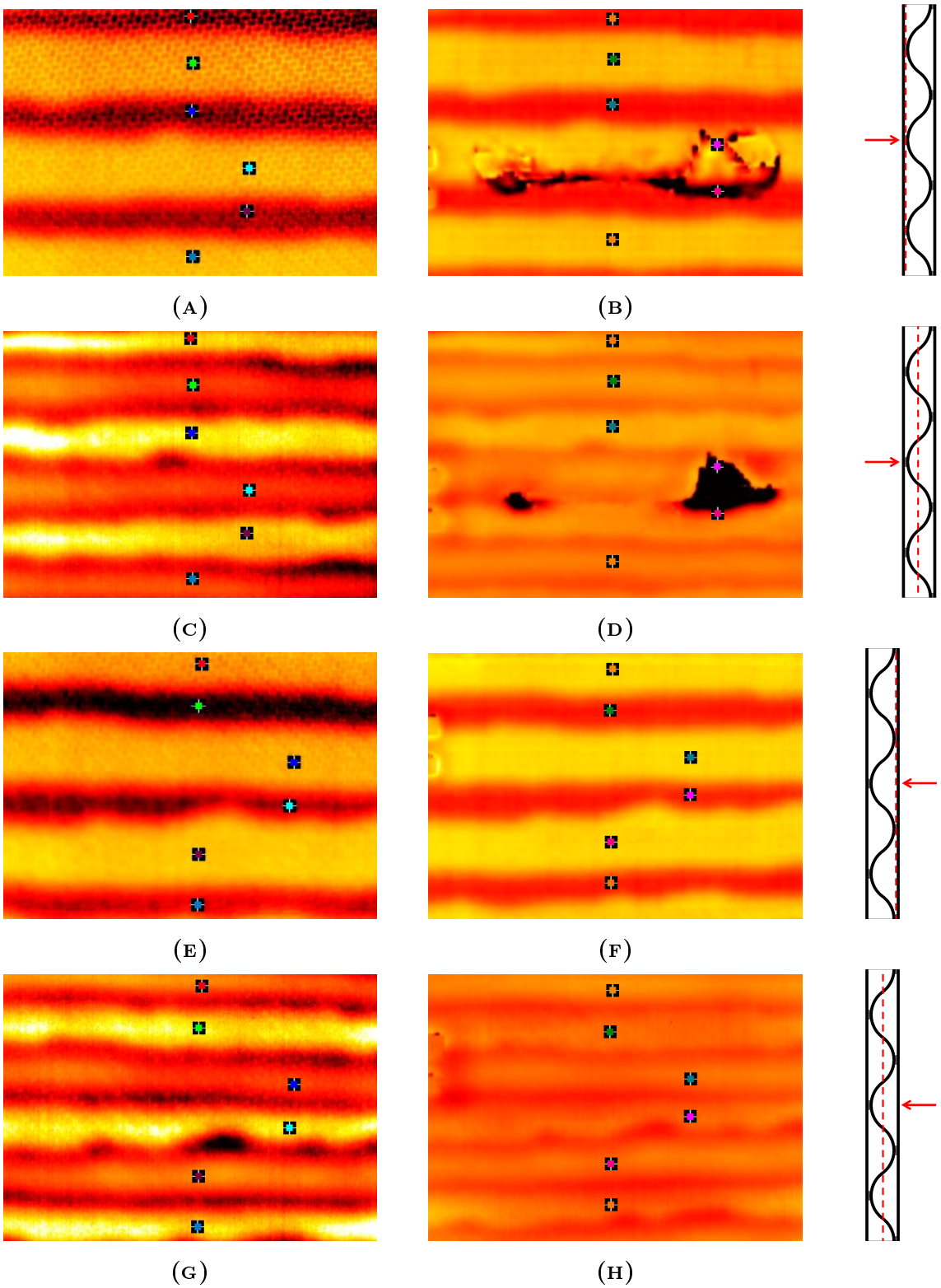

(A) (B)

(C) (D)

(E) (F)

(G) (H)

FIGURE 6.11: Thermography inspection of CSP_2 before (BI) and after (AI) bird impact test: (A) Impact side BI, (B) Impact side AI, (C) Impact-mid side BI, (D) Impact-mid side AI, (E) Rear side BI, (F) Rear side AI, (G) Rear-mid side BI, (H) Rear-mid side AI.

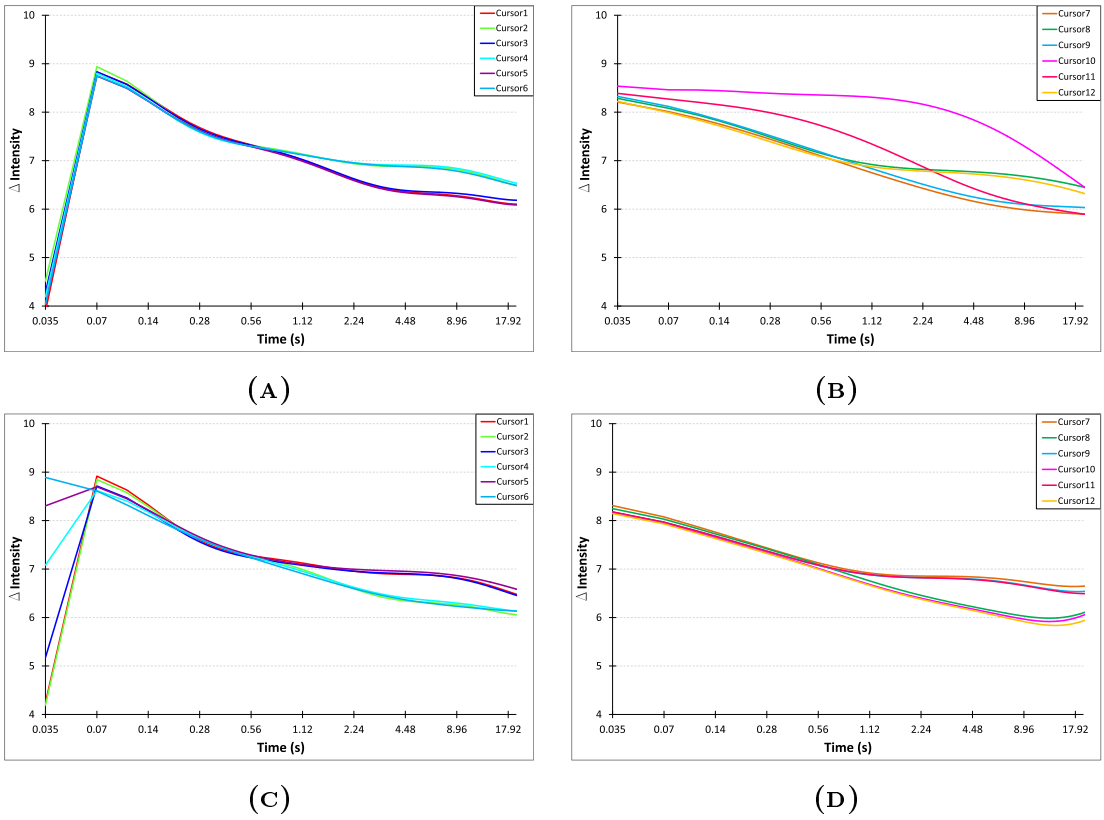

Figure 6.12: Thermal characteristics for CSP_2 before (BI) and after (AI) bird impact test: (A) Impact side BI, (B) Impact side AI, (C) Rear side BI and (D) Rear side AI.

clearly where the damage occurred and its extent. The infrared image shows that the damage was bigger than observed during the visual inspection of the sample. The damage of the sample can also be identified from Figure 6.12. The thermal characteristics for the purple and pink markers split completely from the remaining curves. This confirms that a significant change in the thermal characteristics of the material occurred as a result of the induced damage.

Figures 6.11 C and 6.11 D show the middle plane of the corrugated sample. Since the images were taken from the impact side of the sample, the strong interference with the severe surface damage can be seen in Figure 6.11 D as black spots. Due to the strong interference, the internal structure of the sample was assessed from the mid plane images taken from the non-impacted side of the sample.

Figures 6.11 E and 6.11 F show the separation point of the rear side of the sample. The images show no surface or subsurface damage. This was also confirmed from the corresponding thermal characteristics graphs shown in Figure 6.12 D. The thermal characteristics coincide together for the corresponding markers, similarly to the non-impacted sample characteristics (see Figure 6.11 C).

Figures 6.11 G and 6.11 H show the inspection images of the mid plane of CSP_2. It can be seen that the sample did not suffer from any internal damage. This is also confirmed in the thermal characteristics graph, shown in Figure 6.12 D.

6.4.2.3 Corrugated sandwich panel CSP_3

The infrared images from the thermography inspection of CSP_3 are shown in Figure 6.13. The corresponding thermal characteristics graphs are shown in Figure 6.14. Figures 6.13 A-6.13 D and Figures 6.13 A-6.13 B illustrate the impact side of the corrugated panel and Figures 6.13 E-6.13 H and Figures 6.14 C-6.14 D illustrate the rear side of the sample. The locations of markers was chosen to show in best way the differences in the heat characteristics. The locations of markers in the images on the left hand side correspond to the locations of the markers in the images of the impacted samples. This allows for a comparison of the heat characteristics of the samples before and after impact.

The separation point of the impact side of CSP_3 is shown in Figures 6.13 A and 6.13 B. From these two figures it can be seen that there was no indication of damage on the impact side of the panel. This can be also confirmed in the thermal characteristics graph shown in Figure 6.14 B. The the thermal characteristics of the corresponding markers are coincident, indicating that no damage had occurred in the location of the markers.

Figures 6.13 C and 6.13 D show the middle plane of CSP_3. The same patterns are visible on the infrared images taken before and after impact. Moreover, no changes are visible in the thermal characteristics graphs shown in Figures 6.14 A and 6.14 B. It can be concluded that the internal structure of CSP_3 remained undamaged after the bird impact test.

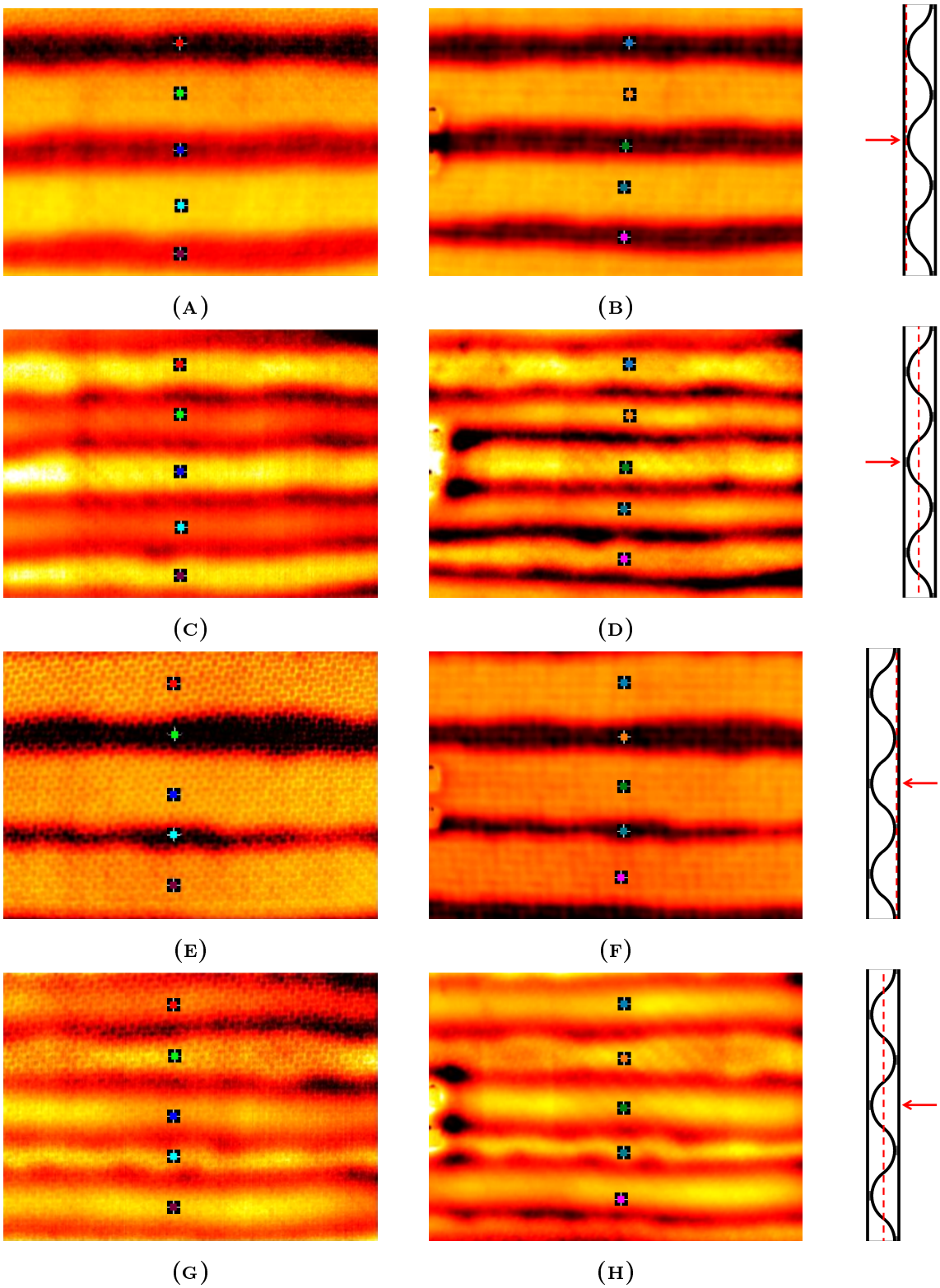

FIGURE 6.13: Thermography inspection of CSP_3 before (BI) and after (AI) bird impact test: (A) Impact side BI, (B) Impact side AI, (C) Impact-mid side BI, (D) Impact-mid side AI, (E) Rear side BI, (F) Rear side AI, (G) Rear-mid side BI and (H) Rear-mid side AI.

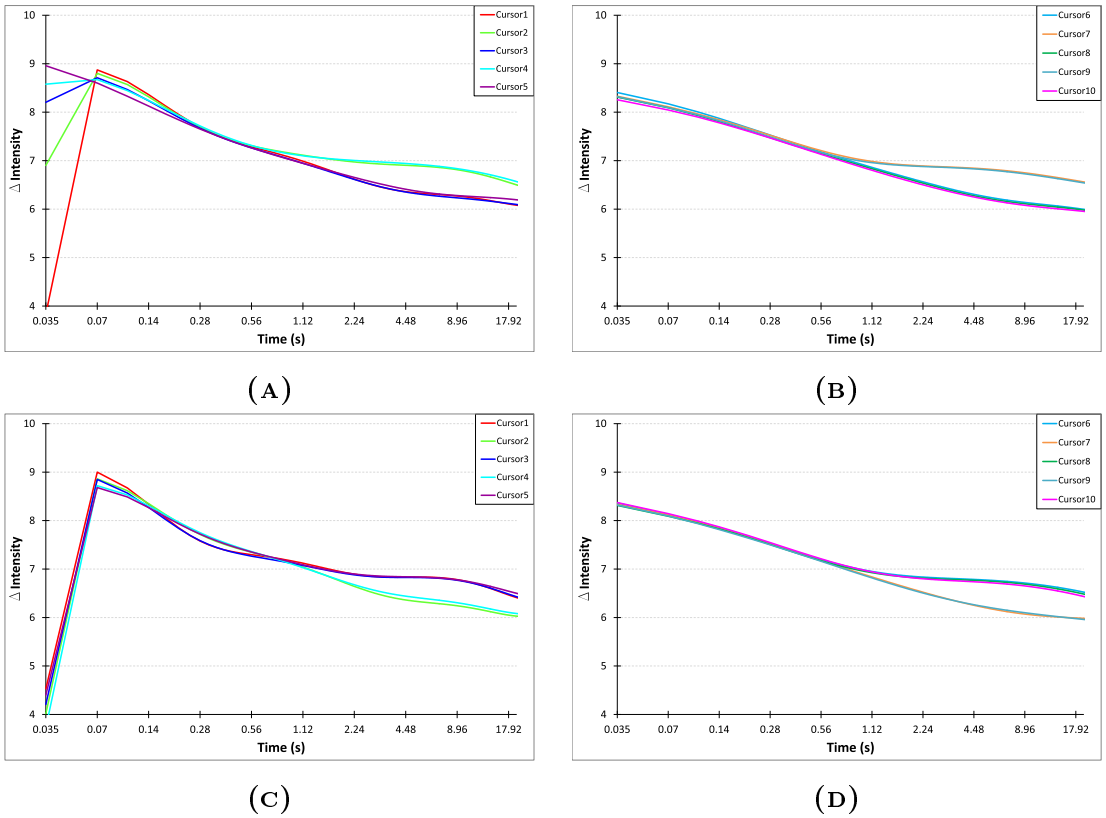

Figure 6.14: Thermal characteristics for CSP_3 before (BI) and after (AI) bird impact test: (A) Impact side BI, (B) Impact side AI, (C) Rear side BI and (D) Rear side AI.

Figures 6.13 E and 6.13 F show the separation point of CSP_3 non-impacted side. Comparison of the inspection results before and after impact proved that there was no damage of the rear surface of CSP_3. This was confirmed from the thermal characteristics graph, shown in Figure 6.14 D. After the separation point, well visible on the graph, the characteristics for the corresponding markers remain coincident, proving that there were no changes in the material due to damage.

The infrared images of the middle plane, taken from the rear side, did not show any type of internal damage of the sample (see Figures 6.13 G and 6.13 H). There was no debonding or subsurface damage visible in the infrared images. The thermal characteristics graph confirmed that no internal damage of the sample had been induced during the impact (see Figure 6.14 D).

6.4.2.4 Tubular sandwich panel TSP_1

The images from the thermography inspection of TSP_1 are shown in Figure 6.15. The corresponding thermal characteristics graphs are shown in Figure 6.16. Figures 6.15 A-6.15 D and Figures 6.15 A-6.15 B illustrate impact side and Figures 6.15 E-6.15 H and Figures 6.16 C-6.16 D illustrate the rear side of the sample. The locations of markers was chosen to show in best way the differences in the heat characteristics. The locations of markers in the images on the left hand side correspond to the locations of the markers in the images of the impacted samples. This allows for a comparison of the heat characteristics of the samples before and after impact.

The separation point for the inspection of TSP_1 is shown in Figures 6.15 A and 6.15 B. The comparison of the images, taken before and after the impact, showed no changes under the impact face sheet of the panel. The initial defects visible in the image taken before the impact did not grow after the bird impact. The thermal characteristics graph (Figure 6.16 B) confirmed that there was no subsurface damage of the sample. Since the markers were placed in the location with no defects, there was no separation of the characteristics curves. The same coincidence of the curves was observed before and after the bird impact. This indicates that the impacted side of the panel did not suffer from any damage after impact.

Infrared images of the middle plane of TSP_1 are shown in Figures 6.15 C and 6.15 D. These images confirmed that there was no damage of the internal structure of the sample.

Figures 6.15 E and 6.15 F show the separation point of the rear side of the tubular panel TSP_1. A comparison of the images shows that the rear face sheet of the sample did not suffer from any damage during the impact. This was confirmed from the thermal characteristic graphs, shown in Figures 6.16 C and 6.16 D. The characteristics curves are coincident, which proves that there was no change in the material due to damage.

The inspection of the middle plane of the TSP_1 rear surface is shown in Figures 6.15 G and 6.15 H. From both figures it can be seen that there were no changes in the internal structure of the sample. The integrity of the sample can be also confirmed from the thermal characteristics graphs, shown in Figures 6.16 C i 6.16 D.

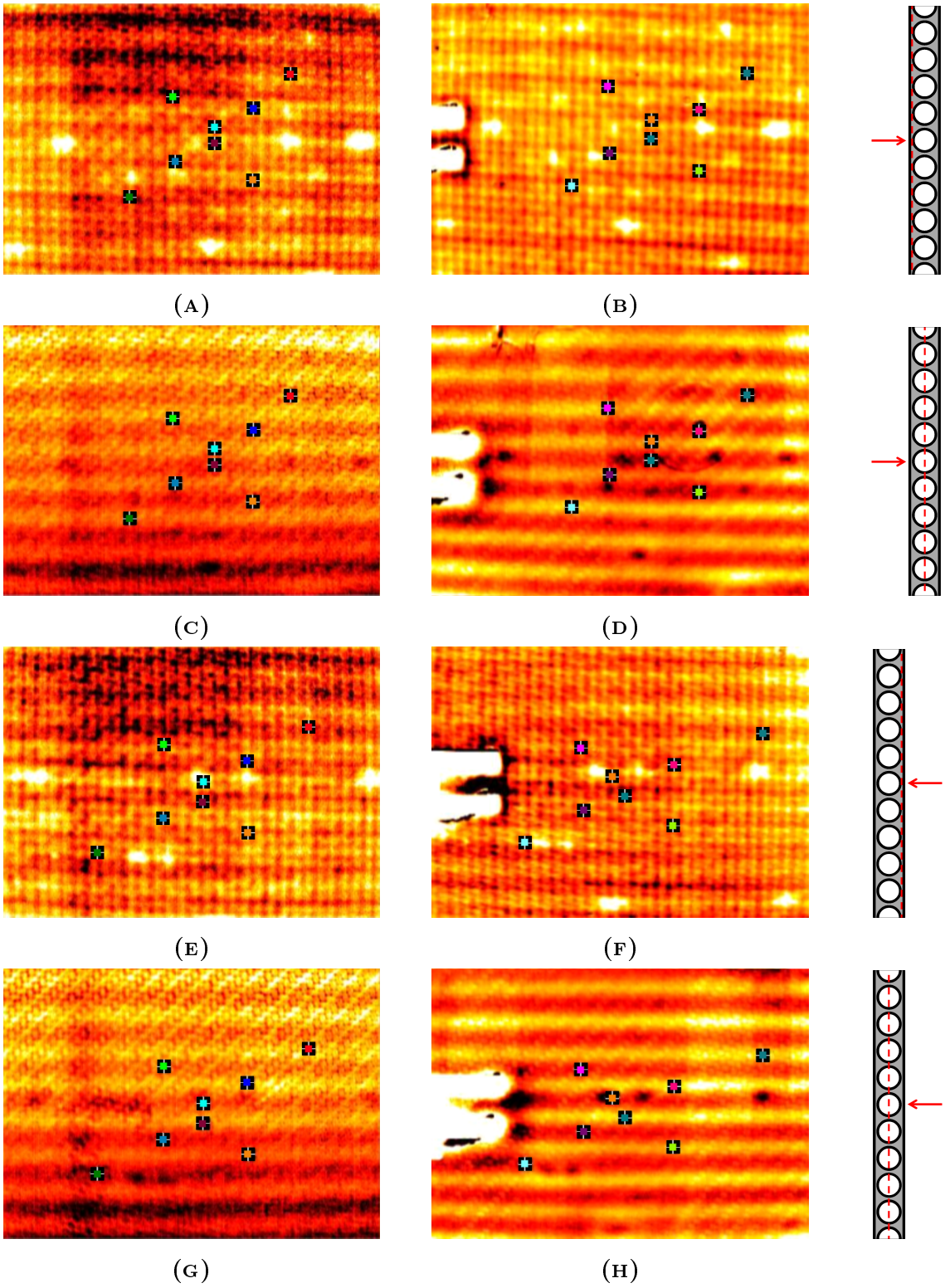

FIGURE 6.15: Thermography inspection of TSP_1 before (BI) and after (AI) bird impact test: (A) Impact side BI, (B) Impact side AI, (C) Impact-mid side BI, (D) Impact-mid side AI, (E) Rear side BI, (F) Rear side AI, (G) Rear-mid side BI and (H) Rear-mid side AI.

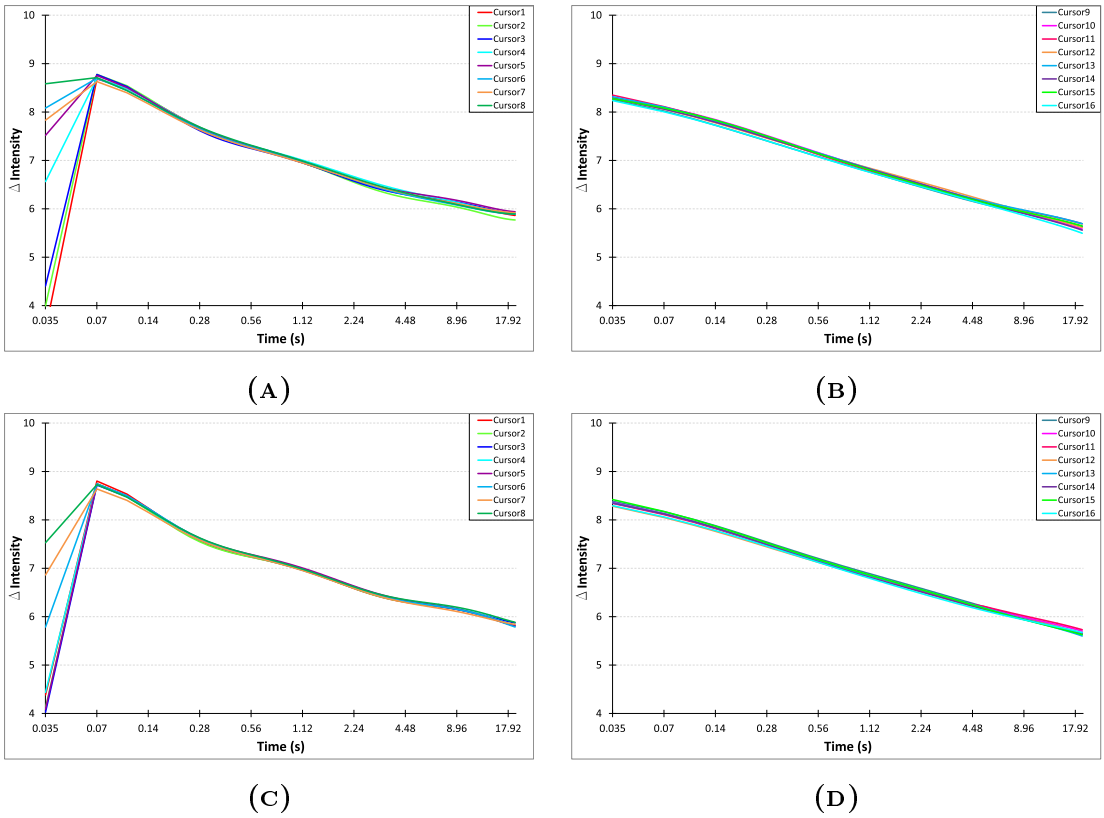

Figure 6.16: Thermal characteristics for TSP_1 before (BI) and after (AI) bird impact test: (A) Impact side BI, (B) Impact side AI, (C) Rear side BI and (D) Rear side AI.

6.4.2.5 Tubular sandwich panel TSP_2

The infrared images from the thermography inspection of TSP_2 are shown in Figure 6.17. The corresponding thermal characteristics graphs are shown in Figure 6.18. Figures 6.17 A-6.17 D and Figures 6.18 A-6.18 B illustrate the impact side and Figures 6.17 E-6.17 H and Figures 6.18 C-6.18 D illustrate the rear side of the panel. The locations of markers was chosen to show in best way the differences in the heat characteristics. The locations of markers in the images on the left hand side correspond to the locations of the markers in the images of the impacted samples. This allows for a comparison of the heat characteristics of the samples before and after impact.

The separation point of the impact side of TSP_2 is shown in Figures 6.17 A and 6.17 B. A comparison of the images shows that the tubular panel did not suffer

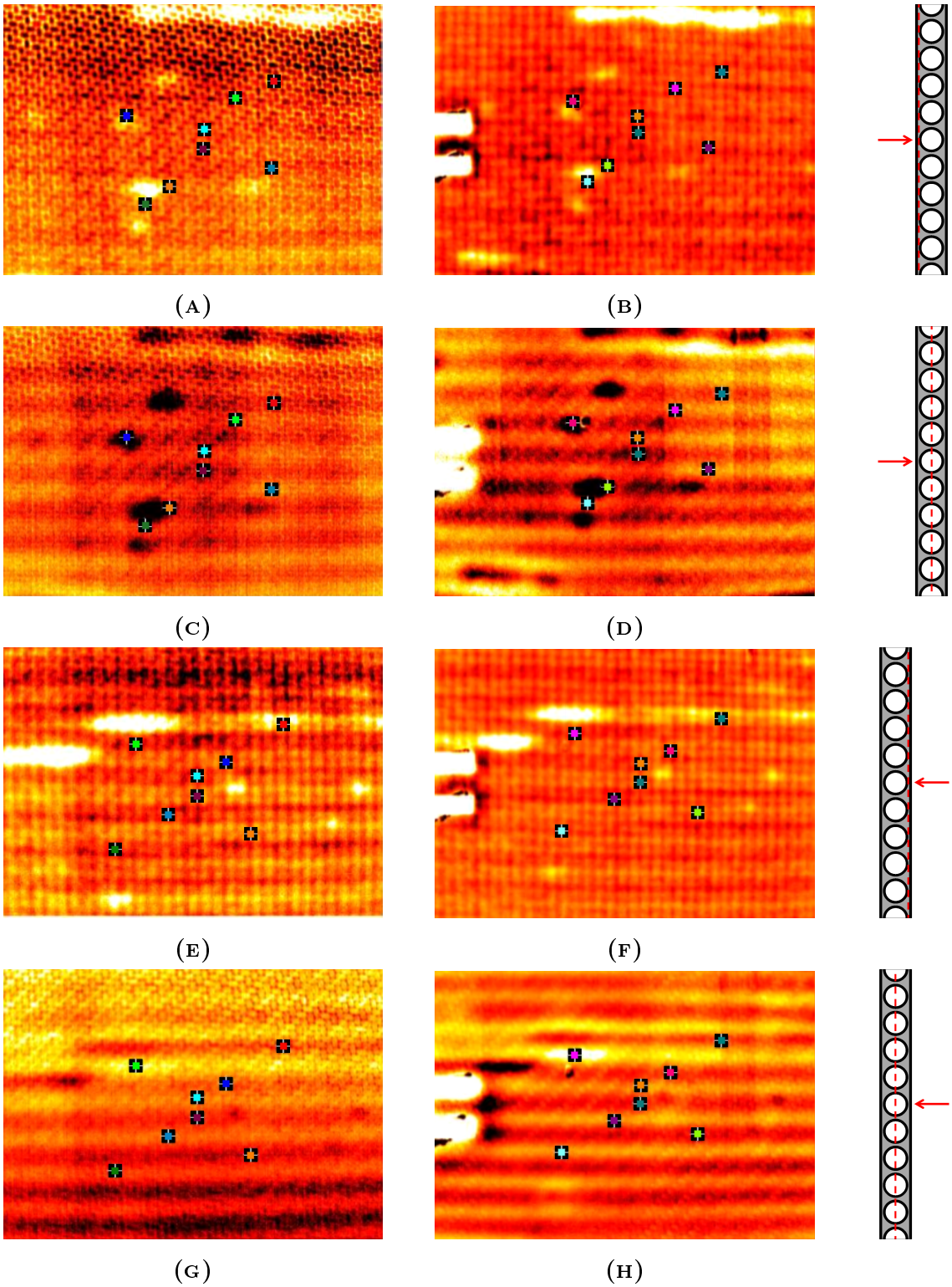

FIGURE 6.17: Thermography inspection of TSP_2 before (BI) and after (AI) bird impact test: (A) Impact side BI, (B) Impact side AI, (C) Impact-mid side BI, (D) Impact-mid side AI, (E) Rear side BI, (F) Rear side AI, (G) Rear-mid side BI and (H) Rear-mid side AI.

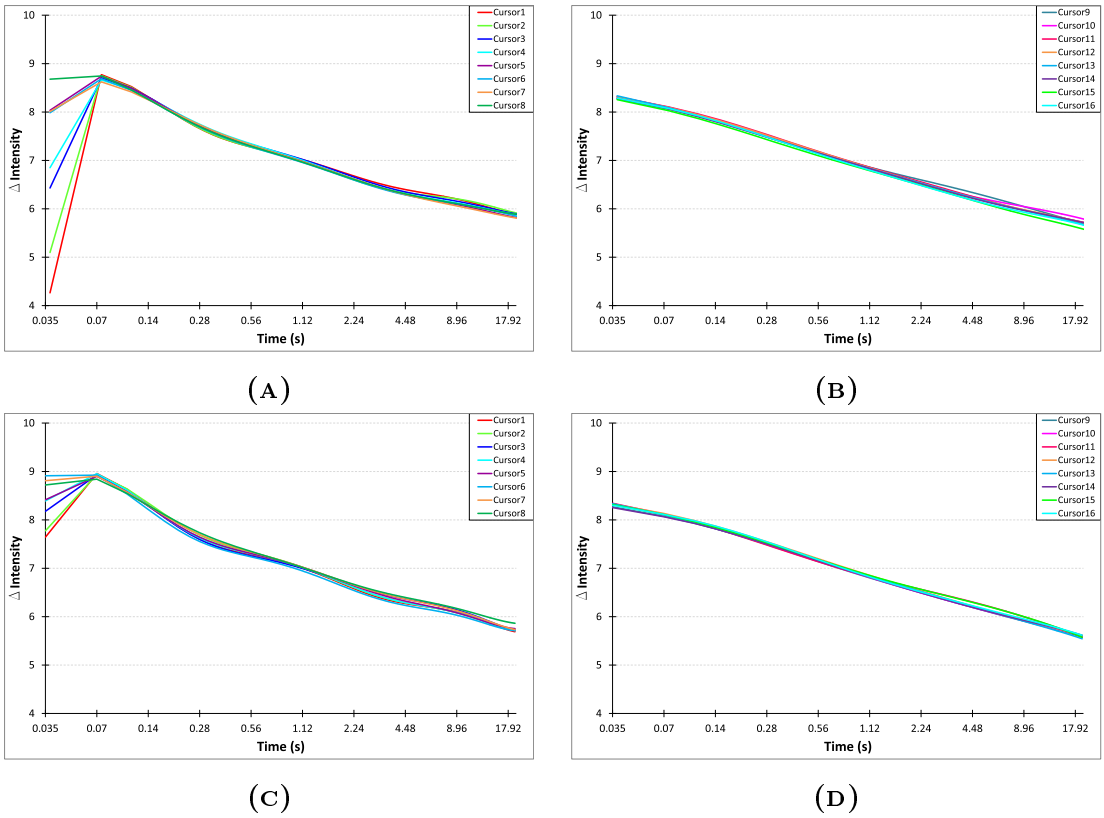

Figure 6.18: Thermal characteristics for TSP_2 before (BI) and after (AI) bird impact test: (A) Impact side BI, (B) Impact side AI, (C) Rear side BI and (D) Rear side AI.

from any damage of the impacted surface. The initial defects visible in Figure 6.17 A showing the state before impact did not grow. The lack of damage was also confirmed by the thermal characteristics graph, shown in Figure 6.18 B. The characteristics curves do not split which indicates that there was no change in the sample structure in the marker locations.

The infrared images of the middle plane of TSP_2 before and after impact are shown in Figures 6.17 C and 6.17 D. Both figures show black spots in the locations of the initial defects which correspond to the locations of the defects visible under the face sheet of the panel. No damage was observed in the infrared images, therefore, the internal structure of the sample did not suffer any damage from the impact.

The separation point of TSP_2 before and after impact is shown in Figures 6.17 E and 6.17 F respectively. A comparison of the images shows that the sample did not

suffer from any damage of the rear face sheet. Only the initial defects are visible on both images as white spots. The lack of damage can be confirmed with the thermal characteristics graphs shown in Figure 6.18 C and 6.18 D. All the characteristics curves remain together for the whole acquisition time, which indicates no change in the material in the markers locations.

Infrared images of the middle plane for the rear side inspection of TSP_2 are shown in Figures 6.17 G and 6.17 H. A comparison of the images did not reveal any type of internal damage of the sample after the impact. No damage was confirmed from the thermal characteristics graph, shown in Figures 6.18 C and 6.18 D

6.4.2.6 Tubular sandwich panel TSP_3

The infrared images from the thermography inspection of TSP_3 are shown in Figure 6.19. The corresponding thermal characteristics graphs are shown in Figure 6.20. Figures 6.19 A-6.19 D and Figures 6.20 A-6.20 B) illustrate the impact side and Figures 6.19 E-6.19 H and Figures 6.20 C-6.20 D) illustrate the rear side of the panel. The locations of markers was chosen to show in best way the differences in the heat characteristics. The locations of markers in the images on the left hand side correspond to the locations of the markers in the images of the impacted samples. This allows for a comparison of the heat characteristics of the samples before and after impact.

The separation point of the impacted side of TSP_3 is shown in Figures 6.19 A and 6.19 B. It is evident that there is no indication of damage on the impacted side of the panel. This is also confirmed from the thermal characteristics graph, shown in Figure 6.20 B. Thermal characteristics for corresponding markers remain together, which indicates that no damage occurred in the locations of the markers.

The middle plane images from the inspection of the impact side of TSP_3 before and after impact are shown in Figures 6.19 C and 6.20 D respectively. A comparison of both figures shows that the internal structure of the sample was undamaged. No changes with respect to the non-impacted sample were observed in the infrared image of the impacted sample.

Figures 6.19 E and 6.19 F illustrate the separation point of the rear side of TSP_3. A comparison of the figures shows that the initial defects, present in the sample

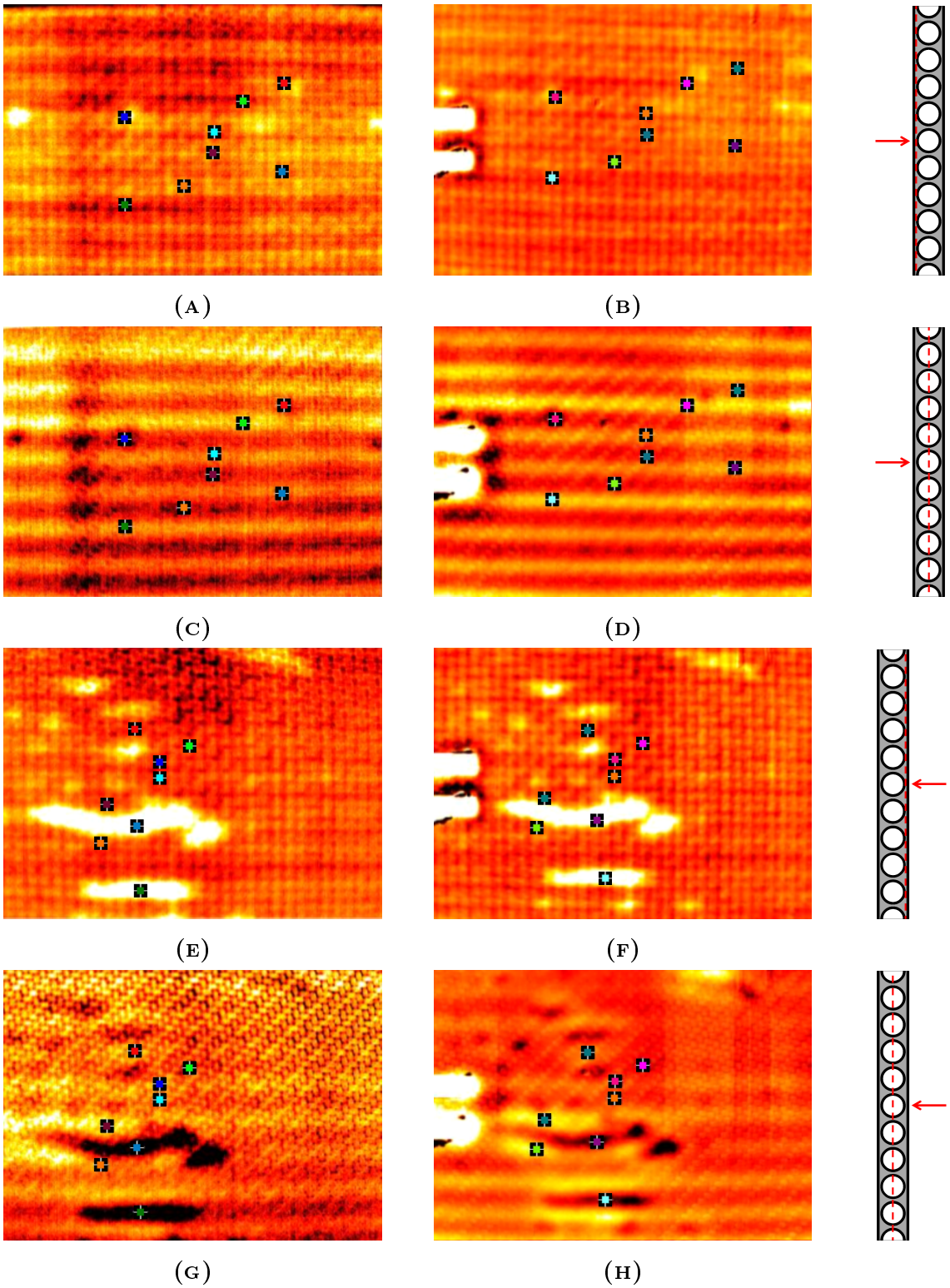

Figure 6.19: Thermography inspection of TSP_3 before (BI) and after (AI) bird impact test: (A) Impact side BI, (B) Impact side AI, (C) Impact-mid side BI, (D) Impact-mid side AI, (E) Rear side BI, (F) Rear side AI, (G) Rear-mid side BI and (H) Rear-mid side AI.

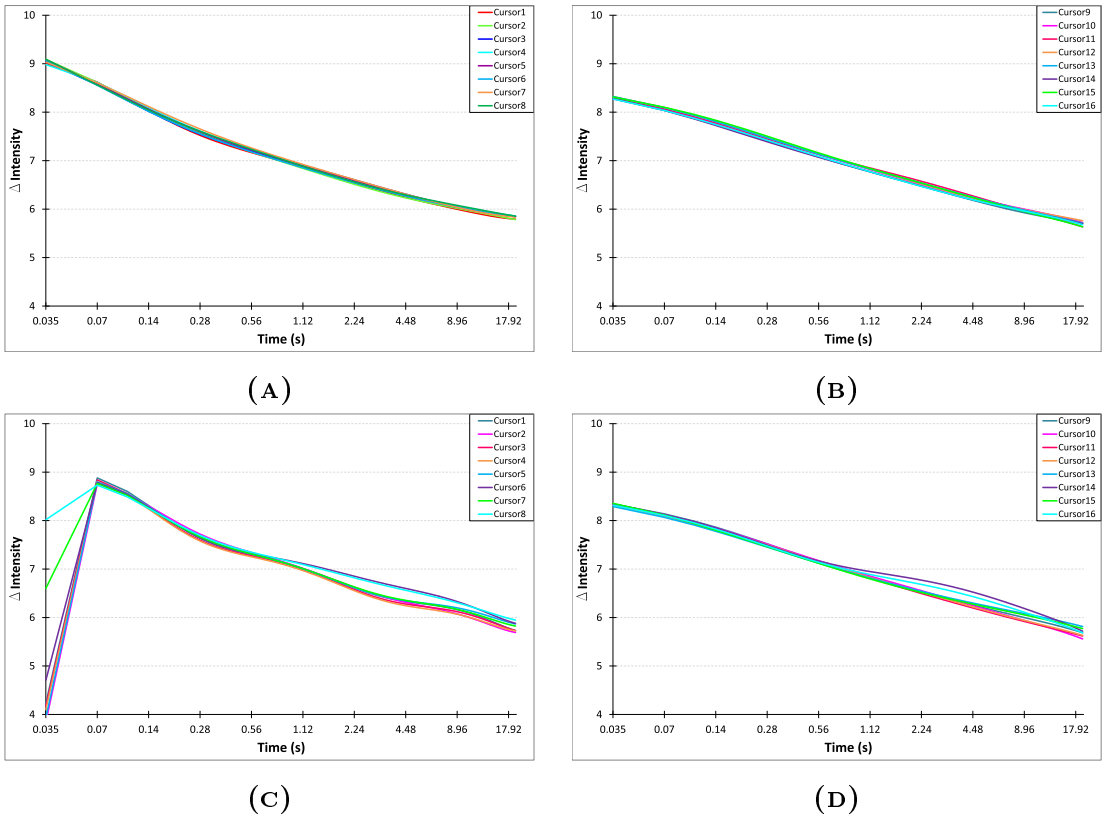

Figure 6.20: Thermal characteristics for TSP_3 before (BI) and after (AI) bird impact test: (A) Impact side BI, (B) Impact side AI, (C) Rear side BI and (D) Rear side AI.

structure before the impact, remain the same after the impact. Therefore, no indication of damage of the sample was observed. The thermal characteristics graphs shown in Figures 6.20 A and 6.20 B confirmed that the sample did not suffer from any subsurface damage. Two markers were located on the initial defects to show the influence of initial structure imperfections on the thermal characteristics. The changes in the thermal characteristics of both defects before and after impact can be identified as changes in the curve slopes (blue and purple curves) in Figures 6.20 A and 6.20 B respectively. The similarities in the thermal characteristic curves before and after impact confirmed that the sample did not get damaged after the bird impact.

Figures 6.19 G and 6.19 H show the middle plane for the inspection of the rear side of TSP_3. They indicate high level of interference in the location of the initial

defects (see black spots in both figures). It is evident that the locations of the defects correspond in the images of the sample, taken before and after impact. No additional defects are visible in the infrared images, therefore, it can be concluded that TSP_3 did not suffer from any internal damage after the bird impact test.

6.4.2.7 Tubular sandwich panel TSP_1 inspection after damage threshold impact

The infrared images from the final thermography inspection of TSP_1 are shown in Figure 6.21. The final inspection was performed after the tubular panel was impacted with the damage threshold velocity of $V_{DTV} = 235\frac{m}{s}$. Figures 6.21 A-6.21 D and Figures 6.21 A-6.21 B illustrate the impact side and Figures 6.21 E-6.21 H and Figures 6.22 C-6.22 D illustrate the rear side of the panel. The corresponding thermal characteristics graphs are shown in Figure 6.22. The markers locations for the thermal characteristics were chosen to show in the best way the changes of the characteristics of samples after impact.

The separation point of the impact side of TSP_1 is shown in Figures 6.21 A and 6.21 B. It is evident that the sample got damaged after the bird impact. The damage of the sample is concentrated in the vicinity of the impact location. The damage is also indicated very well on the heat characteristics graph, shown in Figure 6.22 B. The purple line, corresponding to the purple marker located on the black spot, is separated from other lines which indicates damage in the material. Moreover, the light blue and blue curves are slightly separated from the other curves which indicates that there might be some delamination initiation at the location of the corresponding markers.

Figures 6.21 C and 6.21 D show the middle plane for the inspection of impact side of TSP_1. Figure 6.21 D shows the damage of the tubular sample internal structure. Comparing the damage shapes with Figure 6.21 B, it is evident that the damage shape had changed. This indicates that the depth of the damage was quite significant. Therefore, from Figures 6.21 B and 6.21 D could be concluded that not only the face sheet of the tubular panel TP_1 got damaged but also the composite tube. However, from both figures it can be seen that the damage was limited to the area between the three central tubes.

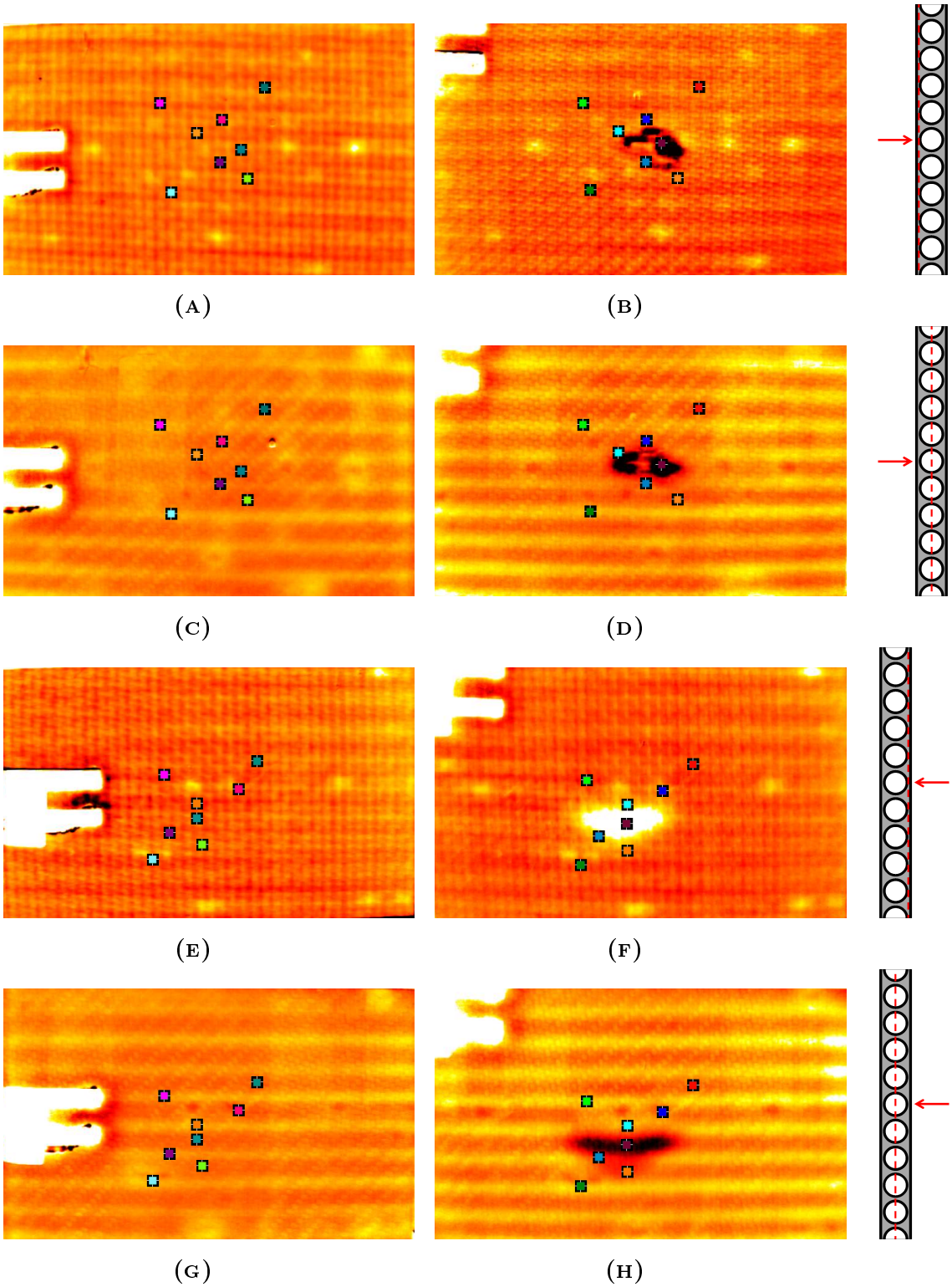

FIGURE 6.21: Thermal characteristics for TSP_1 before (BI) and after (AI) damage threshold impact test: (A) Impact side BI, (B) Impact side AI, (C) Impact-mid side BI, (D) Impact-mid side AI, (E) Rear side BI, (F) Rear side AI, (G) Rear-mid side BI and (H) Rear-mid side AI.

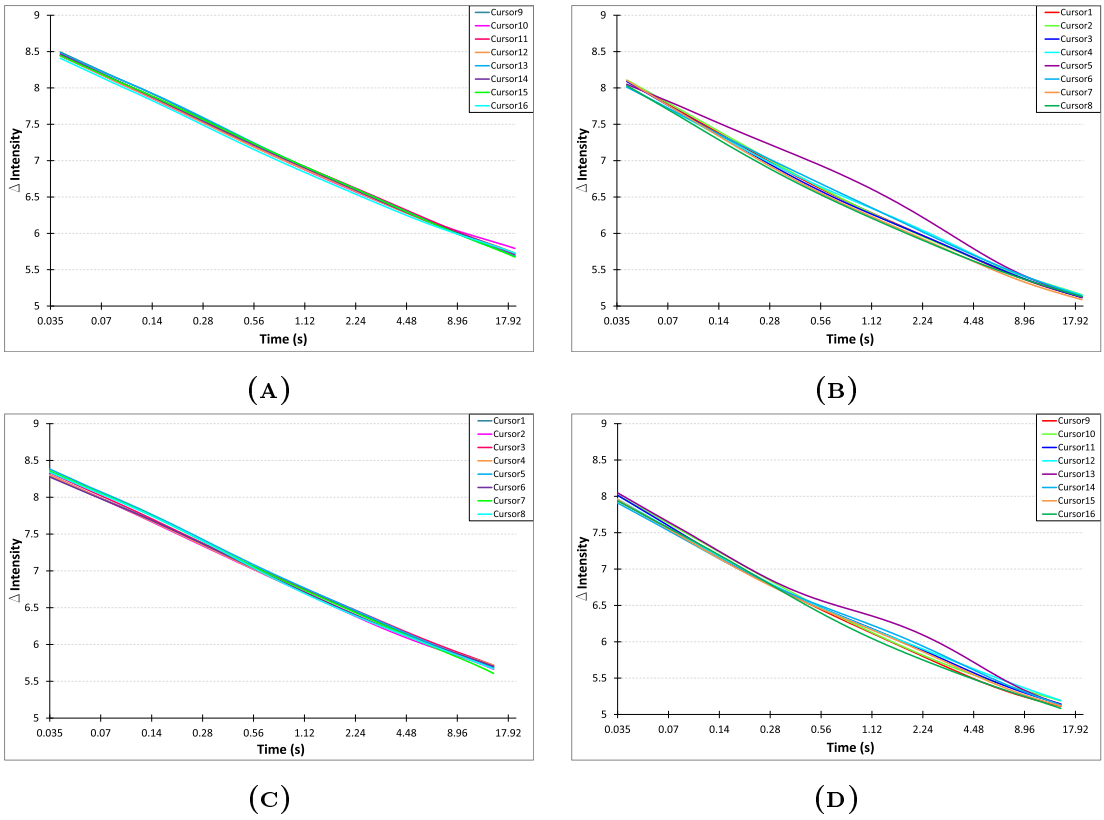

Figure 6.22: Thermal characteristics for TSP_1 before (BI) and after (AI) damage threshold impact test: (A) Impact side BI, (B) Impact side AI, (C) Rear side BI and (D) Rear side AI.

Figures 6.21 E and 6.21 F show the separation point for the inspection of the rear surface of the sample. A comparison of both figures (before and after impact) indicates that that there was significant damage on the rear side of the panel, which was not visible during the visual inspection. Therefore, the damage of the sample was not restricted to the impacted face sheet only, but it also affected the rear side of the panel. The damage of the material is confirmed from the thermal characteristics graph, shown in Figure 6.22 D. The purple curve, corresponding to the purple marker located on the white spot (see Figure 6.21 F), splits significantly from the remaining curves. This indicates that the material got damaged in the vicinity of the purple marker location.

The middle plane for the rear side inspection of TSP_1 is shown in Figures 6.21 G

and 6.21 H. Comparison of the figures clearly shows that the rear face sheet got damaged. The high interference visible in the middle plane image (black spot in in Figure 6.21 F) indicates that the damage of the rear side of the sample was severe.

6.5 Discussion

The bird impact tests were performed to investigate the soft body impact resistance of the novel composite sandwich panels. Initially they were performed at a velocity corresponding to 120% of the take-off safety speed of most of the commercial aircraft including Boeing 747 and Airbus A380.

The novel composite sandwich panels introduce a significant mass saving over the corresponding solid composite panels of the same thickness. The mass of an equivalent 10 mm thick solid carbon fibre panel is approximately $m = 288\ g$. The masses of the corrugated and tubular panels are respectively $m_{CSP} = 90\ g$ and $m_{TP} = 180\ g$, i.e. they are more than 3 times and 1.6 times lighter than the solid composite panel respectively.

One of the biggest concerns of the bird impact experiment was the quality of the manufactured birds and their ability to reproduce the hydrodynamic behaviour in every test case.

The images illustrating the bird impact sequence (see Figure 6.4) showed that the behaviour of the bird was hydrodynamic along the entire impact duration. Such behaviour was expected based on the bird impact theory. As soon as the bird touched the plate, its material started splashing on the target surface. The longitudinal motion of the fluid changes into a radial motion while the bird energy is transferred to the plate. The hydrodynamic behaviour of the bird proves that the bird density is the primary parameter in the energy transfer and that the mechanical properties of the bird did not influence the energy transfer.

The impact resistance of the novel composite samples was assessed based on the extent of the damage caused by the impacting bird. The surface damage of the sample was examined during the visual inspection of the samples and the subsurface (internal) damage of the panels was examined during the thermographic inspection.

Both forms of the corrugated and tubular sandwich panels inspection were described in Section 6.4.

Three corrugated sandwich panels were subjected to bird impact at a velocity of $V_i = 115\frac{m}{s}$. In all cases, the corrugated sandwich panels absorbed the bird impact energy. The face sheets of two panels got damaged during the impact. No subsurface damage of the samples was observed. Moreover, the rear face of the corrugated samples did not have any indication of damage.

The infrared inspection of CSP_1 after impact showed that it suffered only from visible damage of the impacted surface. The extent of the damage was sightly bigger than the one observed in the visual inspection of the sample. However, the internal structure of the corrugated panel CSP_1 was intact. No delamination of the corrugated panel or back face sheet was observed. Moreover, there was no debonding between the face sheet panels, the corrugated panel and the foam core.

Inspection of CSP_2 showed severe damage of the impacted surface. However, the damage was only restricted to the impacted face sheet and no damage of the internal structure was observed. During the inspection, no damage of the rear surface of the panel was detected. Moreover, no debonding between the face sheet panels, the corrugated panel and the foam was observed.

The thermography inspection of CSP_3 showed that the sample was not damaged during the bird impact test. The impacted and rear surfaces of the sample did not suffer from any subsurface damage. Moreover, there was no indication of debonding between the face sheet panels, the corrugated panel and the foam core.

The first set of bird impact tests on the novel tubular sandwich panels was performed with a bird impact velocity of $V_i = 115\frac{m}{s}$. In all impact cases, the entire bird energy was absorbed by the panels. The samples manufactured from carbon fibre face sheets with carbon fibre tubes and foam core showed excellent impact resistance to the bird impact. Visual and thermographic inspection of the tubular samples showed that all the samples remained intact and did not suffer from any external or internal damage.

The thermographic inspection of TSP_1 did not reveal any indication of damage of the panel. The thermal characteristics graphs and the infrared images proved that there was no internal damage of the sample, which is the biggest threat for

composite materials. There was no debonding between the composite tubes and the face sheet panels or foam core. Moreover, the rear surface of the composite panel remained intact.

The same results were observed for samples TSP_2 and TSP_3.

Since the first impact tests did not cause any damage to the tubular sandwich panels, it was decided to investigate their soft body damage threshold. Three shots were performed at velocities of $V_{i1TSP} = 160\frac{m}{s}$, $V_{i2TSP} = 172\frac{m}{s}$ and $V_{i3TSP} = 210\frac{m}{s}$ for the tubular panels TSP_1, TSP_2 and TSP_3 respectively. The bird impact energies for the corresponding velocities were $E_{i1TP} = 317\ J$, $E_{i2TP} = 346\ J$ and $E_{i3TP} = 547\ J$. For these impact velocities the energy of the bird was absorbed and no damage was detected within the samples structure during the inspections.

Finally, it was decided to test the tubular sandwich panels at the maximum impact pressure of $p_i = 40\ bar$. Since the bird release system was designed for bird velocities of approximately $120\frac{m}{s}$, the release of the bird became a considerable concern for the remaining samples. Therefore, it was decided to increase the thickness of the sabot floor from 4 mm to 20 mm to prevent sabot floor penetration through the sabot splitter channel.

The thermographic inspection of TSP_1 after the damage threshold impact test showed that the extend of the panel damage was much higher than the one observed during the visual inspection of the sample. The bird impacting with $V_{DTV} = 235\frac{m}{s}$ induced damage on both sides of the panel. The impacted side of the panel got damaged in close vicinity of the impact location. Moreover, subsurface damage of the impacted side was revealed during the thermographic inspection. The thermographic inspection also exposed subsurface damage of the rear face sheet of the panel. The high interference and different shapes of the damage, visible in the images of the separation point and the middle plane, indicate that the damage of the sample interior was severe.

Snap shots of the bird impact sequence are shown in Appendix C.2. From the figures it can be seen that the bird did not preserve its initial shape after the release from the sabot.

In all cases, the kinetic energy of the bird was absorbed by the panel. The visual inspection of the tubular samples showed damage of the impacted surface of the

panels as described in Section 6.4. The thermographic inspection of the tubular samples revealed the subsurface damage. Debonding between the composite tubes and the face sheets was the main damage mode. From the infrared images it could be seen that the tubular structure restricted the damage propagation between the tubes. Such damage propagation restriction is highly desirable for aircraft structures, since any occurring damage could be enclosed in a finite region of the structure.

Lack of internal damage and surface damage are quite unusual for composite materials. Usually, composites suffer from barely visible damage of the impacted surface and quite extensive damage of the internal structure. Implementation of the novel composite panels could reduce the problem related to the barely visible damage of composites.

The good impact resistance of the corrugated and tubular sandwich panels could be of significant interest to aircraft manufacturers, as well as to other areas of industrial design where soft body impact resistance has an influence on the safety of structures and people. Moreover, these two designs enable for a considerable mass reduction in comparison to the solid composite panels of the same thickness.

Further studies are required in order to validate the impact resistance of the corrugated and tubular sandwich panels subjected to an impact with a hard impactor. Moreover, additional tests consisting of soft body impact with bigger projectiles are required to assess the performance of the samples for higher impact energies.

6.6 Conclusions

- The gelatine bird model used was able to reproduce the hydrodynamic behaviour of a real bird during the impact test.
- The corrugated panels are more than 3 times lighter than the solid carbon epoxy panel of the same thickness. The tubular panels are more than 1.6 times lighter than the corresponding solid carob epoxy panels.
- The corrugated sandwich panels showed good impact resistance for the bird impact at a velocity of $V_i = 120\frac{m}{s}$. The impacted panels suffered only from visible impact damage of the face sheets. No internal damage of the samples was detected during the performed thermographic inspection.

- The tubular sandwich panels showed excellent impact resistance for velocities up to $V_i = 210\frac{m}{s}$. There was no indication of damage on the impacted surface for this type of sandwich samples. Furthermore, the internal structure and the rear surface remained undamaged after impact.

- The damage threshold of the composite tubular panels for the soft body impact was found at $V_{DTV} = 235\frac{m}{s}$. For such high impact velocity, the sample suffered from visible damage on the impacted surface. Moreover, delamination underneath the impacted face sheet was detected during the thermographic inspection. Considerable damage was also detected underneath the rear surface of the impacted panel.

Chapter 7

Numerical modelling of bird strike on novel composite panels

7.1 Introduction

This chapter provides a description of the numerical modelling of bird impact on the novel composite panels. For better understanding, the structure of the chapter is illustrated in Figure 7.1.

In the first part of the chapter, the validation of the SPH bird model is described. The model was used further to validate the gelatine bird, used in the experiment of Chapter 6, with an additional test case of bird impact on a thin aluminium plate.

In the subsequent section, the model development for the corrugated and tubular panels is described. In this section, the model creation and all the assumptions and parameters defining the model are presented.

Subsequently, the analysis of the bird impact results on the novel composite panels is presented together with a comparison of the numerical and experimental results. To evaluate the impact resistance of the novel sandwich panels, analysis of the bird impact on the standard sandwich panel was performed. Furthermore, the results of the analyses were compared in terms of the damage extent and energy absorption.

Finally, the conclusions drawn from the bird impact analysis and comparison to the experimental results are presented.

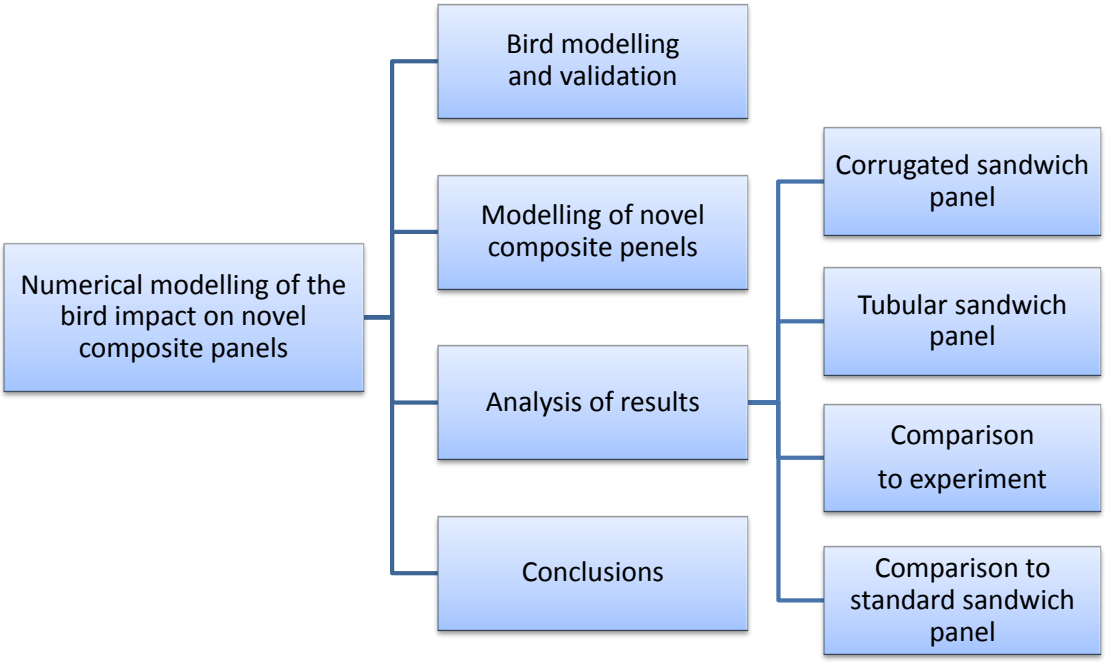

FIGURE 7.1: Chapter 7 structure.

7.2 Bird modelling and validation

In order to perform reliable numerical analysis of the bird impact, it was necessary to first validate the bird model. Similarly to the case of bird impact on the rotating fan blades, the bird for the bird impact on composite samples was modelled with SPH particles.

The bird validation was based on a comparison of the bird impact pressures with the calculated Hugoniot and stagnation pressures for an impact velocity of $V_i = 115\frac{m}{s}$. Based on the validated numerical bird model, the validation of the birds used for the tests was performed. The gelatine bird was validated by comparison of the numerical and experimental results for the bird impact on the thin aluminium plate.

Even though the bird used for the experiment was initially cylindrical, during the release stage the flat surface of the bird front got rounded, as shown in Figure 7.2 A. Therefore it was decided to model the bird as a hemispherical cylinder. The bird was modelled with 21000 particles with a 1 mm pitch. It was decided to use uniform mesh in order to preserve the same initial distance between the particles and

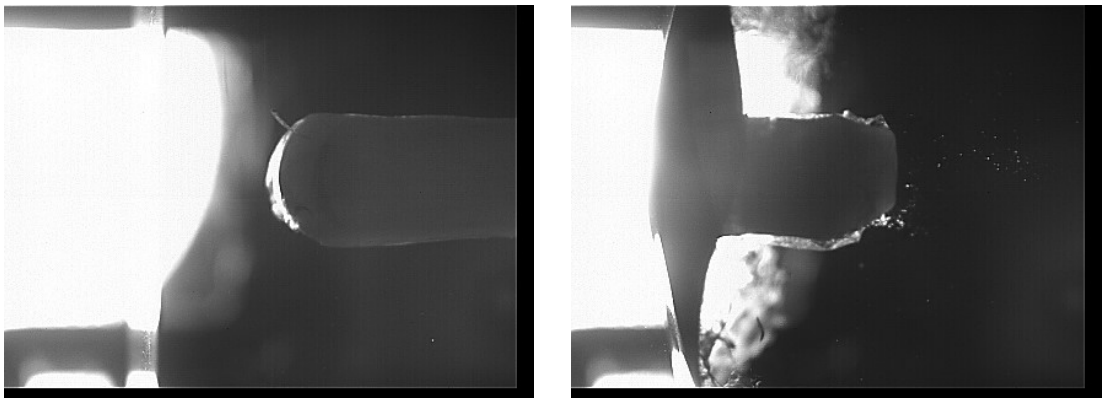

(A) (B)

FIGURE 7.2: The shape of the bird during the impact: (A) Front end of the bird, (B) Back end of the bird.

therefore the initial smoothing length. The initial smoothing length was $h = 1.2\,mm$. The bird was modelled with ELASTIC_PLASTIC_HYDRODYNAMIC material model. The diameter of the bird was equal to $d_b = 25\ mm$, which corresponded to the diameter of the bird used for the bird impact tests. The length to diameter ratio of the bird was equal 2.

The validation tests consisted of two bird impact cases, namely, normal and oblique impact on a rigid target. The rigid target was modelled in LS-DYNA with rigid walls. Five rigid walls were used in order to read the pressures in the centre of impact. A small rigid wall was placed in the centre of impact to determine the impact forces, based on which, the pressures at the centre of impact were calculated. Additional four rigid walls were surrounding the small rigid wall and formed the flat target for the bird. The same technique for pressure readings was used for the oblique impact. However, in this case the rigid walls were defined at an angle $\alpha = 45°$, measured to the direction of the bird motion.

The Hugoniot and the stagnation pressures were calculated from Equation 7.1 7.2 respectively.

$$P_H = \rho\ V_0\ C_0\ \sin\alpha \tag{7.1}$$

$$P_S = \frac{1}{2}\ \rho\ V_0 \tag{7.2}$$

Where ρ is the material density, V_0 is the impact velocity, C_0 is the speed of sound in the material and α is the impact angle.

The density of gelatine was $\rho = 9.7\frac{g}{cm^3}$, the impact velocity was $V_0 = V_i = 115\frac{m}{s}$ and the speed of sound in gelatine was $C_0 = 1481\frac{m}{s}$. Therefore, for the normal impact the Huguniot pressure was $P_H = 165\ MPa$ and the stagnation pressure $P_S = 6.4\ MPa$. For the oblique impact the Huguniot pressure was $P_H = 120\ MPa$. The stagnation pressure is not dependent on the impact angle, therefore, its value was the same for both impact cases. The results of the bird impact analyses for the normal and oblique impact are shown in Figure 7.3. The pressures measured during the analyses and the time were presented in the non-dimensionalised form, obtained by dividing the pressure by the steady flow stagnation pressure value, and the time divided by the theoretical duration of impact (length of the bird divided by its initial velocity).

Based on the calculated pressures and the pressures measured during the bird impact analysis, it could be seen that for the normal impact the results agreed very well. Moreover, the pressure distribution agrees well with the pressure distribution measured by Wilbeck (1978) for a gelatine projectile (see Figures 7.3 A and 7.3 C). In the case of the oblique impact, the stagnation pressure distribution agreed quite well with the pressure distribution obtained by Wilbeck (1978) within their experiments (see Figures 7.3 B and 7.3 D). However, the average pressure value was slightly lower than the calculated stagnation pressure. The peak pressure in the case of the oblique impact did not agree with the calculated value of Hugoniot pressure. The differences might be related to slightly different centre position of the rigid wall. In general, the pressure distribution agrees with the experimental results of Wilbeck (1978). Therefore, the validation of the numerical bird was completed.

In order to validate the gelatine bird manufactured for the experiment, it was decided to perform the bird impact test on a thin aluminium plate. The results from the test were compared to the numerical results in terms of the plate centre displacement and the final deformed shape of the plate.

A plate of 1 mm thickness was made of the aluminium alloy Al 6082-T6. The full length of the aluminium plate was $l = 210\ mm$ and the span between the fitting frames was equal to $l_i = 110\ mm$. Holes were drilled near the edges of the plate to

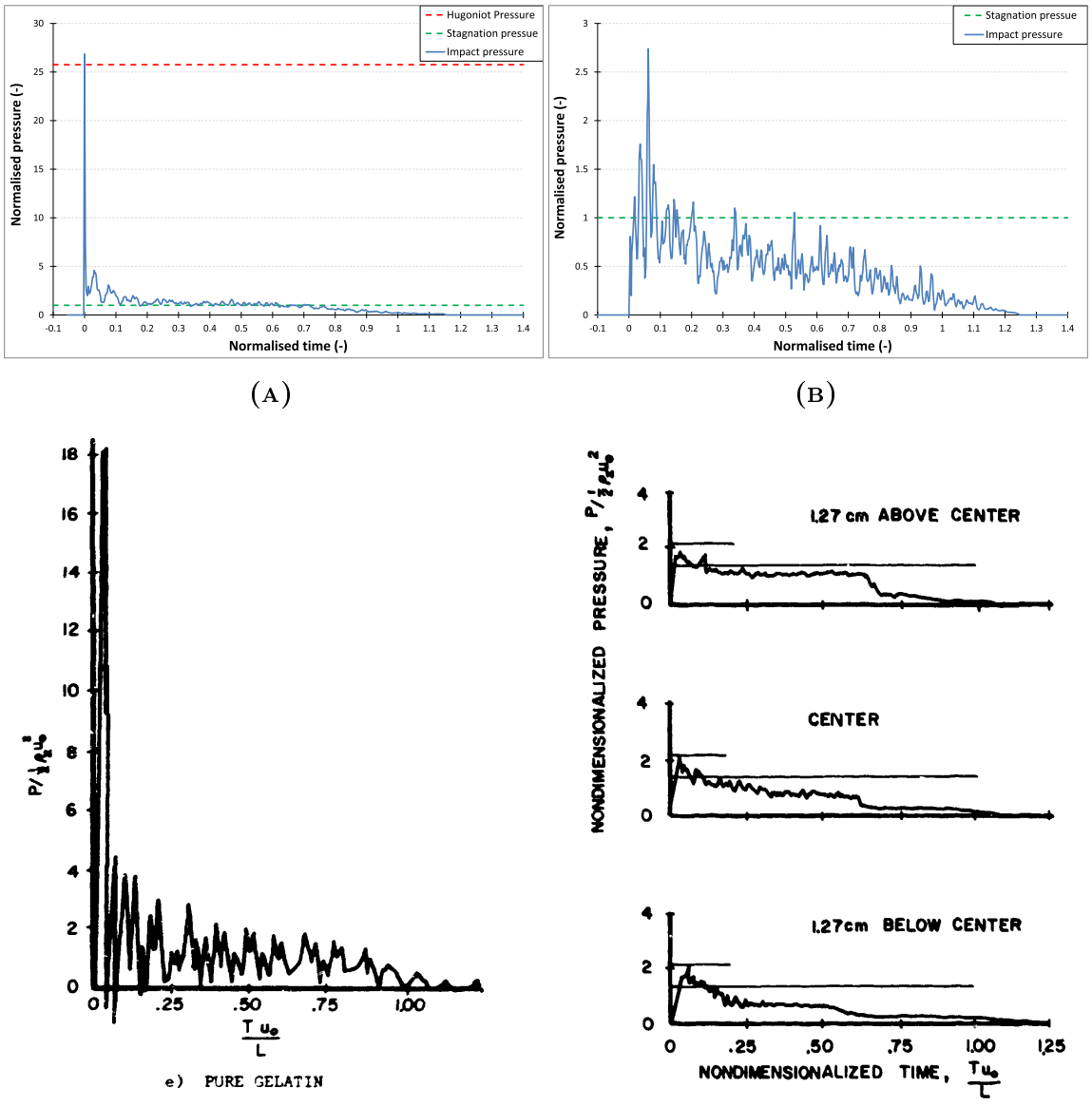

FIGURE 7.3: Bird impact pressures measured at the centre of impact: (A) Normal impact, (B) Oblique impact ($\alpha = 45°$), (C) Normal impact of gelatine projectile (Wilbeck, 1978), (D) Oblique impact ($\alpha = 45°$) of gelatine projectile (Wilbeck, 1978).

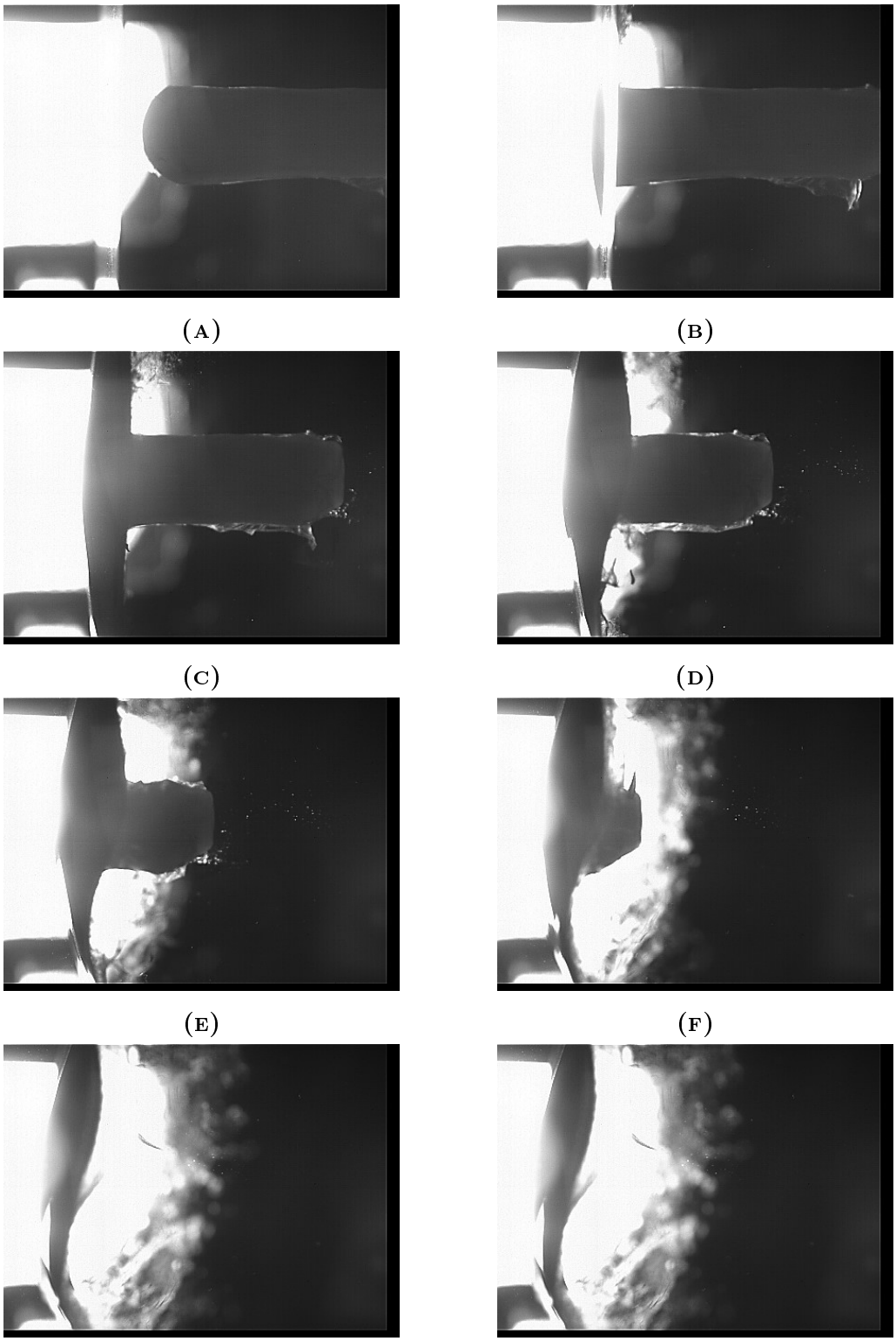

(A) (B) (C) (D) (E) (F) (G) (H)

FIGURE 7.4: Bird impact sequence images at time intervals 0.8 *ms*.

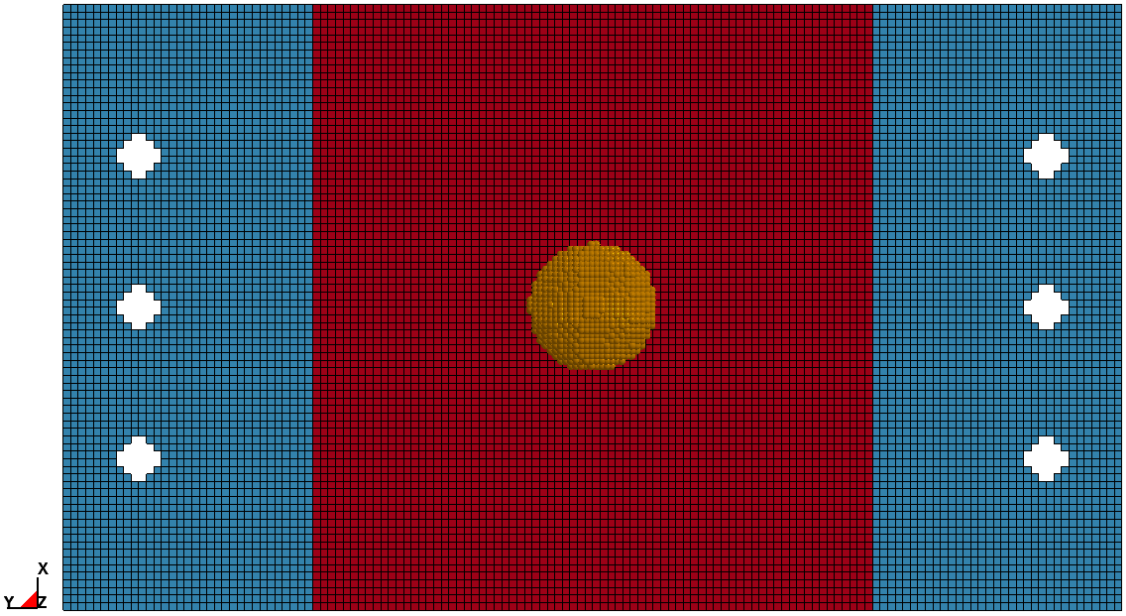

Figure 7.5: Analysis setup for the bird impact on aluminium plate.

allow for fixing the plate directly to the fixing frame with M10 bolts. Such clamping method was necessary to prevent the plate from being ripped off from the clamps during the impact.

The settings for the high speed camera recording the bird impact tests were the same as described in Section 6.2.3. The position of the camera on the side of the safety chamber allowed for recording the deformation of the plate during the experiment. The bird impact velocity measured during the impact test was $V_i = 117\frac{m}{s}$. The bird impact sequence is shown in Figure 7.4. The full sequence of the bird impact is presented in Appendix C.3.

The numerical analysis of the bird impact on the aluminium plate was performed with LS-DYNA. The bird used for the analysis was described previously in this section. The velocity assigned to the bird was equal to the impact velocity measured from the test. An automatic nodes to surface contact algorithm was used to assure the interaction between the bird and the plate. In order to reduce the vibration of the plate after the bird impact, the damping of the plate was activated after there was no more interaction between the bird and the plate. The damping coefficient was calculated based on the natural frequency of the plate. The aluminium plate

was modelled with the Johnson-Cook material model combined with the Gruneisen EOS. The material parameters for the Johnson-Cook material model are shown in Table 7.1 (P. et al., 2013) and the corresponding parameters for the Gruneisen EOS are given in Table 7.2 (Steinberg, 1996).

Table 7.1: Johnson-Cook material properties for Al 6082-T6 (Lesuer, 2000).

Parameter	Notation	Value	Unit
Density	ρ	2.7×10^3	$\frac{kg}{m^3}$
Yield strength	σ_y	305.72	MPa
Young's modulus	E	70×10^3	MPa
Shear modulus	G	27.48×10^3	MPa
Strain hardening modulus	B	304.9	MPa
Strain rate dependence coefficient	C	0.00437	-
Temperature dependence exponent	m	1.31	-
Strain hardening exponent	n	0.6796	-
Melting temperature	T_m	1878	K
Heat capacity	C_P	875	$\frac{J}{kgK}$

Table 7.2: Grüneisen EOS parameters for Al 6082-T6 (Steinberg, 1996).

Parameter	Notation	Value	Unit
Velocity curve intercept	C	5.24×10^3	$\frac{m}{s}$
First slope coefficient	S_1	1.4	-
Grüneisen coefficient	γ_0	1.97	-
First order volume correction coefficient	b	0.48	-

Six elements through the thickness of the plate were used to correctly reproduce the bending behaviour of the plate. The element size in the in plane direction was 1.5 mm. In order to make the numerical model as close to the reality as possible, the holes in the plate were modelled by removing the elements. Fixed boundary conditions were applied to the elements at the edges of the holes in order to represent the clamping of the plate. Moreover, the elements representing the part of the plate supported by the fixing frame were simply supported in the direction normal to the plate. The bird impact set up is shown in Figure 7.5.

From the images of the bird impact sequence, it can be seen that the bird behaviour was hydrodynamic. Moreover, it could be seen that the maximum displacement

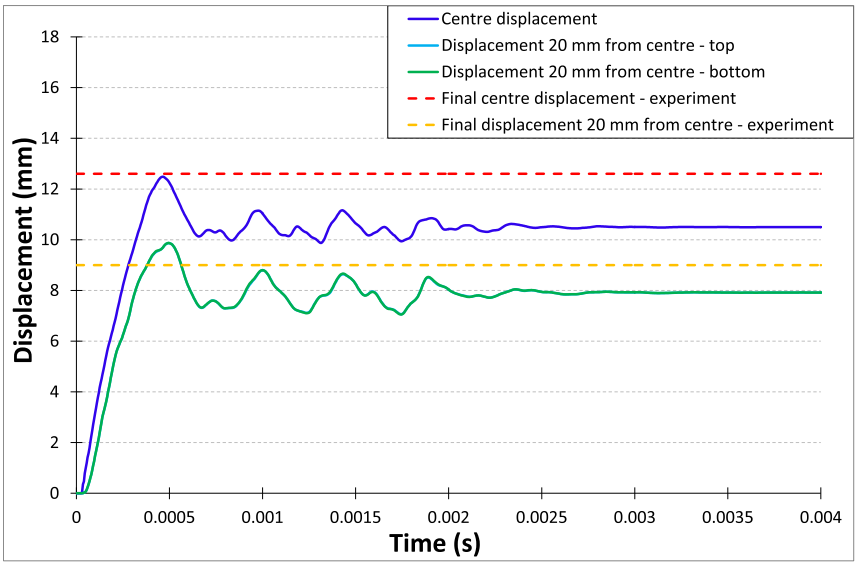

FIGURE 7.6: Displacement time histories measured in the impact centre and 20 *mm* from the centre of impact.

of the aluminium plate was greater than the final displacement. The elastic response of the plate reduced the final displacement after impact termination. The final displacement of the aluminium plate centre was 12.6 *mm* (see Table 7.3). The displacement time history graph is shown in Figure 7.6. Accordingly to the experiment, the maximum displacement of the plate centre was greater than the final displacement. The final displacement measured from the analysis was 10.5 *mm*. The displacements measured 20 *mm* from the maximum displacement were 9 *mm* after the test and 8 *mm* from the numerical analysis.

TABLE 7.3: Aluminium plate displacement after bird impact test.

	Experiment		**Numerical analysis**	
	Centre	20 mm from centre	Centre	20 mm from centre
Maximum displacement	-	-	12.6	9.88
Final displacement	12.6	9	10.5	8

Final deformed shapes of the aluminium plate after the bird impact test and numerical analysis are illustrated in Figure 7.7. White markers in Figure 7.7 indicate the location of the displacement measurement points. It is evident that the final

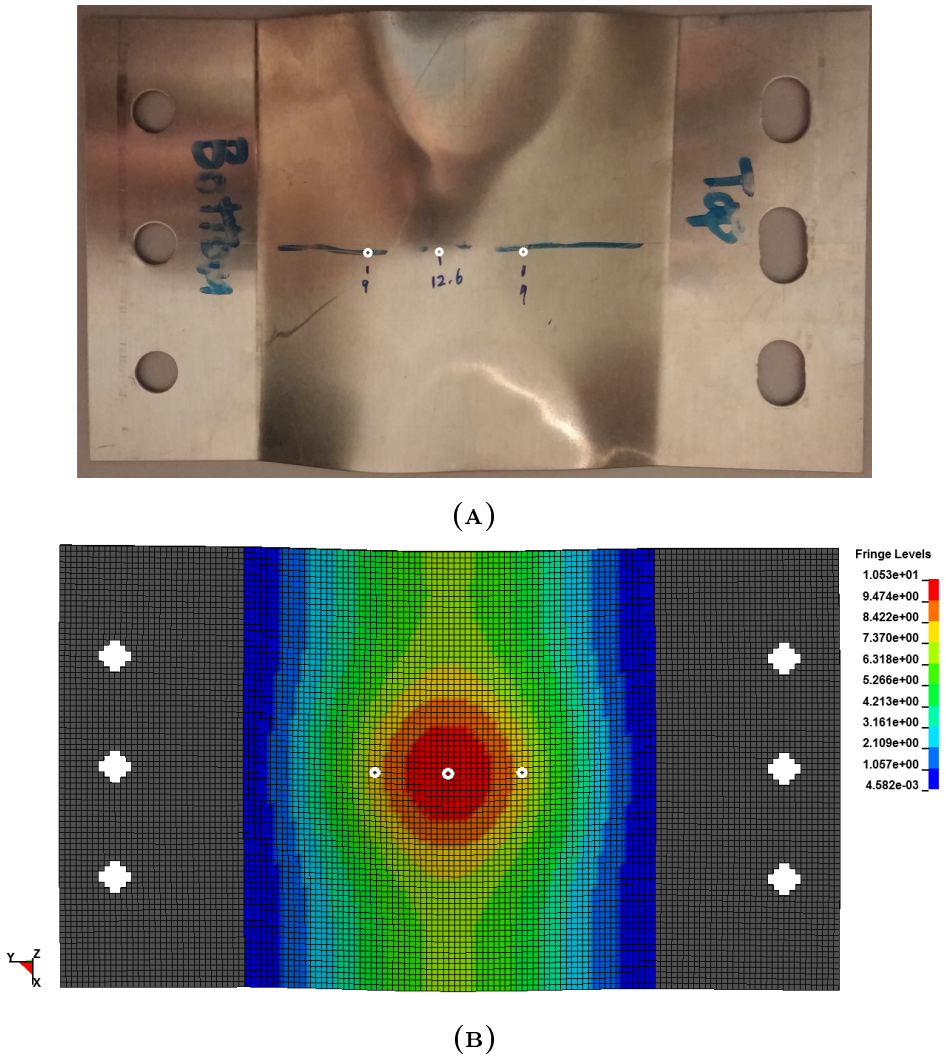

(A)

(B)

Figure 7.7: Final deformed shapes of the aluminium plate: (A) Test, (B) Resultant displacement (*mm*) obtained from numerical analysis. White circles indicate the displacement measurement points.

deformed shape obtained from the test corresponds to the final deformed shape of the plate from the numerical analysis. However, there are slight differences related to the symmetry of the deformation. In the case of the numerical analysis, the deformation of the plate was symmetrical while in the case of the test the deformation of the plate was not symmetrical. This could be related to the slightly shifted centre of impact. The differences could also be caused by the difference in the support

definition in LS-DYNA. The largest displacement of the plate was in the centre of impact.

The numerical bird modelled with SPH particles was validated based on the bird impact theory proposed by Wilbeck (1978). Good agreement between the theory and numerical analyses was obtained for the normal and oblique bird impacts on the rigid targets in terms of impact pressures. Moreover, the comparison of the pressure distributions were in good agreement between the numerical analysis and experiment performed by Wilbeck (1978). After the validation of the SPH bird, the bird used in the experiments was validated based on the numerical results. Good agreement between the test and numerical results was obtained in terms of the final deformed shapes of the plate and the measured displacements. These results proved that the bird manufactured from gelatine mixture was capable of reproducing adequately the loading on the impacted structures.

7.3 Modelling of novel composite panels

In this section, the development of the numerical models of the corrugated and tubular panels is presented. Since both plates were modelled with the same material models, the description of both models is provided in the same section.

Figures 7.8 A and 7.8 B present the cross sections of the corrugated and tubular sandwich panels respectively. Only the part of the model was shown for better visibility of the mesh of the structures. The blue elements represent the carbon fibre, grey the adhesive and yellow the polyurethane foam. The red line corresponds to the zero thickness cohesive elements layer implemented between the face sheets. The mesh of the cross sectional area of the sample was discretised to ensure the best possible uniform elements distribution in terms of shape and size.

In both cases, the top and bottom face sheet panels were modelled with four elements through the thickness. This enables to correctly represent the bending behaviour of the face sheets during the impact. The thickness of the face sheets was $t = 1\ mm$ which gives a single element thickness of $t_e = 0.25\ mm$. The elements represent the layers of the composite prepreg used for manufacturing of the face sheet panels. The thickness of the top face sheets was split into two separate interfaces and the zero

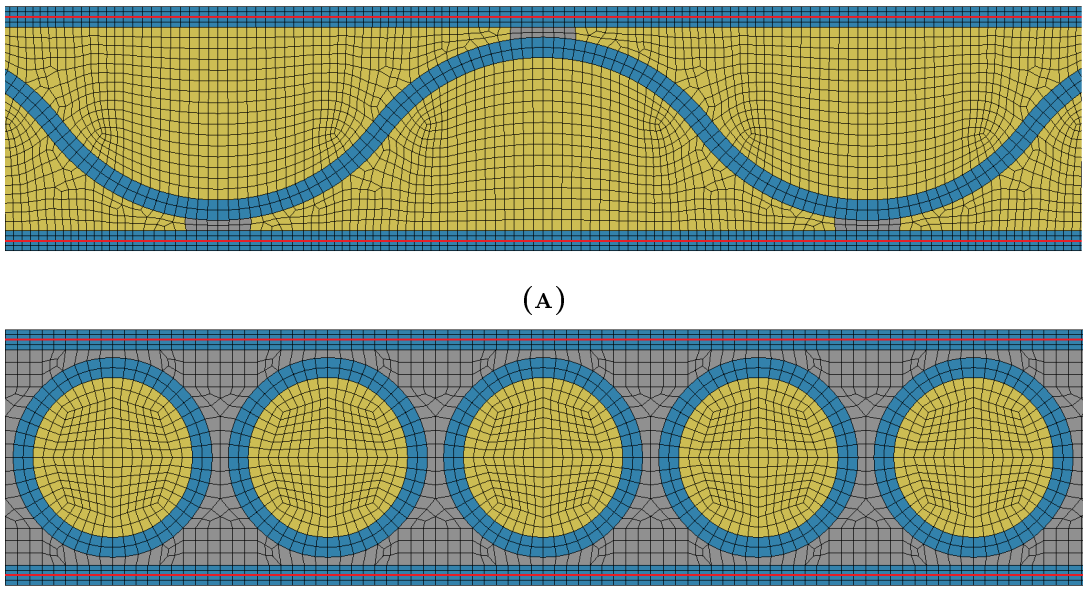

(A)

(B)

Figure 7.8: Mesh of novel composite sandwich panels: (A) CSP, (B) TSP.

thickness cohesive elements were implemented between these two interfaces. This allowed for modelling of delamination of the top and bottom face sheets. It was decided to do not implement the cohesive elements in between every single layer of elements to save computational time of the analysis.

The in-plane (i.e. XY plane) size of the elements was 0.525 $mm \times 0.9$ mm and 0.589 $mm \times 0.84$ mm for the impact centre of CSP and TSP respectively. However, it should be highlighted that a bias mesh was used in order to increase the mesh density in the location of impact. Therefore, the mesh density varies between the ends and the centre of the panels.

The corrugated panel and the tubes were modelled with two elements through the thickness. In this case, cohesive elements were not implemented between the composite layers.

The carbon fibre composite tubes and panels were modelled with MAT_59 - MAT_COMPOSITE_FAILURE_SOLID_MODEL. This composite material model allows for modelling of composite failure in all three directions. Failure of the material is governed by the Cheng and Hallquist (2004) failure criteria.

Fulfilment of a single criterion results in equalisation of the corresponding stresses and material constants to zero. Complete failure of the material is represented by the material erosion, which occurs when the stresses in all three directions σ_x, σ_y and σ_z are equal to zero (LSTC, 2014). The constant stress solid element with a single integration point was used for modelling of the composite materials (element type 1). A detailed description of this material model was provided in Chapter 3. The history variables were defined for the composite material in order to extract the information of the failure mode of the composite material.

The interface between two layers of face sheet elements was modelled with MAT_138 - MAT_COHESIVE_MIXED_MODE. MAT_138 is a cohesive material model which allows for modelling delamination in composite material models based on the bilinear traction separation law. A four point cohesive solid element was used to model the cohesive zone (element type 19). The name of the element is misleading because the cohesive element consists of 8 nodes. The "four points" are related to the number of integration points through the thickness of the element. The thickness of the cohesive layer was equal to $t_{CZ} = 0\ mm$. The cohesive layer is shown in Figure 7.8 as a red line between the elements of the top and bottom face sheets. A detailed description of this material model was provided in Chapter 3.

The polyurethane adhesive used for bonding the composite parts together was modelled with MAT_13 - MAT_ISOTROPIC_ELASTIC_FAILURE. MAT_13 is a non-iterative plasticity material model with a simple plastic strain failure criterion. This material model allows for representing the elastic and shear behaviour of the adhesive. The failure of the material is based on the plastic failure strain. Optional erosion of the failed element can be used by setting the REM parameter to 1. For the purpose of the impact analysis, the failure criterion with material erosion was used.

Finally, the polyurethane foam used in the novel sandwich panels was modelled with MAT_154 - MAT_DESHPANDE_FLECK_FOAM. MAT_154 is an isotropic, continuum based material model for crushable foams. This material allows for modelling of shear and tensile failure of the foam material resulting in erosion of the failed elements. A detailed description of this material model was provided in Chapter 4.

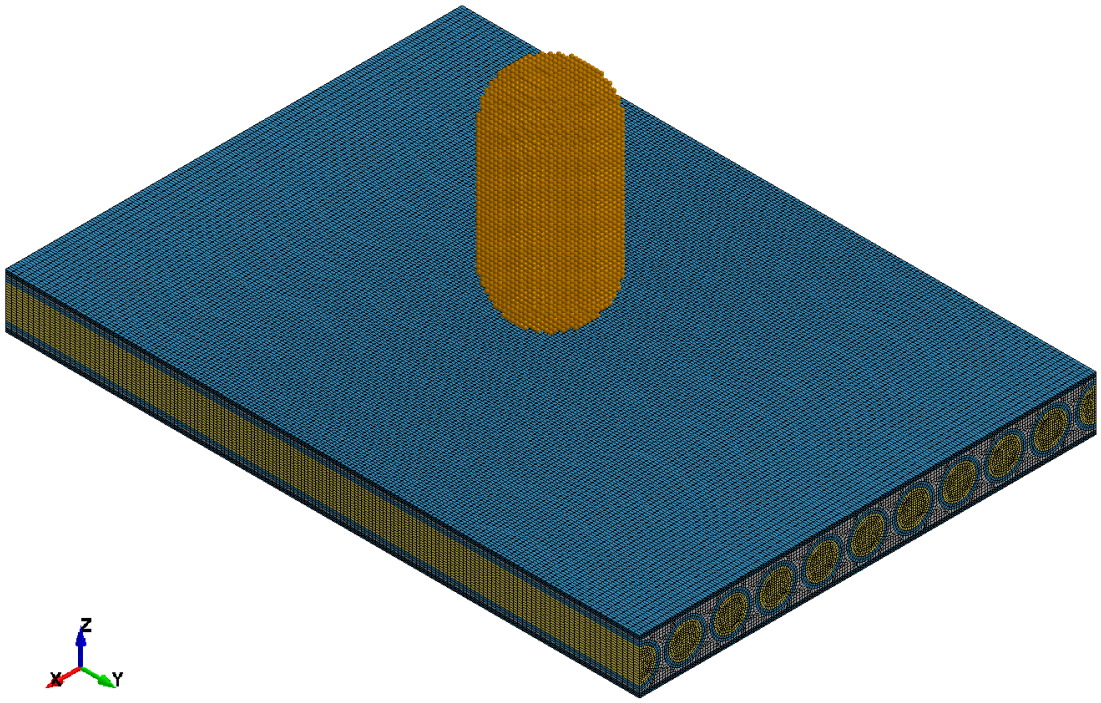

Figure 7.9: Initial configuration for the analysis of bird impact on TSP.

Since the strengths of the foam and the adhesive are significantly lower than the strength of the carbon fibres, their strengths control the strength of the interfaces between the composite panels and the core and adhesive. Therefore, the interfaces between the panel components were modelled as merged nodes. In order to prevent the inter penetrations of the materials, ERODING_SINGLE_SURFACE contact was used. The eroding option was chosen to preserve the contact between the components of the sandwich panels in case of internal elements erosion.

The description and validation of the SPH bird, used for the bird impact analyses on the novel sandwich panels, is provided in Section 7.2. The bird was given a velocity of 115 $\frac{m}{s}$ in the $-Z$ direction (see Figure 7.9 for a coordinate system orientation).

The ERODING_NODES_TO_SURFACE contact algorithm was chosen to model the interaction between the bird and the composite panel. The eroding contact was chosen to assure the contact between the bird and the internal layers of the sandwich panels in case any of the top layer elements are eroded.

In addition to the erosion criteria implemented in the corresponding material models,

an additional element erosion criterion was defined to prevent numerical instabilities related to negative volume in solid elements. In the impact analyses, high distortion of the elements can cause the element volume to become negative. Such numerical instability causes termination of the analysis. Therefore, to prevent this kind of instabilities, the erosion criterion based on the minimum time step was activated in the CONTROL_TIMESTEP card. The element deletion is triggered when the initial time step is reduced by a factor defined in the CONTROL_TERMINATION card.

The termination time of the analysis was set to $t_{tCSP} = 0.0016\ s$ for CSP and $t_{tTSP} = 0.001\ s$ for TSP. This allowed for a complete separation of the bird from the plate after impact. However, the analyses were terminated before the panels returned to complete equilibrium. No damping was used to reduce the vibrations of the panels after impact. The database histories were saved in time intervals of $t_{DB} = 1 \cdot 10^{-6}\ s$ and the database d3plots were plotted in time intervals of $t_{d3plot} = 1 \cdot 10^{-5}\ s$.

7.4 Analysis of results

In this section the results from the analyses of the bird impact on the corrugated and tubular sandwich panels are presented. The results of the analysis show the extent of damage induced to the panels and energy absorption capabilities of entire panels and their components. Furthermore, a comparison of the damage of the tested samples to the numerical results was performed. Finally the bird impact on the standard sandwich panel was modelled, and these results were compared to the results of corrugated and sandwich panel analyses.

The initial configuration of the bird impact on the novel composite sandwich panel (i.e. TSP) is shown in Figure 7.9.

7.4.1 Corrugated panel

The corrugated model for the numerical analysis was described in Section 7.3. Figures 7.10 A and 7.10 B show the failure of the material on the top and bottom composite face sheets of CSP. It is evident that only the impacted face sheet suffered

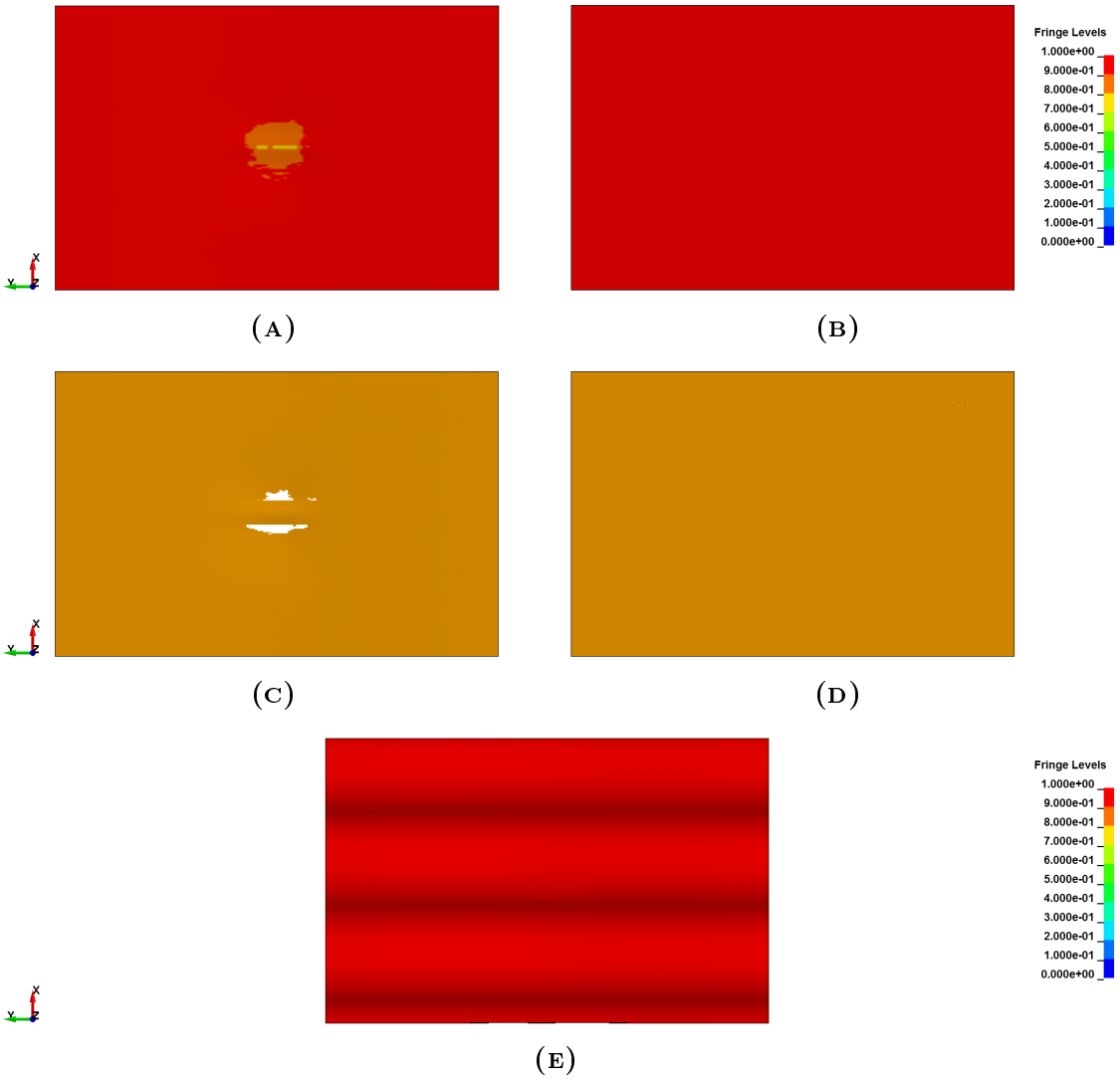

Figure 7.10: Failure of the corrugated sandwich panel: (A) Top face sheet, (B) Bottom face sheet, (C) Delamination of top panel face sheet, (D) Delamination of bottom panel face sheet, (E) Corrugated panel.

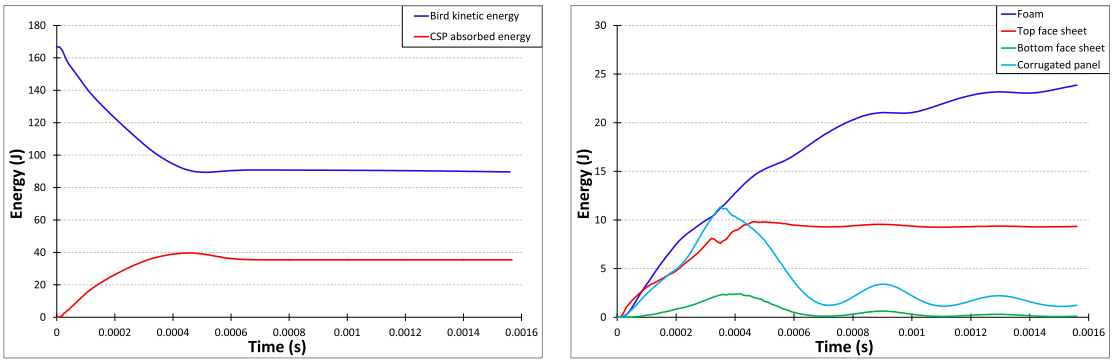

(A) (B)

FIGURE 7.11: (A) Bird kinetic energy and total energy absorbed by CSP, (B) Energy absorbed by individual components of CSP.

from damage. Moreover, only one failure criterion for the material was fulfilled. The history variables revealed that the damage of the material was only due to compression. This could imply that in reality no damage to the sample would be induced. Damage of the CSP face sheet was not symmetrical which could be expected from a numerical analysis. This was related to the unsymmetrical distribution of the SPH particles in the bird volume. However, unsymmetrical damage is more realistic in the case of composites materials.

The interfaces of the top and bottom face sheets of CSP are shown in Figures 7.10 C and 7.10 D. Delamination of the interface results in the deletion of cohesive elements used to model the interface. Some extent of delamination can be seen within the interface of the CSP top face sheet. The delaminated area was on both sides of the corrugated panel wave in the vicinity of the impact centre. The interface of the rear face sheet did not suffer from any delamination (see Figure 7.10 D).

Figure 7.10 E indicates that the corrugated panel did not suffer from any damage.

Figure 7.11 A shows the energy absorbed by the corrugated sandwich panel and the kinetic energy of the bird. From this graph it can be seen that the energy absorbed by the panel was not equal to the initial kinetic energy of the bird. It was related to the splashing of the bird. The bird longitudinal motion was changed into a radial motion of the bird particles after it reached the target. Therefore, a considerable amount of the bird initial energy was conserved by the bird particles. Some of

the energy was absorbed by CSP and the rest was used for the change of the bird motion direction. Figure 7.11 B shows the energy absorption of the CSP individual components. It is evident that the highest amount of energy was absorbed by the foam core. Considerable amount of energy was absorbed by the top face sheet of CSP and the corrugated panel. In the case of the top face sheet, the energy was absorbed by the failure of the fibres. From the graph it can be seen that the absorbed energy of the corrugated panel and the rear face sheet was recovered after the bird impact.

7.4.2 Tubular sandwich panel

Since the purpose of the bird impact investigation was to determine the soft body impact resistance of the samples at a velocity of $V_i = 115\ \frac{m}{s}$, only this impact case was modelled in LS-DYNA. The tubular sandwich panel model development for the numerical test was described in Section 7.3.

Figures 7.12 A and 7.12 B illustrate the failure of the top and bottom face sheets of TSP. From these figures it is evident that none of the face sheets suffered from any damage after the impact. The red colour of the fringe levels indicates no failure of the material and blue indicates complete failure of the composite material. The vicinity of the impact centre and the edges of the sample were free from any damage.

No delamination damage was observed in Figures 7.12 C and 7.12 D, where the interfaces of the top and the rear face sheets of the panel are shown.

Figures 7.12 A and 7.12 B show the carbon fibre tubes used for the core reinforcement. It is evident that there was no damage of the composite tubes.

From the energy time history graphs, shown in Figure 7.13, it can be seen that only a small part of the bird kinetic energy was absorbed by TSP. A significant part of the bird impact energy was used to change the motion direction of the bird material. The low energy absorption of the panel is related to its high stiffness - negligible elastic deformation of the target was observed during the impact. Figure 7.13 B shows the energy absorption of the TSP individual components. The highest amount of energy was absorbed by the carbon tubes and the adhesive. The foam and both face sheets absorbed similar amounts of energy.

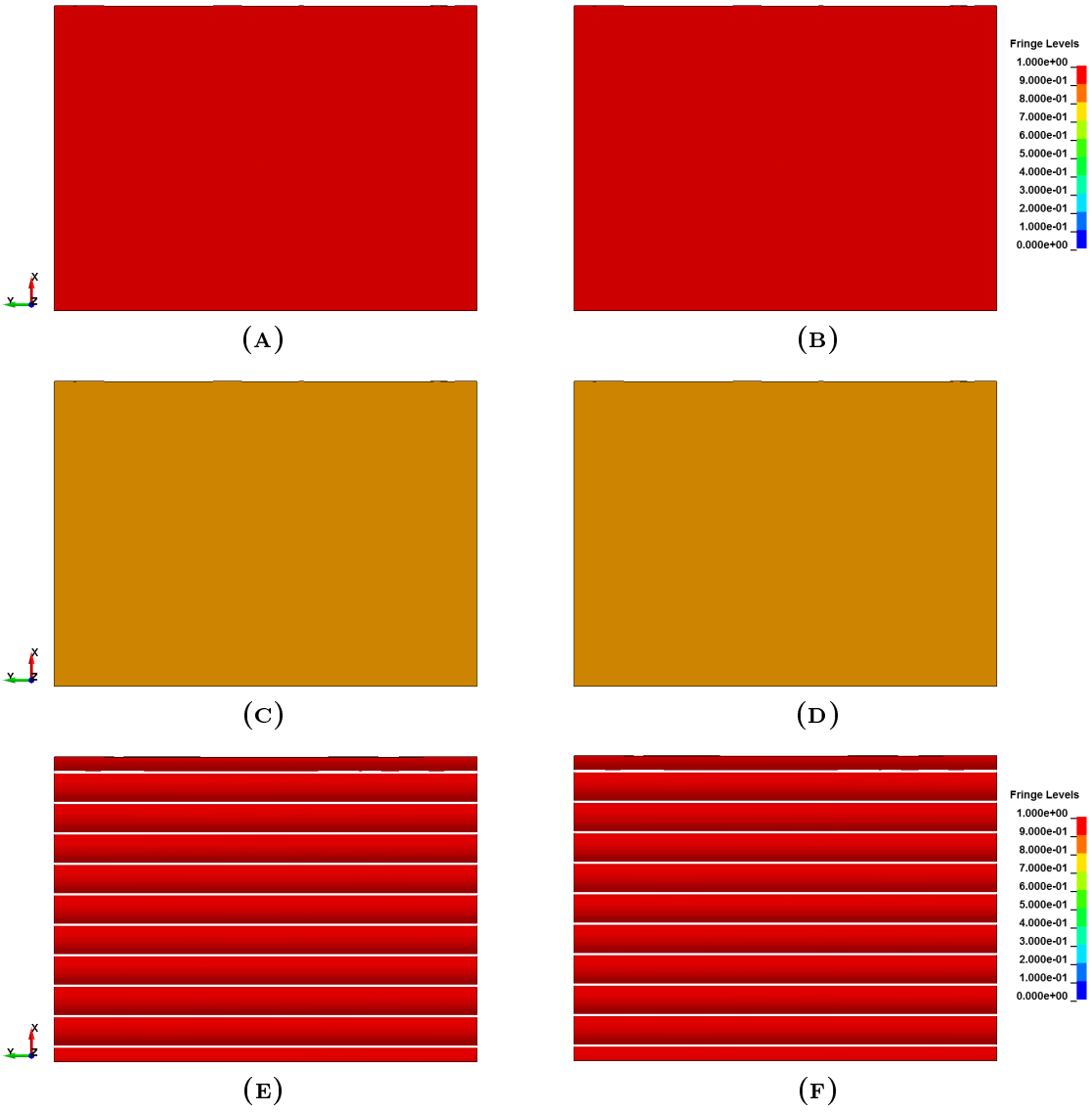

Figure 7.12: Failure of the tubular sandwich panel: (A) Top face sheet, (B) Bottom face sheet, (C) Delamination of top panel face sheet, (D) Delamination of bottom panel face sheet, (E) Tubes top, (F) Tubes bottom.

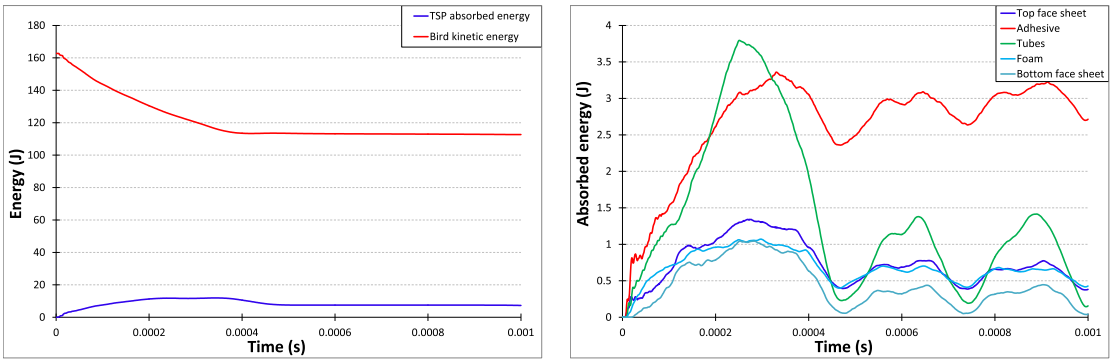

(A) (B)

FIGURE 7.13: (A) Bird kinetic energy and total TSP absorbed energy, (B) Energy absorbed by individual components of TSP.

7.4.3 Comparison with experiment

7.4.3.1 Corrugated sandwich panel

The results of the bird impact on CSP showed that two out of the three samples were damaged during the test. Since there was a significant discrepancy of the results between the cases, it was decided to compare the numerical results to the sample with not very severe damage. Therefore, sample CSP_1 was chosen as a representative case for the comparison of experimental and numerical results. The accuracy of the numerical results was assessed by comparison of the failure of the face sheet panels with the infrared images of the separation point of CSP_1. It was decided to compare the results to the images of the separation point as on these images the surface and subsurface damage of the sample was visible.

Figure 7.14 shows the comparison of the damage extent between the numerical and experimental results. The infrared images of the separation point of the top and bottom sides of CSP_1 are shown in Figures 7.14 A and 7.14 B respectively. The failure of the top and bottom face sheet panels is shown in Figures 7.14 C and 7.14 D respectively. Delamination of the face sheet panels interfaces is shown in Figures 7.14 E and 7.14 A respectively.

From the comparison of Figures 7.14 A, 7.14 C and 7.14 E can be seen that the damage in the case of the numerical analysis was limited to the impact centre. Similarly, in

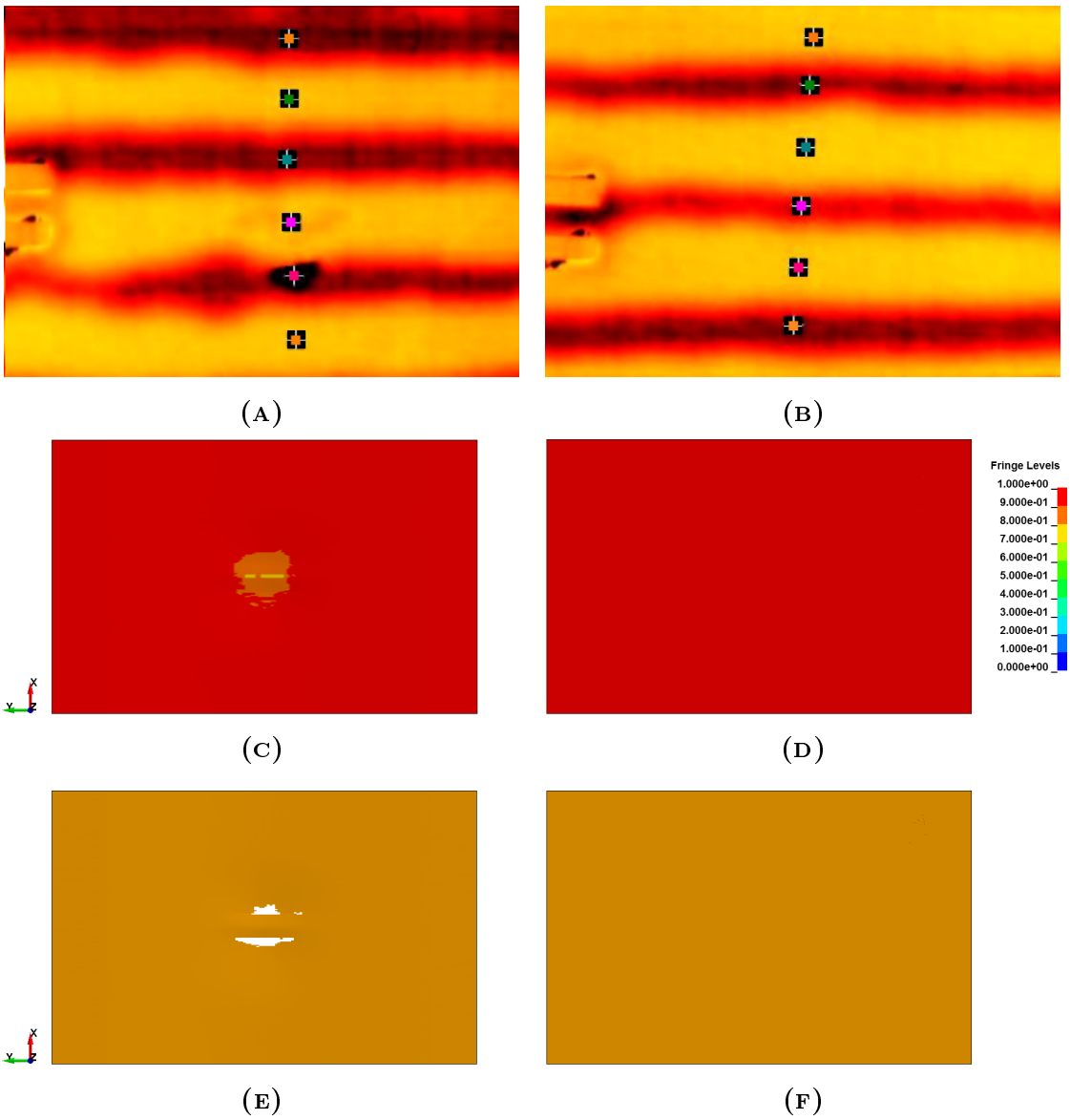

Figure 7.14: Comparison of experimental and numerical results in terms of damage extent for the test and numerical analysis of the bird impact on CSP_3: (A) Top face separation point, (B) Bottom face separation point (C) Top face sheet, (D) Bottom face sheet, (E) Delamination of top face sheet, (F) Delamination of bottom face sheet.

the test the damage was in the vicinity of the impact centre. However, the numerical results showed a larger damage area of approximately 168 mm^2. Inspection of the panel, Section 6.4.2.1, revealed that the sample suffered from more localised spall with a triangular delamination area of approximately 65 mm^2 on the border of the bird impact. There was no indication of delamination except the one surrounding the spall, while in the numerical analysis there was a significant delamination area in the vicinity of the impact centre.

A comparison of the separation point of the non-impacted side of the sample, the failure and the delamination of the bottom face sheet is shown in Figures 7.14 B, 7.14 D and 7.14 F respectively. It showed good accuracy of the numerical results in terms of damage of the bottom face sheet. No indication of damage can be seen on the rear side of the panels.

A comparison of the numerical results with the impacted sample showed reasonably good accuracy of the numerical results. In both cases, the damage of the top face panel was in the vicinity of the impact area, however, different extent of damage and damage modes were observed. Furthermore, no damage was observed far from the impact location in both cases. For both analysis and experiment, no indication of damage of the rear face sheet was observed.

7.4.3.2 Tubular sandwich panel

The results of the bird impact on TSP showed that none of the three samples were damaged during the impact test. For the comparison purpose, the experimental results of TCP_1 were chosen, because of the lowest level of initial imperfections within the TCP_1 internal structure, evident from the infrared images taken. It was therefore considered to be closest to the numerical model structure, which is free of any imperfections.

Figure 7.15 shows the comparison of damage extent between the numerical and experimental results. The infrared images of the separation point of the top and bottom sides of TSP_1 are shown in Figures 7.15 A and 7.15 B respectively. The failure of the top and bottom face sheet panels is shown in Figures 7.15 C and 7.15 D respectively. Delamination of the face sheet panels interfaces is shown in Figures 7.15 E and 7.15 A respectively.

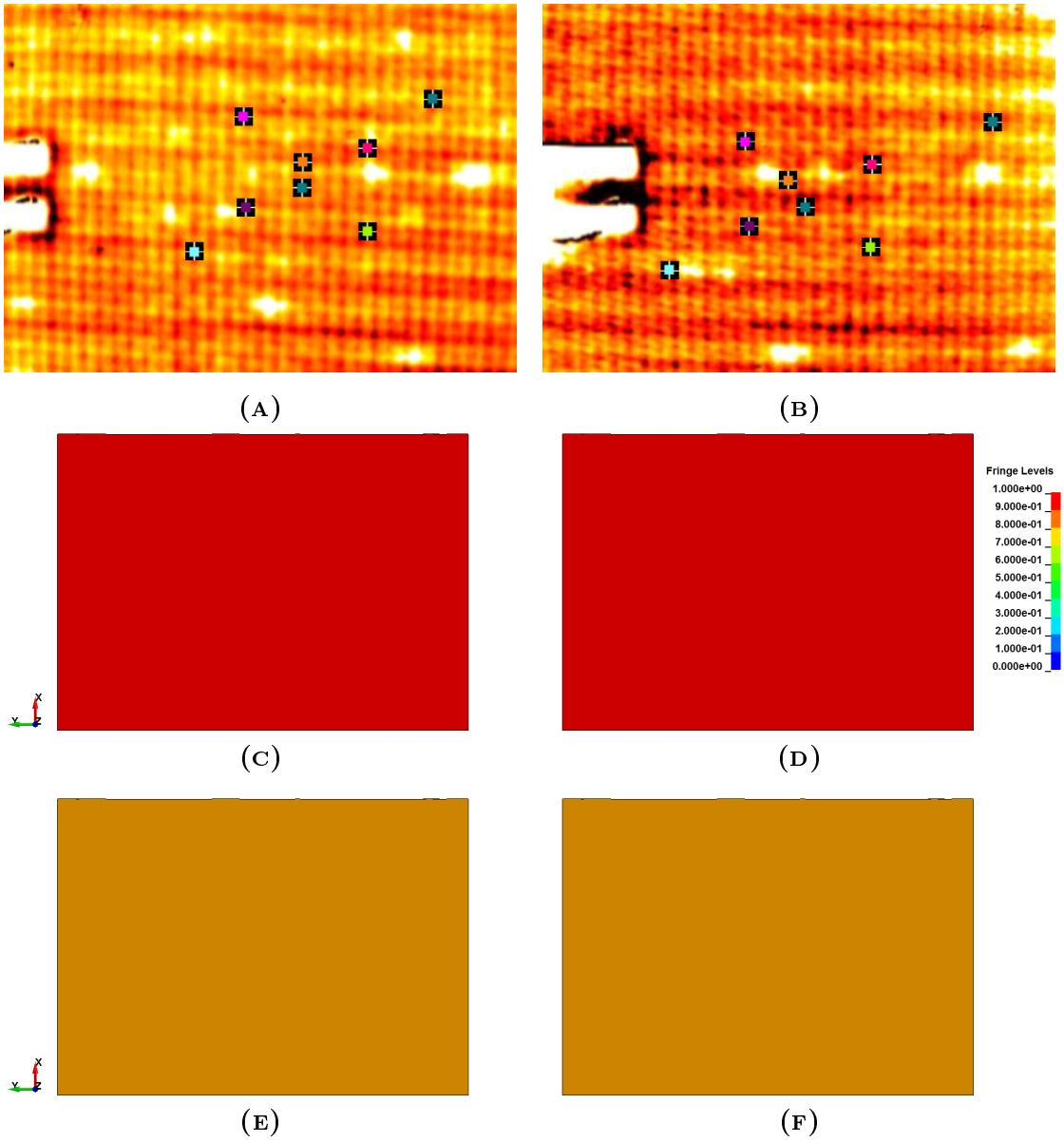

Figure 7.15: Comparison of experimental and numerical results in terms of damage extent for the test and numerical analysis of the bird impact on TSP_1: (A) Top face separation point, (B) Bottom face separation point (C) Top face sheet, (D) Bottom face sheet, (E) Delamination of top panel face sheet, (F) Delamination of bottom panel face sheet.

A comparison of the results showed that the numerical results agreed very well with the experimental results. No damage to the sample was induced during the numerical analysis. Moreover, both the experimental and the numerical results showed no delamination of the face sheet interfaces.

7.4.4 Comparison with standard sandwich panel

In order to assess the improvement on the impact resistance of the novel panels with respect to the standard sandwich panel (SSP) of equivalent thickness, a numerical analysis of bird impact on a standard composite sandwich panel was performed. Subsequently, the results of all bird impact analyses were compared in terms of the damage extent and the absorbed energy.

The standard sandwich panel was modelled in accordance to the CSP and TSP panels. The thickness of the panel was $t_{SSP} = 12\ mm$. The composite face sheets were modelled with MAT_59 and the foam core was modelled with MAT_154. The thickness of the face sheets and the foam core was 1 mm and 10 mm respectively.

A comparison of the damage extent on the top and bottom face sheet panels of SSP, CSP and TSP is shown in Figure 7.16. From the comparison of the top face sheets (see Figures 7.16 A, 7.16 C and 7.16 E), it can be seen that the most severe damage was induced to SSP, and it was concentrated in the vicinity of the impact centre. Due to complete failure of the material, some elements were eroded. In the case of CSP, only a small damage of the top face sheet is visible in the impact centre. TSP did not suffer from any damage. A comparison of the bottom face sheets of SSP, CSP and TSP (see Figures 7.16 B, 7.16 D and 7.16 F) shows that only the bottom face sheet of SSP suffered from some damage. However, in this case the damage was not very pronounced and is visible in the form of two longitudinal cracks.

Figure 7.17 shows the delamination of the top and bottom interfaces of SSP, CSP and TSP. From the comparison of the top face sheet delamination areas (see Figures 7.17 A, 7.17 C and 7.17 E), it is evident that the largest delamination area was observed in the SSP interface. This was expected from the severe damage of the top face sheet. Some extent of delamination is also visible in the vicinity of the impact centre of CSP. TSP did not suffer from delamination in the top face sheet interface. Delamination of the bottom face sheet is shown in Figures 7.17 B, 7.17 D and 7.17 F

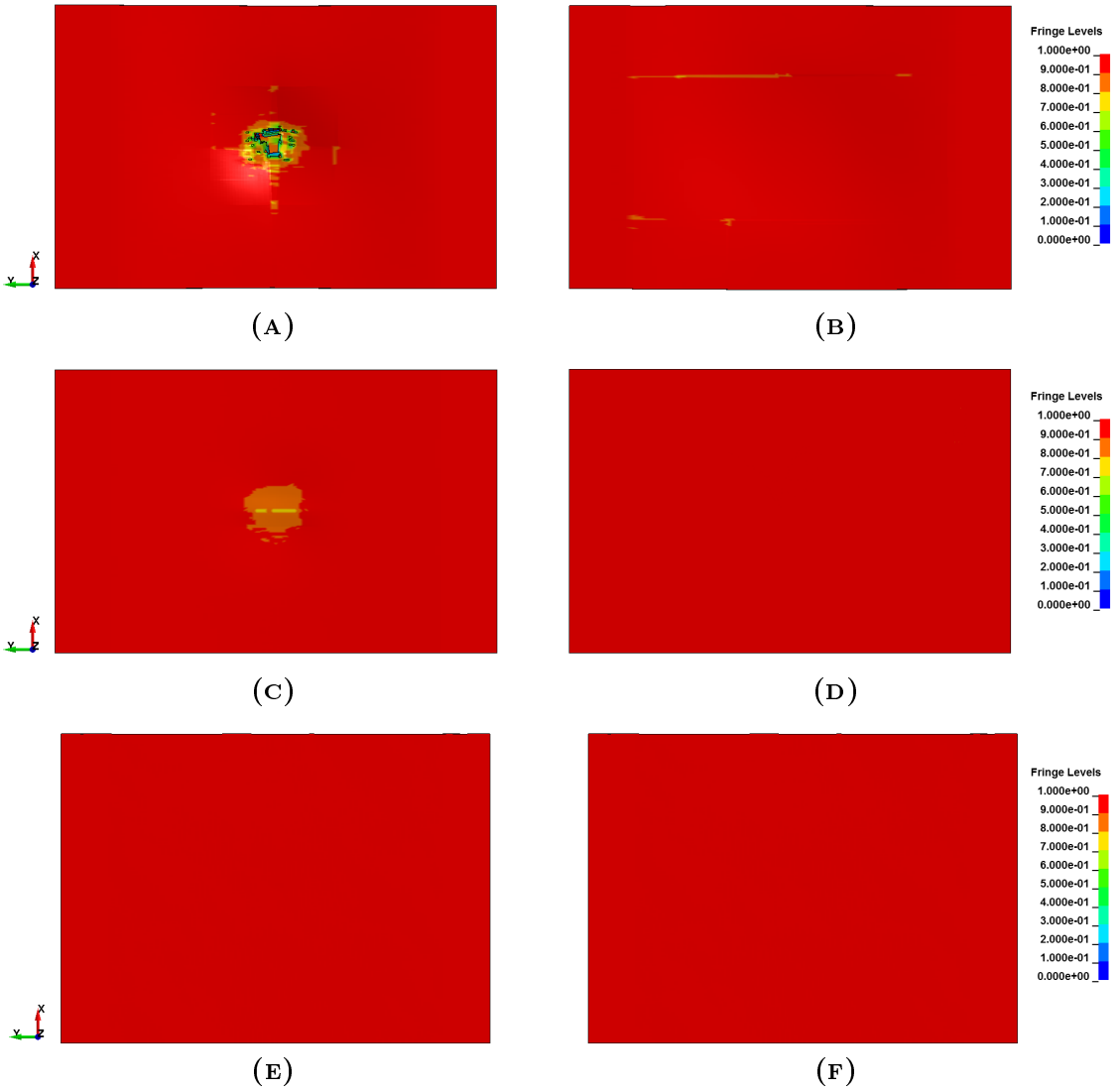

Figure 7.16: Comparison of numerical results in terms of damage extent of: (A) SSP top face sheet, (B) SSP bottom face sheet (C) CSP top face sheet, (D) CSP bottom face sheet, (E) TSP top face sheet, (F) TSP bottom face sheet.

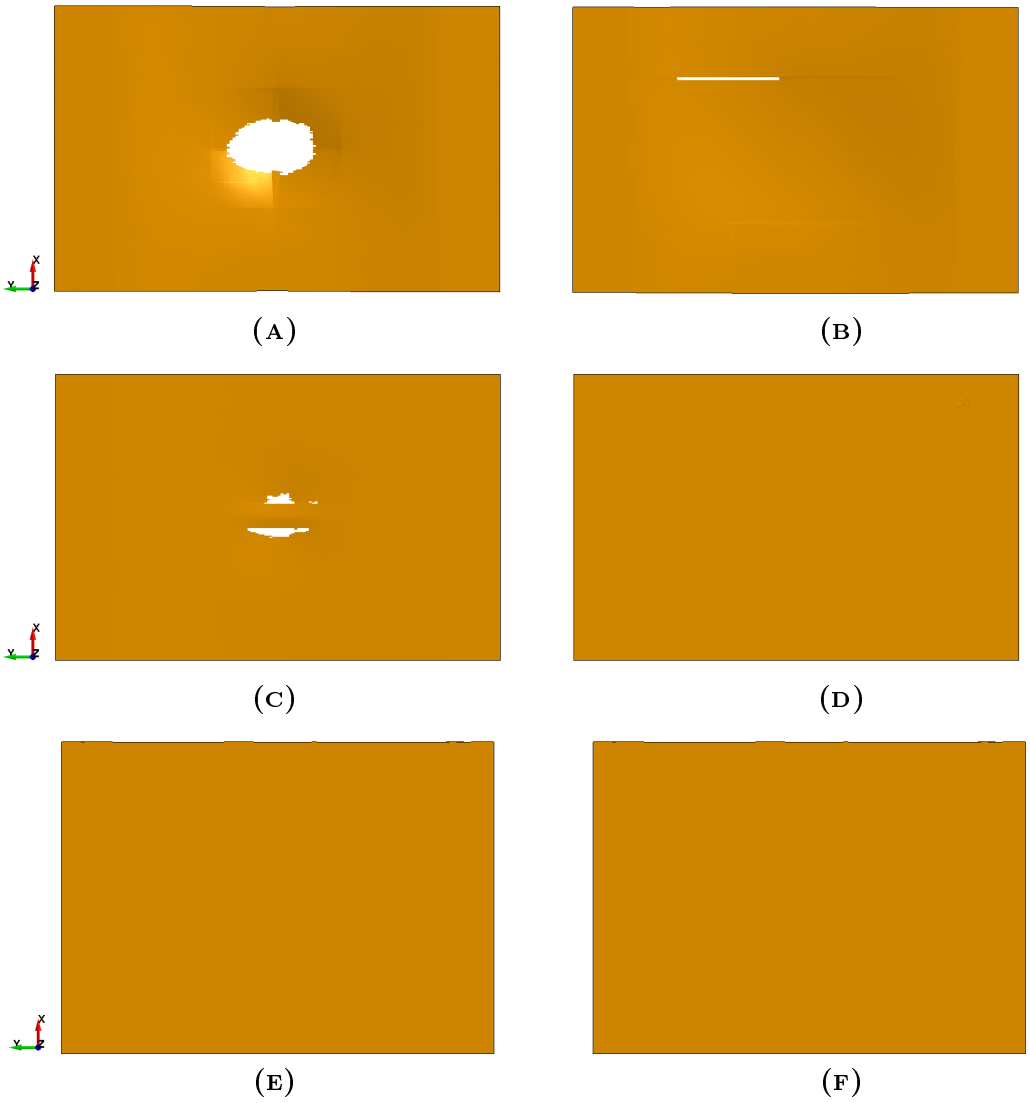

Figure 7.17: Comparison of numerical results in terms of delamination extent of: (A) SSP top face sheet, (B) SSP bottom face sheet (C) CSP top face sheet, (D) CSP bottom face sheet, (E) TSP top face sheet, (F) TSP bottom face sheet.

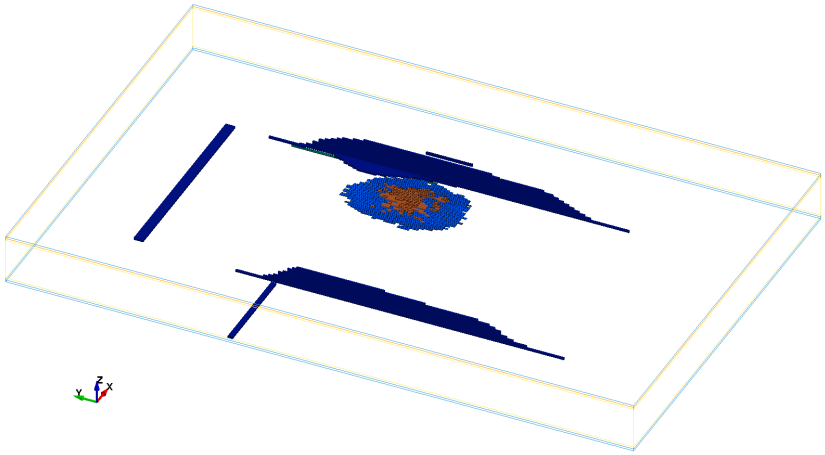

(A) SSP

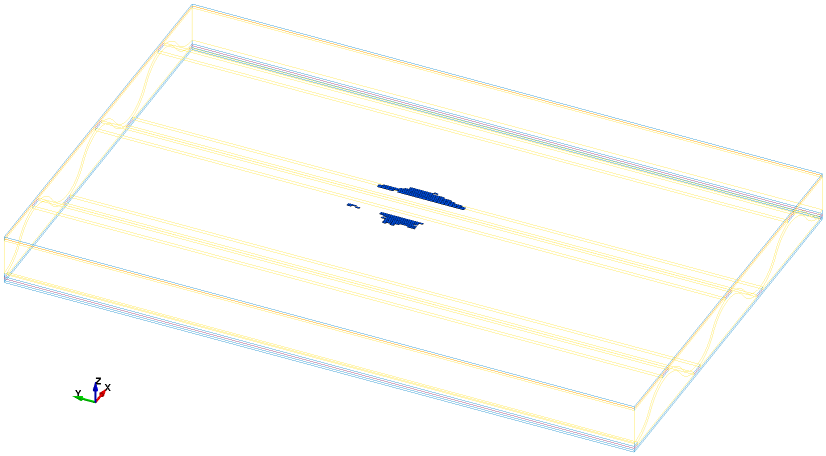

(B) CSP

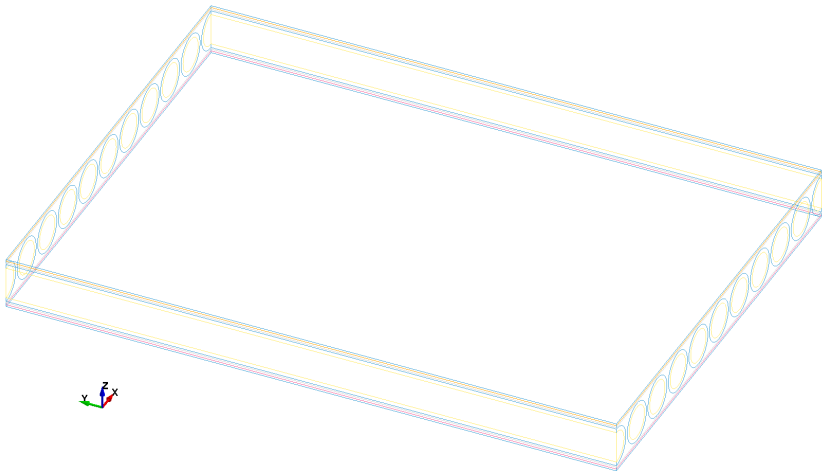

(C) TSP

FIGURE 7.18: Elements eroded fro the analyses due to failure: (A) SSP, (B) CSP, (C) TSP.

for SSP, CSP and TSP respectively. Only in the case of SSP the bottom face sheet suffered from delamination. The delamination was located underneath the crack damage visible in Figure 7.16 B.

Figure 7.18 shows the elements eroded due to failure of the material for all components. In the case of SSP, two areas of debonding between the foam and the bottom face sheet are visible in Figure 7.18 A. Moreover, there was a failure of the foam core material within the sample. Debonding between interfaces of different components or failure of the core did not occur in the cases of the novel sandwich panels (see Figures 7.18 B i 7.18 C).

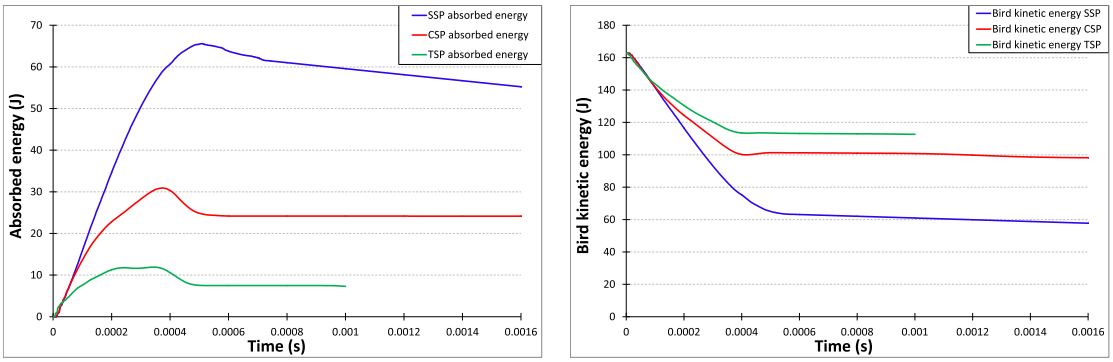

(A) (B)

Figure 7.19: (A) Energy absorbed by individual components of sandwich panels, (B) Bird kinetic energy.

Figure 7.19 shows a comparison of the energy absorption and bird kinetic energy of different panels. The highest energy was absorbed in the case of SSP. Most of the bird kinetic energy was absorbed through the delamination and failure of the top face sheet of the panel. Moreover, the significant damage of the top face sheet panel led to a considerable compression of the foam what further increased the absorbed energy. CSP absorbed around 50% less energy than SSP. The smallest amount of impact energy was absorbed by TSP. This was related to the very high stiffness of the panel. In this case, the bird impact energy was absorbed mainly for the change in the motion direction.

The novel composite sandwich panels showed considerable improvement in terms of the damage extent in comparison to the standard standard sandwich panel. For

CSP, the damage area was reduced only to the location of the impact, with a small area of delamination. In the case of TSP, no damage was induced to the sample. Due to the lack of failure of the face sheet panel, the energy absorbed by the novel structures was lower in comparison to SSP.

7.5 Conclusions

- The validation of the numerical bird model was performed through a comparison of the impact pressures applied to the target by the impacting projectile. The pressure distribution agreed with the experimental results of Wilbeck (1978) and the corresponding stagnation and Hugoniot pressure values were adequately reproduced. Furthermore, the validated numerical bird was used to model the impact on the thin aluminium plate. Based on this investigation, the gelatine bird used for the experiment was validated through a comparison of the final deformed shapes of the plate and the impact centre displacement. The comparison of the results indicated a good level of reliability of the impact loads induced by the gelatine birds.

- The numerical investigation of bird impact on the novel composite sandwich panels performed with LS-DYNA showed good accuracy of the analyses results in terms of damage extent.

- In the case of bird impact on CSP, the damage of the sample was concentrated in the vicinity of the impact centre, which was also observed within the experimental results. However, the damage modes in the test and analysis were different.

- The numerical and experimental results of bird impact on TSP were in very good agreement. In both cases, no damage of the sample was observed.

- The comparison of CSP and TSP to SSP showed significant improvement of the impact resistance of the novel sandwich panels. Bird impact on SSP resulted in severe damage of the sample, including failure and delamination of the top face sheet, damage of the foam core and debonding between the foam core and the rear face sheet. For CSP, the damage was not very pronounced and it was

restricted to the vicinity of the impact location. No damage was observed on the TSP.

Chapter 8

Conclusions and future work suggestions

8.1 Conclusions

8.1.1 Modelling of bird strike on metallic fan blade

- Three parametric studies were performed in order to improve the understanding of bird strike on jet engine blades and to validate the models against available experimental data. The first study considered the influence of the bird shape on the plastic deformation of the blade. The second study examined the influence of impact timing in other words bird slice size (for multiple blade impacts). The third study considered the influence of impact location along the length of the blade. Within these studies, it was paramount, from an engineering standpoint, to accurately reproduce the permanent deformation of the blade, as it is strongly related to engine damage.

- All analyses were performed with the finite element – SPH models for which, mesh sensitivity was removed through a convergence analyses. Contact algorithm comparison was done in order to model blade – bird interaction correctly. The particle to particle contact algorithm was used in all simulations, since there was energy dissipation in analyses performed with particle to surface contact algorithm.

- In the bird shape investigation hemispherical ended cylinder and ellipsoidal birds were considered. Bird shape had a significant influence on plastic deformation of the impacted blade. The bird body diameter and mass of the bird part cut off by the blade are two main parameters which affect the magnitude of the blade plastic deformation. A larger diameter, in the case of hemispherical bird, resulted in a higher magnitude of the blade loading and consequently a higher deformation of the blade.

- The simulation results indicate that there is a strong influence of bird impact timing and location on the extent of blade deformation. The differences in magnitude of the contact force vary between simulations and are related to the size of the bird slice. The contact force peak was the highest in the case where the bird is initially located at radius $r_0 = 514\ mm$ from the axis of rotation of the blade assembly, the tangential initial position of the bird relative to the blade was defined by an angle of 20.76° between the leading edge blade tip and the bird centre of gravity and the initial axial position of the front end of the bird was located at $X = 14\ mm$ ahead of the leading edge blade tip (this is the case labelled as X_0 in the previous sections). Only in this case a contact between the leading and trailing blade was observed. In all other cases the contact force peaks were lower and caused only local deformation of the leading edge of the impacted blade. Furthermore, it was observed that with increase of the bird slice size cut by the first blade the magnitude of the contact forces acting on the second blade reduced.

- The study of the influence of impact location on the leading blade deformation revealed that the location of the bird impact have considerable influence on the blade response. This was mainly due to changes in the bird slice size caused by the change in the blade pitch at the impact location. In all the cases local deformation of the leading edge of the blade was significant. The numerical results were assessed by comparison with the blade recovered from the physical experiment and indicated a good level of reliability of the numerical results.

8.1.2 Modelling of transient response of composites

- Single element tests on the chosen composite material models were performed to assess and validate the composite material models available in LS-DYNA. Furthermore, the double cantilever beam (DCB) delamination mode I analyses were performed to assess and validate the techniques for modelling delamination in composites in LS-DYNA. The validation analyses were performed in order to choose the most appropriate composite modelling techniques for modelling of bird impact on the novel composite sandwich panels.

- The results of the single element tests for MAT_22, MAT_59 and MAT_221 showed good accuracy between the numerical and the analytical results. The results revealed that material model MAT_22 does not allow for modelling of compressive failure in any of the fibre directions. The remaining two material models were able to model failure of the composites for all loading cases in all fibre directions.

- Validation of the composite material models revealed that none of the composite material models works with the shock Equation of State. Hence, the shock wave formation and propagation in the material cannot be modelled with any of the investigated material models. This can have a significant influence on the accuracy of the results for modelling of impact phenomena.

- The results for the delamination of DCB mode I tests modelled with the contact algorithm and the cohesive elements showed that both of these techniques offered the same accuracy of the results. In both cases the accuracy and stability of the results were highly dependent on the mesh density along the crack growth direction. Furthermore, the fracture toughness of the interface is a crucial parameter, which governs the behaviour and load carrying capacity of the modelled interface. The cohesive traction does not influence the strength of the interface. However, its value has a significant influence on the numerical stability of the solution. Delamination modelled with cohesive elements is more expensive in terms of computational time than delamination modelled with a contact algorithm. On the other hand, it allows for visualisation of the delamination extent.

8.1.3 Composite sandwich panels

- The literature review on the impact resistance of composite sandwich pa-nels revealed superior impact resistance of the sandwich panels with through thickness core reinforcement.

- The numerical techniques for modelling of low density foams were reviewed and validated with the single element tests and indentation tests. The capabilities of reproducing compressive behaviour and modelling failure of the foam core were assessed during the validation tests.

- The validation tests revealed that MAT_57 and MAT_83 are suitable to represent fully recoverable elastomeric foams and MAT_63 and MAT_154 are suitable to represent crushable foams. Furthermore, the Deshpande-Fleck (MAT_154) foam material model is the only one from the investigated foam material models, which allows for modelling of foam material failure resulting in element erosion.

8.1.4 Bird strike experiments

- The infrared thermography method was chosen to perform non-destructive inspection of the novel corrugated and tubular composite sandwich panels. The inspection revealed that the corrugated sandwich panels were of good quality with no hidden delaminations. However, some imperfections related to the uneven distribution of the adhesive and not even height of the corrugated waves of the corrugated panel were visible on the infrared images. The inspection of tubular samples revealed many air bubbles underneath the face sheet panels. The air bubbles were mostly located on the periphery of the samples, therefore they did not have a strong influence on the impact resistance of the sample.

- In order to assess the soft body impact resistance of the novel composite panels, three corrugated and three tubular composite sandwich coupons were impacted with the gelatine bird at a velocity of $V_i = 115\frac{m}{s}$. The impact resistance of the panels was assessed in terms of the damage extent. Furthermore, the results of the bird impact tests were compared to the numerical results.

- The corrugated panels showed good impact resistance for the bird impact. Only one of the samples suffered from pronounced damage of the impacted face sheet. One sample suffered from very small spall damage close to the impact location and one sample did not suffer from any top face sheet damage. None of the cases showed internal damage or delamination of the corrugated sandwich panels. Moreover, the rear surface of the sample was intact in all of the impacted panels.

- The tubular panels showed excellent impact resistance for a velocity of $V_i = 210\frac{m}{s}$. There was no indication of damage on the impacted surface for any of the tubular sandwich panels. Furthermore, the internal structure and the rear surface remained undamaged after the bird impact in the all the cases. Due to the lack of any damage of the tubular sandwich panels it was decided to investigate the soft body damage threshold of the panels. This was determined to be $V_{iBL} = 235\frac{m}{s}$. Such high impact velocity resulted in the visible damage on the impacted face of the panel. The thermographic inspection revealed delamination in the vicinity of the impact location. Moreover, considerable debonding area was detected underneath the rear face sheet of the panel.

8.1.5 Numerical modelling of bird strike on novel composite panels

- The numerical investigation of bird impact on the novel composite sandwich panels performed with LS-DYNA showed good accuracy of the analyses results in terms of damage extent. In the case of bird impact on the corrugated sandwich panel, the damage of the sample was concentrated in the vicinity of the impact centre, which was also observed within the experimental results. However, the damage modes in the test and analysis were slightly different. The numerical and experimental results of bird impact on the tubular sandwich panels were in very good agreement. In both cases, no damage of the sample was observed.

- The comparison of the corrugated and the tubular sandwich panels to the equivalent sandwich panel showed significant improvement of the impact resistance of the novel sandwich panels. Bird impact on equivalent panel resulted

in severe damage of the sample, including failure and delamination of the top face sheet, damage of the foam core and debonding between the foam core and the rear face sheet. For corrugated sandwich panel, the damage was not very pronounced and it was restricted to the vicinity of the impact location. No damage was observed on the tubular sandwich panels.

8.2 Further work suggestions

The aim of this work was to examine the bird impact resistance of the novel corrugated and tubular composite sandwich panels. The impact resistance of the composite samples was assessed based on the damage extent induced to the samples during the impact. All the samples showed good impact resistance to the soft body impact. Furthermore, numerical analysis with commercially available tools for modelling of impact phenomena were employed to model the impact response of the samples. Finally, numerical results for the bird impact on the corrugated and tubular sandwich panels were compared with results of bird impact on the equivalent sandwich panel. A considerable improvement of the bird impact resistance of the novel samples was observed during the results comparison. However, some areas for further work and improvement were determined:

- Further tests on the soft body impact resistance of the novel panels are required. It is recommended to investigate the impact resistance of the panels subjected to impact with larger projectiles. This would enable for examination of the panels at higher impact energy.

- The hard body impact resistance of the novel samples was not a focus on this investigation. However, it would be essential to investigate the damage extent induced to the samples impacted with a solid, hard impactor.

- In order to show the improvement on the impact resistance of the novel panels, impact tests of the equivalent composite sandwich and solid panels are recommended. This would enable for a direct comparison of the damage extent and energy absorption of the samples.

- It is recommended to investigate the compressive after impact strength of the novel sandwich panels. It is expected to be significantly improved especially in the case of the tubular samples, where the damage extent can be reduced to few tubes only.

- Tubular samples showed excellent impact resistance for the soft body impact. It would be of high interest to assess the performance of the tubular design in case of a ballistic impact. For the ballistic purpose a more complex tubular design could be investigated. It would consist of few composite tubes separated with the foam to imitate the biomimetic structure.

- It is highly desirable to improve and unify the manufacturing process of the corrugated and tubular composite sandwich panels. Unification of the process would reduce the cost of samples manufacturing. Moreover, it would allow to remove the imperfections from the manufactured panels. This can further improve the impact resistance of the novel panels.

- Further improvement on the composite material models is recommended in order to increase the reliability and accuracy of the numerical results. The studies on the existing composite material models revealed that none of the models allowed for modelling of shock waves in the composite materials. Therefore, the implementation of the EOS into the material model could increase the accuracy of modelling of impact phenomena on composite structures. Moreover, none of the composite models allows to account for the rate sensitivity of composite materials.

Bibliography

Abrate, S. (1997). Localised impact on sandwich structures with laminated facings. *Applied Mechanics Reviews*, 50(2):69–82.

Abrate, S. (1998). *Impact on composite structures*. Cambridge University Press.

Abrate, S. (2008). Criteria for yielding or failure of cellular materials. *Journal of Sandwich Structures and Materials*, 10(1):5–51.

Air France (2010). *Airbus A380-800*. Air France Virtual Airlines, first edition.

Airoldi, A. and Cacchione, B. (2005). Numerical analysis of bird impact on aircraft structures undergoing large deformations and localised failure. *Impact Loading of Lightweight Structures*, 49.

Airoldi, A. and Cacchione, B. (2006). Modelling of impact forces and pressures in lagrangian bird strike analyses. *International Journal of Impact Engineering*, 32(10):1651–1677.

Alfano, G. and Crisfield, M. A. (2001). Finite element interface models for the delamination analysis of laminated composites: mechanical and computational issues. *International Journal for Numerical Methods in Engineering*, 50(7):1701–1736.

Altenbach, H. (2004). *Computational material science: From basic principles to material properties*. Springer Science & Bussiness Media.

Anderson, T. and Madenci, E. (2000). Experimental investigation of low-velocity impact characteristics of sandwich composites. *Composite Structures*, 50(3):239 – 247.

Anghileri, M., Castelletti, L., and Mazza, V. (2005). Bird strike: apporaches to the analysis of impacts with penetration. *Impact loading on lightweight structures*, 49:63–74.

Anghileri, M. and Sala, G. (1996). Theoretical assessment, numerical simulation and comparison with tests of birdstrike on deformable structures. In *ICAS, Congress, 20th, Naples, Italy, Proceedings. Vol. 1; UNITED STATES; 8-13 Sept. 1996.*

Audic, S., Berthillier, M., Bonini, J., Bung, H., and Combescure, A. (2000). Prediction of bird impact in hollow fan blades. In *36th AIAA/ASME/SAE/ASEE Joint Propulsion Conference and Exhibit.* American Institute of Aeronautics and Astronautics.

Avdelidis, N. P., Almond, D. P., Dobbinson, A., Hawtin, B., Ibarra-Castanedo, C., and Maldague, X. (2004). Aircraft composites assessment by means of transient thermal ndt. *Progress in Aerospace Sciences*, 40(3):143 – 162.

Avdelidis, N. P. and Moropoulou, A. (2004). Applications of infrared thermography for the investigation of historic structures. *Journal of Cultural Heritage*, 5(1):119 – 127.

Aymerich, F., Dore, F., and Priolo, P. (2008). Prediction of impact-induced delamination in cross-ply composite laminates using cohesive interface elements. *Composites Science and Technology*, 68(12):2383 – 2390. Deformation and Fracture of Composites: Analytical, Numerical and Experimental Techniques, with regular papers.

Bala, S. (2006). Best practices for modeling recoverable low density foams - by example. `http://blog2.d3view.com/best-practices-for-modeling-recoverable-low-density-foams-by-example/`. Accessed 10.08.2013.

Baral, N., Cartie, D. D. R., Partridge, I. K., Baley, C., and Davies, P. (2010). Improved impact performance of marine sandwich panels using through-thickness reinforcement: Experimental results. *Composites Part B: Engineering*, 41(2):117 – 123.

Barber, J. P., Fry, P. F., Klyce, J. M., and Taylor, H. R. (1977). Impact of soft bodies on jet engine fan blades. Technical Report AFML-TR-77-29, University of Dayton Research Institute.

Barber, J. P., Taylor, H. R., and Wilbeck, J. S. (1978). Bird impact forces and pressures on rigid and compliant targets. *Technical Report*, AFFDL-TR-77-60.

Barenblatt, G. I. (1959). The formation of equilibrium cracks during brittle fracture. general ideas and hypotheses. axially-symmetric cracks. *Journal of Applied Mathematics and Mechanics*, 23(3):622 – 636.

Barenblatt, G. I. (1962). The mathematical theory of equilibrium cracks in brittle fracture. *of Advanced Applied Mechanics*, 7:55–129.

Bayandor, J., Thomson, R. S., Scott, M., Nguyen, M. Q., and Elder, D. J. (2003). Investigation of impact and damage tolerance in advanced aerospace composite structures. *International Journal of Crashworthiness*, 8(3):297–306.

Bazant, Z. P. and Planas, J. (1997). *Fracture and size effect in concrete and other quasibrittle materials*. CRC Press.

Beard, S. and Chang, F.-K. (2002a). Design of braided composites for energy absorption. *Journal of Thermoplastic Composite Materials*, 15(1):3–12.

Beard, S. and Chang, F.-K. (2002b). Energy absorption of braided composite tubes. *International Journal of Crashworthiness*, 7(2):191–206.

Belytschko, T., Liu, W. K., and Moran, B. (2000). *Nonlinear finite elements for continua and structures*. John Wiley & Sons, New York, USA.

Benzeggagh, M. L. and Kenane, M. (1996). Measurement of mixed-mode delamination fracture toughness of unidirectional glass/epoxy composites with mixed-mode bending apparatus. *Composites Science and Technology*, 56(4):439–449.

Boeing (2014). 787 dreamliner. `http://www.boeing.com/boeing/commercial/787family/programfacts.page`. Accessed: 24.06.2014.

Brewer, J. C. and Lagace, P. A. (1988). Quadratic stress criterion for initiation of delamination. *Journal of Composite Materials*, 22(12):1141–1155.

Budgey, R. (2000). The development of a substitute artificial bird by the international birdstrike research group for use in aircraft component testing. *International Bird Strike Committee, Report*, IBSC25-WP-IE3.

Buitrago, B. L., Garcia-Castillo, S. K., and Barbero, E. (2010a). Experimental analysis of perforation of glass/polyester structures subjected to high-velocity impact. *Materials Letters*, 64(9):1052 – 1054.

Buitrago, B. L., Santiuste, C., Sanchez-Saez, S., Barbero, E., and Navarro, C. (2010b). Modelling of composite sandwich structures with honeycomb core subjected to high-velocity impact. *Composite Structures*, 92(9):2090 – 2096. Fifteenth International Conference on Composite Structures.

Bunsell, A. R. . (1988). *Fibre reinforcement for composite materials*. North Holland.

Camacho, G. T. and Ortiz, M. (1996). Computational modelling of impact damage in brittle materials. *International Journal of Solids and Structures*, 33:2899 – 2938.

Camanho, P. P. and Davila, C. G. (2002). Mixed - mode decohesion finite elements for the simulation of delamination in composite materials. Technical Report NASA/TM-2002-211737, NASA.

Camanho, P. P., Davila, C. G., and de Moura, M. F. (2003). Numerical simulation of mixed-mode progressive delamination in composite materials. *Journal of Composite Materials*, 37(16):1415–1438.

Camanho, P. P. and Matthews, F. L. (1999). Delamination onset prediction in mechanically fastened joints in composite laminates. *Journal of Composite Materials*, 33(10):906–927.

Cantwell, W. J. (1988). The influence of target geometry on the high velocity impact response of cfrp. *Composite Structures*, 10(3):247 – 265.

Cantwell, W. J., Curtis, P. T., and Morton, J. (1986). An assessment of the impact performance of cfrp reinforced with high-strain carbon fibres. *Composites Science and Technology*, 25(2):133 – 148.

Cantwell, W. J. and Morton, J. (1989). Comparison of the low and high velocity impact response of cfrp. *Composites*, 20(6):545 – 551.

Cantwell, W. J. and Morton, J. (1990). An assessment of the residual strength of an impact-damaged carbon fibre reinforced epoxy. *Composite Structures*, 14(4):303–317.

Cantwell, W. J. and Morton, J. (1991). The impact resistance of composite materials - a review. *Composites*, 22(5):347 – 362.

Caprino, G. (1984). Residual strength prediction of impacted cfrp laminates. *Journal of Composite Materials*, 18(6):508–518.

Chang, F. K. and Chang, K. Y. (1987). A progressive damage model for laminated composites containing stress concentrations. 21:834–855.

Charles, J.-P. and Guedra-Degeorges, D. (1991). Impact damage tolerance of helicopter sandwich structures. *Advanced Materials/Affordable Processes.*, 23:51–61.

Chen, M. C. (1999). Predicting progressive delamination of composite material specimens via interface elements. *Mechanics of Composite Materials and Structures*, 6(4):301–317.

Cheng, W. and Hallquist, J. (2004). Implementation of three-dimensional compsite failure model into dyna3d. acessed 29.08.2014.

Chevrolet, D., Audic, S., and Bonini, J. (2002). Bird impact analysis on a bladed disk. Technical Report RTO-MP-089, RTO AVT.

Choi, H. Y. and Chang, F. K. (1992). A model for predicting damage in graphite/epoxy laminated composites resulting from low-velocity point impact. *Journal of Composite Materials*, 26(14):2134–2169.

Collombet, F., Bonini, J., and Lataillade, J. L. (1996). A three-dimensional modelling of low velocity impact damage in composite laminates. *International Journal for Numerical Methods in Engineering*, 39(9):1491–1516.

Croop, B. and Lobo, H. (2009). Selecting material models for the simulation of ffoam in ls-dyna. In *7th European LS-DYNA Conference*.

Cui, H.-P., Wen, W.-D., and Cui, H.-T. (2009). An integrated method for predicting damage and residual tensile strength of composite laminates under low velocity impact. *Computers & Structures*, 87:456 – 466.

Cui, W. C. and Wisnom, M. R. (1993). A combined stress-based and fracture-mechanics-based model for predicting delamination in composites. *Composites*, 24(6):467–474.

Davila, C., Moura, M., and Camanho, P. (2001). Mixed-mode decohesion elements for analyses of progressive delamination. In *42nd AIAA/ASME/ASCE/AHS/ASC Structures, Structural Dynamics and material Conference*, volume AIAA-01-1486, pages 1–12.

Davila, C. G. and Johnson, E. R. (1993). Analysis of delamination initiation in postbuckled dropped-ply laminates. *AIAA journal*, 31(4):721–727.

De Vuyst, T., Vignjevic, R., and Campbell, J. C. (2005). Coupling between meshless and finite element methods. *International Journal of Impact Engineering*, 31(8):1054–1064.

DeMoura, M. F. S. F., Goncalves, J. P. M., Marques, A. T., and Castro, P. M. S. T. D. (1997). Modeling compression failure after low velocity impact on laminated composites using interface elements. *Journal of Composite Materials*, 31(15):1462–1479.

Deshpande, V. S. and Fleck, N. A. (2000). Isotropic constitutive models for metallic foams. *Mechanics and Physics of Solids*, 48:1253–1283.

DirectPlastics (2015). Acetal rod. *http://www.directplasticsonline.co.uk/Acetal$_R$od.html*. Accessed on 04.03.2015.

Dobyns, A., Federici, F., and Young, R. (1998). Bird strike analysis and test of a spinning s-92 tail rotor. In *AHS Affordable Composite Structures Conference*.

Dolber, R. A., Wright, S. E., Weller, J. R., and Begier, M. J. (2014). Wildlife strikes to civil avircraft in the united states, 1990-2013. Technical Report 20, Federal Aviation Administration.

Donea, J., Giuliani, S., and Halleux, J. (1982). An arbitrary lagrangian-eulerian finite element method for transient dynamic fluid-structure interactions. *Computer Methods in Applied Mechanics and Engineering*, 33:689 – 723.

Du Bois, P. A. (2009). The numerical simulation of foam - an example of inter-industrial synergy. In Hiermaier, S., editor, *Predictive Modeling of Dynamic Processes*, pages 27–42. Springer US.

Dugdale, D. S. (1960). Yielding of steel sheets containing slits. *Journal of the Mechanics and Physics of Solids*, 8(2):100 – 104.

DVA (2009). *Boeing 747-400 Airfraft Operations Manual*. Delta Virtual Airlines, first edition.

EASA (2007). Certification specification for engines - cs-e. Technical report, European Aviation Safety Agency.

Easycomposites (2010). Pre-preg carbon fibre flat sheet.

Elmarakbi, A. M., Hu, N., and Fukunaga, H. (2009). Finite element simulation of delamination growth in composite materials using ls-dyna. *Composites Science and Technology*, 69(14):2383–2391.

Finn, S. R. and Springer, G. S. (1993). Delaminations in composite plates under transverse static or impact loads - a model. *Composite Structures*, 23(3):177 – 190.

Flesher, N. D., Chang, F.-K., Janapala, N. R., and Starbuck, J. M. (2011). A dynamic crash model for energy absorption in braided composite materials - part ii: Implementation and verification. *Journal of Composite Materials*, 45(8):867–882.

Flores-Johnson, E. A. and Li, Q. M. (2011). Experimental study of the indentation of sandwich panels with carbon fibre-reinforced polymer face sheets and polymeric foam core. *Composites Part B: Engineering*, 42(5):1212 – 1219.

Fu Chang, S., Song, Y., and Lu, D. X. (1998). Unified constitutive equation of fam materials. *Engineering, Materials and Technology*, 120:212–217.

Fuoss, E., Straznicky, P. V., and Poon, C. (1998). Effects of stacking sequence on the impact resistance in composite laminates part 1: parametric study. *Composite Structures*, 41(1):67 – 77.

Gao, Y. and Bower, A. (2004). A simple technique for avoiding convergence problems in finite element simulations of crack nucleation and growth on cohesive interfaces. *Modelling and Simulation in Materials Science and Engineering*, 12(3):453.

GEAviation (2014). The genx engine. http://www.geaviation.com/commercial/engines/genx/. Accessed: 24.06.2014.

Gemkow, S. (2013). *Modelling of damage in orthotropic materials: icluding strain-softening effects in dynamic problems*. PhD thesis, Cranfield University.

German, J. (1996). *Podstawy mechaniki kompozytow wloknistych*. Wydawnictwo Politechniki Krakowskiej.

Geubelle, P. H. and Baylor, J. S. (1998). Impact-induced delamination of composites: a 2D simulation. *Composites Part B: Engineering*, 29(5):589 – 602.

Gingold, R. A. and Monaghan, J. J. (1977). Smoothed particle hydrodynamics: Theory and application to non-spherical stars. *Mon.Not.Roy.Astron.Soc.*, 181:375.

Goncalves, J., Moura, M. D., Castro, P. D., and Marques, A. (2000). Interface element including point-to-surface constraints for three-dimensional problems with damage propagation. *Engineering Computations*, 17(1):28–47.

GoodFellow (2008). Polycarbonate (pc) rod - material information. http://www.goodfellow.com/E/Polycarbonate-Rod.html. Accessed 04.03.2015.

Gordnian, K., Hadavinia, H., Mason, P., and Madenci, E. (2008). Determination of fracture energy and tensile cohesive strength in mode i delamination of angle-ply laminated composites. *Composite Structures*, 82(4):577 – 586.

Goyal, V. H., Huertas, C. A., Leutwiler, T. R., and Borrero, J. R. (2006a). Robust bird-strike modeling based on sph formulation using ls-dyna. In *Structures, Structural Dynamics, and Materials and Co-located Conferences*. American Institute of Aeronautics and Astronautics.

Goyal, V. K., Huertas, C. A., and Vasko, T. J. (2013). Bird-strike modelling based on the lagrangian formulation using ls-dyna. *American Transactions on Engineering & Applied Sciences*, 2:57–81.

Goyal, V. K. G., Huertas, C. A., Leutwiler, T. R., and Borrero, J. R. (2006b). Robust bird-strike modeling based on ale formulation using ls-dyna. In *Structures, Structural Dynamics, and Materials and Co-located Conferences*, pages –. American Institute of Aeronautics and Astronautics.

Griffith, A. A. (1921). The phenomena of rupture and flow in solids. *Philosophical Transactions of the Royal Society of London. Series A, Containing Papers of a Mathematical or Physical Character*, 221(582-593):163–198.

Guida, M., Marulo, F., Meo, M., Grimaldi, A., and Olivares, G. (2011). Sph - lagrangian study of bird impact on leading edge wing. *Composite Structures*, 93(3):1060 – 1071.

Gustin, J., Joneson, A., Mahinfalah, M., and Stone, J. (2005). Low velocity impact of combination kevlar/carbon fiber sandwich composites. *Composite Structures*, 69(4):396 – 406.

Hallquist, J. O. (2006). *LS-DYNA theory manual*. Livermore Software Technology Corporation (LSTC), 971st edition.

Hanssen, A., Girard, Y., Olovsson, L., Berstad, T., and Langseth, M. (2006). A numerical model for bird strike of aluminium foam-based sandwich panels. *International Journal of Impact Engineering*, 32(7):1127 – 1144.

Hashin, Z. (1980). Failure criteria for unidirectional fiber composites. *Journal of Applied Mechanics*, 47:329–334.

Hazizan, M. A. and Cantwell, W. J. (2002). The low velocity impact response of foam-based sandwich structures. *Composites Part B: Engineering*, 33(3):193 – 204.

Heimbs, S. (2011). Bird strike simulations on composite aircraft structures. In *SIMULIA Customer Conference*.

Heimbs, S. and Bergman, T. (2012). High-velocity impact behaviour of prestressed composite plates under bird strike loading. *International Journal of Aerospace Engineering*, 2012.

Hellen, T. K. (2005). On the method of virtual crack extensions. *International Journal for Numerical Methods in Engineering*, 9:187207.

Hillerborg, A., Modeeer, M., and Petersson, P. E. (1976). Analysis of crack formation and crack growth in concrete by means of fracture mechanics and finite elements. *Cement and Concrete Research*, 6(6):773 – 781.

Hitchen, S. A. and Kemp, R. M. J. (1995). The effect of stacking sequence on impact damage in a carbon fibre/epoxy composite. *Composites*, 26(3):207 – 214.

Hoof, J. V., Worswick, M. J., Stranznicky, P. V., and Bolduc, M. (1999). Effects of post-failure modelling on the response of ballistically impacted composites. In *Proceedings at ICCM12*.

Horrigan, D. P. W., Aitken, R. R., and Moltschaniwskyj, G. (2000). Modelling of crushing due to impact in honeycomb sandwiches. *Journal of Sandwich Structures and Materials*, 2(2):131–151.

Hou, J., Petrinic, N., Ruiz, C., and Hallett, S. (2000). Prediction of impact damage in composite plates. *Composites Science and Technology*, 60(2):273 – 281.

Hou, J. P., Petrinic, N., and Ruiz, C. (2001). A delamination criterion for laminated composites under low-velocity impact. *Composites Science and Technology*, 61(14):2069 – 2074.

Hu, N., Zemba, Y., Fukunaga, H., Wang, H. H., and Elmarakbi, A. M. (2007). Stable numerical simulations of propagations of complex damages in composite structures under transverse loads. *Composites Science and Technology*, 67:752–765.

Hung, K. S., Nilsson, L., and Zhong, Z. H. (1995). Numerical studies on the delamination mechanism in laminated composites under impact loading. In *Tenth International Conference on Composite Materials. V. Structures*, pages 623–630.

Iannucci, L. and Donadon, M. V. (2006). Bird strike modelling using new woven flass failure model. In *9th Internation LS-DYNA Users Conference*.

Ivanez, I., Santiuste, C., Barbero, E., and Sanchez-Saez, S. (2011). Numerical modelling of foam-cored sandwich plates under high-velocity impact. *Composite Structures*, 93(9):2392 – 2399.

Jenq, S. T., Hsiao, F. B., Lin, I. C., Zimcik, D. G., and Ensan, M. N. (2007). Simulation of a rigid plate hit by a cylindrical hemi-spherical tip-ended soft impactor. *Computational Materials Science*, 39(3):518–526.

Johnson, A. F. and Holzapfel, M. (2003). Modelling soft body impact on composite structures. *Composite Structures*.

Joshi, S. P. and Sun, C. T. (1985). Impact induced fracture in a laminated composite. *Journal of Composite Materials*, 19(1):51–66.

Kolling, K., Werner, A., Erhart, T., and Du Bois, P. A. (2007). An elastic damage model for the simulation oof recoverable polymeric foams. In *LS-DYNA Anwenderforum*.

Kolling, K., Werner, A., Erhart, T., and Du Bois, P. A. (2009). Simulation of recoverable foams under impact loading. In Hiermaier, S., editor, *Predictive Modeling of Dynamic Processes*, pages 9–25. Springer US.

KVSteel (2009). En24 steel. http://www.kvsteel.co.uk/steel/EN24T.html. Accessed 05.03.2015.

Lammerant, L. and Verpoest, I. (1996). Modelling of the interaction between matrix cracks and delaminations during impact of composite plates. *Composites Science and Technology*, 56(10):1171 – 1178.

Langrand, B., Bayart, A. S., Deletombe, E., and Chauveau, Y. (2002). Assessment of multi-physics fe methods for bird strike modelling - application to a metallic riveted airframe. *Internation Journal of Crashworthiness*, 7:415–428.

Lascoup, B., Aboura, Z., Khellil, K., and Benzeggagh, M. (2010). Impact response of three-dimensional stitched sandwich composite. *Composite Structures*, 92(2):347 – 353.

Lavoie, M., Gakwaya, A., Ensan, M. N., Zimcik, D., and Nandlall, D. (2009). Bird's substitute tests results and evaluation of available numerical methods. *International Journal of Impact Engineering*, 36:1276 – 1287.

Lee, M. J., Cho, T. M., Kim, W. S., Lee, B. C., and Lee, J. J. (2010). Determination of cohesive parameters for a mixed-mode cohesive zone model. *International Journal of Adhesion and Adhesives*, 30(5):322–328.

Lee, S. M. (1993). An edge crack torsion method for mode iii delamination fracture testing. *of Composites Techology & Research*, 15(3):193–201.

Lesuer, D. R. (2000). Experimental investigations of material model for ti-6al-4v and 2024-t3 aluminium. Technical Report DOT/FAA/AR-00/25, US Department of Transportation, Federal Aviation Administration.

Leung, S. Y. Y., Sadeghinia, M., Pape, H., and Ernst, L. J. (2011). Prediction of mixed-mode interfacial fracture from cohesive zone finite element model: Testing and determination of fracture process parameters. In *Thermal, Mechanical and Multi-Physics Simulation and Experiments in Microelectronics and Microsystems (EuroSimE), 2011 12th International Conference on*, pages 1/7–7/7.

Li, J. and O'brien, T. K. (1996). Simplified data reduction methods for the ect test for mode iii interlaminar fracture toughness. Technical report, NASA.

Lin, J. I. (2004). Dyna3d: A nonlinear, explicit, three-dimensional finite element code for solid and structural mechanics, user manual.

Liu, D., Raju, B. B., and Dang, X. (1998). Size effects on impact response of composite laminates. *International Journal of Impact Engineering*, 21(10):837 – 854.

LSTC (2001). Ls-dyna support. `http://www.dynasupport.com/tutorial/contact-modeling-in-ls-dyna/how-contact-works`. Accessed 05.11.2014.

LSTC (2006). Ls-dyna theory manual.

LSTC (2013a). *LS-DYNA keyword manual volume II: Material models.* Livermore Software Technology Corporation (LSTC), r7.0 edition.

LSTC (2013b). *LS-DYNA keyword user's manual volume I.* Livermore Software Technology Corporation (LSTC), r7.0 edition.

LSTC (2014). Mat59 solids. online. (last accessed 12/10/2014).

LSTC, L.-D. A. W. G. (2012). Modeling guidelines document.

Lucy, L. B. (1977). A numerical approach to the testing of the fission hypothesis. *Astron.J.*, 82:1013–1024.

Luo, R. K., Green, E. R., and Morrison, C. J. (1999). Impact damage analysis of composite plates. *International Journal of Impact Engineering*, 22(4):435 – 447.

M. V. Donadon, M. A. Arbelo, S. F. M. d. A. M. A. A. J. P. (2010). Bird strike modelling in composite stiffened panels. In *11th Pan-American Congress of Applied Mechanics*.

Mahfuz, H., AlMamum, W., and Jeelani, S. (1992). Effect of core density and implanted delamination on the high strain rate response of foam core sandwich composites. *Sandwich Constructions*, 5:597–606.

Maldague, X. (2000). *Applications of Infrared Thermography in Nondestructive Evaluation. Trends in optical nondestructive testing.* Elsevier, 1st edition.

Mao, R. H., Meguid, S. A., and Ng, T. Y. (2007). Finite element modeling of a bird striking an engine fan blade. *Journal of Aircraft*, 44(2):583–596. RX: 850816 (on Jun 30, 2010).

Mao, R. H., Meguid, S. A., and Ng, T. Y. (2008). Transient three dimensional finite element analysis of a bird striking a fan blade. *International Journal of Crashworthiness*, 4(1):79–96.

Mao, R. H., Meguid, S. A., and Ng, T. Y. (2009). Effects of incidence angle in bird strike on integrity of aero-engine fan blade. *International Journal of Crashworthiness*, 14(4):295–308. RX: 850816 (on Jun 30, 2010).

Martin, N. F. (1990). Nonlinear finite-element analysis to predict fan-blade damage due to soft-body impact. *Journal of Propulsion and Power,*, 6(4):445–450.

Martindale, I. (1994). Bird ingestion and the rolls-royce wide chord fan. Technical Report IBSC22 WP80, Bird Strike Committee Europe.

Matzenmiller, A., Lubliner, J., and Taylor, R. L. (1995). A constitutive model for anisotropic damage in fiber-composites. *Mechanics of Materials*, 20(2):125–152.

McCallum, S. C. and Constantinou, C. (2005). The influence of bird-shape in bird-strike analysis. *5th European LS-Dyna Users Conference*. Cited By (since 1996): 1.

McCarthy, M. A., Xiao, J. R., McCarthy, C. T., Kamoulakos, A., Ramos, J., Gallard, J. P., and Melito, V. (2005). Modelling bird impacts on an aircraft wing part 2: Modelling the impact with an sph bird model. *Applied Composite Materials*, 10(1):51–59.

Meola, C. and Carlomagno, G. M. (2010). Impact damage in gfrp: New insights with infrared thermography. *Composites Part A: Applied Science and Manufacturing*, 41(12):1839 – 1847.

Metallurgie, F. (2010). Etat actuel du marche des alliages a hautes performances destinés au marche de l'aeronautique (us). `http://www.france-metallurgie.com/index.php/2010/03/25/eta-cateul-du-marche-des-allaiges-a-hautes-performances-destinees-au-marche-de-laeronautique-us/`. Accessed 24.06.2014.

Mi, Y., Crisfield, M. A., Davies, G. A. O., and Hellweg, H. B. (1998). Progressive delamination using interface elements. *Journal of Composite Materials*, 32(14):1246–1272.

Mines, R. A. W., Worrall, C. M., and Gibson, A. G. (1998). Low velocity perforation behaviour of polymer composite sandwich panels. *International Journal of Impact Engineering*, 21(10):855 – 879.

Miyachi, T., Okumura, H., and Ohtake, K. (1991). An analysis of the effect of centrifugal force on the impact resistance of composite fan blades for turbo-fan engines. In *International Pacific Air and Space Technology Conference and Aircraft Symposium, 29th, Gifu, Japan; 7-11 Oct. 1991*, volume SAE PAPER 912047.

Mohmmed, R., Zhang, F., Sun, B., and Gu, B. (2013). Finite element analyses of low-velocity impact damage of foam sandwiched composites with different ply angles face sheets. *Materials & Design*, 47(0):189 – 199.

Needleman, A. (1987). A continuum model for void nucleation by inclusion debonding. *Journal of Applied Mechanics*, 54:525.

Nguyen, T. K. D., Zhao, Y., Hill, E., and Wang, C. S. (2006). After-impact compressive strength prediction for laminated composites. In *47th AIAA/ASME/ASCE/AHS/ASC Structures, Structural Dynamics, and Materials Conference; Newport, RI; USA; 1-4 May 2006*, volume AIAA Paper 2006-1693. American Institute of Aeronautics and Astronautics.

Ortiz, M. and Pandolfi, A. (1999). Finite-deformation irreversible cohesive elements for three-dimensional crack-propagation analysis. *International Journal for Numerical Methods in Engineering*, 44(9):1267–1282.

P., Y., W., G., Z., T., P., S., and R., Y. (2013). Dynamic mechanical behaviour of 6082-t6 aluminium alloy. *Advances in Mechanical Engineering*, 2013. Article ID 878016.

Parks, D. M. (1974). A stiffness derivative finite element technique for determination of crack tip stress intensity factors. *International Journal of Fracture*, 10(4):487–502.

Peng, L. L., Gong, X. J., and Guillaumat, L. (2011). Numerical simulation of damage propagation in cfrp laminates repaired by external bonded patches under tensile loading. In *18th International conference on composite materials*, Jeju Island, South Korea.

Petersson, P. E. (1981). *Crack growth and development of fracture zones in plain concrete and similar materials*. PhD thesis, Lund University.

Petrossian, Z. and Wisnom, M. R. (1998). Prediction of delamination initiation and growth from discontinuous plies using interface elements. *Composites Part A: Applied Science and Manufacturing*, 29:503 – 515.

Pinho, S. T., Camanho, P. P., and DeMoura, M. F. (2004). Numerical simulation of the crushing process of composite materials. *International Journal of Crashworthiness*, 9(3):263–276.

Prichard, J. C. and Hogg, P. J. (1990). The role of impact damage in post-impact compression testing. 21:503–511. Research supported by SERC; NR: 27 RX: 7 (on Aug 31, 2011).

Products, Q. E. P. (2003a). Acetal copolymer product data sheet. Accessed: 20.03.2014.

Products, Q. E. P. (2003b). Polycarbonate product data sheet. Accessed 04.03.2014.

Quek, S. C., Waas, A., Shahwan, K. W., and Agaram, V. (2004a). Compressive response and failure of braided textile composites: Part 2 - computations. *International Journal of Non-Linear Mechanics*, 39(4):649 – 663.

Quek, S. C., Waas, A. M., Shahwan, K. W., and Agaram, V. (2004b). Compressive response and failure of braided textile composites: Part 1 - experiments. *International Journal of Non-Linear Mechanics*, 39(4):635 – 648.

Rajaneesh, A., Sridhar, I., and Rajendran, S. (2009). Numerical modeling of low velocity impact response on metal foam ccore sandwich panels: effect of various facesface materials. In *18th International conference on composite materials*.

Rajbhandari, S. P., Scott, M. L., Thomson, R. S., and Hachenberg, D. (2002). An approach to modelling and predictind impact damage in composite structures. 23rd Congress of International Council of the Aeronautical Sciences.

Raju, I. (1987). Calculation of strain-energy release rates with higher order and singular finite elements. *Engineering Fracture Mechanics*, 28(3):251 – 274.

Raju, K. S., Smith, B. L., Tomblin, J. S., Liew, K. H., and Guarddon, J. C. (2008). Impact damage resistance and tolerance of honeycomb core sandwich panels. *Journal of Composite Materials*, 42(4):385–412.

Rao, S. (1999). *The Finite Element mothod in engineering*. ButElsevier-Heinemann, 3rd edition.

Ratcliffe, J. G. (2004). Characterization of the edge crack torsion (ect) test for mode iii fracture toughness measurement of laminated composites. Technical report, NASA.

Reeder, J. R. (1992). An evaluation of mixed - mode delamination failure criteria. Technical Report TM 104210, NASA.

Reedy, E. D., Mello, F. J., and Guess, T. R. (1997). Modeling the initiation and growth of delaminations in composite structures. *Journal of Composite Materials*, 31(8):812–831.

Reyes, A., Hopperstad, O., Berstad, T., Hanssen, A., and Langseth, M. (2003). Constitutive modeling of aluminum foam including fracture and statistical variation of density. *European Journal of Mechanics - A/Solids*, 22(6):815 – 835.

Reyes, A., Hopperstad, O. S., Berstad, T., and Langseth, M. (2004). Implementation of a constitutive model for aluminum foam including fracture and statistical variation of density. In *8th International LS-DYNA users conference.*

Rhodes, M. D. (1975). Impact fracture of composite sandwich structures. In *Proceedings of the 16th Structures, Structural Dynamics and Materials Conference.* AIAA.

Rice, J. R. (1968). A path independent integral and the approximate analysis of strain concentration by notches and cracks. *Journal of Applied Mechanics*, 35:379–386.

Richardson, M. O. W. and Wisheart, M. J. (1996). Review of low-velocity impact properties of composite materials. *Composites Part A: Applied Science and Manufacturing*, 27(12):1123 – 1131.

Riks, E. (1979). An incremental approach to the solution of snapping and buckling problems. *International Journal of Solids and Structures*, 15(7):529 – 551.

Rybicki, E. and Kanninen, M. (1977). A finite element calculation of stress intensity factors by a modified crack closure integral. *Engineering Fracture Mechanics*, 9(4):931 – 938.

Sanchez-Saez, S., Barbero, E., Zaera, R., and Navarro, C. (2005). Compression after impact of thin composite laminates. *Composites Science and Technology*, 65(13):1911 – 1919.

Scheider, I. and Brocks, W. (2003). Simulation of cup-cone fracture using the cohesive model. *Engineering Fracture Mechanics*, 70(14):1943 – 1961. Cohesive Models.

Schellekens, J. C. J. and DeBorst, R. (1994). Free edge delamination in carbon-epoxy laminates: a novel numerical/experimental approach. *Composite Structures*, 28(4):357 – 373.

Schweizerhof, K., Weimar, K., Munz, T., and Rottner, T. (1998). Crashworthiness analysis with enhanced composite material models in ls-dyna - merits and limits. Detroit. Livermore Software.

Seidl, M., Hughes, K., and DeVuyst, T. (2013). Modelling internal gas flows in a single stage gas gun using eulerian/lagrangian coupling in ls-dyna. In *9th European LS-DYNA Conference*.

Serifi, E., Hirth, A., Matthaei, S., and Mullerschon, H. (2003). Modelling of foams using mat83 - preparation and evaluation of experimental data. In *4th European LS-DYNA users conference*.

Shahwan, K. W. and Waas, A. M. (1997). Non–self–similar decohesion along a finite interface of unilaterally constrained delaminations. *Proceedings of the Royal Society of London. Series A: Mathematical, Physical and Engineering Sciences*, 453(1958):515–550.

Shepard, S. M. (1997). Introduction to active thermography for non-destructive evaluation. *Anti-Corrosion Methods and Materials*, 44(4):236–239. cited By (since 1996)33.

Shepard, S. M. (2007). Flash thermography of aerospace composites. In *IV Conferencia Panamericana de END Buenos Aires*.

SIMULIA (2013). *Abaqus/CAE User's guide*. Dassault Systems Simulia Corporation.

Siow, Y. P. and Shim, V. P. W. (1998). An experimental study of low velocity impact damage in woven fiber composites. *Journal of composite materials*, 141-143:35.

Slik, G., Vogel, G., and Chawda, V. (2006). Material model validation of a high efficient energy absorbing foam. In *5th LS-DYNA Forum*.

Song, S., Waas, A. M., Shahwan, K. W., Xiao, X., and Faruque, O. (2007). Braided textile composites under compressive loads: Modeling the response, strength and degradation. *Composites Science and Technology*, 67(1516):3059 – 3070.

Steinberg, D. J. (1996). Equation of state and strength properties of selected materials. Technical Report UCRL-MA-106439, Lawrence Livermore National Laboratory. Cited By (since 1996): 109.

Stoker, H. C. (1999). *Developments of the arbitrary lagrangian-eulerian method in non-linear solid mechanics applications to forming processes*. PhD thesis, Universiteit Twente.

Stoll, F. and Brockman, R. A. (1997). Finite element simulation of high-speed soft-body impacts. volume 1, pages 334–344, New York, USA. AIAA, New York, NY, United States. Cited By (since 1996): 6.

Swegle, J. W., Hicks, D. L., and Attaway, S. W. (1995). Smoothed particle hydrodynamics stability analysis. *Journal of Computational Physics*, 116(1):123–134. Cited By (since 1996): 137.

Thorpe, J. (2012). 100 years of fatalities and destroyed civil aircraft due to bird strikes. Technical Report IBSC30/WP, International Bird Strike Committee, Stavanger, Norway.

Torre, L. and Kenny, J. M. (2000). Impact testing and simulation of composite sandwich structures for civil transportation. *Composite Structures*, 50(3):257 – 267.

Tsai, S. W. and Wu, E. M. (1971). A general theory of strength for anisotropic materials. *Journal of Composite Materials*, 5(1):58–80.

Turon, A., Davila, C. G., Camanho, P. P., and Costa, J. (2007). An engineering solution for mesh size effects in the simulation of delamination using cohesive zone models. *Engineering Fracture Mechanics*, 74(10):1665–1682.

Tvergaard, V. (1990). Effect of fibre debonding in a whisker-reinforced metal. *Materials Science and Engineering*, 125(2):203 – 213.

Tvergaard, V. and Hutchinson, J. W. (1992). The relation between crack growth resistance and fracture process parameters in elastic-plastic solids. *Journal of the Mechanics and Physics of Solids*, 40(6):1377 – 1397.

Tvergaard, V. and Hutchinson, J. W. (1993). The influence of plasticity on mixed mode interface toughness. *Journal of the Mechanics and Physics of Solids*, 41(6):1119 – 1135.

Vaidya, A. S., Vaidya, U. K., and Uddin, N. (2008). Impact response of three-dimensional multifunctional sandwich composite. *Materials Science and Engineering: A*, 472:52 – 58.

Vaidya, U. K., Nelson, S., Sinn, B., and Mathew, B. (2001). Processing and high strain rate impact response of multi-functional sandwich composites. *Composite Structures*, 52:429 – 440. Design and Manufacturing of Composite Structures.

Velmurugan, R., Babu, M. G., and Gupta, N. K. (2006). Projectile impact on sandwich panels. *International Journal of Crashworthiness*, 11(2):153–164.

Vignjevic, R. and Campbell, J. C. (2009). Review of development of the smooth particle hydrodynamics (sph) method. In Hiermaier, S., editor, *Predictive Modeling of Dynamic Processes*, pages 367–396. Springer US.

Vignjevic, R., Orlowski, M., DeVuyst, T., and Campbell, J. C. (2013). A parametric study of bird strike on engine blades. *International Journal of Impact Engineering*, 60:44 – 57.

Vignjevic, R., Reveles, J. R., and Campbell, J. C. (2006a). Sph in a total lagrangian formalism, meshless methods. *Computer Methods in Engineering and Science*, 14(3):181–198.

Vignjevic, R., Vuyst, T. D., and Campbell, J. C. (2006b). A frictionless contact algorithm for meshless methods. *Computer Methods in Engineering and Science*, 13(1):35–48.

Villanueva, G. R. and Cantwell, W. J. (2004). The high velocity impact response of composite and fml-reinforced sandwich structures. *Composites Science and Technology*, 64(1):35 – 54.

Wang, B., Zhang, G., Wang, S., Ma, L., and Wu, L. (2014). High velocity impact response of composite lattice core sandwich structures. *Applied Composite Materials*, 21(2):377–389.

Wang, J., Waas., A. M., and Wang, H. (2012). Experimental study on the low-velocity impact behavior of foam-core sandwich panels. In *53rd AIAA/ASME/ASCE/AHS/ASC Structures, Structural Dynamics and Materials Conference*.

Widjanarko, T., Tinsley, L., Roy, R., and Mehnen, J. (2012). Characterisation and performance assessment of a pulsed-thermography camera system for component degradation inspection. In *1st International Conference on Through-life Engineering Services Cranfield*.

Wilbeck, J. S. (1978). Impact behavior of low strength projectiles. *Air Force Materials Lab, AFML-TR-77-134*.

Wilbeck, J. S. and Barber, J. P. (1978). Bird impact loading. Technical Report AD-A148 083, The Shock and Vibration Information Center.

Wisnom, M. R. (2012). The role of delamination in failure of fibre-reinforced composites. *Philosophical Transactions of the Royal Society*, 370:1850–1870.

Wittmann, F., Rokugo, K., Bralhwiler, E., Mihashi, H., and Simonin, P. (1988). Fracture energy and strain softening of concrete as determined by means of compact tension specimens. *Materials and Structures*, 21(1):21–32.

Xiao, X., Botkin, M. E., and Johnson, N. L. (2009). Axial crush simulation of braided carbon tubes using mat58 in ls-dyna. *Thin-Walled Structures*, 47(6-7):740–749.

Zhang, X. (1998). Impact damage in composite aircraft structures - experimantal testing and numerical simulation. *Journal of aerospace engineering*, 212:245.

Zheng, S. and Sun, C. (1995). A double-plate finite-element model for the impact-induced delamination problem. *Composites Science and Technology*, 53(1):111 – 118.

Appendix A

MATLAB script for determination of failure mode for MAT_22 and MAT_59

```
char c;
char s;
char alfa;

% Composite material constants in fibre directions
E1=70800;
E2=42700;
E3=8000;
nu21=0.125;
nu31=0.037;
nu32=0.062;
nu12=nu21*E1/E2
nu13=nu31*E1/E3
nu23=nu32*E2/E3
G12=10600;
G13=4400;
G23=2500;
sigmaT1=1119;
sigmaT2=617;
sigmaT3=60;
sigmaC1=-768;
sigmaC2=-463;
sigmaC3=-30;
SH12=146;
SH13=93;
```

```
SH23=53;

     % Define the stress state of the element
        sigmaX=284
        sigmaY=0
        sigmaZ=0
        ShXY=0
        ShXZ=0
        ShYZ=0

        alfa= pi/4    %define the ply orientation

c=cos(alfa)
s=sin(alfa)

%stress matrix AB plane fibres

stressXYZ = [sigmaX ShXY ShXZ; ShXY sigmaY ShYZ; ShXZ ShYZ sigmaZ]

%rotation matrix around Z axis

R = [c -s 0; s c 0; 0 0 1]
RT = transpose(R)

%stresses in the coordinate system rotated around Z axis

stress123 = RT*stressXYZ*R
%stress123 = [S_1 Sh_12 Sh_13; Sh_12 S_2 Sh_23; Sh_13 Sh_23 S_3]

S_1 = stress123(1,1)
S_2 = stress123(2,2)
S_3 = stress123(3,3)
Sh_12 = stress123(1,2);
Sh_13 = stress123(1,3);
Sh_23 = stress123(2,3);

%Chang chang criterias - tension
fprintf('MAT_22 - CHANG CHANG FAILURE')

if S_1 > 0 && S_2>0 && Sh_12>0.001;
    %tensile fibre
```

```
    CC1 = (S_1/sigmaT1)^2
    v(1)=CC1;
    w{1}='CC1';
        %tensile transverse
    CC3 = (S_2/sigmaT2)^2 + (Sh_12/SH12)^2
    v(2)=CC3;
    w{2}='CC3';

    for i=1:2;
        if v(i)>0.99
            fprintf('Failed in: %s \n \n', w{i})
        end
    end

elseif S_1  > 0;
    %tensile fibre
    CC1 = (S_1/sigmaT1)^2
    v(1)=CC1;
    w{1}='CC1';

    for i=1;
        if v(1)>0.99
            fprintf('Failed in: %s \n \n', w{1})
        end
    end

elseif S_2 > 0;

    %tensile transverse
    CC3 = (S_2/sigmaT2)^2 + (Sh_12/SH12)^2
    v(1)=CC3;
    w{1}='CC3';

    for i=1;
        if v(1)>0.99
            fprintf('Failed in: %s \n \n', w{1})
        end
    end

elseif S_3 > 0;
      %tensile transverse
```

```
    CCD4 = (S_3/sigmaT3)^2 + (Sh_13^2+Sh_23^2/SH13^2)^2
    v(3)=CCD4;
    w{3}='CCD4';
    for i=3;
        if v(3)>0.99
            fprintf('Failed in: %s \n \n', w{3})
        end
    end

elseif S_2 < -0.001;
    %compression
    CC2 = (S_1/sigmaC1)^2
    for i=1;
        if v(1)>0.99
            fprintf('Failed in: %s \n \n', w{1})
        end
    end

else
    %tensile transverse
    CC3 = (S_2/sigmaT2)^2 + (Sh_12/SH12)^2
    v(1)=CC3;
    w{1}='CC3';

    %tensile transverse
    CCD4 = (S_3/sigmaT3)^2 + (Sh_13^2+Sh_23^2/SH13^2)^2
    v(2)=CCD4;
    w{2}='CCD4';
    for i=1:2;
        if v(3)>0.99
            fprintf('Failed in: %s \n \n', w{3})
        end
    end

end

fprintf('MAT_59 - CHANG-HALQUIST FAILURE \n')

%Cheng - Halquist

if S_1 > 0.001 && S_2>0.001;
```

```
% Fibre failure under tension
    CH1 = (S_1/sigmaT1)^2 + (Sh_12/SH12)^2 + (Sh_13/SH13)^2
    v(1)=CH1;
    w{1}='CH1';

    % Matrix failure under transverse tension
    CH2 = (S_2/sigmaT2)^2 + (Sh_12/SH12)^2 + (Sh_13/SH13)^2
    v(2)=CH2;
    w{2}='CH2';

    %Longitudinal shear
    CH3 = (S_1/sigmaT1)^2 + (Sh_13/SH13)^2
    v(3)=CH3;
    w{3}='CH3';

    %Transverse shear
    CH4 = (S_2/sigmaT2)^2 + (Sh_13/SH13)^2
    v(4)=CH4;
    w{4}='CH4';

    for j=1:4;
        if v(j)>0.99
            fprintf('Failed in: %s \n \n', w{j})
        end
    end

elseif S_1 > 0.001;
    % Fibre failure under tension
    CH1 = (S_1/sigmaT1)^2 + (Sh_12/SH12)^2 + (Sh_13/SH13)^2
    v(1)=CH1;
    w{1}='CH1';

    %Longitudinal shear
    CH3 = (S_1/sigmaT1)^2 + (Sh_13/SH13)^2
    v(2)=CH3;
    w{2}='CH3';

    for j=1:2;
        if v(j)>0.99
            fprintf('Failed in: %s \n \n', w{j})
        end
```

```
    end

elseif S_2 > 0.001;

    % Matrix failure under transverse tension
    CH2 = (S_2/sigmaT2)^2 + (Sh_12/SH12)^2 + (Sh_13/SH13)^2
    v(1)=CH2;
    w{1}='CH2';

    %Transverse shear
    CH4 = (S_2/sigmaT2)^2 + (Sh_13/SH13)^2
    v(2)=CH4;
    w{2}='CH4';

    for j=1:2;
        if v(j)>0.99
            fprintf('Failed in: %s \n \n', w{j})
        end
    end

elseif S_3 > 0.001;
            %delamination failure
    CH5 = (S_3/sigmaT3)^2 + (Sh_13/SH13)^2 + (Sh_23/SH23)^2
    v(5)=CH5;
    w{5}='CH5';
    for i=5;
        if v(i)>0.99
            fprintf('Failed in: %s \n \n', w{i})
        end
    end

elseif S_1 < -0.001 && S_2 < -0.001;
    %fibre failure under longitudinal COMPRESSION
    CH6 = (S_1/sigmaC1)^2
    v(1)=CH6;
    w{2}='CH6';
    %Matrix failure under transverse compression
    CH7 = S_2^2/(SH12+SH23)^2 + ((sigmaC2/(SH12+SH23))^2-1)*(S_2/sigmaC2) +
    (Sh_12/SH12)^2 + (Sh_23/SH23)^2
    v(2)=CH7;
    w{2}='CH7';
```

```
    for i=1:2;
        if v(i)>0.99
            fprintf('Failed in: %s \n \n', w{i})
        end
    end
elseif S_1 < -0.001;
    %fibre failure under longitudinal COMPRESSION
    CH6 = (S_1/sigmaC1)^2
    v(6)=CH6;
    w{6}='CH6';
    for i=6;
        if v(i)>0.99
            fprintf('Failed in: %s \n \n', w{i})
        end
    end

elseif S_2 < -0.001;

    %Matrix failure under transverse compression
    CH7 = S_2^2/(SH12+SH23)^2 + ((sigmaC2/(SH12+SH23))^2-1)*(S_2/sigmaC2) +
    (Sh_12/SH12)^2 + (Sh_23/SH23)^2
    v(7)=CH7;
    w{7}='CH7';

    for j=7;
        if v(j)>0.99
            fprintf('Failed in: %s \n \n', w{j})
        end
    end

    %SHEAR FAILURE

else

    % Fibre failure under tension
    CH1 = (S_1/sigmaT1)^2 + (Sh_12/SH12)^2 + (Sh_13/SH13)^2
    v(1)=CH1;
    w{1}='CH1';

    % Matrix failure under transverse tension
```

```
    CH2 = (S_2/sigmaT2)^2 + (Sh_12/SH12)^2 + (Sh_13/SH13)^2
    v(2)=CH2;
    w{2}='CH2';

    %Longitudinal shear
    CH3 = (S_1/sigmaT1)^2 + (Sh_13/SH13)^2
    v(3)=CH3;
    w{3}='CH3';

    %Transverse shear
    CH4 = (S_2/sigmaT2)^2 + (Sh_13/SH13)^2
    v(4)=CH4;
    w{4}='CH4';

    %delamination failure
    CH5 = (S_3/sigmaT3)^2 + (Sh_13/SH13)^2 + (Sh_23/SH23)^2
    v(5)=CH5;
    w{5}='CH5';

    %Matrix failure under transverse compression
    CH7 = S_2^2/(SH12+SH23)^2 + ((sigmaC2/(SH12+SH23))^2-1)*(S_2/sigmaC2) +
    (Sh_12/SH12)^2 + (Sh_23/SH23)^2
    v(6)=CH7;
    w{6}='CH7';

    %fibre under through thickness COMPRESSION
    CH8 = S_3^2/(SH13+SH23)^2 + ((sigmaC3/(SH13+SH23))^2-1)*(S_3/sigmaC3) +
    (Sh_13/SH13)^2 + (Sh_23/SH23)^2
    v(7)=CH8;
    w{7}='CH8';

    for j=1:7;
        if v(j)>0.99
            fprintf('Failed in: %s \n \n', w{j})
        end
    end
end
```

Appendix B

Single element tests of composite material models in LS-DYNA

Additional results from single element test performed with LS-DYNA for different solid composite material models are presented in this Appendix. The results consist of stress-strain relations for the CA and BC planes, as well as tables with the failure strengths and failure strains.

B.1 MAT_22

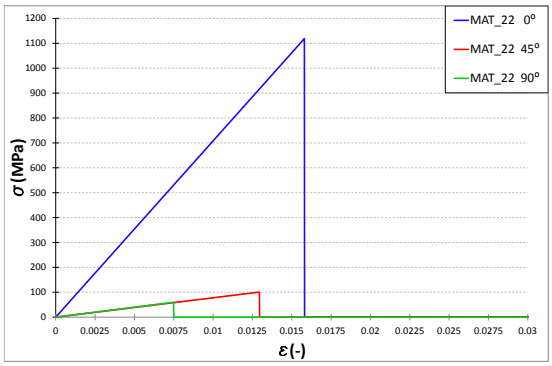

(A) Tension in AC plane

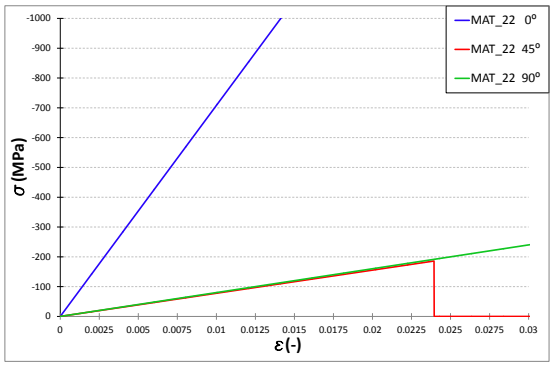

(B) Compression in AC plane

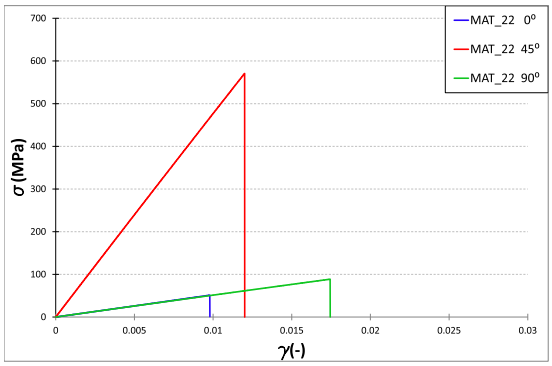

(C) Shear in AC plane

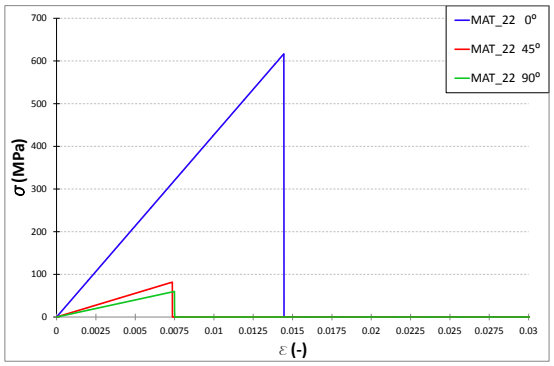

(D) Tension in BC plane

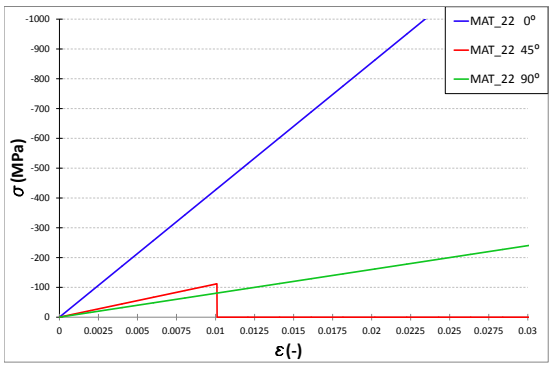

(E) Compression in BC plane

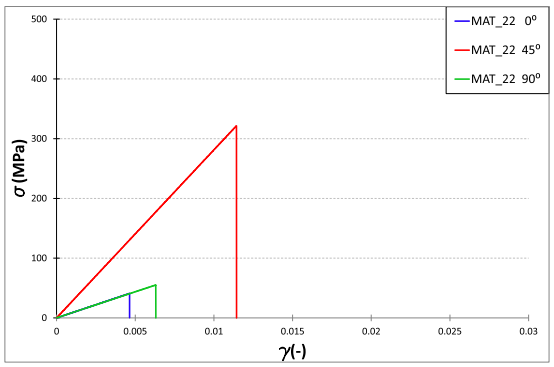

(F) Shear in BC plane

Figure B.1: MAT_22 single element test results for 0°, 45° and 90° material orientation in AC plane(A-C) and BC plane (D-F).

Table B.1: Failure strengths for MAT_22 in AC plane.

MAT_22 AB					
	LAYUP	LS-DYNA INPUT	LS-DYNA OUTPUT	Error	FC
TENSION	0°	1119	1118.95	0.00%	CC1
	45°	101	100.787	-0.21%	CC4
	90°	60	59.935	0.11%	CC4
COMPRESSION	0°	-	-	-	-
	45°	-	100.787	-	CC4
	90°	-	-	-	-
SHEAR	0°	93	51.232	44.91%	CC1
	45°	-	569.475	-	CC4
	90°	93	88.649	4.68%	CC4

Table B.2: Failure strengths for MAT_22 in BC plane.

MAT_22 BC					
	LAYUP	LS-DYNA INPUT	LS-DYNA OUTPUT	Error	FC
TENSION	0°	617	616.804	0.03%	CC4
	45°	82	81.813	-0.23%	CC4
	90°	60	59.935	0.11%	CC3
COMPRESSION	0°	-	-	-	-
	45°	-	111.970	-	CC4
	90°	-	-	-	-
SHEAR	0°	56	41.006	26.78%	CC4
	45°	-	321.632	-	CC4
	90°	56	55.091	1.62%	CC3

Table B.3: Failure strains for MAT_22 in AC plane.

MAT_22 AC					
	LAYUP	LS-DYNA INPUT	LS-DYNA OUTPUT	Error	FC
TENSION	0°	0.015805	0.015814	-0.06%	CC1
	45°	-	0.012966	- %	CC4
	90°	0.0075	0.007522	-0.29%	CC4
COMPRESSION	0°	-	-	-	-
	45°	-	0.023985	-	CC4
	90°	-	-	-	-
SHEAR	0°	0.021136	0.019592	7.31%	CC1
	45°	-	0.024019	-	CC4
	90°	0.021136	0.034886	65.05%	CC4

Table B.4: Failure strains for MAT_22 in BC plane.

MAT_22 BC					
	LAYUP	LS-DYNA INPUT	LS-DYNA OUTPUT	Error	FC
TENSION	0°	0.01445	0.014465	0.01%	CC4
	45°	-	0.007376	-0.63%	CC4
	90°	0.0075	0.007521	-0.04%	CC3
COMPRESSION	0°	-	-	-	-
	45°	-	0.010111	-	CC4
	90°	-	-	-	-
SHEAR	0°	0.020385	0.009285	54.45%	CC4
	45°	-	0.022878	-	CC4
	90°	0.020385	0.012623	38.08%	CC3

B.2 MAT_59

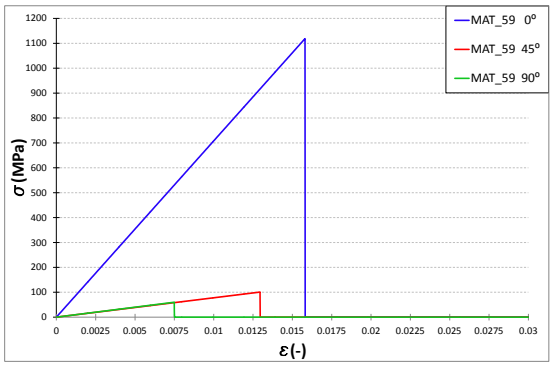

(A) Tension in AC plane

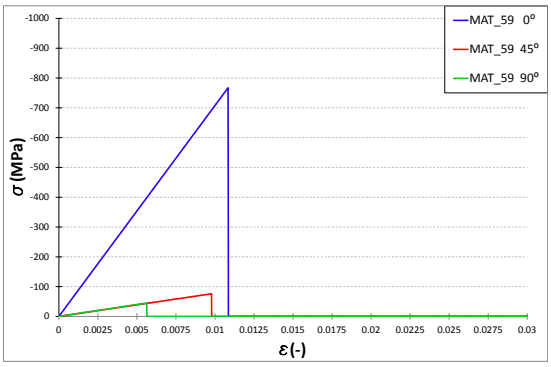

(B) Compression in AC plane

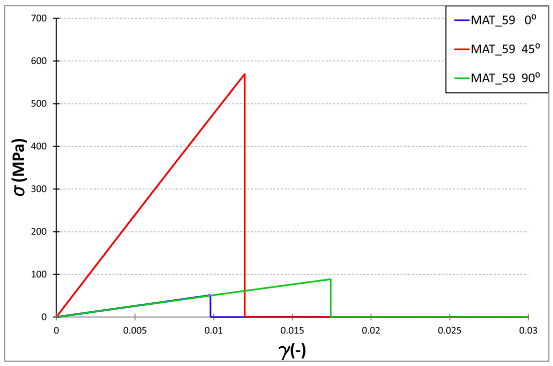

(C) Shear in AC plane

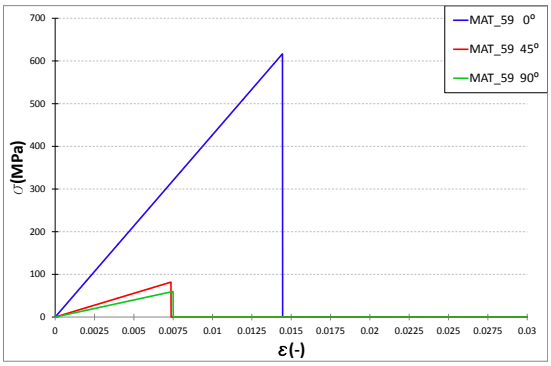

(D) Tension in BC plane

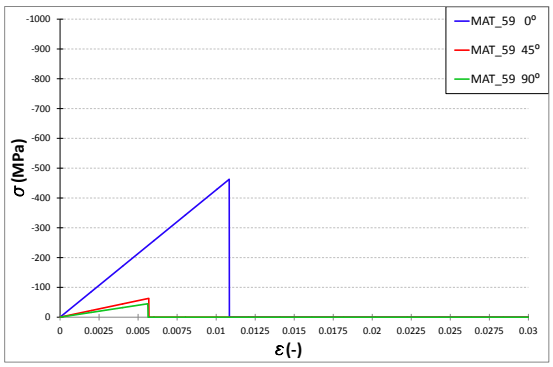

(E) Compression in BC plane

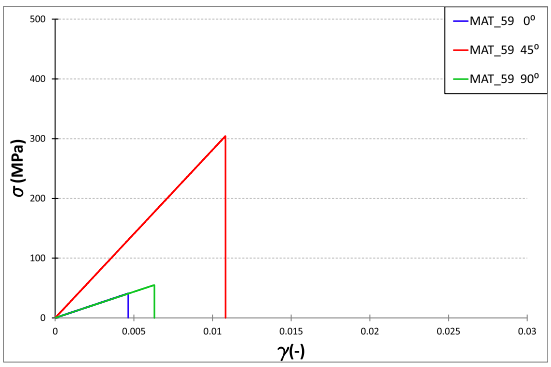

(F) Shear in BC plane

FIGURE B.2: MAT_59 single element test results for 0°, 45° and 90° material orientation in AC plane(A-C) and BC plane (D-F).

Table B.5: Failure strengths for MAT_59 in AC plane.

MAT_59 AC					
	LAYUP	LS-DYNA INPUT	LS-DYNA OUTPUT	Error	FC
TENSION	0°	1119	1118.95	0.00%	CH1
	45°	101	100.787	0.21%	CH5
	90°	60	59.935	0.11%	CH5
COMPRESSION	0°	-768	-767.367	0.08%	CH6
	45°	-	-75.984	-	CH8
	90°	-45	-44.925	0.17%	CH8
SHEAR	0°	93	91.449	1.67%	CH5
	45°	-	559.408	-	CH8
	90°	93	92.956	0.05%	CH5

Table B.6: Failure strengths for MAT_59 in BC plane.

MAT_59 BC					
	LAYUP	LS-DYNA INPUT	LS-DYNA OUTPUT	Error	FC
TENSION	0°	617	616.804	0.03%	CH5
	45°	82	81.813	-0.23%	CH5
	90°	60	59.935	0.11%	CH2
COMPRESSION	0°	-463	-462.925	0.80%	CH8
	45°	-	-63.118	-	CH8
	90°	-45	-45.925	0.17%	CH7
SHEAR	0°	56	55.790	0.37%	CH5
	45°	-	308.474	-	CH5
	90°	56	55.966	0.06%	CH5

Table B.7: Failure strains for MAT_59 in AC plane.

MAT_59 AC					
	LAYUP	LS-DYNA INPUT	LS-DYNA OUTPUT	Error	FC
TENSION	0°	0.015805	0.015814	-0.06%	CH1
	45°	-	0.012966	-	CH5
	90°	0.0075	0.007522	-0.29%	CH5
COMPRESSION	0°	0.010848	0.010869	-0.20%	CH6
	45°	-	0.009798	-	CH8
	90°	0.005625	0.005646	-0.37%	CH8
SHEAR	0°	0.013774	0.019592	7.31%	CH5
	45°	-	0.024019	-	CH8
	90°	0.013774	0.034886	65.05%	CH5

Table B.8: Failure strains for MAT_59 in BC plane.

MAT_59 BC					
	LAYUP	LS-DYNA INPUT	LS-DYNA OUTPUT	Error	FC
TENSION	0°	0.01445	0.014465	0.01%	CH5
	45°	-	0.007376	-0.63%	CH5
	90°	0.0075	0.007521	-0.04%	CH2
COMPRESSION	0°	-	-	-	CH8
	45°	-	0.010111	-	CH8
	90°	-	-	-	CH7
SHEAR	0°	0.013774	0.009285	54.45%	CH5
	45°	-	0.022878	-	CH5
	90°	0.013774	0.012623	38.08%	CH5

B.3 MAT_221

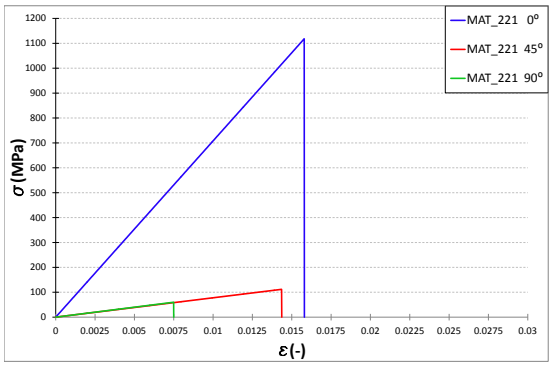

(A) Tension in AC plane

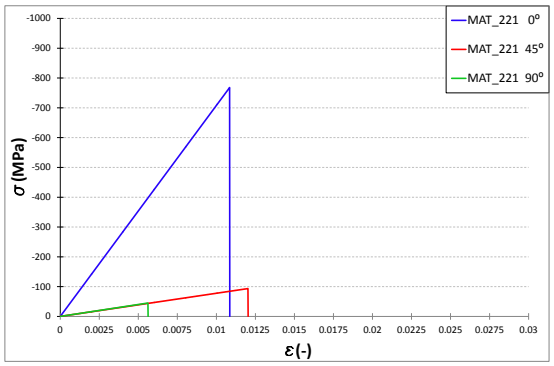

(B) Compression in AC plane

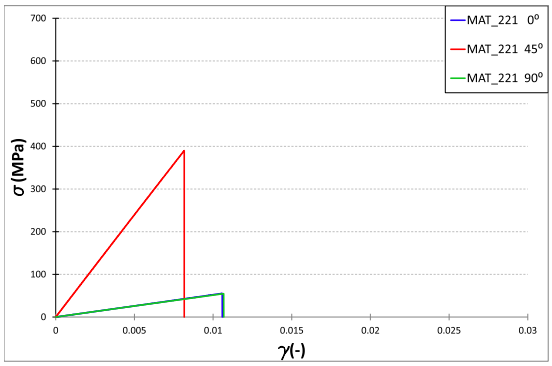

(C) Shear in AC plane

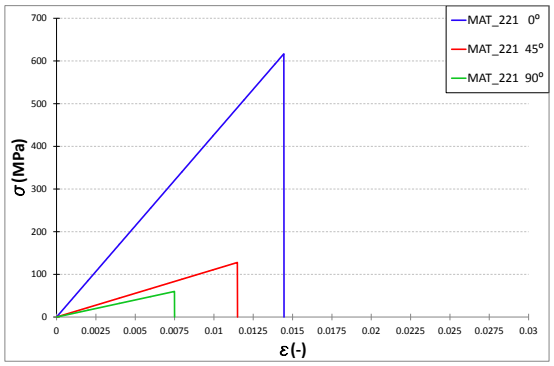

(D) Tension in BC plane

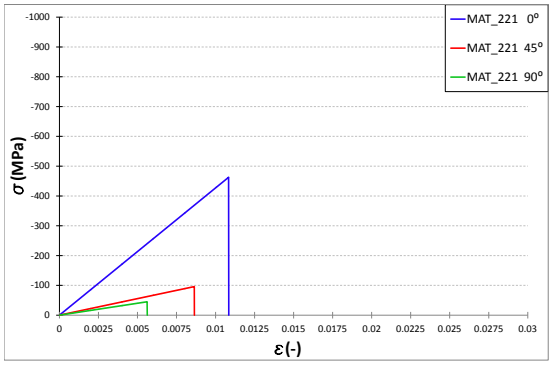

(E) Compression in BC plane

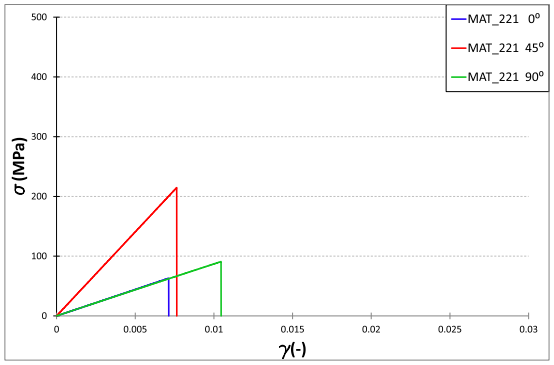

(F) Shear in BC plane

Figure B.3: MAT_221 single element test results for 0°, 45° and 90° material orientation in AC plane(A-C) and BC plane (D-F).

Table B.9: Failure strengths for MAT_221 in AC plane.

MAT_221 AC					
	LAYUP	LS-DYNA INPUT	LS-DYNA OUTPUT	Error	FC
TENSION	0°	1119	1118.25	0.07%	-
	45°	101	111.768	-10.67%	-
	90°	60	59.935	0.11%	-
COMPRESSION	0°	-768	-768.075	-0.01%	-
	45°	-	-75.984	-	-
	90°	-45	-44.925	0.17%	-
SHEAR	0°	93	55.900	39.90%	-
	45°	-	209.408	-	-
	90°	93	55.900	39.90%	-

Table B.10: Failure strengths for MAT_221 in BC plane.

MAT_221 BC					
	LAYUP	LS-DYNA INPUT	LS-DYNA OUTPUT	Error	FC
TENSION	0°	617	616.804	0.03%	-
	45°	82	127.866	-26.60%	-
	90°	60	59.935	0.11%	-
COMPRESSION	0°	-463	-462.803	0.04%	-
	45°	-	-95.852	-	-
	90°	-45	-44.925	0.17%	-
SHEAR	0°	56	56.010	-0.02%	-
	45°	-	308.474	-	-
	90°	56	55.016	-0.02%	-

Table B.11: Failure strains for MAT_221 in AC plane.

MAT_221 AC					
	LAYUP	LS-DYNA INPUT	LS-DYNA OUTPUT	Error	FC
TENSION	0°	0.015805	0.015804	-0.00%	-
	45°	-	0.014366	-	-
	90°	0.007500	0.007502	-0.03%	-
COMPRESSION	0°	0.010848	0.010859	-0.10%	-
	45°	-	0.012032	-	-
	90°	0.005625	0.005626	-0.01%	-
SHEAR	0°	0.013774	0.021170	-0.16%	-
	45°	-	0.016337	-	-
	90°	0.013774	0.021361	-1.06%	-

Table B.12: Failure strains for MAT_221 in BC plane.

MAT_221 BC					
	LAYUP	LS-DYNA INPUT	LS-DYNA OUTPUT	Error	FC
TENSION	0°	0.01445	0.014455	0.04%	-
	45°	-	0.011503	-	-
	90°	0.0075	0.007502	-0.02%	-
COMPRESSION	0°	0.010843	0.010849	-0.05%	-
	45°	-	0.008647	-	-
	90°	0.005625	0.005626	-0.01%	-
SHEAR	0°	0.013774	0.014259	30.05%	-
	45°	-	0.015280	-	-
	90°	0.013774	0.020917	-2.61%	-

Appendix C

Bird impact experiment

C.1 Sequence of the bird impact on the novel composite sandwich panel

(C.1.1)

(C.1.2)

(C.1.3)

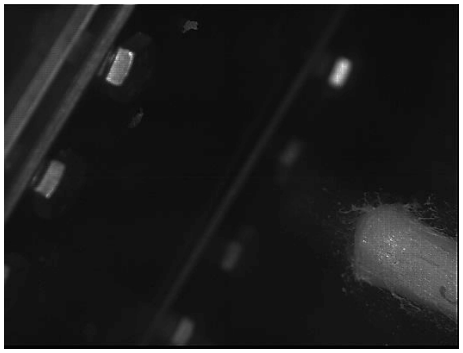

(C.1.4)

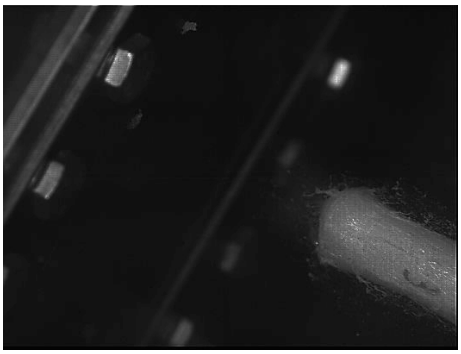

(C.1.5)

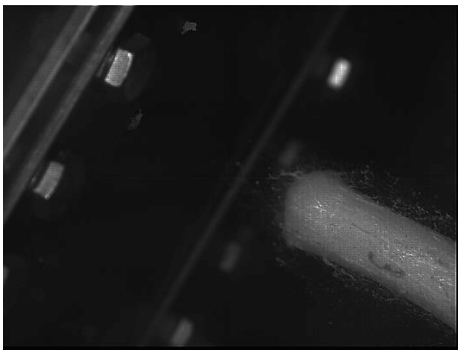

(C.1.6)

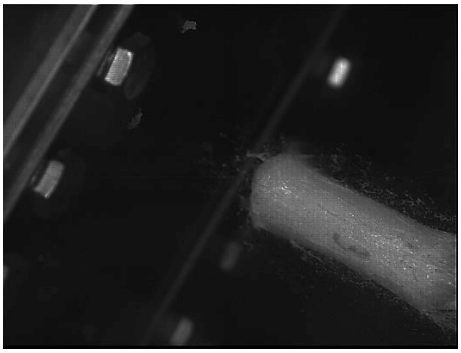

(C.1.7)

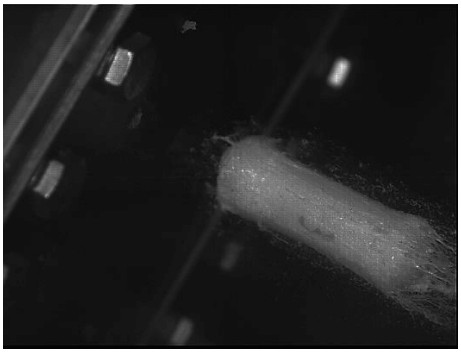

(C.1.8)

(C.1.9)

(C.1.10)

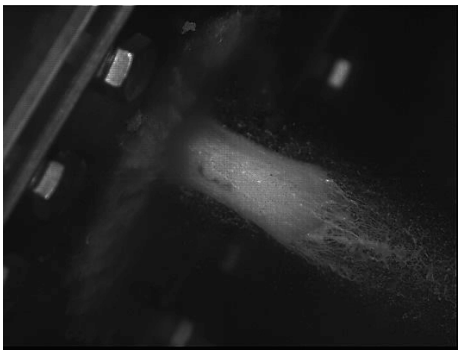

(C.1.11)

(C.1.12)

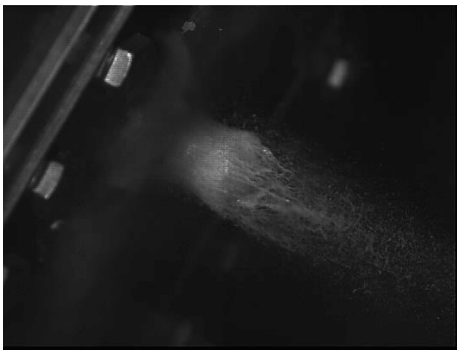

(C.1.13)

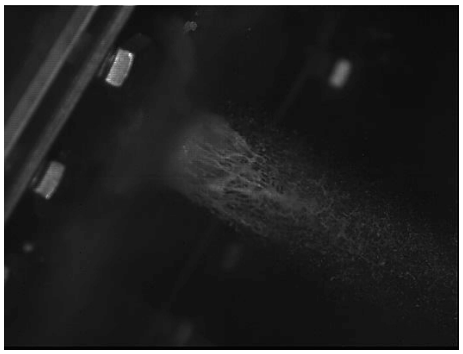

(C.1.14)

(C.1.15)

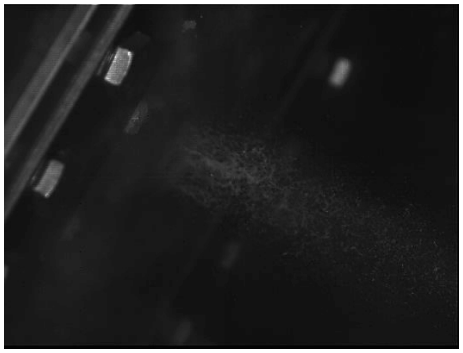

(C.1.16)

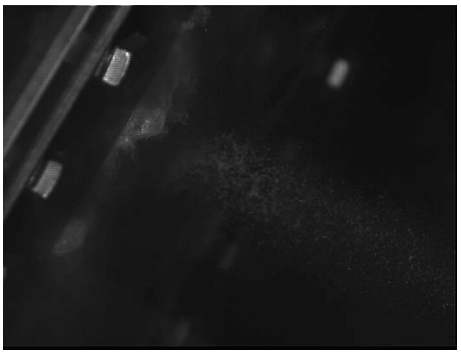

(C.1.17)

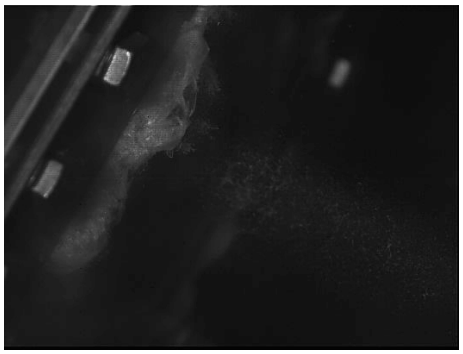

(C.1.18)

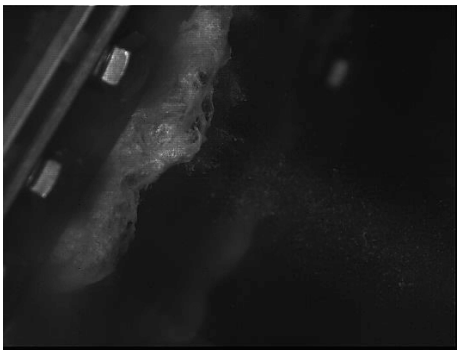

(C.1.19)

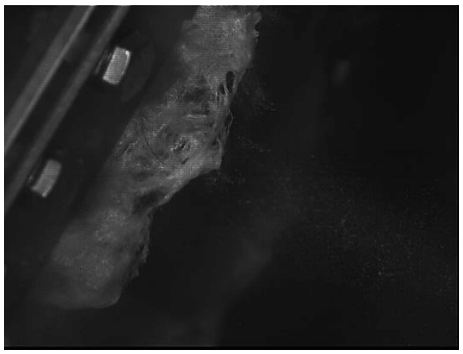

(C.1.20)

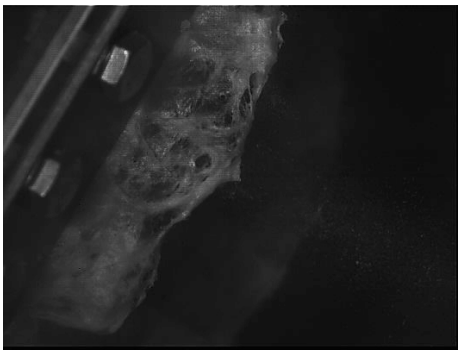

(C.1.21)

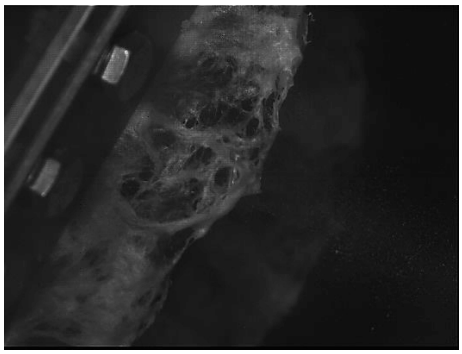

(C.1.22)

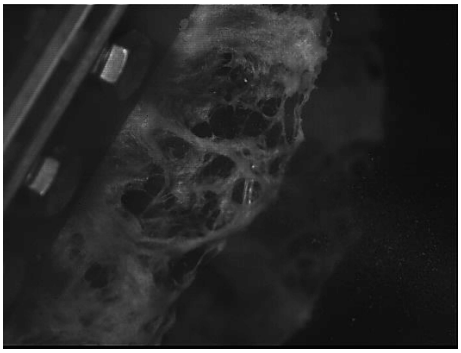

(C.1.23)

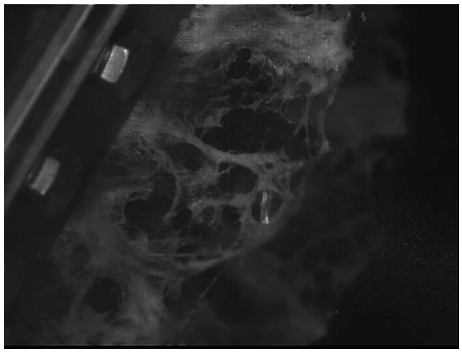

(C.1.24)

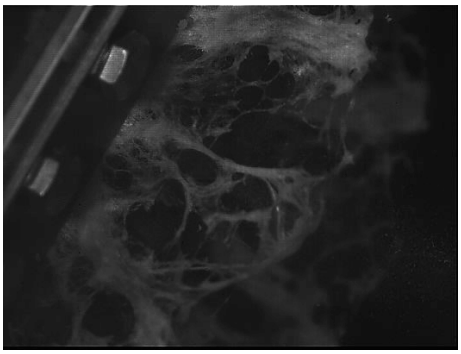

(C.1.25)

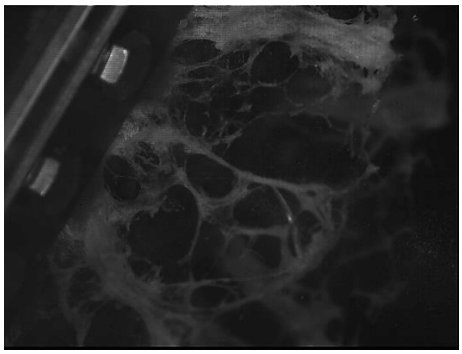

(C.1.26)

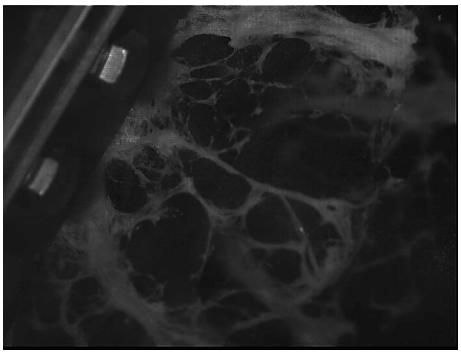

(C.1.27)

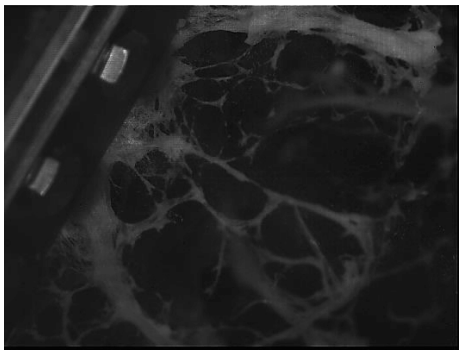

(C.1.28)

FIGURE C.1: Bird impact sequence images at time intervals of 0.8 *ms* - bird impact on CSP_1

C.2 Sequence of the damage threshold impact on TCP1

(C.2.1)

(C.2.2)

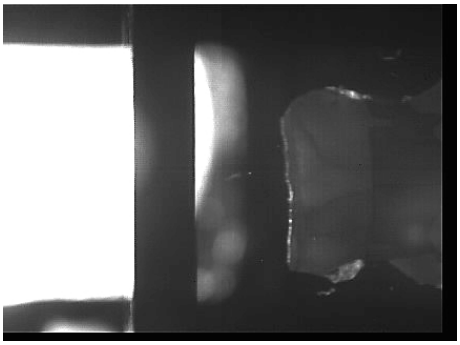

(C.2.3)

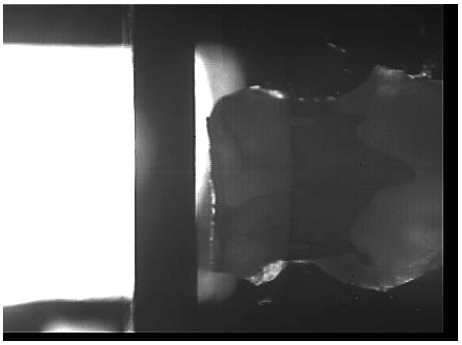

(C.2.4)

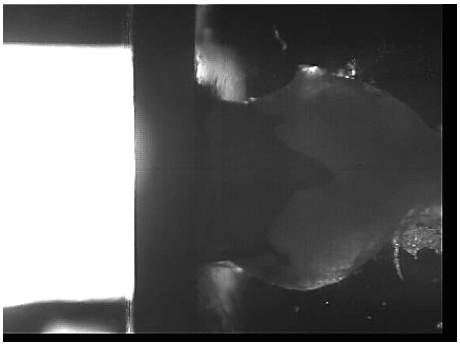

(C.2.5)

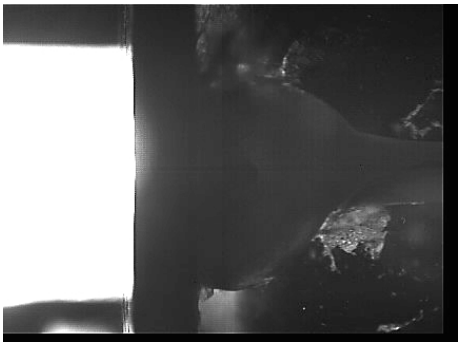

(C.2.6)

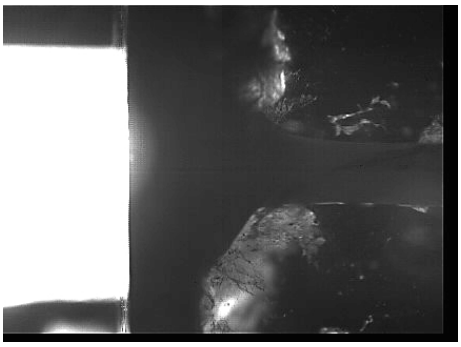

(C.2.7)

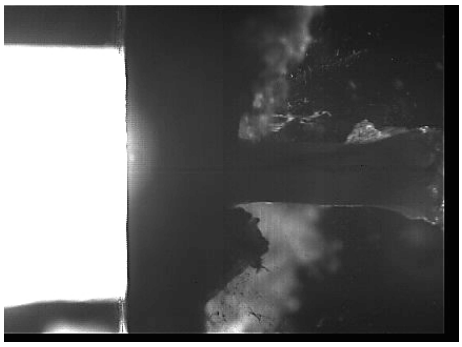

(C.2.8)

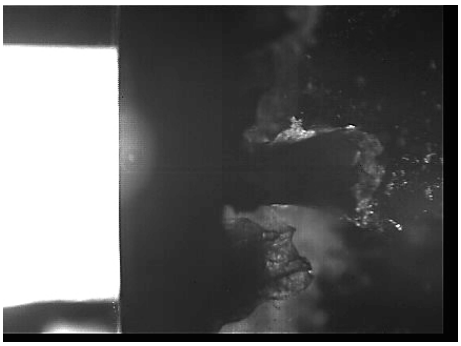

(C.2.9)

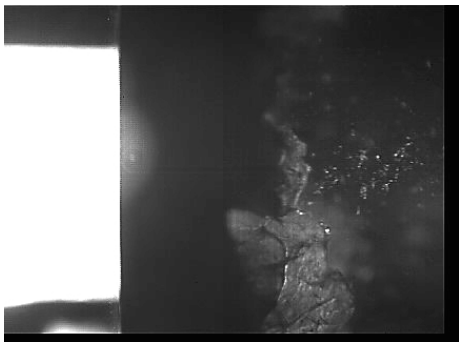

(C.2.10)

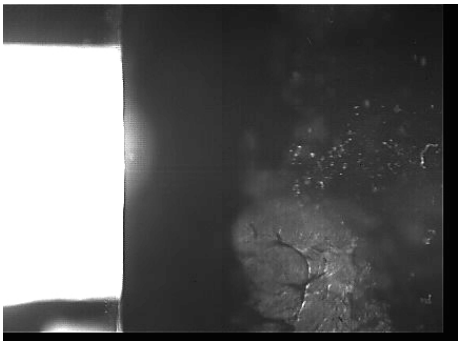

(C.2.11)

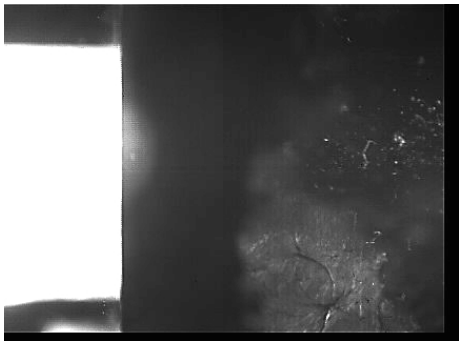

(C.2.12)

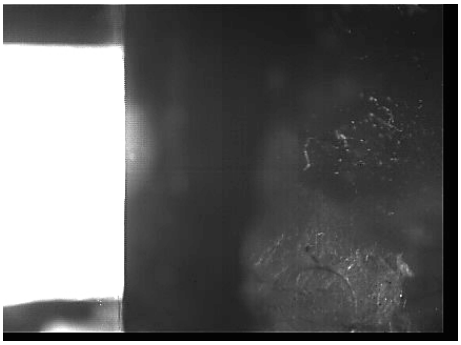

(C.2.13)

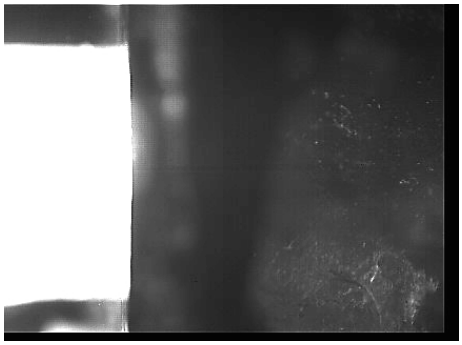

(C.2.14)

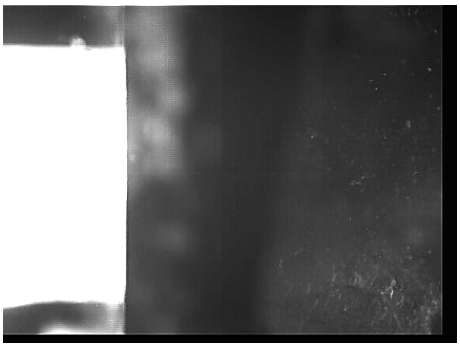

(C.2.15)

(C.2.16)

Figure C.2: Bird impact sequence images at time intervals of 0.8 *ms* - damage threshold impact on TSP_1.

C.3 Sequence of bird impact on the aluminium plate

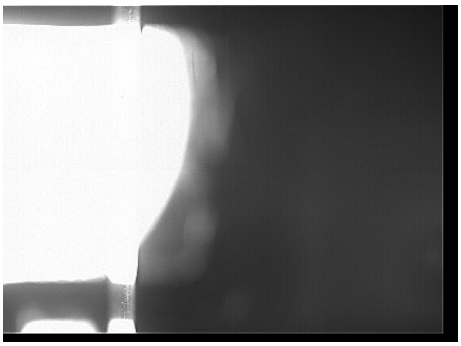

(C.3.1)

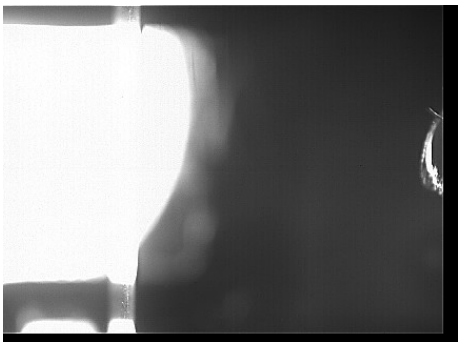

(C.3.2)

(C.3.3)

(C.3.4)

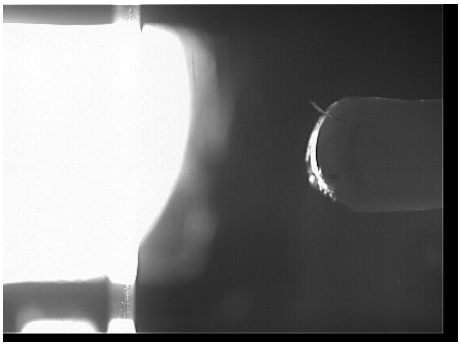

(C.3.5)

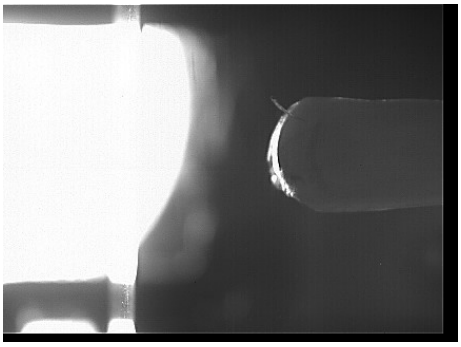

(C.3.6)

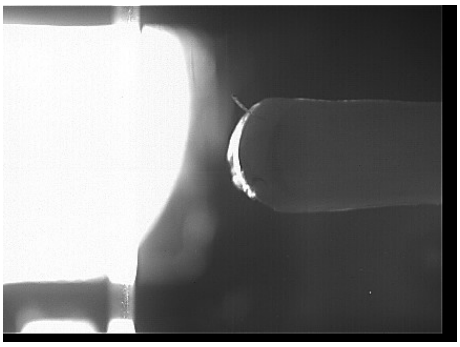

(C.3.7)

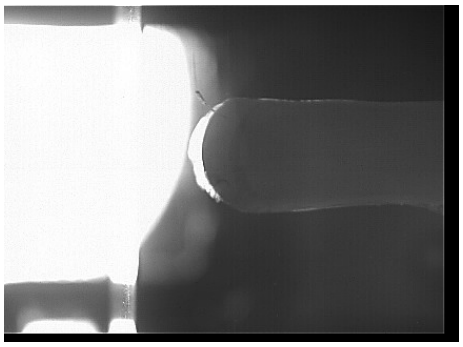

(C.3.8)

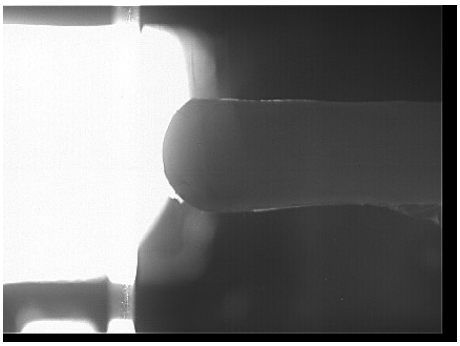

(C.3.9)

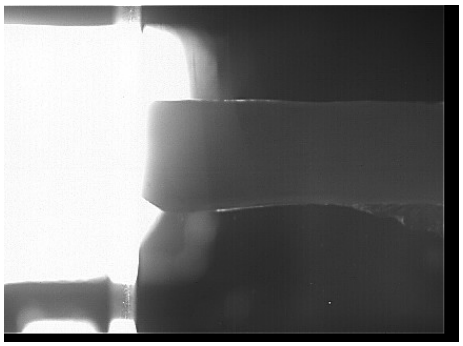

(C.3.10)

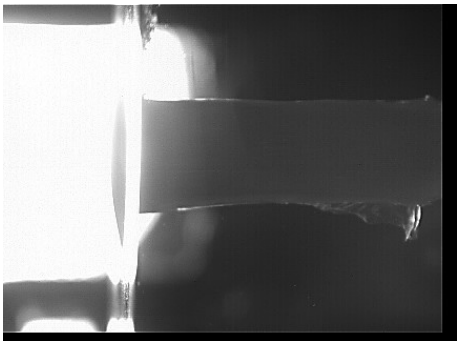

(C.3.11)

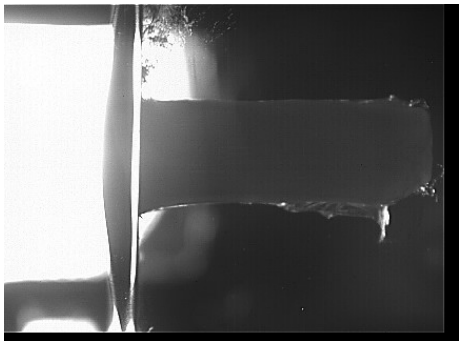

(C.3.12)

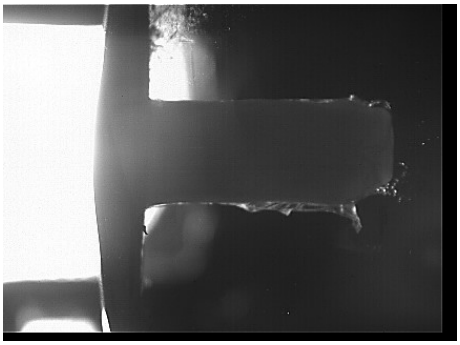

(C.3.13)

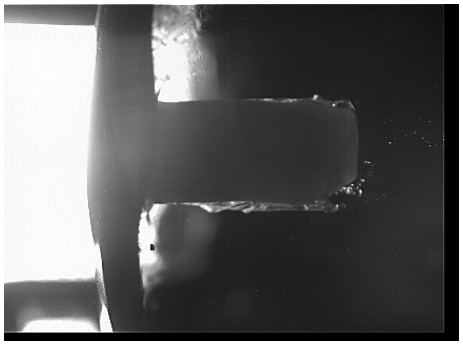

(C.3.14)

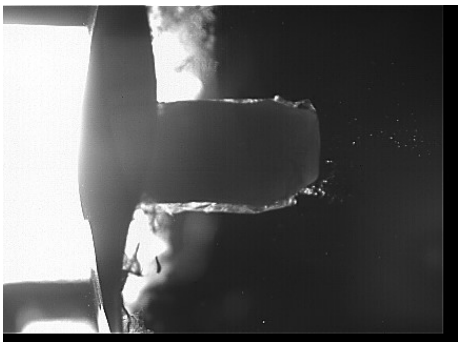

(C.3.15)

(C.3.16)

(C.3.17)

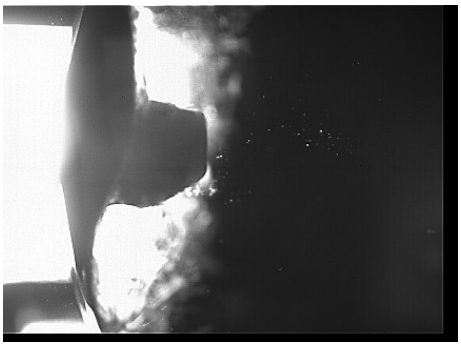

(C.3.18)

(C.3.19)

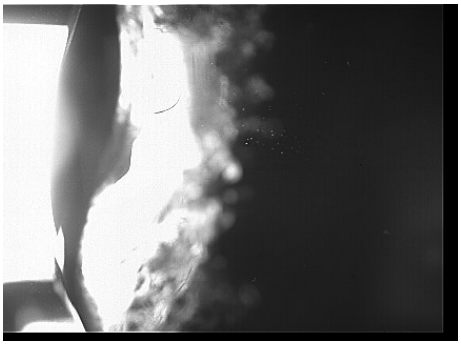

(C.3.20)

(C.3.21)

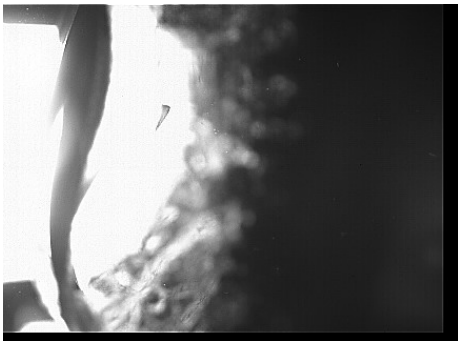

(C.3.22)

(C.3.23)

(C.3.24)

(C.3.25)

(C.3.26)

(C.3.27)

(C.3.28)

(C.3.29)

(C.3.30)

(C.3.31)

(C.3.32)

(C.3.33)

(C.3.34)

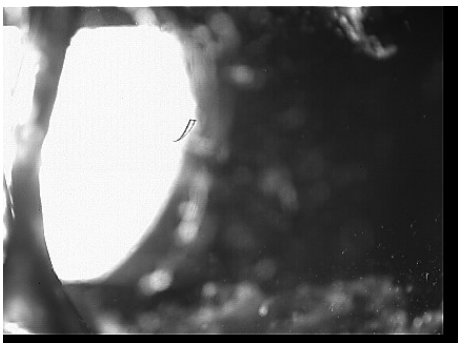

(C.3.35)

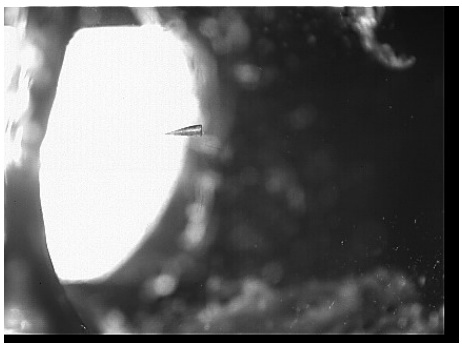

(C.3.36)

Figure C.3: Bird impact sequence images at time intervals of 0.8 *ms* - aluminium plate.